RF MAGNETRON–SPUTTERED ZNO THIN FILMS:
ON THE EVOLUTION OF MICROSTRUCTURE AND RESIDUAL STRESSES

by

İSTEM ÖZEN

Submitted to the Graduate School of Engineering and Natural Sciences
in partial fulfillment of
the requirements for the degree of
Doctor of Philosophy

Sabancı University

August 2006

RF MAGNETRON–SPUTTERED ZNO THIN FILMS:
ON THE EVOLUTION OF MICROSTRUCTURE AND RESIDUAL STRESSES

APPROVED BY:

Assoc. Prof. Dr. Mehmet Ali GÜLGÜN
(Dissertation Supervisor)

Prof. Dr. Sabri ALTINTAŞ

Assoc. Prof. Dr. Levent DEMİREL

Assist. Prof. Dr. Cleva OW–YANG

Assist. Prof. Dr. Melih PAPİLA

DATE OF APPROVAL: 15th September 2006

© 2006 by İstem ÖZEN
ALL RIGHTS RESERVED.

RF MAGNETRON–SPUTTERED ZNO THIN FILMS:
ON THE EVOLUTION OF MICROSTRUCTURE AND RESIDUAL STRESSES

İstem ÖZEN

Materials Science and Engineering, PhD Dissertation, 2006

Supervisor: Assoc. Prof. Dr. Mehmet Ali GÜLGÜN

Keywords: ZnO, thin film, RF magnetron sputtering, residual stress, texture.

ABSTRACT

Thin ZnO films (200–500 nm) were deposited onto glass, mica, and Si(100) substrates, to study the relations between microstructure and residual stresses. The ranges for the substrate temperature, chamber pressure, and RF power were room temperature–200 °C, 0.009–0.4 mbar, and 100–125 W, respectively.

The strain measurements by x-ray diffraction and the biaxial stress model showed that the films were under residual compressive stresses from -2 to -8 GPa. 5–11 percent of those stresses were induced by the thermal expansion coefficient mismatch, while the so-called growth stresses formed the majority.

The films were strongly textured along the (002)-direction with additional (101)-texture under specific conditions. The texture of the film–substrate interface played a significant role in the average film texture and the residual stress.

Variations from the previously developed structure zone models (SZM) and the microstructures in the pressure ranges beyond those SZMs were investigated by scanning electron microscopy. Several mechanisms of microstructure evolution and consequent stress development were proposed.

Thermal annealing and aging removed the growth stresses and improved the texture. Annealing caused pore clustering and crack formation. Thus, annealing should be treated with caution when used as a method for stress relaxation. Buffer layer

deposition and in–chamber heat treatment were proposed as alternatives to post–deposition annealing.

Annealing led to structures on the ZnO film surface up to 100 nanometers in width and 1 micrometer in height. This was attributed to the stress-induced directional diffusion.

RF MAGNETRON SIÇRATMA İLE ÜRETİLMİŞ ZNO İNCE FİLMLER:
MİKROYAPININ VE ARTIK GERİLMENİN EVRİMİ ÜZERİNE

İstem ÖZEN

Malzeme Bilimi ve Mühendisliği, Doktora Tezi, 2006

Tez Danışmanı: Doç. Dr. Mehmet Ali GÜLGÜN

Anahtar kelimeler: ZnO, ince film, RF magnetron sıçratma, artık gerilme, tercihli yönlenme.

ÖZET

Bu çalışmada, mikro-yapı ve artık gerilme arasındaki ilişkileri incelemek üzere, ZnO ince filmler (200–500 nm), cam, Si(100), ve mika altlıklar üzerine kaplanmıştır. Altlık sıcaklığı, hazne basıncı ve RF kaynağı gücü sırasıyla oda sıcaklığı–200 °C, 0.009–0.4 mbar ve 100–125 W arasında değiştirilmiştir.

X-ışını kırınımı ile ölçülen gerinim ve eşeksenli gerilme modeli filmlerde basma yönünde -2 ile -8 GPa arasında artık gerilme olduğunu göstermiştir. Bu gerilmelerin yüzde 5-11'i ısıl genleşme katsayısı uyuşmazlığından kaynaklanmış, artık gerilmenin çoğunu ise büyüme gerilmeleri oluşturmuştur.

Filmler (002) yönünde kuvvetli tercihli yönlenmeyle büyümüş, bazı kaplama koşullarında ek olarak (101) yönlenmesine rastlanmıştır. Film ile altlık ara yüzey yapısı tercihli yönlenmeyi ve artık gerilmeyi etkilemiştir.

Literatürde daha önce sunulmuş olan yapı–bölgesi modelleri ile olan farklılıklar ile bu modellerin içermediği basınç aralıklarındaki mikro-yapı incelenmiştir. Filmlerdeki mikro-yapının ve buna bağlı artık gerilmenin oluşumunu açıklamak üzere çeşitli mekanizmalar öne sürülmüştür.

Isıl tavlama ve yaşlandırma filmlerdeki büyüme gerilmelerini gidermiştir. Isıl tavlama sonucu oluşan gözenek büyümesi filmlerde çatlaklara sebep olmuştur. Bu nedenle ısıl tavlama gerilme giderilmesinde dikkatle uygulanmalıdır.

Isıl tavlama sonucu bazı filmlerin yüzeylerinde yaklaşık 100 nanometre genişliğe ve 1 mikrometre yüksekliğe kadar nano-çubuk büyümesi gözlenmiştir. Bu davranış, gerilmeye bağlı tercihli yönlenmiş difüzyon ile açıklanmıştır.

To the memory of my beloved grandfather ***MEHMET AKYÜREK.***

To my family and to all who taught me.

Sevgili dedem ***MEHMET AKYÜREK****'in anısına.*

Aileme ve bütün öğretenlerime.

ACKNOWLEDGEMENTS

There are so many people who have been helpful to me in one way or another throughout my six years of this PhD marathon.

First of all, I would like to thank all the sapient minds from every continent, who have pursued knowledge with righteousness throughout history, and thus paved the way for us, inspired us, and encouraged us.

I would like to express my respect and gratitude to my supervisor Dr. Mehmet Ali Gülgün for supporting and guiding me throughout my doctorate, his patience, and always having an open door whenever I needed one. His ingenious remarks paved the way to putting this dissertation together. I will always remember and be inspired by his enthusiasm, hard work, and good heart.

Special thanks go to my dissertation committee member Dr. Cleva Ow-Yang for her guidance throughout my doctorate experience as well as the tedious work of revision on my dissertation and to my former dissertation committee member Dr. Meriç Özcan for his collaboration and guidance. I acknowledge the members of my defense committee Dr. Melih Papila, Dr. Sabri Altıntaş, and Dr. Levent Demirel for their valuable comments and revisions on the dissertation draft. I also would like to mention my admiration for Dr. Alpay Taralp for his continuous support, contagious enthusiasm, and constructive encouragement, and Dr. Ali Alpar for being a source of inspiration and a role model. I thank Dr. Yaşar Gürbüz for his cooperation about my clean room practice and helping me schedule my experiments. I thank all the other former and present faculty members of the Materials Science and Engineering Program of Sabancı University (Dr. Burak Erman, Dr. Yuda Yürüm, Dr. Naci İnci, Dr. Canan Atılgan, Dr. Yusuf Menceloğlu, Dr. Ali Rana Atılgan, Dr. Gürsel Sönmez, Dr. Gürhan Kalay) for

giving me the opportunity to be a member of this dynamic, educational, and friendly environment, and their willingness to share deep knowledge and invaluable time.

Words cannot express my gratitude to our laboratory specialist and clean room technician Bülent Köroğlu. This study would simply be impossible to complete without his dedication, energy, and helpfulness in the clean room.

I am indebted to my dearest friends, for being with me through the thick and thin. I have to start with Zeynep Berik and Işın Önol; I was very lucky to start my journey in this university with them and to still have them by my side after all these years. I am indebted to my friend Ahu Gümrah Dumanlı, for being much more than the best office mate/neighbor, for the delicious food, for the ears, and for bearing with me when I was the most unbearable. I can never forget the memory of Ali Oytun Gökhan, his contagious smile, and his creative ways of trying to cheer me up—may he rest in peace.

I feel very lucky to have the love and support of my dear friends that I left in cities far away: Özgür Keşaplı Didrickson, Özlem Çirli; Elif Gündüz, Güçlü İnsel, Kerem Bora, and all the former "Latife" residents—their touch from afar meant a lot. I also thank the wonderful people I met in SU for delighting various periods of my life at this university: Başak Yenier (for being the precious yet humble herself), Alper Arslan (for our intriguing discussions on almost anything and for showing me that opposites attract—but not necessarily), Demet Teker and Nalan Bilgin (my two short-term but wonderful flat mates), Markus Kolodzie (I am still proud of ″our lab″), Yavuz Ekşi (I hope to hear the tunes and have you share your brightness again some day), Can Sümer (for the positive energy in the office during that summer and witnessing me create the ″thesis.doc″ file), Emre Özlü (for his generosity, effortlessly showing me that it was easier than it seemed, and his wonderful illustration work in my dissertation), Emre Heves and Yalçın Yamaner (for helping me overcome the madness in the clean room during the most critical months), Taner Tunç and Lale Tunçyürek (for the coffee and the laugh that kept me awake during the writing period), Burcu Saner, Ayşe Özlem Sezerman, Aslı Nalbant, Ayça Erden, and Canan Barıştıran (fresh blood to the MAT group—it was great to feel your presence by my side every now and then), Dr. Atakan Gürkan, Dr. Defne Üçer, Dr. Ersin Göğüş, and Dr. Emrah Kalemci (I am very happy to have our paths crossed once more after our METU years and to have shared with you a piece of this experience), Billur Sakintuna, Teoman Naşkalı, Mutlu Doğruel, and Burcu

Kaplan (for helping me keep contact with the outer world). I thank all the other present and former Materials Science Engineering graduates as well as all my friends in SUSS, SUAAT, and SU War Opponents (and Turgay Oğur) for enriching my life in many ways.

I have been proud to be a member of the first group of graduate students of the Materials Science and Engineering Program of SU. I want to thank the following people for sharing this joy with me: Dr. Arzu Altay (who was also my ally right from the start, fed me, and taught me a lot in the laboratory), Dr. Yeşim Müge Çalık, Dr. Kazım Acatay, Dr. Mustafa Demir, Dr. Serdal Kırmızıaltın, and last but not least, future doctor and all-time genius Çınar Öncel (for giving me the laugh when I expected it the least but probably needed it the most).

I will always feel privileged to have witnessed and taken part in the establishment of a new and bright university. I wholeheartedly thank all the SU family for that matter. I want to single out with thanks our former administrative affairs specialist Saila Kurtbay for always being like an elder sister to me and to all the graduate students. My special thanks go to our laboratory specialist Burçin Yıldız for brightening my day in the XRD–NMR laboratory, where there was no sunshine. I also thank the current administrative staff (including Zehra Öner, Işıl Önal Karabudak, Çağla Gürsu) and the laboratory specialists of FENS (Sibel Pürçüklü, Tuğba Baytekin Birkan) for their warmth and the effort they put in trying to resolve the issues. I am indebted to the Information Technologies personnel Şenol Yıldırım and Mustafa Yörükoğlu for saving my computer's and my files' lives numerous times, and never hesitating to spend their valuable time to help me. I greatly appreciate all the Information Center staff, especially Mehmet Manyas, Bahadır Barut, and Faik Keskin, for their devotion to their work and helping me access any resource I needed. I thank all my former students for giving me the chance to have the valuable teaching experience with them as well as all the former and present residents of Irmak 2-Mutlukent for sharing the same roof with me. I also thank our superintendent Erdoğan İnce for taking care of us, Gül Altınoluk, Dr. Zehra Kalkan, Dr. Tolga Taymaz, and all the SU workers for their genuine kindness the services.

I would like to express my gratitude to the following people for their technical support and enthusiastic help during my laboratory work: Baybars Oral (Vaksis,

Ankara), Rıza Özersay (Nanospek, Istanbul), Carlos Gamiz (Bruker AXS, Karlsruhe), Jents Bretchbül (Bruker AXS, Karlsruhe), Mustafa Kemal Öztürk (Gazi University, Ankara), Kağan Yurdal, Attila Alkan (Brisa, İzmit), and Mehmet Güler (Sabancı University, Istanbul).

I sincerely thank Dr. Hugo Thienpont (Vrije University of Brussels), Dr. Peter Van Daele (University of Ghent), Dr. Geert Van Steinberge (University of Ghent), Nina Hendricxs (University of Ghent), Erwin Bosman (University of Ghent), and Dr. Daryush Ila (Alabama A&M University) for our valuable collaborations within various projects throughout my doctoral education.

I appreciate SPIE Press, IOP, Elsevier, Academic Press, Pergamon Press, AVS, AIP, ACS, Dr. Glen Kovach, Dr. Tony Evans, Dr. Ümit Özgür, Dr. Russell F. Messier, and Dr. Boris Movchan, for giving me the permission to reprint graphs and illustrations from their publications, and all the authors of the works that were cited in this study for giving me a chance to build a basis for my dissertation. I acknowledge Dr. Selçuk Dursun for helping me formatting my dissertation and providing the necessary documents for finalizing the submission process and Nancy Karabeyoğlu for helping me fix the language.

I particularly want to thank Dr. Jorge Cham for creating the wonderful environment that is the PhD Comics[i], and everyone in PhD Comics Phorum for all the badgers, turtles, mushrooms, hippos, elephants, and the virtual hugs that kept me sane during the last months, and for teaching me a lot. I love our herd, our unique jargon, and the madly evolving complexity of the world we take part in. I also thank ABD Survival Guide[ii], Gordon Rugg[iii], and Marian Petre[iii] for providing valuable insight about the obstacles arising during the PhD period, Radio Paradise and RadyoSU for the wonderful music (and the latter for accepting my song requests during long and lonely nights in the laboratory).

Last, but most important of all, I owe deep thanks to my dear family. I have to start with Aytanga and Ceylan—I could have never achieved that much without their strength, their generosity, and their faith in me. I hope I can prove to be worth what they have given to me throughout the rest of my life. I can not thank my grandparents Mehmet and Mediha enough, for their patience and for always making me feel that I

was doing right whenever I felt lost. I also thank Deniz, Volkan, Behnan, and Huşper, who did not leave me without a piece of their loving support, while I have always been preoccupied.

I apologize from anyone whom I have unwillingly forgotten to mention. I wish plenty of mental alertness and patience for all my friends who are pursuing their studies. I wish all the graduates to have the conscience, common sense, courage, and power to use the things we achieved here in a good way for the rest of our lives.

Peace.

---

i. www.phdcomics.com

ii. www.abdsurvivalguide.com

iii. Rugg, G. and Petre, M., The Unwritten Rules of PhD Research, 2nd Ed., 2005, Open University Press, Berkshire, England.

TABLE OF CONTENTS

ABSTRACT iv

ÖZET vi

ACKNOWLEDGEMENTS ix

TABLE OF CONTENTS xiv

LIST OF FIGURES xviii

LIST OF TABLES xxxv

LIST OF SYMBOLS AND ABBREVIATIONS xxxix

CHAPTER 1 1

INTRODUCTION 1

1.1. ZnO as a Ceramic Material 3

1.1.1. Structure 3

1.1.2. Optical, Electrical, Piezoelectric, and Mechanical Properties 5

1.2. Functional Thin Films 10

1.2.1. Structure-Zone Models 10

1.2.2. Texture in Thin Films 18

1.2.3. Mechanical Properties and Residual Stresses in Thin Films 20

1.3. ZnO as a Functional Thin Film Material 35

1.3.1. Microstructure 36

1.3.2. Mechanical Properties and Residual Stresses 44

1.3.3. Optical and Electrical Properties 52

1.4. Thin Film Deposition 54

1.4.1. Radio Frequency Magnetron Sputtering 56

1.5. Measurement of Residual Stresses in Thin Films 63

CHAPTER 2 67
AIM AND MOTIVATION.. 67
CHAPTER 3 71
EXPERIMENTAL PROCEDURES 71
3.1. Substrate Preparation 71
3.2. Film Deposition 73
3.3. Post-deposition Treatments...79
3.3.1. Thermal Annealing 79
3.3.2. Aging 80
3.4. Material Characterization 80
3.4.1. Microstructure..81
3.4.2. Crystal Structure and Residual Stress Analysis 82
3.4.2.1. Phase analysis and strain measurement 82
3.4.2.2. Calculation of the average residual stress 86
3.4.2.3. Calculation of the thermal stresses 95
3.4.2.4. Calculation of grain size 99
CHAPTER 4 100
RESULTS 100
4.1. General Structure of the As-deposited ZnO Thin Films..........................100
4.2. Residual Stresses in ZnO Thin Films 104
4.2.1. Substrate Effects on the Residual Stress...104
4.2.2. Contribution of Thermal Mismatch Strain on the Residual Stress 107
4.2.3. Effects of the Deposition Parameters on Residual Stresses..............110
4.3. Effects of the Deposition Parameters on the Film Microstructure 115
4.4. Effects of the Deposition Parameters on the Film Texture......................120
4.5. Effects of the Buffer layer on the Residual Stress, Texture, and Microstructure..123
4.6. Stress Relaxation by Thermal Annealing or Aging 128
CHAPTER 5 149
DISCUSSION 149
5.1. Microstructure and Texture of ZnO Thin Films 149
5.1.1. Effect of the Substrate Material on the Film Microstructure............154

5.1.2. Effect of the Deposition Parameters on the Film Microstructure and Texture 158
5.1.3. Effect of Buffer Layer Deposition on the Film Microstructure 171
5.1.4. Grain Size 173
5.1.5. Section Summary 174
5.2. Residual Stresses and Their Origins 175
5.2.1. Thermal Expansion Mismatch between ZnO and the Substrate Materials 177
5.2.2. Argon Entrapment inside the Films 180
5.2.3. Microstructure-Related Factors: "Growth Stresses" 182
5.2.3.1. Effects of the deposition parameters on the residual stresses revisited 185
5.2.3.2. Effects of the buffer layer on the "growth stresses" 195
5.2.4. Section Summary 196
5.3. Stress Relaxation 197
5.3.1. Stress Relaxation Mechanisms and Relevant Causes of Residual Stress 198
5.3.2. Drawbacks of Stress Relaxation and Possible Solutions 202
5.3.3. Section Summary 212

CHAPTER 6 214
CONCLUDING REMARKS AND FUTURE WORK 214

APPENDICES 218
A. Cleaning Procedure for Glass Substrates 218
B. Powder Diffraction Standards 220
B.1. ZnO 220
B.2. Si 222
B.3. Mica 225
C. Representative XRD Spectra of the Crystalline Substrates 229
C.1. Si 229
C.2. Mica 230
D. Temperature Calibrations for the RFMS System 231
D.1. Equilibrium temperature around the substrate holder during film deposition 231

D.2. Heating and cooling curves of the main chamber and the substrate holder before and after deposition. 232
E. Optical Transmittance Measurements 233
E.1. Experimental Procedure..233
E.2. Results..234
BIBLIOGRAPHY...240
VITA 259

LIST OF FIGURES

Figure 1.1. Various crystal structures of ZnO formed by Zn (shaded gray) and oxygen (black) atoms (Reprinted from Ref. [13]; published with permission from AIP.). 3

Figure 1.2. (a) Natural zincite crystals. (Left: Copyright by Lou Perloff / Photo Atlas of Minerals [20]; right: Copyright by O. Dziallas 2005 [21].) (b) Zinc oxide single crystal produced by microwave processing [22]. (c) Crystal set of planes and Miller indices of wurtzite-type zinc oxide. 4

Figure 1.3. Univariant *p-T* curve between two phases of ZnO [23, 24]. 5

Figure 1.4. Stages of film growth: (a) island formation, (b) layer formation, (c) combined island and layer formation...11

Figure 1.5. The first structure zone model, proposed by Movchan and Demchishin. (Reprinted from Ref. [51]; original figure by Ref. [55]; published with permission from SPIE Press and Elsevier Publishing Ltd.)...13

Figure 1.6. Two different growth behaviors for columnar films: (a) tapered columns, (b) parallel-walled columns...13

Figure 1.7. Representation of the structure zone model modified by Thornton. (Reprinted from Ref. [51]; original figure by Ref. [51, 54]; published with permission from SPIE Press and AVS Publishing Ltd.)...................14

Figure 1.8. Zone model for the grain structure of vapor deposited metal films modified at low temperatures, including the fine equiaxed grain

structure (Reprinted from Ref. [58]; with permission from Elsevier Publishing Ltd.). 15

Figure 1.9. Zone model for the grain structure of vapor deposited metal films modified to include the bimodal grain size distribution in Zone T, also including the mechanisms that are proposed to control the grain structure in each of the zones. (Reprinted from Ref. [58]; with permission from Elsevier Publishing Ltd.). 15

Figure 1.10. The fractal grain structure at different length scales for thin films grown under low adatom mobility (Reprinted from Ref. [59]; published with permission from AVS). 16

Figure 1.11. Revised zone model with sub-zones of Zone 1 depending on film thickness and the mobility of adatoms induced by energetic ion bombardment (Reprinted from Ref. [59]; published with permission from AVS). 17

Figure 1.12. A recent structure-zone model developed by Messier and Trolier-McKinstry. (Reprinted from Ref. [51]; original figure by Ref. [63]; published with permission from SPIE Press and Elsevier Publishing Ltd.)..17

Figure 1.13. Demonstration of texture in columnar thin films. (a) Polycrystalline: the crystallites are randomly distributed on the substrate. (b) Polycrystalline with strong texture: the crystallites have a preferred orientation with respect to the substrate plane. (c) Single crystal: Perfect texture; all the crystals are oriented in the same direction with respect to all three axes..19

Figure 1.14. Development of residual compressive and tensile stresses in thin films. When the substrate and the film have shrunk with different amounts, the resulting bending moments bend the laminate. The dashed arrows show the direction of bending, and the solid arrows show the direction of the residual stress in the material after the system is bent...22

Figure 1.15. Coating deformation and buckling due to compressive stress on oxide layers. (a) Optical microscope image of a SiO_2 coating on

PMMA [83]. (b) Thermally grown alumina film formed at 1100 °C after 10 h and then furnace cooled to room temperature (Reprinted from Ref. [84] with permission from Elsevier Publishing Ltd.)...............24

Figure 1.16. Commonly observed cracking patterns [86]. (Reprinted from Ref. [86] with permission from Elsevier Publishing Ltd.). 25

Figure. 1.17. A schematic indicating the sequence of events when a compressed film buckles and spalls away from a substrate (Reprinted from Ref. [84] with permission from Elsevier Publishing Ltd.). 28

Figure 1.18. Characteristic buckling configurations. (a) An imperfection with no apparent buckle, (b) an imperfection (arrowed) at the perimeter of an axi-symmetric buckle, (c) an imperfection (arrowed) at one end of a telephone cord buckle, (d) two competing buckle delamination morphologies: telephone cord and a straight-sided buckle with a ridge crack that extends to within a buckle width of the front, (e) a FIB cross-section through the buckle with the ridge crack. ((a), (b), (c) reprinted from Ref. [90]; (d), (e) reprinted from Ref. [88]; all with permission from Elsevier Publishing Ltd.) 29

Figure 1.19. A buckling map derived from the mechanics of buckle propagation. The three domains are identified. (Reprinted from Ref. [84] with permission from Elsevier Publishing Ltd.) 30

Figure 1.20. The relative surface uplift, δ/h, as a function of the compressive stress, relative to the critical value for buckling. (Reprinted from Ref. [84] with permission from Elsevier Publishing Ltd.) 32

Figure 1.21. The measured and critical buckle sizes plotted as a function of the stress. (Reprinted from Ref. [84] with permission from Elsevier Publishing Ltd.) 32

Figure 1.22. The structure-phase zone model with the residual stress effect. The independent parameters are the oxygen partial pressure (p_{O_2}) and the deposition rate (R). (Adapted from Ref. [25] with permission from IOP Publishing Ltd.) 38

Figure 1.23. SEM micrographs for the zone matrix developed by Polley and Carter: (a) Zone A microstructure for 0.005 M solution concentration and 0.25 T_m deposition temperature in plane (left) and cross-sectional (right) views; (b) Zone T microstructure for 0.01 M solution concentration and 0.35 T_m deposition temperature in plane (left) and cross-sectional (right) views; (c) Zone 2 microstructure of 0.005 M solution concentration and 0.45 T_m deposition temperature in plane (left) and cross-sectional (right) view. (Reprinted from Ref. [135] with permission from Elsevier Publishing Ltd.) 39

Figure 1.24. Structure-zone matrix for ZnO films deposited by combustion chemical deposition. (Adapted from Ref. [135] with permission from Elsevier Publishing Ltd.) 40

Figure 1.25. Comparison of various structure zone models Reprinted from Ref. [136]; published with permission from the authors.)................................42

Figure 1.26. XRD spectra of RF-sputtered ZnO (---) and ZnO:Al (—) films of different thicknesses. From bottom to top the films were 170 and 370 nm (ZnO) and 40 and 360 nm (ZnO:Al) thick. The vertical bars display the diffraction pattern of zincite powder (JCPDS-No. 36-1451) [25, 138]. (Reprinted from Ref. [25] with permission from IOP Publishing Ltd.). 42

Figure 1.27. SEM images of the surfaces of ZnO films deposited on different buffer layer thicknesses: (a) no buffer layer; (b) 50-Å thick; (c) 100-Å thick; (d) 200-Å thick; (e) 500-Å thick. (Adapted from Ref. [141] with permission from Elsevier Publishing Ltd.). 43

Figure 1.28. XRD spectra of ZnO films deposited on different buffer layer thicknesses: (a) no buffer layer; (b) 50-Å thick; (c) 100-Å thick; (d) 200-Å thick; (e) 300-Å thick; (f) 500-Å thick. (The indices (0002) and (0004) correspond to the indices (002) and (004) in our study, respectively.) (Reprinted from Ref. [141] with permission from Elsevier Publishing Ltd.). 43

Figure 1.29. (a) Normalized crack length as a function of normalized load. (b) Critical buckling loads (P_c) in relation with buckling (Reprinted from Ref. [147]; published with permission from AIP.). 46

Figure 1.30. The total stress in a zinc oxide film calculated from the deflection measurements (open symbols) and the x-ray diffraction measurements (full symbols). (Reprinted from Ref. [156] with permission from IOP Publishing Ltd.)..50

Figure 1.31. (a) Dependence of the film stress on the sputtering pressure for ZnO and ZnO:Al films with sputtering parameters: P_{RF} = 30 W, h_{ZnO} = 120 nm, $h_{ZnO:Al}$ = 350 nm [138]. (b) Strain (left) and stress (right) of ZnO and ZnO:Al films depending on the $P_{DC}/(P_{DC} + P_{RF})$ ratio with sputtering parameters $P_{DC} + P_{RF}$ = 80 W and p_{Ar} = 0.8 Pa [25, 138]. (Reprinted from Ref. [25] with permission from IOP Publishing Ltd.)..51

Figure 1.32. The impact of an atom or ion on a surface produces sputtering from the surface as a result of momentum transfer from the incoming particle. No melting of the material occurs, unlike many other deposition techniques..56

Figure 1.33. Schematics for the RF magnetron sputtering method. The substrate is placed in a low-pressure chamber between two electrodes. The electrons are driven by an RF power source, which generates a plasma and ionizes the gas (*e.g.*, Ar) between the electrodes. A DC potential drives the ions towards the target, knocks atoms off the target, and condenses them on the substrate surface. A strong magnetic field is applied to contain the plasma surface of the target to increase the deposition rate...58

Figure 1.34. Plasma glow (a) around the substrate holder and the holder arm (present study), (b) around the target [167]. 59

Figure 3.1. The radio frequency magnetron sputtering (RFMS) system placed in a Class–1000 clean room. 74

Figure 3.2. Schematics of the RFMS deposition system. 76

Figure 3.3. A close look at the main chamber. 77

Figure 3.4 The positions and the indices of the substrates on the holder. The gray circles represent the temperature measuring strips. The measurable temperatures are: i) 43–54 °C, ii) 60–93 °C, iii) 93–126 °C, iv) 132–148 °C. 77

Figure 3.5. Heating and cooling curves for the annealing furnaces. 80

Figure 3.6. Sample cutting for cross-sectional SEM analysis. 81

Figure 3.7. XRD measurement configuration. (Adapted from Ref. [108].) 83

Figure 3.8. Sample placement configuration for XRD measurements. 84

Figure 3.9. Variable-temperature XRD set-up. 85

Figure 3.10. Demonstration of Bragg's Law. Only the reflections that have the required angle of incidence interfere constructively and yield an XRD peak. (Adapted from Ref. [204].) 86

Figure 3.11. Determining compressive and tensile stresses via the shift in the x-ray diffraction peaks (for the biaxial strain model, the stress along the direction 3 is zero, and equal amounts of stresses are present in along directions 1 and 2. For clarity, only the stress in the direction 1 is shown in the figure). 88

Figure 3.12. Theoretical compressive stress as a function of left-shift of the (002)-peak of the ZnO crystallites, calculated by the biaxial strain model. $\Delta(2\theta) = 2\theta_{sample} - 2\theta_{standard}$. ♦ = σ, = σ'. 94

Figure 3.13. Configuration of the dilatometer system. The sample is placed into the holder inside the furnace. As the sample expands, it pushes the pushrod and the effect is transferred onto the inductive transducer. The pressure signal is converted to a strain value based on the instrument calibration and monitored by the software. 98

Figure 3.14. The configuration of the substrate laminate sample. The three layers were attached to each other with double-sided adhesive carbon tapes and an aluminum wire. 98

Figure 4.1. The columnar structure of a ZnO film sample on a glass substrate: (a) T_s = RT (Set 17 in Table 3.1; $h \approx 458$ nm, $w_{bottom} \approx 10$–40 nm, $w_{top} \approx$ 25–55 nm), (b) T_s = 200 °C (Set 16 in Table 3.1; $h \approx 200$ nm, $w_{bottom} \approx 4$–10 nm, $w_{top} \approx 40$–93 nm). 101

Figure 4.2. The columnar structure of a ZnO film sample on a Si(100) substrate: (a) T_s = RT (Set 17 in Table 3.1; $h \approx 237$ nm, $w \approx 79$ nm), (b) T_s = 200 °C (Set 16 in Table 3.1; $h \approx 246$ nm, $w \approx 46$ nm). 102

Figure 4.3. XRD analysis of (a) commercial ZnO powder, and (b) a representative example of a ZnO film grown on glass at RT (Set 17 in Table 3.1). The vertical bars represent the peak positions of a stress-free reference powder (JCPDS-No. 36-1451). The ZnO thin film possesses only the (002)-peak, and its multiple, the (004)-peak. 103

Figure 4.4. EDX profile of a ZnO film sample on glass substrate, deposited at T_s = 200 °C (Set 16 in Table 3.1). The accelerating voltage was 20 keV, and the count rate was 3.1 kcps. The graph shows a close-view between 0 and 4.5 keV. Insert is the SEM image of the scanned film portion (13x9 μm^2). No argon peak could be detected at these conditions (K_{α_1}(Ar) = 2.958 keV). The signals other than those of oxygen and zinc arise from the glass substrate. 104

Figure 4.5. Warping of ZnO-glass system after deposition (not to scale; Set 17 in Table 3.1). The film thickness is ~400 nm, and the substrate is ~160 μm-thick. σ_c = -5.46 GPa. 105

Figure 4.6. Position of the (002)-peak in as-deposited ZnO films depending on the substrate type. The initial substrate temperature was 200 °C (Set 16 in Table 3.1). 106

Figure 4.7. (a) Strain (dL/L_o) and (b) TEC values (α) for ZnO, mica, silica glass, and Si(100), in the temperature range of 20–350 °C in the substrate plane direction. Details on the measurement method were presented in Section 3.4.2.3. 108

Figure 4.8. Total (σ_c) vs. thermal stress (σ_{th}) as a function of the substrate material for T_s = 200 °C, p = 0.02 mbar, P_{RF} = 100 W (Set 16 in Table 3.1).

Thermal stresses were due to the mismatch between the TEC of ZnO and the substrates. The remaining amount of stress among the total is called the *intrinsic stress* (σ_{int}). 109

Figure 4.9. Variation of residual planar compressive stress (σ_c) in the (002) plane, depending on the deposition conditions for ZnO films on glass substrate (Set 2–Set 11 in Table 3.1). By convention, a compressive residual stress has a negative value. In the figure, the absolute value of σ_c is given for ease of comparison. See Fig. 4.10–4.12 for the separate effects of the deposition parameters on σ_c. 111

Figure 4.10. Effect of chamber pressure (p) on the residual compressive stress (σ_c) at constant substrate temperature (T_s) and RF power (P_{RF}), for three different pairs of T_s and P_{RF}. By convention, a compressive residual stress has a negative value. In the figure, the absolute value of σ_c is given for ease of comparison. (Refer to Table 4.5 for sample labels.) (*:30 min annealing at 200 °C under vacuum in the chamber.) 112

Figure 4.11. Effect of substrate temperature (T_s) on the residual compressive stress (σ_c), at constant chamber pressure (p) and RF power (P_{RF}), for three different pairs of p and P_{RF}. By convention, a compressive residual stress has a negative value. In the figure, the absolute value of σ_c is given for ease of comparison. (Refer to Table 4.6 for sample labels.)..113

Figure 4.12. Effect of RF power (P_{RF}) on the residual compressive stress (σ_c), at constant substrate temperature (T_s) and chamber pressure (p), for three different pairs of T_s and p. By convention, a compressive residual stress has a negative value. In the figure, the absolute value of σ_c is given for ease of comparison. (Refer to Table 4.7 for sample labels.) (*:30 min annealing at 200 °C under vacuum in the chamber.) 114

Figure 4.13. Microstructure of the as-deposited films, ordered in increasing residual stress (see Table 3.1 for sample labels). (a) Set 6, (b) Set 8, (c) Set 7, (d) Set 3. 115

Figure 4.14. SEM images of the ZnO film grown on glass at T_s = RT, p = 0.2 mbar, P_{RF} = 125 W (Set 7 in Table 3.1): (a) top surface (GS_{SEM} ≈ 56 nm), (b) cross-section (h ≈ 278 nm, w ≈ 44 nm)....................................116

Figure 4.15. SEM images of the ZnO film grown on glass at T_s = RT, p = 0.4 mbar, P_{RF} = 100 W (Set 3 in Table 3.1): (a) top surface (GS_{SEM} ≈ 50–150 nm), (b) cross-section (h ≈ 280 nm, w_{bottom} ≈ 40 nm, w_{top} ≈ 120 nm). 117

Figure 4.16. SEM image of the ZnO film grown on glass at T_s = 200 °C, p = 0.2 mbar, P_{RF} = 125 W (Set 8 in Table 3.1): ($GS_{SEM,equiaxed}$ ≈ 21–32 nm, $GS_{SEM,diamond}$, (b) cross-section (h ≈ 400 nm, w_{bottom} ≈ 15–33 nm, w_{top} ≈ 70–80 nm). 118

Figure 4.17. SEM image of the ZnO film grown on glass at T_s = 200 °C, p = 0.2 mbar, P_{RF} = 125 W (Set 6 in Table 3.1): (a) top surface ($GS_{SEM,equiaxed}$ ≈ 20–35 nm, $GS_{SEM,diamond/tringular}$ ≈ 97–216 nm), (b) cross-section (h ≈ 463 nm, w_{bottom} ≈ 28 nm, w_{top} ≈ 84 nm). 119

Figure 4.18.a. XRD spectra (θ–2θ) of the ZnO film grown on glass at T_s = 200 °C, p = 0.4 mbar, P_{RF} = 125 W (Set 5 in Table 3.1). 120

Figure 4.18.b. XRD spectra (θ–2θ) of the ZnO film grown on glass at T_s = 200 °C, p = 0.2 mbar, P_{RF} = 125 W (Set 8 in Table 3.1). 121

Figure 4.18.c. XRD spectra (θ–2θ) of the ZnO film grown on glass at T_s = 200 °C, p = 0.2 mbar, P_{RF} = 125 W (Set 6 in Table 3.1). 121

Figure 4.18.d. XRD spectra (θ–2θ) of the ZnO film grown on glass at T_s = 200 °C, p = 0.02 mbar, P_{RF} = 125 W (Set 9 in Table 3.1). 122

Figure 4.18.e. XRD spectra (θ–2θ) of the ZnO film grown on glass at T_s = RT, p = 0.2 mbar, P_{RF} = 125 W (Set 7 in Table 3.1). 122

Figure 4.19. XRD spectra (θ–2θ) of the ZnO film grown on glass at T_s = 200 °C, p = 0.2 mbar, P_{RF} = 125 W, with an initial buffer layer (set 13 in Table 3.1; see Table 3.2 for details)...123

Figure 4.20. Variation of residual stress (σ_c), for ZnO film grown on glass at T_s = 200 °C, p = 0.2 mbar, P_{RF} = 125 W (Set 13), depending on the pre-deposited ZnO buffer layer (Set 12): ZnO film on annealed buffer

layer on a fresh substrate (13D), or on an acid-cleaned substrate (13B), and ZnO film on an as-deposited buffer layer on a fresh substrate (13C), or on an acid-cleaned substrate (13A) (see Table 3.1, 3.2, and 4.8 for sample labels and stress values). By convention, a compressive residual stress has a negative value. In the figure, the absolute value of σ_c is given for ease of comparison. 124

Figure 4.21. Microstructure of the top surface of the ZnO films grown on glass at T_s = 200 °C, p = 0.2 mbar, P_{RF} = 125 W, ordered in decreasing residual stress. (a) Without a buffer layer (Set 8; σ_c = -3.32 GPa; $GS_{SEM,equiaxed}$ ≈ 21–32 nm, $GS_{SEM,diamond}$ ≈ 126 nm), (b) with a buffer layer (Sample 13A; σ_c = -2.60 GPa; GS_{SEM} = 19–51 nm), (c) with a pre-annealed buffer layer (sample 13D; σ_c = -1.09 GPa; GS_{SEM} = 19–51 nm; see Table 4.8). 126

Figure 4.22. Microstructure of the cross-section of the ZnO films grown on glass at T_s = 200 °C, p = 0.2 mbar, P_{RF} = 125 W, ordered in decreasing residual stress. (a) Without a buffer layer (Set 8; σ_c = -3.32 GPa; h ≈ 400 nm, w_{bottom} ≈ 15–33 nm, w_{top} ≈ 70–80 nm), (b) with a buffer layer (Sample 13A; σ_c = -2.60 GPa; h ≈ 314 nm, w ≈ 48 nm), (c) with a pre-annealed buffer layer (sample 13D; σ_c = -1.09 GPa; h ≈ 248 nm; see Table 4.8). 127

Figure 4.23. Warping of ZnO-glass system after deposition and after annealing (not to scale). 128

Figure 4.24. Position of the (002)-peak of the ZnO films with T_{s_0} = 200 °C, depending on the substrate type (Set 16 in Table 3.1): (a) as-deposited, (b) after post-deposition annealing in air for 1 hour at 600 °C. Annealing the films eliminates the stresses. 129

Figure 4.25. Comparison of planar stresses of the ZnO films with T_{s_0} = 200 °C, depending on the substrate type (Set 16 in Table 3.1): as-deposited and after post-deposition annealing in air for 1 hour at 600 °C. 130

Figure 4.26. SEM images of ZnO on Si(100) with T_{s_0} = 200 °C (Set 17 in Table 3.1). (a) as-deposited (GS_{SEM} ≈ 43 nm), (b) 28 months-old (GS_{SEM} ≈

42 nm), (c) annealed in air at 600 °C for 1 h (GS_{SEM} ≈ 43–130 nm), (d) 28-months-old film, annealed at 600 °C for 6 h (GS_{SEM} ≈ 57–130 nm). 131

Figure 4.27. Increasing intensity of the (002)-peak of ZnO on Si(100) substrate (Set 18 in Table 3.1), as the temperature was increased from room temperature to 170 °C. All the residual stress was eliminated during cooling, and the sample was stress-free after the heating process. 132

Figure 4.28. Effect of annealing on the peak position and intensity of the (002)-peak of ZnO films grown on glass at T_s = RT, p = 0.2 mbar, P_{RF} = 125 W (Set 7 on Table 3.1) (a) annealed in argon, (b) annealed in air. No significance difference was observed depending on the annealing atmosphere. Both annealing experiments were performed at 600 °C for 6 hours. 133

Figure 4.29. Shift of the (002)-peak of ZnO indicating residual stresses. The data shows the effect of a) substrate material, b) aging and annealing of ZnO on the glass substrate, c) aging and annealing on the Si(100) substrate. The vertical line represents the position of the (002)-peak in stress-free ZnO powder JCPDS-No. 36-1451. The (002)-peaks of aged ZnO films were scaled with those of the as-deposited films for comparison (see Table 4.10 and Fig. 4.30 for sample labels and stress values). 134

Figure 4.30. Comparison of planar stresses of the ZnO films with T_{s_0} = 200 °C, depending on the substrate type (Set 16 in Table 3.1): as-deposited, after post-deposition annealing in air for 1 hour at 600 °C and aged 28 months. 135

Figure 4.31. Variation of residual stress (σ_c), for ZnO films grown on glass substrates at T_s = 200 °C (see Table 3.1 and 4.9). The residual stress decreases by in-chamber annealing at the deposition temperature for 30 min, both in oxygen (Set 11) and in vacuum (Set 10), with respect to the case with no annealing (Set 8). By convention, a compressive residual stress has a negative value. In the figure, the absolute value of σ_c is given for ease of comparison. 137

Figure 4.32. XRD spectra (θ–2θ) of the ZnO films grown on glass at T_s = 200 °C, p = 0.2 mbar; (a) P_{RF} = 100 W, 30 min vacuum annealing in the chamber at 200 °C (Set 10 in Table 3.1); (b) P_{RF} = 125 W, 30 min annealing in O_2:Ar (2:5 v/v) inside the chamber at 200 °C (Set 11 in Table 3.1). 138

Figure 4.33. Damage on the films by annealing in air at 600 °C for 6 h: (a) Void formation within the ZnO film on glass (Set 16 in Table 3.1); (b) interfacial damage in the ZnO film on Si(100) (Set 17 in Table 3.1); (c) destroyed interface of the ZnO film on glass (Set 19 in Table 3.1). 139

Figure 4.34. Crack formation on ZnO film on glass substrate (Set 17 in Table 3.1) through pore clustering upon annealing (in air at 600 °C for 6 h)...........140

Figure 4.35. Crack formation on ZnO film on glass substrate (Set 17 in Table 3.1) through grain boundary detachment upon aging (in air for 28 months). 141

Figure 4.36. Buckling in the ZnO film on glass substrate (Set 16 in Table 3.1; aged 28 months in air), occurred presumably around a pre-existing defect on the substrate...142

Figure 4.37. Two different types of buckles: (a) a straight-sided buckle on the ZnO film on glass with T_s = RT (Set 17 in Table 3.1); (b) a curved-sided buckle on the ZnO film on Si(100) with T_s = 200 °C (Set 16 in Table 3.1). Film in (b) was aged 28 months in air. Both films were annealed in air at 600 °C for 6 hours. 143

Figure 4.38. Buckling and local loss of adhesion in the ZnO film upon stress relaxation (Set 16 in Table 3.1; annealed in air at 600 °C for 6h): (a) buckles seen from the side view of the film, (b) protrusions on the film surface, (c) crack at the protrusion center. 144

Figure 4.39. Bulging and cracking in the ZnO film on glass upon prolonged aging (Set 16 in Table 3.1; aged 28 months in air)..145

Figure 4.40. Cracking in the ZnO film on glass upon prolonged aging (28 months), followed by annealing (in air at 600 °C for 6h): (a) Set 17 in Table 3.1; (b) Set 16 in Table 3.1. 146

Figure 4.41. Initial stage of crystal growth on the ZnO film surface upon annealing (Set 16 in Table 3.1; annealed in air at 600 °C for 6h). The crystallites in this sample have grown up to 205 nm in diameter. 147

Figure 4.42. Growth of ZnO crystallites on the film surface upon annealing. (a) ZnO on glass (Set 20 in Table 3.1). The nano-rod thickness was about 100 nm, and the rods elongated up to 916 nm. (b) ZnO on Si(100) (Set 16 in Table 3.1). The thickness of the crystallites is between 82–149 nm, and their height is between 36–174 nm. Both films were annealed in air at 600 °C for 6h. 148

Figure 5.1. A recent structure-zone model developed by Messier and Trolier-McKinstry, also showing the region of operation in part of our study discussed in Sec. 5.1 (T_s = RT–200 °C, p = 6.8–15 mTorr, P_{RF} = 100 W). (Adapted from Ref. [51]; original figure by Ref. [63]; published with permission from SPIE Press and Elsevier Publishing Ltd.). 151

Figure 5.2 A film structure with a randomly-oriented layer at the substrate interface. Only the fastest growing directions survive and form the strongly textured film...156

Figure 5.3. Two different growth behaviors on an initial layer of textured nuclei. The nuclei continue to grown in the preferred orientation. The film microstructure depends on the nucleation density and the growth rate of different crystal faces. 156

Figure 5.4. Various forms of hexagonal crystal structures. Grains of a hexagonal material could take any of these forms depending on its chemistry and the relative growth rate of different surfaces depending on the growth conditions. 159

Figure 5.5. Crystal planes and Miller indices of hemimorphic wurtzite-type zinc oxide. The angle between the hexagonal {001} and each triangular {101} surface is 32° [25]. 160

Figure 5.6. SEM images of the ZnO films on glass deposited at low p (0.2 mbar) and high P_{RF}. (125 W) Drawings on the right side illustrate the possible forms of the encircled grains in the SEM images. (a) Set 7 (b) Set 8, (c) Set 6. 160

Figure 5.7. A film structure with a randomly-oriented layer at the substrate interface. The grains are free to grow in all directions. Additional nucleation may take place during growth. 162

Figure 5.8. (a) A polycrystalline structure with random texture. (b) The position of a ZnO unit cell with respect to the substrate plane to give a (101)-reflection in the XRD spectra. (c) XRD spectra (θ–2θ) of the ZnO film grown on glass at T_s = 200 °C, p = 0.2 mbar, P_{RF} = 125 W (Set 8 in Table 3.1). 164

Figure 5.9. (a) A polycrystalline structure with fiber texture. (b) The position of a ZnO unit cell with respect to the substrate plane to give a (002)-reflection in the XRD spectra. (c) XRD spectra (θ–2θ) of the ZnO film grown on glass at T_s = RT, p = 0.2 mbar, P_{RF} = 125 W (Set 7 in Table 3.1). 165

Figure 5.10. SEM images of the ZnO film grown on glass at T_s = 200 °C, p = 0.2 mbar, P_{RF} = 125 W. (a) ZnO on fresh glass substrate (Set 6 in Table 3.1). No (101)-reflection was observed in the XRD spectra from this sample. (b) ZnO on fresh glass substrate (Set 6 in Table 3.1). (101)-reflection was observed in the XRD spectra from this sample. (c) ZnO on acid-cleaned glass substrate (Set 8 in Table 3.1). A more intense (101)-reflection was observed in the XRD spectra from this sample then from the sample in (b). 168

Figure 5.11. Total (σ_c) vs. thermal stress (σ_{th}) as a function of the substrate material for T_s = 200 °C, p = 0.02 mbar, P_{RF} = 100 W (Set 16 in Table 3.1). Thermal stresses were due to the mismatch between the TEC of ZnO and the substrates. The remaining amount of stress among the total is called the *intrinsic stress* (σ_{int})..................................178

Figure 5.12. Microstructure of the as-deposited films, in order of increasing residual stress: (a) σ_c = -2.88 GPa (Set 6); (b) σ_c = -3.32 GPa (Set 8);

(c) σ_c = -3.83 GPa (Set 7); (d) σ_c = -6.78 GPa (Set 3) (see Table 3.1 for sample labels)..190

Figure 5.13. Void formation and consequent cracking in the annealed films. 203

Figure 5.14. Pore formation at the interface decreasing the overall compressive stress...204

Figure 5.15. A curved-sided buckle on the ZnO film on Si(100) with T_s = 200 °C (Set 16 in Table 3.1). The residual compressive stress after deposition was -4.70 GPa. Film was aged 28 months in air, and later annealed in air at 600 °C for 6 hours. The residual stresses were eliminated by aging...206

Figure 5.16. Bulging and cracking in the ZnO film on glass upon prolonged aging (Set 16 in Table 3.1; aged 28 months in air. The residual compressive stress after deposition was -3.94 GPa. The residual stresses were eliminated by aging...206

Figure 5.17. Demonstrations of mass transport on the surface of ZnO films, about one month after film deposition. (a) Set 8, (b) Set 3, (c) Set 6. (See Table 3.1 for sample labels.)...210

Figure 5.18. Growth of ZnO crystallites on the film surface upon annealing (Set 20 in Table 3.1). The nano-rod thickness was about 100 nm, and the rods elongated up to 916 nm...211

Figure 5.19. Demonstrations of elecromigration in Al films: (a) Hillock growth (original source: Ref. [225], courtesy of L. Berenbaum, reprinted from Ref. [50]); (b) Whisker bridging two conductors (courtesy of R. Knoell, AT & T Bell Laboratories, reprinted from Ref. [50])................211

Figure 5.20. (a) Chemical vapor deposition of ZnO with Au catalyst [224]. (b) ZnO nano-rods grown by MOVPE on a very thin buffer layer of ZnO [129, 130]. 212

Figure C.1.1. A representative XRD spectrum of Si(100) wafer. 229

Figure C.2.1. A representative XRD spectrum of mica (muscovite) sheet. 230

Figure D.1.1. Temperature near the substrate holder (~1 cm), as measured by a thermocouple (see Fig. 3.3). The plasma conditions were: P_{RF} = 150 W, P_{DC} = 30 W, V_{Ar} = 35 cm^3/min, p_{Ar} = 0.1 mbar. The chamber was initially heated up to 300 °C for 5 min, then the heater was turned off. The temperature had decreased down to 100 °C when the deposition started. It reached equilibrium at ~80 °C during the course of deposition. 231

Figure D.2.1. Temperature during heating before deposition, as measured by a thermocouple near the substrate holder (~1 cm; see Fig. 3.3) and temperature indicator strips on the substrate holder (see Fig. 3.4). The measurements were done under vacuum. 232

Figure D.2.2. Temperature during cooling after deposition, as measured by a thermocouple near the substrate holder (~1 cm; see Fig. 3.3). The conditions were: V_{Ar} = 20 cm^3/min, p_{Ar} = 0.02 mbar, turbo pump at full speed. 232

Figure E.1.1. The measurement set-up of the UV–VIS–NIR spectrophotometer. 233

Figure E.1.2. The sample holder for the spectrophotometer. The sample was stuck vertically to the frame on the left, and the frame on the right was left empty for reference measurement. The beam passed through the hole inside each frame. 234

Figure E.2.1. Transparent ZnO film on glass substrate. 235

Figure E.2.2. Optical transmittance as a function of substrate temperature during deposition, at p = 0.4 mbar and P_{RF} = 125 W. The T_s values were 200 °C (Set 5) and RT (Set 4). (The shaded area represents the transmittance of the glass substrate.) 236

Figure E.2.3. Optical transmittance as a function of substrate temperature during deposition, at p = 0.4 mbar and P_{RF} = 100 W. The T_s values were 200 °C (Set 2) and RT (Set 3). (The shaded area represents the transmittance of the glass substrate.) 236

Figure E.2.4. Optical transmittance as a function of chamber (argon) pressure during deposition, at T_s = 200 °C and P_{RF} = 125 W. The pressure

values were 0.02 mbar (Set 9), 0.2 mbar (Set 8), and 0.4 mbar (Set 5). (The shaded area represents the transmittance of the glass substrate.) 237

Figure E.2.5. Optical transmittance as a function of chamber (argon) pressure during deposition, at T_s = RT and P_{RF} = 125 W. The pressure values were 0.2 mbar (Set 7) and 0.4 mbar (Set 4). (The shaded area represents the transmittance of the glass substrate.) 237

Figure E.2.6. Optical transmittance as a function of RF power during deposition, at T_s = 200 °C and p =0.4 mbar. The P_{RF} values were 100 W (Set 2) and 125 W (Set 5). (The shaded area represents the transmittance of the glass substrate.) 238

Figure E.2.7. Optical transmittance as a function of RF power during deposition, at T_s = RT and p =0.4 mbar. The P_{RF} values were 100 W (Set 3) and 125 W (Set 4). (The shaded area represents the transmittance of the glass substrate.) 238

Figure E.2.8. Optical transmittance as influenced by annealing. The deposition conditions were: T_s = 200 °C, p = 0.2 mbar, and P_{RF} = 125 W (Set 8). The film sample was treated in the chamber at 200 °C for 30 min in O_2:Ar (2:3 v/v) atmosphere (Set 11). Post-deposition annealing was applied in air at 600 °C for 6 h to both the as-deposited and the in-chamber annealed samples. (The shaded area represents the transmittance of the glass substrate.) 239

LIST OF TABLES

Table 1.1. Properties of common transparent conductive oxide (TCO) materials [25]. 6

Table 1.2. Piezoelectric and dielectric properties of some non-ferroelectric materials [41]. 7

Table 1.3. Some mechanical properties of ZnO collected by Özgür *et al.* [13]. C_{ij} are the elastic stiffness constants. The details of the measurements are given in the box below the table. The reference numbers belong to the study by Özgür *et al.* [13]. 8

Table 1.4. Lattice parameters of a number of the prospective substrate materials for ZnO, compiled by Özgür *et al.* [13]. 35

Table 1.5. Hardness and elastic modulus for bulk and epitaxial ZnO measured by nano-indentation [143]. 45

Table 1.6. Distribution of *c*-axis orientation of zinc oxide films grown on different substrates [156]. 49

Table 1.7. Some values for the thermal expansion coefficient (α) of ZnO used in the literature. 65

Table 1.8. Review articles on diffraction stress analysis with a short description of the contents according to various categories [184]. 66

Table 3.1. ZnO thin film deposition variables. Unless otherwise stated, all substrates were prepared by the acid cleaning method described in Section 3.1. DC power was 30 W for all depositions. 78

Table 3.2. Substrate details about Set13. Four different samples were prepared to elucidate the effects of the pre-deposited ZnO layer on the residual stress. See Section 3.1 for the substrate cleaning method. 79

Table 3.3. Lattice spacings and the corresponding diffraction angles of the stress-free powder standard JCPDS-No. 36-1451 [205]....................................87

Table 3.4. Elastic stiffness constants of ZnO [149, 206, 207].......................................91

Table 4.1. Variation of lattice parameter (c), XRD peak width at half-intensity ($FWHM$), percent tensile strain ($\%\varepsilon_z$), grain size (GS_{XRD}), and total compressive stress (σ_c) of as-deposited (0) ZnO films on glass (G), mica (M), and Si(100) (S) substrates for an initial substrate temperature of 200 °C (Set 16). The XRD data belongs to the (002)-peak. The reference lattice constant for the unstressed ZnO (c_o) is taken from JCPDS -No. 36-1451. The error range in σ_c is ±0.26 GPa, due to equipment offset...106

Table 4.2. TEC values (α) measured by dilatometry the substrates along the planar direction of the substrate, as described in Section 3.4.2.3. The same measurement was repeated for the ZnO powder (Merck, Darmstadt, Germany). 107

Table 4.3. Comparison of the total (σ_c), thermal (σ_{th}), and the remaining intrinsic stress (σ_{int}) of as-deposited (0) ZnO films on glass (G), mica (M), and Si(100) (S) substrates, deposited at an initial substrate temperature of 200 °C (Set 16). The XRD data belongs to the (002)-peak. σ_c is calculated by Eq. 3.16a, and σ_{th} is calculated from Eq.3.32. σ_{int} the difference between σ_c and σ_{th}. The error range in σ_c due to equipment offset is ±0.26 GPa..109

Table 4.4. Variation of residual stress in the (002) plane depending on the deposition conditions for ZnO films on glass substrate. See Table 3.1 for sample labels. For ease of comparison, the compressive stresses were listed in decreasing order. $\sigma_{c,ave}$ was calculated from Eq. 3.16a with the data from the (002) XRD peak for each sample. The error range is ±0.55 GPa..111

Table 4.5. Effect of chamber pressure (p) on the residual compressive stress at constant substrate temperature (T_s) and RF power (P_{RF}), for three different pairs of T_s and P_{RF} on glass substrate. $\sigma_{c,ave}$ was calculated from Eq. 3.16a with the data from the (002) XRD peak for each sample. The error range is ±0.55 GPa. 112

Table 4.6. Effect of substrate temperature (T_s) on the residual compressive stress at constant chamber pressure (p) and RF power (P_{RF}), for three different pairs of p and P_{RF}. $\sigma_{c,ave}$ was calculated from Eq. 3.16a with the data from the (002) XRD peak for each sample. The error range is ±0.55 GPa..113

Table 4.7. Effect of RF power (P_{RF}) on the residual compressive stress at constant substrate temperature (T_s) and chamber pressure (p), for three different pairs of T_s and p. $\sigma_{c,ave}$ was calculated from Eq. 3.16a with the data from the (002) XRD peak for each sample. The error range is ±0.55 GPa..114

Table 4.8. Variation of residual stress for Set 13, depending on the pre-deposited ZnO buffer layer (Set 12). Film deposition conditions were: P_{RF} = 125 W, p = 0.2 mbar, T_s = 200 °C. The error range is ±0.55 GPa...........125

Table 4.9. Variation of lattice parameter (c), XRD peak width at half-intensity ($FWHM$), percent tensile strain ($\%\varepsilon_z$), grain size (GS_{XRD}), and total compressive stress (σ_c) of ZnO films on different substrates for an initial substrate temperature of 200 °C (Set 16). The XRD data belongs to the (002)-peak. The reference lattice constant for the unstressed ZnO (c_o) was obtained from JCPDS-No. 36-1451. The results are given for the as-deposited (0) and the thermally annealed (1) films on glass (G), mica (M), and Si(100) (S) substrates. The error range in σ_c due to equipment offset is ±0.26 GPa..........................130

Table 4.10. Variation of lattice parameter (c), XRD peak width at half-intensity ($FWHM$), percent tensile strain ($\%\varepsilon_z$), grain size (GS_{XRD}), and total compressive stress (σ_c) of ZnO films on different substrates with an initial substrate temperature of 200 °C (Set 16). The XRD data belongs to the (002)-peak. The reference lattice constant for the

unstressed ZnO (c_o) is taken from JCPDS-No. 36-1451. The results are given for the as-deposited (0), the thermally annealed (1), and the aged (2) films on glass (G) and Si(100) (S) substrates. The error range in σ_c due to equipment offset is ±0.26 GPa for the as-deposited and annealed films, and +0.73/-0.66 for the aged films. 135

Table 4.11. Variation of residual stress for ZnO films grown on glass substrates at T_s = 200 °C (see Table 3.1). The residual stress decreases by in-chamber annealing at the deposition temperature for 30 min, both in O_2:Ar (2:5 v/v) and in vacuum. $\sigma_{c,ave}$ was calculated from Eq. 3.16a with the data from the (002) XRD peak for each sample. The error range is ±0.55 GPa..137

Table B.1.1. JCPDS data of hexagonal wurtzite ZnO (No. 36-1451) [205]................220

Table B.2.1. JCPDS data of face-centered cubic Si (No. 27-1402) [205]...................222

Table B.2.2. JCPDS data of face-centered cubic Si (No. 75-0589) [205]...................223

Table B.2.3. JCPDS data of body-centered cubic Si (No. 72-1088) [205]..................224

Table B.3.1. JCPDS data of monoclinic mica (No. 83-1808) [205]............................225

Table E.2.1. Variation of residual stress in the (002) plane depending on the deposition conditions for ZnO films on glass substrate. See Table 3.1 for sample labels. For ease of comparison, the compressive stresses were listed in decreasing order. $\sigma_{c,ave}$ was calculated from Eq. 3.16a with the data from the (002) XRD peak for each sample. The error range is ±0.55 GPa..235

LIST OF SYMBOLS AND ABBREVIATIONS

Symbols

a, b, c	lattice parameters of crystallographic unit cell
$\mathbf{a}$	acceleration vector
b	separation radius
B	bulk modulus
$\mathbf{B}$	magnetic field vector
C_{ij}	stiffness constant
d	lattice spacing
d_{ik}	piezoelectric coefficient relating the applied electric field to resultant strain
$d_{33,\,f}$	effective piezoelectric coefficient
e	electron charge
$e_{31,\,f}$	deflection force, piezoelectric charge of deflected piezoelectric laminated structure
e_{ik}	piezoelectric coefficient relating the applied electric field to resultant stress
$\mathbf{E}$	electric polarization vector
E	elastic modulus (Young's modulus)
E_g	band gap
f	surface stress
$\mathbf{F}$	force vector
G	energy release rate in a crack
G_0	elastic energy per unit area, stored in the unbuckled film
G_c	fracture toughness
h	layer thickness

H	hardness
m	mass
M	bending moment
n	refractive index
N	charge carrier concentration
p	pressure
P_c	critical buckling load
P_{RF}	radio-frequency source power
P_{DC}	direct current source power
ppm	parts per million
Q	charge
R	deposition rate
T	transition
T	temperature
%T	%transmittance
T_h	homologous temperature
T_m	melting point
T_s	substrate temperature
v	velocity vector
V	electric potential
V	volumetric flow rate
v/v	by volume
V_O, V'_O, V''_O	oxygen vacancies with an excess charge of 0, -1, and -2, respectively
x, y, z	Cartesian coordinates
Z	dimensionless number that defines the driving force for crack generation
Z^*	Born effective charge
$Zn_i, Zn_i^{\bullet}, Zn_i^{\bullet\bullet}$	zinc interstitials with an excess charge of 0, +1, and +2, respectively
α	thermal expansion coefficient
Γ	fracture resistance
Γ_i°	mode I interface toughness when $\psi = 0$

Γ_i	interface toughness
Γ_0	film toughness
δ	skin depth; dielectric loss angle; buckle separation distance
Δ	difference
ε	measured strain; permittivity
ε_0	permittivity of free space
ε_∞	applied strain
ϕ	angle of in-plane sample rotation in XRD
θ	Bragg angle in XRD
κ	dielectric constant
λ	mode mixity index; wavelength
μ	Hall mobility
ν	Poisson's ratio
Π	buckling index
ρ	electrical resistivity
σ	stress
Σ	adhesion index
φ	a proportionality constant
φ^*	a proportionality constant
ψ	inclination (tilt) angle in XRD; loading phase angle
ω	a proportionality constant; frequency of the incident electromagnetic beam
ω_p	plasma frequency of the material
$\perp$	perpendicular
//	parallel

Abbreviations and Acronyms

at.	atomic
AC	alternating current
AZO	aluminum doped zinc oxide
CTC	compressive-tensile-compressive
DC	direct current

ITO	Tin-doped indium oxide
JCPDS	Joint Committee on Powder Diffraction Standards
M	Match-stick
MBE	molecular-beam epitaxy
MOCVD	metal-organic chemical vapor deposition
RBS	Rutherford back-scattering
RF	radio-frequency
RFMS	radio-frequency magnetron sputtering
RT	room temperature
SEM	scanning electron microscopy
T	transition
TCO	transparent conductive oxide
TEC	thermal expansion coefficient
TEM	transmission electron microscopy
TRIM	transport of ions in matter
XRD	x-ray diffraction
UV	ultraviolet
VIS	visible

Subscripts

$_{ave}$	average
$_{b}$	buckle
$_{c}$	compressive (for stress), critical
$_{cr}$	critical (for stress)
$_{e}$	electron
$_{f}$	film; final; floating
$_{g}$	growth
$_{h}$	homologous
$_{i}$	initial; interface
$_{int}$	intrinsic
$_{m}$	mean; misfit
$_{o}$	initial; stress-free

$_{p}$ plasma; propagation

$_{s}$ spall; substrate

Prefixes

n negative

p positive

CHAPTER 1

INTRODUCTION

A coating is generally called a thin film when its thickness is less than 1 μm [1]. Thin film devices have an increasing importance in terms of providing new energy sources [2-4]. For example, multilayer thin films posses a wide range of absorbance, transmittance and reflectance, provided that the number and thickness of the layers are controlled [2]. The multilayer structures of the appropriate material with thicknesses of several tens or hundreds of nanometers provide high-brightness screens, high-efficiency photocells, or many other energy related products. Thermal barrier coatings and transparent electrodes are also important thin film products [2, 5, 6].

Transparent electrodes are a key component in many newly emerging technologies that require access through an electrically conductive layer in the visible light spectrum, such as energy-efficient windows, solar cell panels, and flat panel displays [5]. Transparency in the visible range and high electrical conductivity intuitively seem incompatible: most transparent materials are insulators and most conductive materials (metals) are opaque [7]. When an electromagnetic wave is incident on a conductor, it interacts with the high density of free electrons at the surface, inducing the collective oscillation of free electrons if the wave frequency (ω) is below the *plasma frequency* (ω_p). If the incident wave frequency is higher than the plasma frequency, the free electrons are unable to follow the wave, and the wave can propagate through the material unperturbed. The parameters that govern the plasma frequency are related in the following equation [7]:

$$\omega_p = \left(\frac{N_e e^2}{m\varepsilon(\omega)} \right)^{1/2} \tag{1.1}$$

Here, e is the electron charge, m is the electron mass. The frequency-dependent dielectric response of the conductor is given by $\varepsilon(\omega)$, and the density of free electrons is given by N_e. From this equation, we see that the free charge carrier concentration is one parameter that could be varied to choose the spectral region of transparency. In the case of transparent conductive oxides (TCO), one could select a doping level sufficiently high to ensure adequate electrical conductivity, while placing the plasma frequency in the near infrared spectral region. Tin-doped indium oxide (ITO), aluminum-doped zinc oxide (AZO) and their derivatives are such examples [5].

Although ITO has been the material of choice for transparent electrodes, the high cost and limited supply of indium have motivated researchers to look for other alternatives [5, 8]. Some alternatives that have been proposed are cadmium stannate (Cd_2SnO_4) and cadmium oxide (CdO). However, the toxicity of cadmium limits the widespread use of these materials. Some other alternatives to ITO and cadmium-based materials are ZnO-based or SnO_2-based; such as the zinc stannates $ZnSnO_3$ and Zn_2SnO_4 [9]. These materials exhibit higher optical transparency but several orders lower electrical conductivity than ITO and cadmium stannates. ZnO is advantageous over SnO_2 in being easier to etch into the desired shapes for electrode structures [9]. ZnO can be wet-etched with NaCl under UV light, dry-etched by $Zn(CH_3)_2$, $Zn(C_2H_5)_2$, $ZnCl_2$, or in CF_2Cl_2 plasma [10].

Although ZnO has many potential technological applications as an alternative transparent electrode material with many other technological applications, the mechanical properties of ZnO thin films such as adhesion, stability towards delamination *etc.*, have not been reported in much detail in literature, although such properties are very important for stable device performance and reliability. Residual stresses are known to exist in thin films, regardless of the type of deposition method, and could be estimated by several direct or indirect methods. These stresses could alter the film properties significantly. In this chapter, the basic background information is summarized including the material properties of ZnO, how they are modified for ZnO thin films, thin film deposition, and general thin film structures.

1.1. ZnO as a Ceramic Material

Below is a brief summary of ZnO material properties. For a more comprehensive review of ZnO material and devices, please refer to [11-17].

1.1.1. Structure

The crystal structures of zinc oxide are rocksalt, zinc blende, and wurtzite [13] (Fig. 1.1). In the wurtzite type, the anions are tetrahedrally coordinated by four cations, and vice versa, so as to form an ordered hexagonal structure with 6-fold symmetry [13, 18]. This structure is based on the hexagonal close-packed structure with one-half of the tetrahedral sites filled [18]. The pyramidal structure of natural zincite mineral, a microwave-produced single crystal ZnO, and the representative crystal planes are shown in Fig. 1.2. The wurtzite structure is the thermodynamically stable structure of ZnO at room temperature (Fig. 1.3), like Zn chalcogenides such as ZnS, ZnSe. The cubic zinc blende ZnO_2 form is rare and can be grown on cubic substrates only [13, 19]. The rocksalt structure is stable only at high pressures [13].

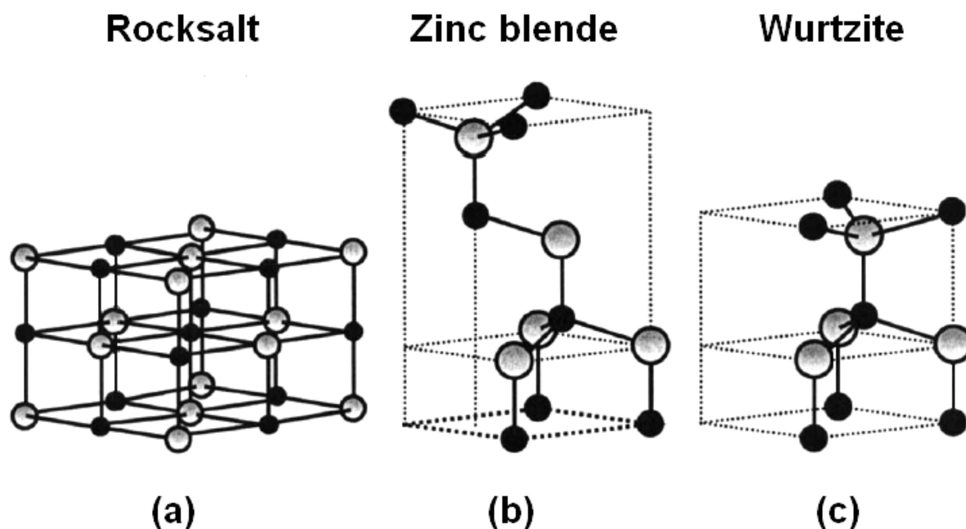

Figure 1.1. Various crystal structures of ZnO formed by Zn (shaded gray) and oxygen (black) atoms (Reprinted from Ref. [13]; published with permission from AIP.).

In nature, this mineral is found with the composition of 8.83% MnO and 91.17% ZnO [20]. Stoichiometric ZnO has a molecular weight of 80.34 g/mol. The lattice constants of ZnO in its hexagonal wurtzite form that have been measured in literature vary in the 3.2475-3.2501 and 5.2042-5.2410 Å ranges for *a* and *c*, respectively [13].

(a)

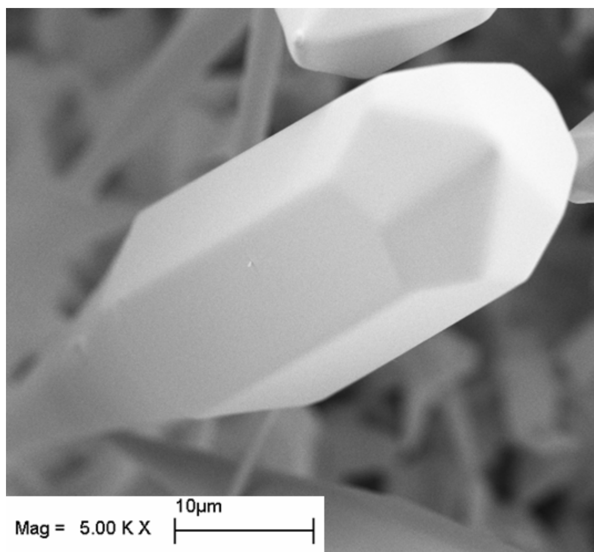

(b)

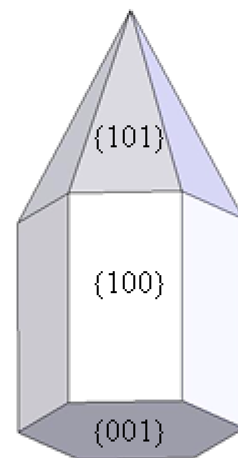

(c)

Figure 1.2. (a) Natural zincite crystals. (Left: Copyright by Lou Perloff / Photo Atlas of Minerals [20]; right: Copyright by O. Dziallas 2005 [21].) (b) Zinc oxide single crystal produced by microwave processing [22]. (c) Crystal set of planes and Miller indices of wurtzite-type zinc oxide.

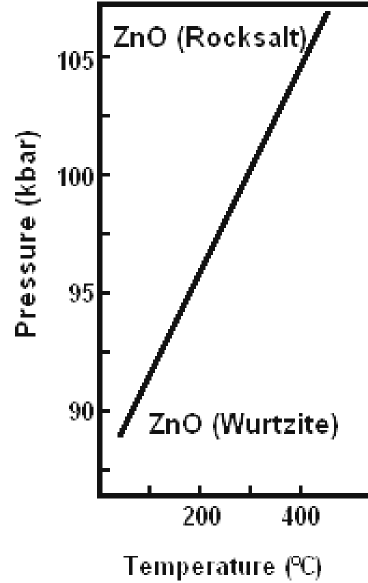

Figure 1.3. Univariant *p*-*T* curve between two phases of ZnO [23, 24].

1.1.2. Optical, Electrical, Piezoelectric, and Mechanical Properties

Pure ZnO is a wide band-gap semiconductor. It is chemically and mechanically more stable, and cheaper than its alternatives [25]. For these reasons, it is a strong candidate to replace conventional semiconductors such as SiC and GaN, with similar lattice constants to ZnO. Some values for the direct band-gap of pure bulk ZnO has been given as 3.3 [26, 27], 3.37 [28], and 3.437 [29] eV. The reported exciton binding energies vary from 60 eV [30] to 65 eV [29]. The refractive index (n) for polarization perpendicular to c-axis ($\mathbf{E}\perp c$) vary from 9.843 to 2.220 in the wavelength (λ) range of 366.43-401.89 nm [13]. For polarization parallel to the c-axis ($\mathbf{E}//c$) and the λ range of 363.71-411.27 nm, n varies from 3.525 to 2.194, near the absorption edge [13]. ZnO is also a piezoelectric material with a piezoelectric coefficient (d_{33}) ranging from 10.5 to 11.5 pC/N [31] and a dielectric constant (κ) ranging from 10.8 to 11.0 [31]. For commercially grown single crystal bulk ZnO, a resistivity (ρ) of $2.8\text{x}10^4$ Ω-cm was achieved [32]. Important electrical and piezoelectric properties are summarized in Table 1.1 and Table 1.2. Some mechanical properties of ZnO are summarized in Table 1.3.

Wurtzite-type ZnO may naturally contain intrinsic defects such as oxygen vacancies ($V_O, V_O^{\bullet}, V_O^{\bullet\bullet}$) and zinc interstitials ($Zn_i, Zn_i^{\bullet}, Zn_i^{\bullet\bullet}$) [13]. [Oxygen vacancies

have lower formation energies then the zinc interstitials [13, 33]. For this reason, in Zn-rich conditions, oxygen vacancies are more abundant than the zinc interstitials. In oxygen-rich conditions, zinc vacancies tend to dominate [13].] As a results of this non-stoichiometry, undoped ZnO has *n*-type conductivity and the electron densities could be as high as 10^{21} cm^{-3} [34]. ZnO could be made either *n*- or *p*-type with intrinsic doping (*i.e.*, with zinc or oxygen ions) or vacancy creation. It can easily be doped *n*-type with extrinsic dopants such as Al, Co and Bi. On the other hand, extrinsic *p*-type doping of ZnO is harder to attain than the *n*-type doping, as in the case with other wide band-gap semiconductors such as GaN and ZnSe [13, 35-37]. Some reasons for this could be the compensation of dopants by low-energy native defects, such as zinc interstitials or oxygen vacancies [38], or background impurities (H^+) [13]; low solubility of the dopant in the host material [39]; and deep impurity level causing significant resistance to the formation of shallow acceptor level [13].

Table 1.1. Properties of common transparent conductive oxide (TCO) materials [25].

Property	**In_2O_3**	**SnO_2**	**ZnO**
Mineral name	—	cassiterite	zincite
Band gap E_g (eV)	3.75	3.7	3.4
Melting point (°C)	≈2000	>1930*	1975
Heat of formation (eV)	9.7	6.0	3.6
Density (g/cm^3)	7.12	6.99	5.67
Relative permittivity	9	9	8.1
Effective electron mass (m^*/m_e)	0.3	0.28	0.28
Dopants	Sn, Ti, Zr, F, Cl	Sb, (As, P), F, Cl	B, Al, In, Ga, Si, Sn, F, Cl
Crystal structure, space group	cubic $I2_13$	tetragonal, rutile $P4_2/mnm$	hexagonal, wurtzite $P6_3/mc$
Lattice parameters (nm)	*a*: 1.012	*a*: 0.474 *c*: 0.319	*a*: 0.325 *c*: 0.5207
Thermal expansion α (300 K) (10^{-6} K^{-1})	6.7	// *c*: 3.7 ⊥ *c*: 4.0	// *c*: 2.92 ⊥ *c*: 4.75
Melting point of the metal (°C)	157	232	420
Average amount of the metal in the earth's crust (ppm)	0.1	40	132

* Decomposition into SnO and O_2 at 1500 °C.

Bulk ZnO exhibits plastic deformation for relatively low loads, compared to GaN [13]. In a nanoindentation study, the critical load for plastic deformation for bulk ZnO was found to be 4-13 mN with a spherical indenter of ~4.2-mm radius [40]. In the same study, hardness (H) was measured as 5±0.1 GPa at a depth of 300 nm. Elastic modulus was found to be constant along that penetration depth, with E = 111.2±4.7 GPa. Compared to GaN, ZnO is softer. The hardness and elastic modulus of GaN were given as 15.5±0.9 GPa, and 210±23 GPa, respectively [40].

Table 1.2. Piezoelectric and dielectric properties of some non-ferroelectric materials [41].

Physical parameter	**Coefficients/figures of merit**	**ZnO [42, 43]**	**AlN [44, 45]**	**PZT (1–3 μm) [46]**
Deflection force, piezoelectric charge of deflected piezoelectric laminated structure	$e_{31,\,f}$ (Cm^{-2})	-1.0	-1.05	-8– -12
Effective piezoelectric coefficient	$d_{33,\,f}$ (pm/V)	5.9	3.9	60–130
	ε_{33}	10.9	10.5	300–1300
Piezoelectric voltage in deflected piezoelectric laminated structure	$e_{31,\,f}/\varepsilon_0\varepsilon_{33}$ (GV/m)	-10.3	-11.3	-0.7– -1.8
Coupling coefficient for plate wave	$e^2_{31,\,f}/\ \varepsilon_0\varepsilon_{33}$ (GPa)	10.3	11.9	6–18
Dielectric loss angle	tanδ (@1 to 10 kHz, 10^5 V/m)	0.01–0.1	0.003	0.01–0.03
Signal-to-noise ratio	$e_{31,\,f}/(\varepsilon_0\varepsilon_{33}\ \tan\delta)^{(1/2)}$ (10^5 Pa$^{1/2}$)	3–10	20	4–8
Coupling coefficient for thickness wave	$d^2_{33,\,f}\cdot c^E_{33}/\ \varepsilon_0\varepsilon_{33}$	7.4%	6.5%	7%–15%

Table 1.3. Some mechanical properties of ZnO collected by Özgür *et al.* [13]. C_{ij} are the elastic stiffness constants. The details of the measurements are given in the box below the table. The reference numbers belong to the study by Özgür *et al.* [13].

Parameters	**Wurtzite**	**Zinc blende**	**Rocksalt**
C_{11} (GPa)	209.7,[a] 206,[b] 157,[c] 190,[d] 207,[e] 209,[f] 230,[g] 231,[h] 246[i]	193[i]	
C_{12} (GPa)	121.1,[a] 117,[b] 89,[c] 110,[d] 117.7,[e] 85,[f] 82,[g] 111,[h] 127[i]	139[i]	
C_{13} (GPa)	105.1,[a] 118,[b] 83,[c] 90,[d] 106.1,[e] 95,[f] 64,[g] 104,[h] 105[i]		
C_{33} (GPa)	210.9,[a] 211,[b] 208,[c] 196,[d] 209.5,[e] 270,[f] 247,[g] 183,[h] 246[i]		
C_{44} (GPa)	42.47,[a] 44.3,[b] 38,[c] 39,[d] 44.8,[e] 46,[f] 75,[g] 72,[h] 56[i]	96[i]	
C_{66} (GPa)	44.29,[a] 44.6,[b] 34,[c] 40,[d] 44.6,[e] 62,[f] 60,[h] 115[i]		
Bulk modulus, B (GPa)	142.4,[j] 183,[k] 170,[l] 160,[m] 162.3,[n] 133.7,[o] 156.8[k]	161.7,[n] 135.3,[o] 154.4[k]	202.5,[j] 228,[p] 205,[m] 205.7,[n] 172.7,[o] 203.3[k]
dB/dP	3.6,[j] 4.0,[p] 4.4,[m] 4.05,[n] 3.83,[o] 3.6[k]	3.95,[n] 3.72,[o] 3.6,[k]	3.54,[j] 4.0,[p] 4.88,[m] 3.90,[n] 3.77,[o] 3.6[k]
Young's modulus, E (GPa)	111.2±4.7[q]		
Hardness, H (GPa)	5.0±0.1[q]		
e_{31} (C/m^2)	-0.62,[r] -0.51,[c] -0.39,[s] -0.53,[t] -0.51,[u] -0.55,[i] -0.66[v]		
e_{33} (C/m^2)	0.96,[r] 1.22,[c] 0.92,[s] 1.19,[t] 1.21,[u] 1.19,[i] 1.30,[v]		
e_{15} (C/m^2)	-0.37,[r] -0.45,[c] -0.46[i]		
e_{14} (C/m^2)		0.69,[i] 0.64[w]	
Spontaneous polarization (C/m^2)	-0.057,[t] -0.047,[x] -0.057[u]		
Born effective charge, Z*	2.06,[t] 2.11,[u] 2.10,[w] 2.1[x]		

Table 1.3 —Continued.

[a] Ultrasonic measurement on single-crystal ZnO grown by chemical reaction in vapor state (Ref. 105).
[b] Surface Brillouin scattering on polycrystalline ZnO film deposited by RF sputtering on (100) Si substrate (Ref. 662).
[c] Acoustic investigation technique on ZnO film deposited by RF magnetron sputtering on sapphire substrate (Ref. 663).
[d] Polarized Brillouin scattering on bulk ZnO single crystal (Ref. 664).
[e] Ultrasonic resonance method on ZnO single crystal (Ref. 665).
[f] Calculated using LDA (Ref. 66).
[g] Calculated using GGA (Ref. 66).
[h] Atomistic calculations based on an interatomic pair potential within the shell-model approach (Ref. 70).
[I] Calculated using *ab initio* periodic linear combination of atomic orbitals (LCAO) method, based mainly on the Hartree-Fock Hamiltonian, with an all-electron Gaussian-type basis set (Ref. 660).
[j] X-ray diffraction using synchrotron radiation on polycrystalline ZnO (99.99% purity) (Ref. 64).
[k] Calculation based on *ab initio* all-electron periodic Hartree-Fock linear combination of atomic orbitals (Ref. 56).
[l] Calculation using molecular-dynamics simulation based on Tersoff's potential (Ref. 133).
[m] Calculation based on modern theoretical HF cluster and full-potential scaler-relativistic linearized-augmental plane wave (Ref. 65).
[n] Calculating using LDA (Ref. 57).
[o] Calculation using GGA (Ref. 57).
[p] X-ray diffraction and 67Zn-Mössbauer spectroscopy on bulk ZnO (Ref. 65).
[q] Spherical nanoindentation on bulk ZnO (Ref. 113).
[r] Resonance-antiresonance method on ZnO single crystal (Ref. 665).
[s] Calculation using modern *ab initio* (Ref. 107).
[t] Calculation using *ab initio* quantum-mechanical level by using through the Berry-phase scheme applied to delocalized crystalline orbitals and through the definition of well-localized Wannier functions (Ref. 661).
[u] Calculation based on *ab initio* using the Berry-phase approach to polarization in solids (Ref. 109).
[v] Calculation using a plane-wave pseudopotential implementation of density-functional theory and density-functional linear response within the local-density approximation (Ref. 101).
[w] Reference 666.
[x] Calculation using the LDA, HF, and a model *GW* scheme (Ref. 87).

ZnO, like other electroceramics (*e.g.,* $BaTiO_3$), contains a significant amount of porosity, up to 5% (v/v) [47]. In their study, Lu *et al.* showed that the major influence on the fracture strength of bulk ZnO was the pore/grain size interaction, rather than the grain size itself. Pore clustering was attributed to the inhomogeneous distribution of defects, while pore-grain interactions increased the probability of fracture via small pores. A high degree of porosity and pore clustering led to the homogenization of crack sizes. The mean strength of ZnO was calculated as 102.37 MPa. The authors emphasized that the mechanical properties such as fracture strength were influenced by the local structure, rather than the average.

1.2. Functional Thin Films

Thin films are structures that are deposited onto a substrate surface by any chemical or physical deposition method (which will be discussed further). When a material is deposited in the form of a thin film, its microstructure is modified compared to its bulk form. This is a result of the existence of a *preferred growth direction* and competing nucleation and growth mechanisms during deposition. It is possible to have control over these by controlling the conditions of the deposition system. Consequently, the film would have a certain *texture*, describing the statistical distribution of grain orientations [48, 49]. Moreover, the films would be restrained at one end, by the substrate surface. Therefore, the film properties would differ from the bulk values. More significantly, they would be anisotropic, owing to the texture.

The physical structure of a thin film is very important in terms of determining its functional properties. However, although much research has been done on the structure of thin films, the state-of-the-art understanding of the growth mechanisms is mostly qualitative. The needs of the flexible display or microcircuit industry require low deposition temperatures at which the adatom mobility is limited, leading to the formation of a columnar morphology. How this columnar structure evolves and other prominent aspects of thin films are highlighted in the next sections.

1.2.1. Structure-Zone Models

Thin film formation can be considered a type of phase transformation and is accomplished by the nucleation and growth processes [2, 50-53]. The basic theory on film growth proposes the three growth models:

i) island (in-thickness; *i.e.,* in the direction of the surface normal) (Volmer–Weber type),

ii) layer (lateral) (Frank–van der Merwe type)

iii) a combination of these two (Stranski–Krastanov type).

These are illustrated in Fig. 1.4. The mechanisms leading to these growth types are as follows [50]: When the bonding between the atoms or molecules of the film material is stronger than that of the film-substrate bonding, the island-type of growth is observed. The smallest stable cluster of the film material nucleates on the substrate and grows in three dimensions. In the reverse case, when the atoms of the film material tend to bond more strongly to the substrate than to each other, the stable clusters grow much more rapidly in two-dimensions namely on the substrate surface, and they form layers on the substrate. In the third case, the initial film growth resembles the second type. However, after the first few monolayers are formed, the interaction between the adatoms and the substrate lessens, and island formation dominates. This is a transition from two-dimensional to three-dimensional growth and seems counter-intuitive due to the increase in surface area. A probable reason for this to be favored is explained by the release of strain energy that accumulated in the film as a result of the two-dimensional growth [50].

After the initial stages of nucleation and growth, the route to the complete film structure contains four basic aspects [50, 54]:

i) shadowing and transport of adatoms onto the substrate,

ii) adsorption and surface diffusion,

iii) incorporation of adatoms into the coating or removal by evaporation or desorption,

iv) transfer of the adatoms to their final positions by bulk diffusion.

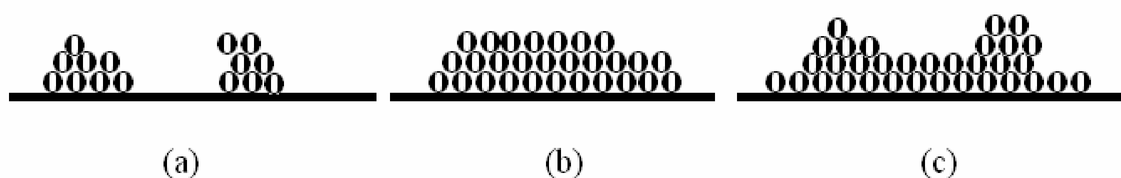

Figure 1.4. Stages of film growth: (a) island formation, (b) layer formation, (c) combined island and layer formation.

The relative dominance of these effects on the adatoms determines the film formation kinetics and hence the final film structure. The film grows with a certain roughness. At the same time, the atom flux directed at the substrate is in most cases not symmetrical with respect to the substrate normal. Consequently, not all the atoms incident on the surface had the same line-of-sight [50, 54], creating a shadowing effect. The adatoms have a limited range of positions to settle onto, causing an anisotropic film structure. This shadowing effect is controlled mainly by the deposition parameters of the system, such as the system geometry and the gas pressure. On the other hand, the diffusion and adsorption-desorption behavior are mainly dictated by the substrate temperature and the resulting adatom mobility on the surface. The dominance of any of these processes are determined by the deposition parameters and the main ones are [52]:

i) the nature of the substrate,

ii) the substrate temperature,

iii) the deposition rate and the film thickness,

iv) the nature and the pressure of the gas medium.

Structure zone models (SZM) have been proposed for classifying the micro- and nano-structure of the deposited films in relation to the combined affect of these factors in thin film literature. The original model was developed for metallic thin films [55] and it was based on the dependence of the microstructure on the homologous temperature (T_h). (Homologous temperature is defined as T/T_m, where T is the system temperature during deposition, and T_m is the melting point of the target material.) The structure model consisted of three zones (Fig. 1.5). In Zone 1 of low adatom mobility (and the *sticking coefficient* being equal to 1 [51], where the sticking coefficient is defined as the ratio of the adatoms that stay on the substrate surface to the overall number of adatoms incident on the surface), the dominating factor was the shadowing effect. The low number of nuclei in this region led to a columnar film structure with inter-columnar voids (*i.e.*, longitudinal porosity) with a few hundred Å of width between them [54, 56, 57], and usually in a honeycomb-like structure [51]. This region also contained a high dislocation density and high residual stresses. The low adatom mobility also led to columns that compete for growth in a power-law shape, forming hierarchical aggregates and cauliflower type structures [51]. In Zone 2, surface diffusion dominated, leading to columnar grains with increased width and well-defined grain boundaries. The increased

substrate temperature led to increased mobility of the film atoms and full-density columnar morphology. The difference between the tapered columns of Zone 1 and the parallel-walled columns of Zone 2 can be seen in Fig. 1.6.

In Zone 3, bulk diffusion dominated and equiaxed grains formed. Several modifications have been made on this model to account for deposition parameters other than the system temperature. Thornton added the pressure effect and defined a transition zone (Zone T) between Zone 1 and Zone 2 [54, 56] (Fig. 1.7). In that model, the increased substrate temperature between Zone 1 and Zone 2 led to densely packed, fibrous grains with weak grain boundaries. As the temperature increased, the Zone 2 columns became faceted, and the temperature for the transition zone shifted to higher temperatures with increasing gas pressure.

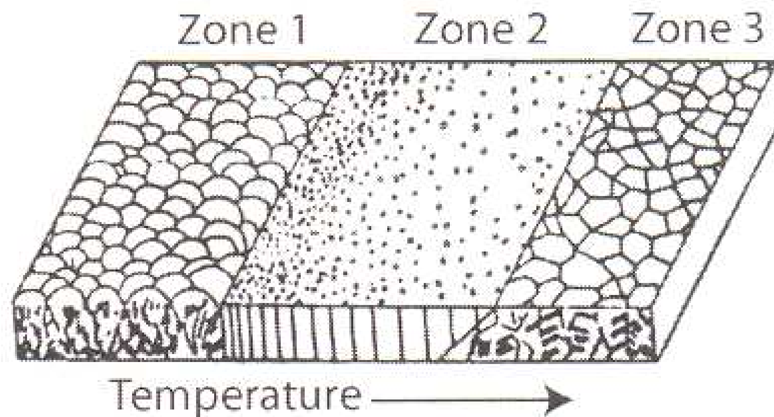

Figure 1.5. The first structure zone model, proposed by Movchan and Demchishin. (Reprinted from Ref. [51]; original figure by Ref. [55]; published with permission from SPIE Press and Elsevier Publishing Ltd.).

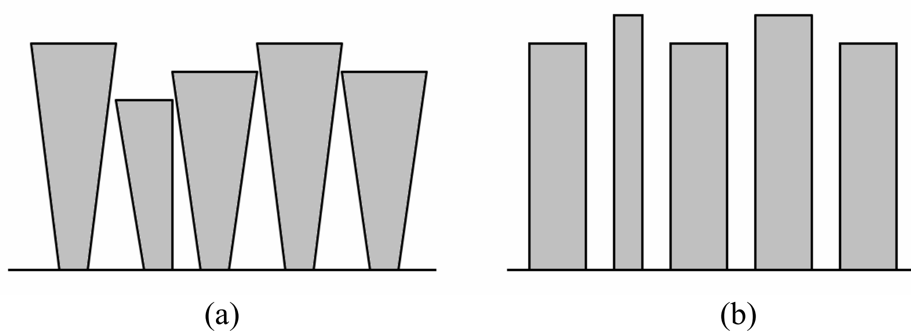

Figure 1.6. Two different growth behaviors for columnar films: (a) tapered columns, (b) parallel-walled columns.

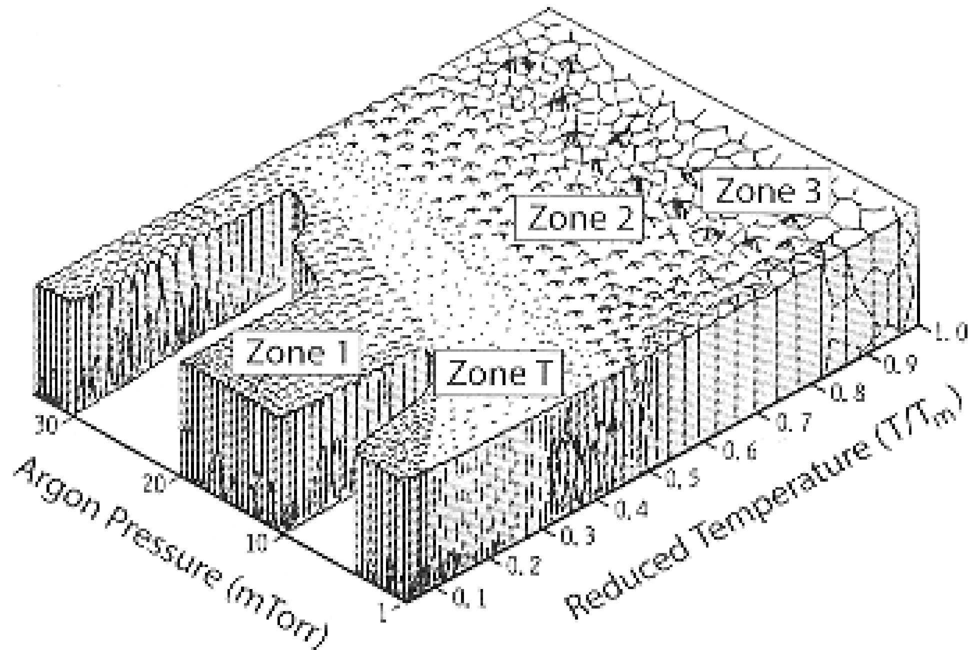

Figure 1.7. Representation of the structure zone model modified by Thornton. (Reprinted from Ref. [51]; original figure by Ref. [51, 54]; published with permission from SPIE Press and AVS Publishing Ltd.).

For metal films, Grovenor *et al.* found that the tapered columns in Zone 1 were not single grains but were instead composed of bundles of smaller and equiaxed grains [58] (Fig. 1.8 and 1.9). They also emphasized the dominance of grain boundary diffusion over surface diffusion, as a factor that was controlling the grain structure in Zone T and Zone 2.

Messier *et al.* included the effect of substrate voltage bias and film thickness through studies on *a*-Ga thin films [59, 60]. They observed that the columns in those thin films were composed of smaller columns with several size scales, in a fractal-like structure. The size scale of those columns expanded from 2 to 300 nm (Fig. 1.10). These nano-, micro-, and macro-columns were also associated with nano-, micro-, and macro-voids [59, 61-63]. These structures were related to the adatom mobility and the mobility sources were summarized as:

i) thermally-induced,

ii) induced by energetic particle bombardment of the film during deposition,

iii) induced by the nature of the vapor species and the relative bond strengths of the materials involved (chemically-induced).

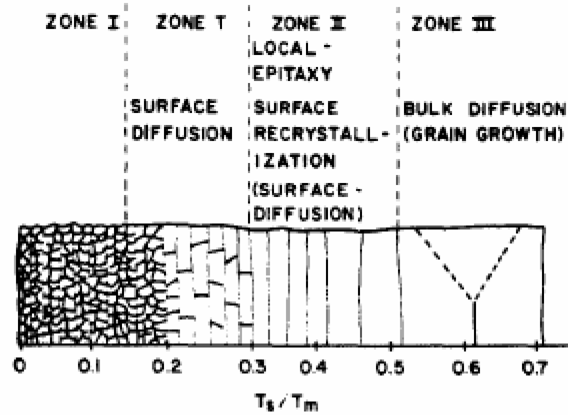

Figure 1.8. Zone model for the grain structure of vapor deposited metal films modified at low temperatures, including the fine equiaxed grain structure (Reprinted from Ref. [58]; with permission from Elsevier Publishing Ltd.).

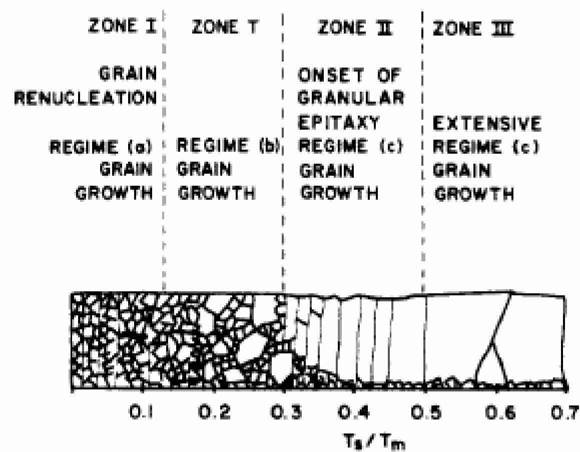

Figure 1.9. Zone model for the grain structure of vapor deposited metal films modified to include the bimodal grain size distribution in Zone T, also including the mechanisms that are proposed to control the grain structure in each of the zones. (Reprinted from Ref. [58]; with permission from Elsevier Publishing Ltd.).

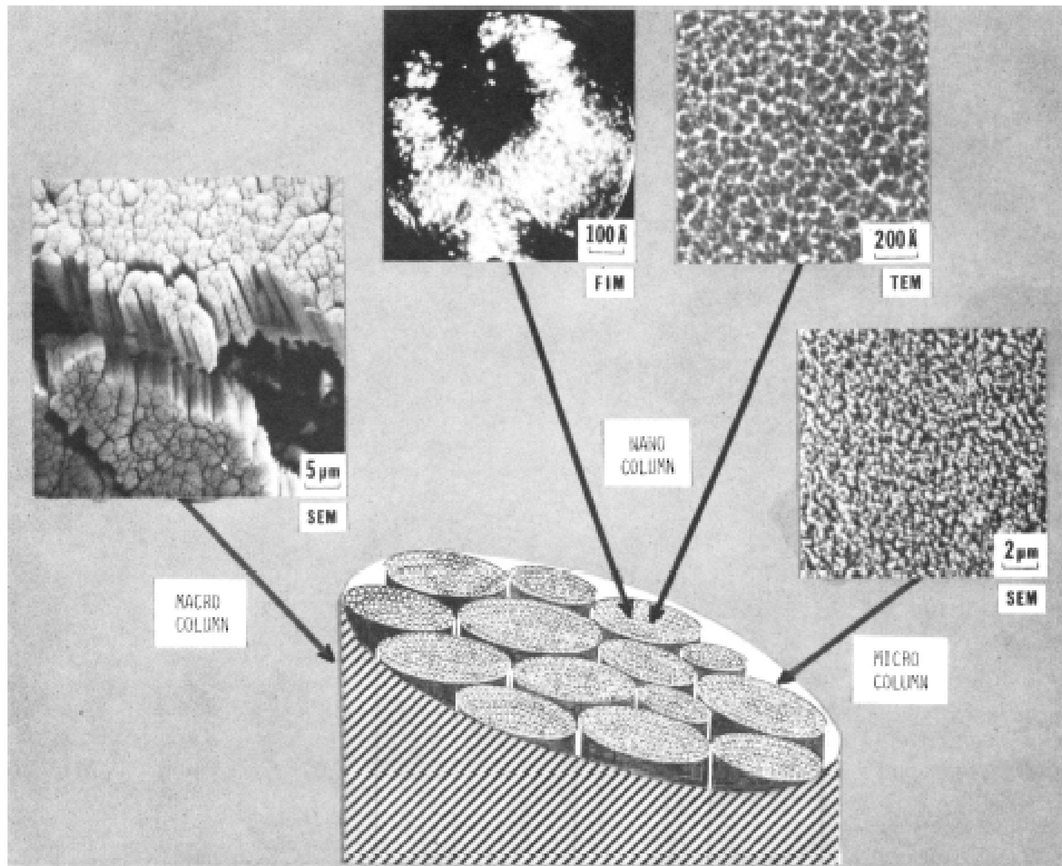

Figure 1.10. The fractal grain structure at different length scales for thin films grown under low adatom mobility (Reprinted from Ref. [59]; published with permission from AVS).

According to the thickness of the film, new sub-zones in Zone 1 were defined to represent the nonlinear thickness evolution [59] (Fig. 1.11). These zones were classified from 1A to 1E, with 1A having the smallest size columns (1-3 nm) and the latter having the largest columns (around 300 nm). The most recent structure zone model for metal films was proposed by Messier and Trolier-McKinstry [63]. In their model, an additional zone of matchstick morphology was defined. In this zone, the columns were parallel to each other and they contained dome-shaped tops (Fig. 1.12).

For a more detailed discussion on the structure zone models and new types of microstructures *sculptured* by careful control of the deposition geometries, see Ref. [51]. For computer simulation of the microstructure formation in columnar thin films, see Ref. [51, 64, 65].

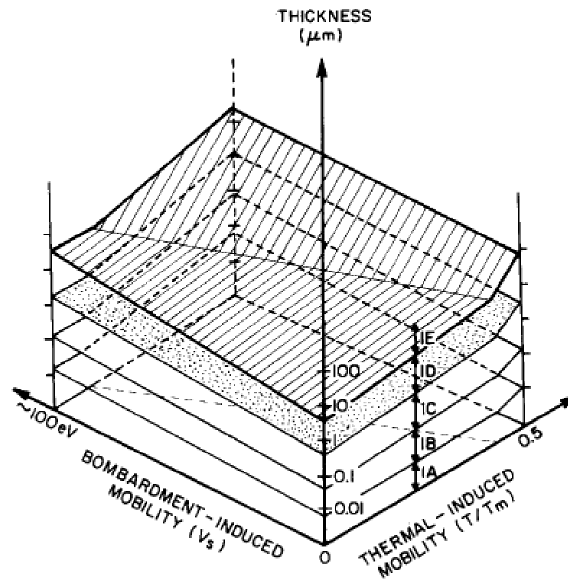

Figure 1.11. Revised zone model with sub-zones of Zone 1 depending on film thickness and the mobility of adatoms induced by energetic ion bombardment (Reprinted from Ref. [59]; published with permission from AVS).

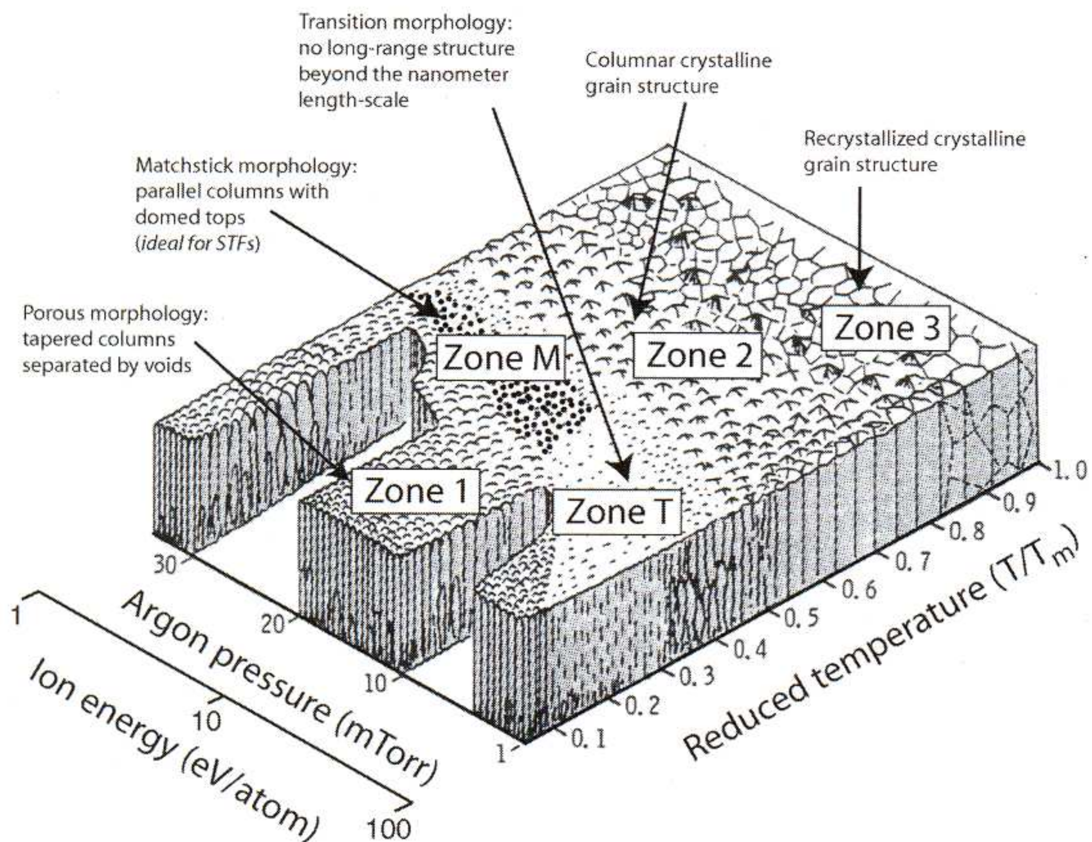

Figure 1.12. A recent structure-zone model developed by Messier and Trolier-McKinstry. (Reprinted from Ref. [51]; original figure by Ref. [63]; published with permission from SPIE Press and Elsevier Publishing Ltd.).

1.2.2. Texture in Thin Films

As mentioned above, the polycrystalline thin films usually have a certain *texture*, describing the statistical distribution of grain orientations [48]. Texture arises in polycrystalline thin films due to the fact that some crystallographic planes can occur with a greater probability than others [49] Texture could be realized as a level of organization of the atoms, one scale higher than the grains. The atoms organize in a short-range order to form the grains, in other words, the single crystal pieces. A group of grains, on the other hand, organize themselves in a certain way, giving the characteristic texture. The crystal structure is a material property, whereas the texture is dictated by the system constraints. The functional properties of a thin film material such as remnant polarization, dielectric constant, elastic modulus are anisotropic due to the texture in the films, thus accurate measurement and control of texture are important [66]. Powder x-ray diffraction methods could be used for this purpose. However, synchrotron radiation would provide more accuracy, owing to the very high intensity of the x-ray beam [67]. In creating pole-figures with an Euler cradle [49], synchrotron radiation would provide increased acquisition speed and resolution by using small steps in both the inclination (tilt) angle (ψ) and the angle of in-plane sample rotation (ϕ) [67].

It was shown that, through the course of growth of crystalline thin films, only those grains with the preferred growth direction survived, presumably to minimize the surface energy [52]. The first studies on texture were done mostly on metal films such as iron [68], Ti [69]. In these studies, it was found that low substrate temperature led to strong texture in metals.

Basically, three types of texture have been defined on polycrystalline thin films [48], which are illustrated in Fig. 1.13 :

i) random,

ii) fiber,

iii) epitaxial.

The conditions promoting any type of these textures were discussed in the previous section. In random texture, there is no preferred orientation of the grains on the substrate surface. As the name implies, all the grains are distributed in random orientations with respect to each other and the substrate plane. This type of texture is

seen when the atoms have low mobility and when there is no preferred growth direction of the unit cell. In fiber texture, one crystallographic axis is parallel to the substrate normal, providing columnar grains parallel to each other, but oriented in different direction with respect to the substrate normal. The major factor creating this type of texture is the shadowing effects during growth. In the third case of epitaxial texture, all three axes of each grain are fixed with respect to the substrate. This type of texture is also called *in-plane texture* and is seen in the films grown on single crystal substrates, where the lattice parameters of the film and the substrate are close to each other.

Apart from these three types, a new type of texture has recently been observed by Detavernier *et al.* This new type of texture was named *axiotaxy* or *off-normal fiber-like texture* and was observed in NiSi [67] and tetragonal α-$FeSiO_2$ [48] films deposited on cubic Si(001) substrates. In this type of texture, a set of planes of the film was aligned with a set of planes of the substrates, but none of the axes of the film were parallel to the substrate normal. Instead, one axis was parallel to the normal of the matching plane in the substrate, making an angle to the substrate surface.

For a more detailed discussion on texture in thin films, see [70-73].

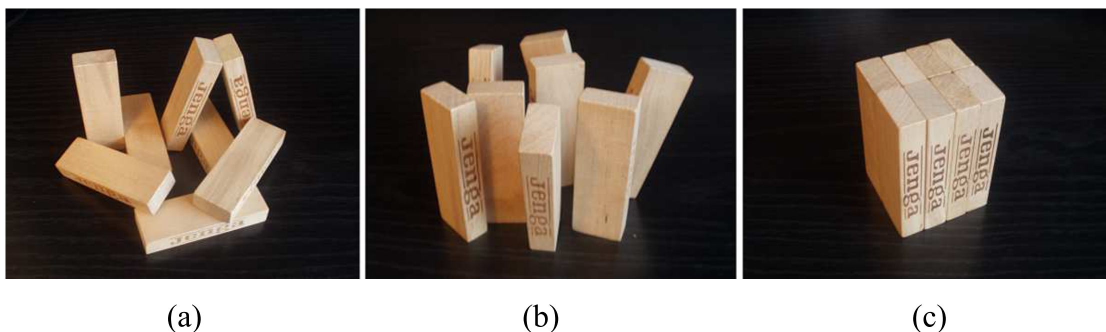

(a) (b) (c)

Figure 1.13. Demonstration of texture in columnar thin films. (a) Polycrystalline: the crystallites are randomly distributed on the substrate. (b) Polycrystalline with strong texture: the crystallites have a preferred orientation with respect to the substrate plane. (c) Single crystal: Perfect texture; all the crystals are oriented in the same direction with respect to all three axes.

1.2.3. Mechanical Properties and Residual Stresses in Thin Films

Thin films are constrained in a film-substrate composite system, which makes the film properties very anisotropic. At the substrate-film interface, the two materials have the same strain as long as adhesion is preserved. However, along the transverse direction, the film is free to move and the stress is zero in this direction. When a force field is applied to the film, in-plane stresses and out of-plane strains are developed. Independent of the presence of an applied field, these out of-plane strains are also created by the residual stresses that develop during film deposition.

It has been extensively observed that thin films had highly anisotropic residual stresses up to several GPa, which were very high compared to the ambient atmospheric pressure of 100 kPa [49]. Metallic films typically possessed tensile stresses from 0.1 to 10 GPa, and the stress usually increased with the melting point of the film material [2]. Stresses in metallic thin films have been investigated in depth. However, the mechanisms leading to the formation and relaxation of these stresses have not been fully understood for ceramic materials [2, 49, 50, 74]. Although residual stress has been defined as ″that which remain in a body and that is stationary and at equilibrium with its surroundings″ [75], it was hardly at equilibrium, changing as a function of time [49, 74, 76]. Thus, for controlling the reliability of the thin film, it would be crucial to understand the formation and stability of the residual stresses [2].

The residual stresses have generally been classified as extrinsic or intrinsic [76], according to the root cause of the stress [50, 74]:

i) thermal expansion coefficient mismatch between the film and the substrate (extrinsic),

ii) lattice mismatch between the film and the substrate (extrinsic),

iii) incorporation of atoms (residual gas or chemical reaction products) (extrinsic or intrinsic),

iv) variation of inter-atomic spacing with crystal size (intrinsic),

v) recrystallization processes (intrinsic),

vi) microscopic voids and dislocations (intrinsic),

vii) phase transformations (intrinsic).

Among these, the structure-dominant intrinsic factors usually dominate over the external affects [74]. Whatever type they belonged to, the perception has been that all residual stresses arose from at least one type of misfit, between the film and the substrate or within the film itself (*i.e.*, between grains or different phases). For example, mismatch at the film-substrate interface caused misfit dislocations and hence destroyed the electrical properties of epitaxial thin films [77]. Moreover, the nature and magnitude of these stresses varied with the deposition method and post-deposition treatments.

Therefore, the properties of a material in thin film form might differ from those of the bulk form, due to several degrees of residual strains and associated stresses originating from the interactions between the film and the substrate. These stresses could be observed in both amorphous and crystalline films. For example, DC-magnetron-sputtered ITO films had residual compressive stresses from -1.7 to -0.4 GPa [78]. The stresses increased with increasing oxygen content in the gas medium. These compressive stresses decreased upon thermal annealing at 250 °C, with simultaneous increase in crystal content and electrical resistivity and decrease in carrier mobility. The decrease of stress was attributed to the lower volume of the crystalline phase than the amorphous phase. Detailed reviews on the residual stress modeling [79]and the factors that effect the residual stresses and the film microstructure [74, 75, 80] could be found in the literature.

Another complication has been that the residual stresses in thin films were dynamic: they changed over time with accompanying changes in the microstructure of the film [49, 74, 76]. Possible stress-relaxation mechanisms included recrystallization within the film, micro-structural variations in the film-substrate interface, plastic flow, creep or other phase transformations. Since stability under normal environmental conditions over time is essential for long-term thin-film device operation, it motivates further investigation of stress dynamics.

Theoretically, the residual stresses in a film deposited on a substrate create bending moments in the film-substrate composite system. The sign of the residual stress depends on the direction of bending (Fig. 1.14). When the film had elongated more than the substrate, the conservation of the film-substrate integrity requires bending of the system towards to substrate. In that case, the film is under compressive planar stress: if there were no constraints on the film, it would take back its flat shape. The situation is the opposite when the film had shrunk more relative to the substrate: the film is under

tensile stress, in the opposite direction with the bending of the system. It was observed that joining of even a few islands increased the stresses at the initial stages of film growth [74]. The tensile stresses were generally caused by voids, whereas the explanation for the cause of compressive stresses was not that straightforward. One explanation was the volume changes during crystallization [74]. For example, the amorphous phase of Bi films was very unstable, and with increased film thickness, spontaneous crystallization occured. Since the density of the crystalline Bi phase was lower, high amounts of compressive stresses were created (up to several GPa) [74].

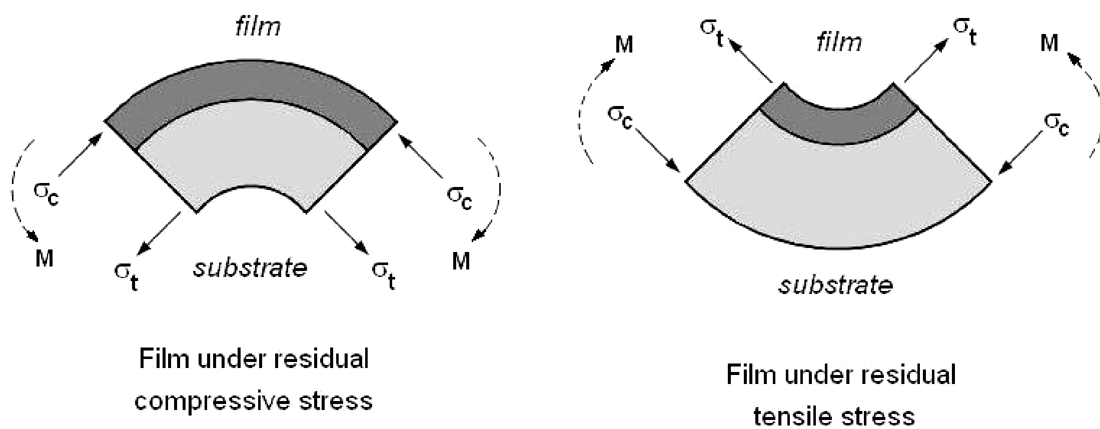

Figure 1.14. Development of residual compressive and tensile stresses in thin films. When the substrate and the film have shrunk with different amounts, the resulting bending moments bend the laminate. The dashed arrows show the direction of bending, and the solid arrows show the direction of the residual stress in the material after the system is bent.

Another proposed cause of residual stresses was *atomic peening*: During deposition, due to the high energy of the adatoms (10–100 eV) [2], ion implantation into the film might have occured, leading to residual compressive stresses. Ttwo competing affects of ion implantation into the film were proposed:

i) The atom was in a metastable position, increasing the local density and hence the strain energy, namely creating an extended defect within the film, and

ii) *Thermal spike* provided by the implanted atom could have released the other implanted atoms from their metastable state, causing them to diffuse through the film to the surface.

The mechanical stability of thin films greatly depended on the amount of adhesion between the film and the substrate: *"The thin film is very fragile, and it depends on the substrate for strength."* [1, 81]. There is not a solid consensus in the scientific literature to define adhesion. Moreover, adhesion has been hard to measure without being influenced by the measurement technique. Several definitions of adhesion and the factors that influence adhesion were summarized as follows [1, 81]:

i) *interfacial adhesion:* The film and the substrate had a well-define interface.

ii) *interdiffusion adhesion*: The interface between the film and the substrate is continued gradually from one material to the other. It was influenced by either the solid-state diffusion or the solubility of one of the materials into the other.

iii) *intermediate layer adhesion*: There was no well-defined interface, but the film and/or the substrate materials for various types of chemical compounds, extending to several monolayers of thickness.

iv) *mechanical interlocking:* The film were partially interlocked by the topographic features on the substrate, since the substrates were never perfectly flat. Therefore, interface area extended, which provided more bonds between the film and the substrate. Thus, rough surfaces could provide more adhesion, provided that severe stresses were not created. Rough surfaces were also not advantageous for vacuum deposition, due to the *shadowing effect*. This effect could have resulted in uncoated areas or microscopic voids or vacancies, which might have initiated adhesion failure.

When the amount of mechanical energy stored inside the film was considerably large (several GPa), it might have been released by crack generation, crack propagation and peeling off of the layer from the substrate [49]. For films with low elasticity, the relaxation would have been via cracks and blisters. If the adhesion was weak, the film would have completely detached from the substrate. On the other hand, strong adhesion would have given rise to film stresses and consequent moments sufficiently high to bend the substrate. In an extreme case, the film would have buckled and led to complete loss of adhesion between the film and the substrate (Fig. 1.15).

Several deposition parameters had particularly strong impact on the film mechanical properties. As an example, the effect of substrate bias on the DC magnetron-sputtered ZrN films' toughness and adhesion to the substrate were

investigated in relation to the residual stresses [82]. When these films had low adhesion on Si substrate, this was attributed to the lattice mismatch of the film and the substrate (a_{ZrN} = 0.4577 nm, a_{Si} = 0.5431 nm) and the differences in the thermal expansion coefficients ($\alpha_{ZrN} = 7.26 \times 10^{-6}$ K^{-1}, $\alpha_{Si} = 2.33 \times 10^{-6}$ K^{-1}). The residual compressive stress contained in the film varied from -0.186 to -1.938 GPa, depending on the DC bias (-45 – +35 V). For the bias value of 50 and 20 V, the thermal expansion-mismatch components of residual stresses were 0.127 and 0.105 GPa, respectively. The critical load for delamination of the ZrN film by scratching was found to be 11.3–23.2 N. The maximum critical load was achieved when the substrate bias was zero. Ion bombardment of the film due to applied substrate bias provided direct momentum transfer and thermal mobility to the species on the surface. Therefore, the film's uniformity, density, and surface coverage increased, while the pinhole density decreased. However, negative bias decreased the practical adhesion, presumably due to the increased residual stress induced by Ar bombardment. Likewise, positive bias produced higher deposition rates and higher residual stress. At the same time, due to the low mobility of the species on the surface, a loose and defective microstructure was created. Thus, positive biasing was not advantageous for the adhesion, either.

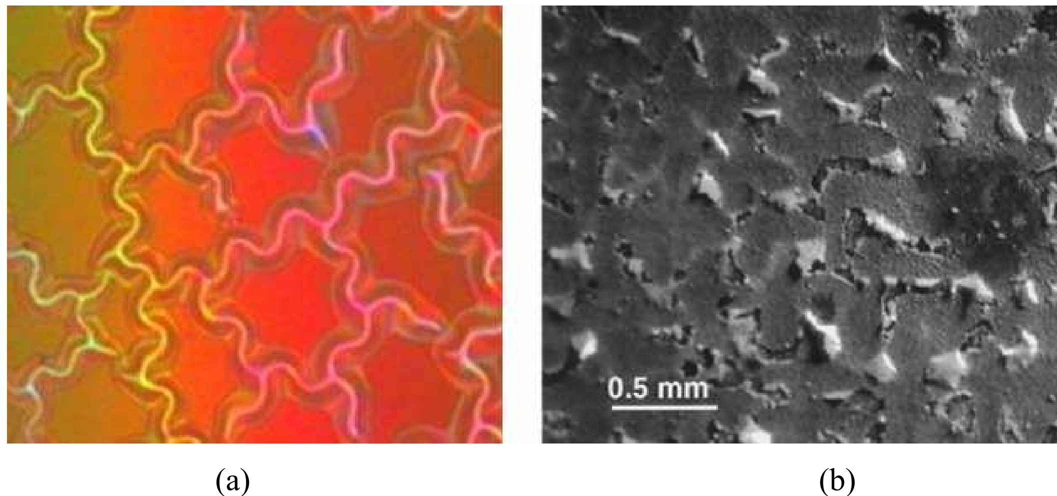

(a) (b)

Figure 1.15. Coating deformation and buckling due to compressive stress on oxide layers. (a) Optical microscope image of a SiO_2 coating on PMMA [83]. (b) Thermally grown alumina film formed at 1100 °C after 10 h and then furnace cooled to room temperature (Reprinted from Ref. [84] with permission from Elsevier Publishing Ltd.).

Crack growth and integrity of the ITO films on polyester substrates were investigated for flexible display applications [85]. The films contained residual compressive stress from -200 to -950 MPa, increasing with increasing thickness. The cracking behavior was also found to be thickness-dependent. A transition from stable to unstable crack growth was observed when the crack length exceeded ten times the film thickness. The critical onset strain for crack generation was found to be 1.18% for 150 nm-thick films under -742 MPa of compressive stress.

Various types of cracks in a thin film are shown in Fig.1.16 [86]. Here, Z is dimensionless number (about unity) that defines the driving force for crack generation. It relates the energy release rate in a crack (G) to the stress involved (σ) as follows:

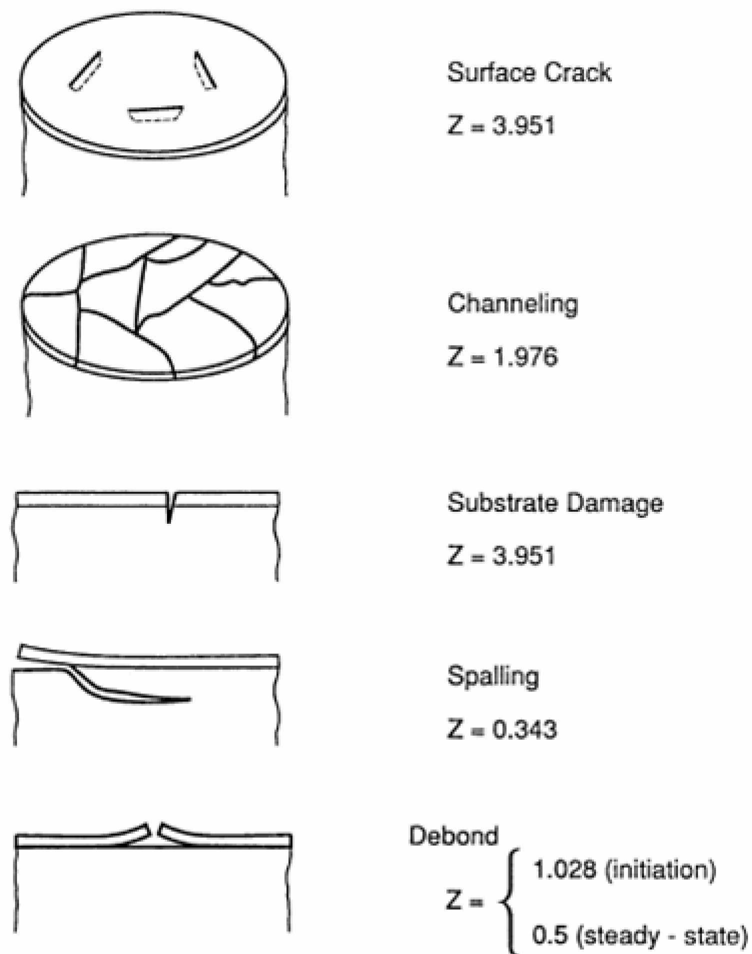

Figure 1.16. Commonly observed cracking patterns [86]. (Reprinted from Ref. [86] with permission from Elsevier Publishing Ltd.).

$$G = Z\sigma^2 h/E_f. \quad (1.2)$$

Here h is the layer thickness, and E_f is the elastic modulus of the film material. The value of Z varies depending on the type of crack and the elastic mismatch between the film and the substrate.

The Z value is not enough for determining whether one of the crack types in Fig.1.16 will be created or not. There is a *critical film thickness,* h_c*,* which limits the crack-free state. Its relation to stress is given as follows [86]:

$$h_c = \Gamma_f E_f / Z\sigma^2. \quad (1.3)$$

Here Γ is the fracture resistance of the film material. Below a thickness of h_c, the film would not exhibit the crack pattern designated by the Z value. The common crack patterns, as shown in Fig. 1.16, have been classified as follows [86]:

i) *surface cracks*: These were nucleated from isolated flaws on the surface. They had a high driving force of formation (high Z), but the stress was not high enough for these cracks to channel through the film. This type of cracks was detrimental for corrosion protection coatings, but tolerable for many other applications.

ii) *channeling*: This was an unstable process; the channels continued propagating until they were stopped by either another channel or an edge. Therefore, a channel network was formed, surrounding isolated islands of the film material. It was often seen in glazes (pottery) and road pavements and could be detrimental for many other applications.

iii) *substrate damage*: This type of cracks had the largest Z value among others. It was formed when the cracks propagated into the film. Thereafter, they could either stabilize within the film or change direction and propagate parallel to the substrate.

iv) *substrate spalling*: This phenomenon occurred when a crack propagated inside the film in a direction parallel to the substrate. This often led to extensive flaking of the film. Owing to the small Z value, it was tolerable for some applications.

v) *debonding*: This was the complete local loss of the adhesion between the film and the substrate. It could have initiated either edge defects or channels, as described above. The driving force for initiation was higher than for the propagated debonding, which in some cases could have been stable. Thus, in some cases, pre-cracks were introduced into the material to take advantage of this phenomenon.

Wang *et al.* reported the mechanisms of spalling and buckle formation in thermally grown 50 μm-thick aluminum oxide films [84]. The growth temperature was 1000 °C. Several factors leading to cracking and the loss of adhesion were summarized as follows:

i) large residual compressive stresses in the film (3–5 GPa) created either during film growth or cooling (due to thermal expansion mismatch),

ii) thickening of the oxide film at high temperature, resulting in increased density available for spalling,

iii) segregation of impurities to the interface,

iv) embrittled interface leading to wedging or buckling. Wedging is promoted by *shear-crack* mechanisms and subsequent inelastic shear deformation.

It was experienced that those shear deformations in the residually compressed thin films caused tensile stress concentration at the film-substrate interface that led to cracking and *spalling* [86, 87]. The mechanisms for buckling are demonstrated in Fig. 1.17:

i) Separation between the film and the substrate developed.

ii) Film buckled. Buckling propagated through the interface.

iii) Buckling induced bending stresses in the film. Consequently, cracking and spalling occurred.

In brittle films, the tensile stress at the top of the buckles could be high enough to create ridge cracks [88]. Then the buckles were rather straight-sided, in contrast to telephone-cable buckles. Several types of buckle formation and the relevant imperfections on the surface are presented in Fig. 1.18.

For a thin film under equibiaxial compressive stress, the critical stress (σ_{cr}) to cause buckling of the film over a circular separation was given as [86, 89]:

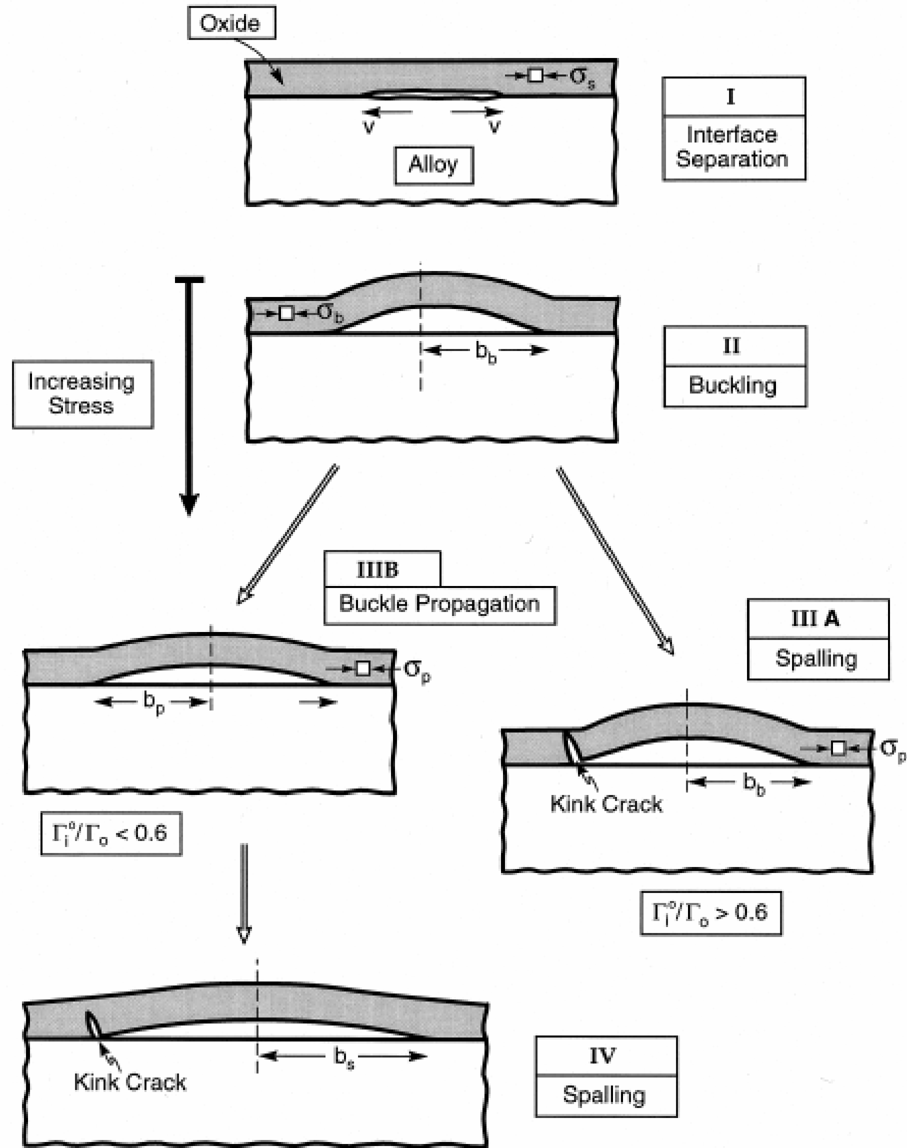

Figure. 1.17. A schematic indicating the sequence of events when a compressed film buckles and spalls away from a substrate (Reprinted from Ref. [84] with permission from Elsevier Publishing Ltd.).

$$\sigma_{cr} = 1.22[E_f / (1- v_f^2)](h/b)^2. \quad (1.4)$$

Here, E_f is the film's elastic modulus, v_f is the film's Poisson's ratio, h is the film thickness and b is the separation radius. When the stress within the film (σ) is greater than σ_{cr}, energy release occurs with a rate of G:

$$G = g_1 G_0[1- (\sigma_{cr} - \sigma)^2], \quad (1.5)$$

where

$$G_0 = (1- \nu_f)h\sigma^2 / E_f, \tag{1.6.a}$$

and

$$g_1 = [1 + 0.9\ (1- \nu_f)]^{-1}. \tag{1.6.b}$$

G_0 is the elastic energy per unit area, stored in the unbuckled film.

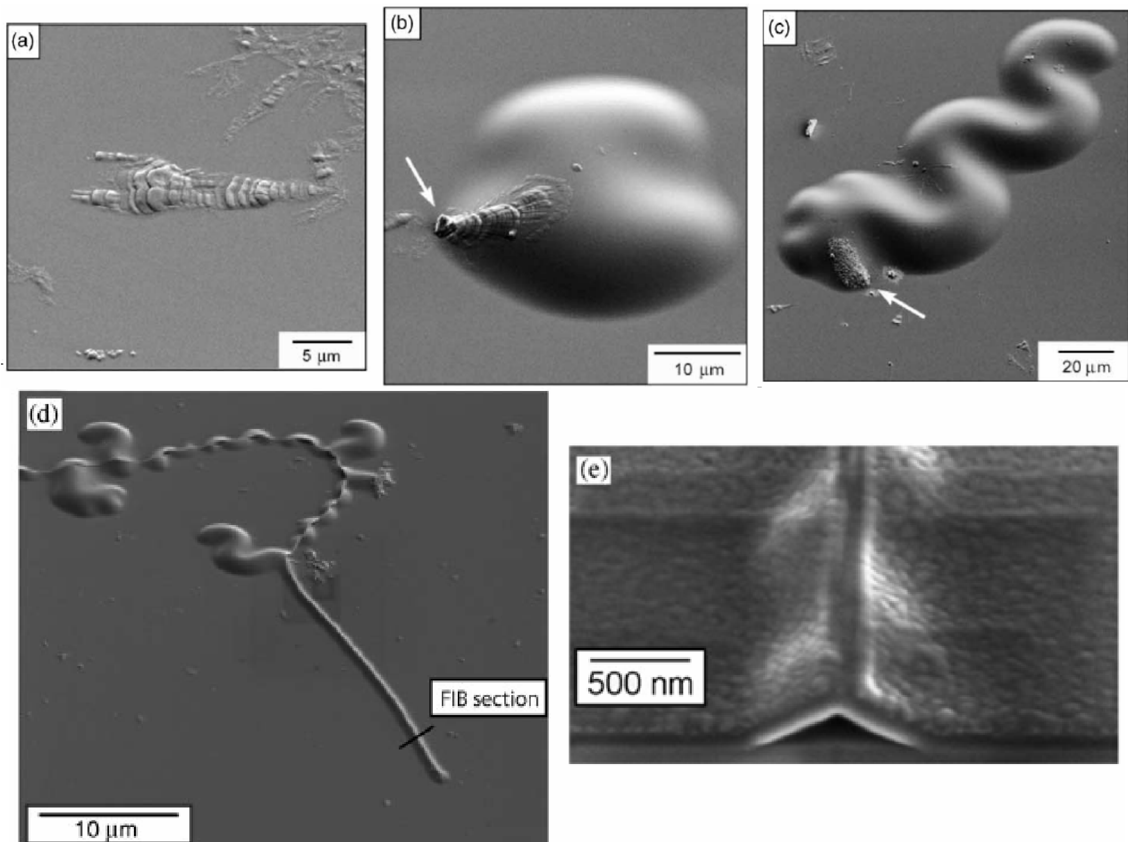

Figure 1.18. Characteristic buckling configurations. (a) An imperfection with no apparent buckle, (b) an imperfection (arrowed) at the perimeter of an axi-symmetric buckle, (c) an imperfection (arrowed) at one end of a telephone cord buckle, (d) two competing buckle delamination morphologies: telephone cord and a straight-sided buckle with a ridge crack that extends to within a buckle width of the front, (e) a FIB cross-section through the buckle with the ridge crack. ((a), (b), (c) reprinted from Ref. [90]; (d), (e) reprinted from Ref. [88]; all with permission from Elsevier Publishing Ltd.)

For the initial separation of the film and the substrate, tensile or shear stresses must exist at the interface [87]. These stresses were formed on non-planar substrates and create crack-like voids at the film-substrate interface [87]. The amount of stress in the film was not the only parameter to determine whether spalling would occur or not [87]. Another critical parameter for the film-substrate separation and buckling was the interfacial toughness, Γ_i, which was a function of the loading phase angle, ψ [84]. Buckling would propagate when

$$G = \Gamma_i. \quad (1.7)$$

A representative buckling map was constructed with three non-dimensional indices (Fig. 1.19.) [84]:

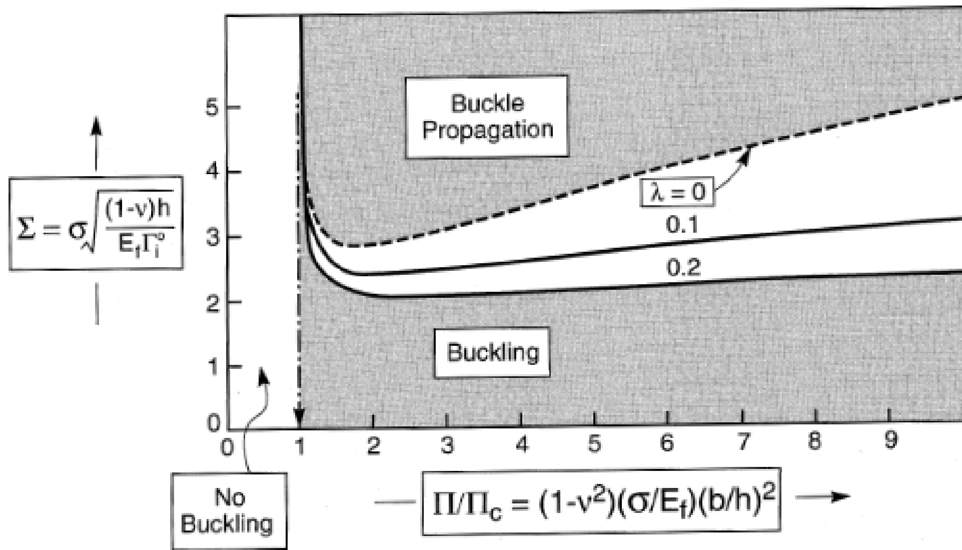

Figure 1.19. A buckling map derived from the mechanics of buckle propagation. The three domains are identified. (Reprinted from Ref. [84] with permission from Elsevier Publishing Ltd.)

i) *buckling index*, Π:

$$\Pi = (1 - \nu_f^2)(\sigma / E_f)(b/h)^2. \quad (1.8)$$

Buckling would not occur unless $\Pi / \Pi_c = 0.22$. The buckle dimensions were related to each other as follows:

$$\delta/h = 1.25\ (\Pi - \Pi_c)^{1/2}, \tag{1.9}$$

where δ was the uplift of the film above the substrate, and h was the film thickness. The relative surface uplift was given as a function of Π / Π_c in Fig. 1.20.

ii) *adhesion index*, Σ:

$$\Sigma = \sigma[h(1- \nu_f)/(E_f \Gamma_i^0)]^{1/2}. \tag{1.10}$$

Γ_i^0 was the mode I interface toughness when the loading phase angle was equal to zero ($\psi = 0$). Buckles would not propagate unless $\Sigma > \Sigma_c \approx 2\text{-}3$.

iii) *mode mixity index*, λ: This parameter depended on the interface roughness.

Considering these factors, three domains of buckle formation were described as follows:

i) $\Pi \leq \Pi_c$: No buckling occured for the whole range of Σ. Although interface separation existed, the overall film adhesion would be preserved.

ii) $\Pi > \Pi_c$ and $\Sigma \leq \Sigma_c$: Buckles were created but they did not propagate. The film adhesion was still stable.

iii) $\Pi > \Pi_c$ and $\Sigma > \Sigma_c$: Buckles were formed and they propagated. The occurrence of *spalling* depended on bending deformation due to buckling, and consequent tensile stress development in the film.

It should be noted that this model was valid only in the case of equibiaxial compressive stress in the film. In the study of Wang *et al.* [84], an external load was applied to the aluminum oxide film in one direction. Axial compressive deformations were applied to the film, by the use of a servo-hydraulic testing system with load control. The maximum compressive stress was 400 MPa and the loading rate was 4 MPa/s. Thus, the stress was not equibiaxial. Nevertheless, the residual compressive stress component dominated. For this reason, the deviation of the measured buckle size from the critical value was small (Fig. 1.21).

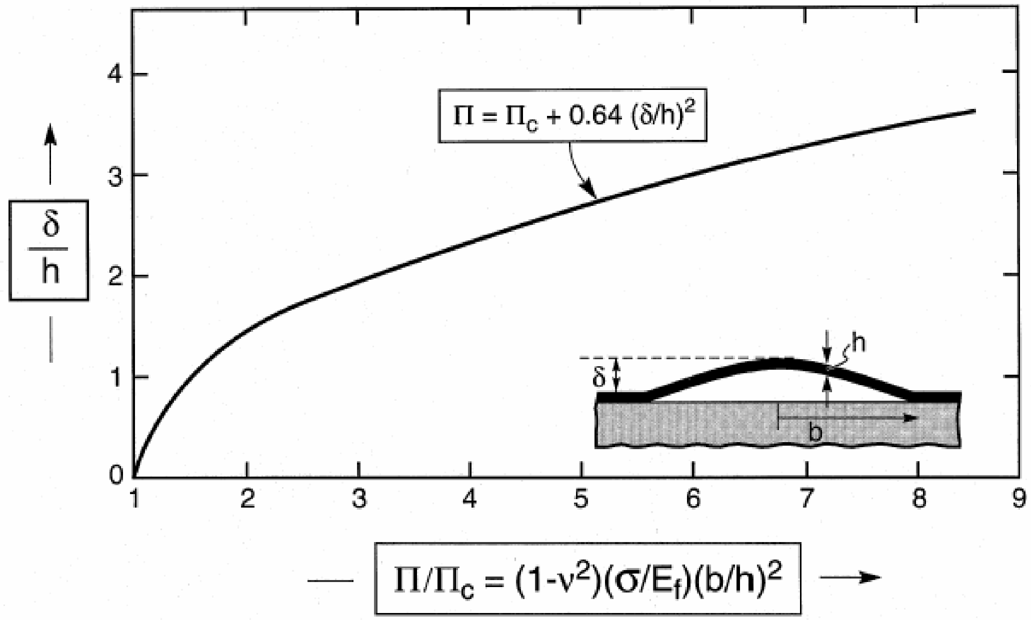

Figure 1.20. The relative surface uplift, *δ*/h, as a function of the compressive stress, relative to the critical value for buckling. (Reprinted from Ref. [84] with permission from Elsevier Publishing Ltd.)

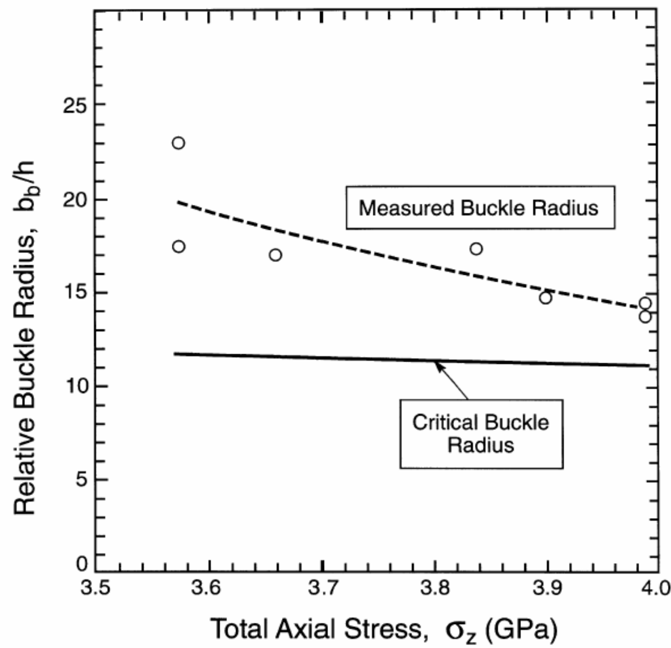

Figure 1.21. The measured and critical buckle sizes plotted as a function of the stress. (Reprinted from Ref. [84] with permission from Elsevier Publishing Ltd.)

Buckling of a stressed film influenced the crack propagation: stress intensified at the buckle perimeter, providing a driving force for delamination and spalling [91]. For a film under biaxial compression, the following set of equations were developed to define the buckling and spalling mechanism in terms of the level of stress that exist in the film [86, 87]. The critical compressive stress value for buckling to occur was:

$$\sigma_{cr} = 1.22[E_f / (1- \nu_f^2)](h/b)^2. \tag{1.11}$$

For a stress level of $\sigma_b > \sigma_{cr}$, the minimum separation that causes asymmetric buckling was given in terms of the stress as:

$$b_b/h = 1.1(E_f/\sigma_b)^{1/2}. \tag{1.12}$$

Those buckles would propagate only if $\sigma_b > \sigma_p$, where

$$\sigma_p = \varphi \, [E_f \Gamma_i°/(1- \nu_f)h]^{1/2}, \tag{1.13}$$

and φ was about 2.5. The corresponding critical buckle radius was given as:

$$b_p/h = \omega(E_f/ \sigma_p)^{1/2}, \tag{1.14}$$

where ω was about 2. Spalling would occur when the stress reached a value of σ_s, where

$$\sigma_s = \varphi^* \, [E_f \Gamma_0/(1- \nu_f)h]^{1/2}. \tag{1.15}$$

φ^* was about 1.7. Once the buckles were formed, their further propagation was limited by the relative values of the film toughness, Γ_0, and the interface toughness, $\Gamma_i°$. For tough interfaces, *i.e.,* $\Gamma_i°/ \Gamma_0 \geq 0.56$, spalling was promoted rather than buckle propagation. In that case:

$$b_s = b_b. \tag{1.16}$$

For interfaces with low toughness, the buckles tended to propagate with σ_p, and the spalling was dictated by the mixity index λ. Interfaces with low toughness could cause very large spall radii. The corresponding spall size, b_s, was given by:

$$b_s/h = \chi \, (E_f/\sigma_p)^{1/2}, \tag{1.17}$$

where

$$\chi \approx 1.1 \exp[0.7(\Gamma_0/\Gamma_i^{\circ}) - 1.25]. \tag{1.18}$$

For 1 μm-thick Ni alloys ($E_1 = 400$ GPa, $E_2 = 200$ GPa), application of this model predicted a critical compressive stress of 2-6 GPa for buckle propagation and spalling [87]. The critical stress value increased with increasing interface toughness.

As mentioned before, for the initial separation of the film and the substrate, tensile or shear stresses must exist at the interface [87]. These stresses were formed on non-planar substrates and created crack-like voids at the film-substrate interface [87]. When the oxide films were subjected to high temperatures, the cracks at the oxide-substrate interface steadily grew [87]. Further stress build-up might have occurred while cooling down from high temperatures, if there was a significant difference between the thermal expansion coefficients of the film and the substrate ($\Delta\alpha$). In that case, for the film to spall, the critical stress value (σ_s) should be exceeded:

$$E_1(\Delta\alpha\Delta T + \varepsilon_\infty)/(1 - \nu) + \sigma_g \geq \sigma_s. \tag{1.19}$$

Here, σ_g was the growth stress operating at the high temperature, and ε_∞ was the applied strain.

For a more comprehensive review on film failure, please refer to [86, 89, 91-94].

1.3. ZnO as a Functional Thin Film Material

As mentioned earlier, ZnO is an important transparent conductive oxide material (TCO). Properties of common TCOs were compared in Table 1.1. The combined optical and electrical properties make ZnO competitive in transparent conductive oxide (TCO) and light emitting device applications. The piezoelectric properties render it a suitable candidate material for surface acoustic wave devices, piezoelectric transducers, actuators, transistors, varistors, *etc.* On the other hand, it can also act as a barrier against UV light and oxygen diffusion. It is a promising alternative for GaN or ZnSe-based blue or UV emitting devices, or for ITO-based TCO panels, and for TiO_2 based protective coatings. For these reasons, there is a great interest on ZnO thin film depositions with various methods on different substrates. Some of the prospective substrates for ZnO film growth and their lattice constants are summarized in Table 1.4 [13].

Table 1.4. Lattice parameters of a number of the prospective substrate materials for ZnO, compiled by Özgür *et al.* [13].

Material	**Crystal Structure**	**Lattice Parameters** a (Å) c (Å)	**Lattice Mismatch** (%)	**Thermal Expansion Coefficient** α_a (10^{-6} K^{-1}) α_c (10^{-6} K^{-1})
ZnO	Hexagonal	3.252 5.213		2.9 4.75
GaN	Hexagonal	3.189 5.185	1.8	5.17 4.55
AlN	Hexagonal	3.112 4.980	4.5	5.3 4.2
α-Al_2O_3	Hexagonal	4.757 12.983	(18.4% after 30° in-plane rotation)	7.3 8.1
6H-SiC	Hexagonal	3.080 15.117	3.5	4.2 4.68
Si	Cubic	5.430	40.1	3.59
$ScAlMgO_4$	Hexagonal	3.246 25.195	0.09	
GaAs	Cubic	5.652	42.4	6.0

Radio frequency magnetron sputtering is one of the most commonly used techniques for ZnO thin film growth [25, 95-112]. Some other methods include DC magnetron sputtering [113-115], solution synthesis [101, 116], laser ablation [117, 118], electron-cyclotron resonance sputtering [37], laser molecular beam epitaxy [119-121], pulsed laser deposition [101, 122], and various chemical vapor deposition methods [30, 123]. While thin films mostly grow in textured polycrystalline form, single crystal bulk growth of ZnO is also possible by special techniques [13, 32].

The important parameters for the ZnO thin film devices are discussed below. Apart from thin films and bulk material, there is recently increasing interest on various types of nano- and micro-structured ZnO and their optical properties, focused mainly on UV lasing [11, 100, 124-132].

1.3.1. Microstructure

Thin films of zinc oxide exhibited a very pronounced (002)-texture on various types of substrates, as demonstrated by XRD measurements. The *c*-axes of the hexagonal zincite crystallites were perpendicular to the substrate surface, leading to columnar structure. The shape of the columns depended on the deposition parameters.

In RF magnetron-sputtered ZnO thin films, kinetic energy of the particles reaching the surface, hence the RF power and pressure were important in determining the degree of crystallinity and texture [25, 95, 96, 98, 99, 101, 102, 111]. Optimum RF power [102, 112], optimum substrate temperature [95, 113], and optimum pressure conditions [96, 102, 112] were aimed to promote maximum grain size. For example, the (002)-peak intensity of the ZnO films increased with increasing RF power [95, 96, 102]. Increasing RF power could have increased the energy of the particles reaching the surface, via direct momentum transfer. Hence, the adatoms gained more mobility and fill the defects in the film. Therefore, structural homogeneity and crystallinity of the structure increased [96, 99]. On the other hand, too high an RF power led to an inhomogeneous structure with poor crystallinity. This happened when the adatoms accumulated so fast that they could not rearrange themselves before the next incident

atoms arrived the surface [102, 104]. Thus, an optimum RF power should be maintained.

Other important parameters to be optimized were total and oxygen partial pressure for maximum degree of texture [95, 111, 112, 115, 133]. Water *et al.* found the optimum oxygen content for strongest texture to be 40% for ZnO films deposited at 200 °C, 150 RF power, and 0.0004 mbar total pressure [95]. Bachari *et al.* found that even 1% of oxygen in the sputtering chamber resulted in increased density of the film and improvement in the column structure [96]. Therefore, the deposition parameters should be optimized to maximize the texture.

The effects of deposition parameters on the microstructure of thin films have been demonstrated in the form of *structure zone models*, as presented in Section 2.1.1. For ZnO thin films, a few modified structure zone models were described recently. One model was proposed by Ellmer [25], for Al-doped, magnetron-sputtered ZnO films. In this model, the variables were the oxygen partial pressure, p_{O_2}, and the deposition rate, R (Fig. 1.22). The model related the phase composition, mechanical stress, grain size, and visible transparency. The substitutional Al dopants occupying the Zn sites caused large strain-free crystallites. This phase had the lowest electrical resistivity. A *stress-valley* was observed extending from the lower left (low R, low p_{O_2}) to the upper right corner (high R, high p_{O_2}) of the zone model. The films with desired property, *i.e.* lowest resistivity and higher transparency, were produced within this valley. These variables form a *technological window* for transparent conductive ZnO applications.

Polley and Carter investigated the structure zones in ZnO films deposited by combustion chemical deposition [134]. The films were deposited on polished, fused quartz substrates. The substrate temperature range was 180-850 °C, corresponding to a homologous temperature range of 0.2-0.5 T_m. Crystal structure and texture was monitored by both XRD and electron diffraction by TEM. The matrix was composed of three general regions, depending on the homologous temperature and the precursor concentration (Fig. 1.22). Zone A consisted of amorphous film with cauliflower-like morphology. This zone of low adatom mobility was similar to Zone 1 in previously developed models. This zone was not expected at those temperature ranges in a conventional zone model. This discrepancy was attributed to the differences in film forming mechanisms in the deposition method used. The basic difference was the high

amount of impurities that could be eliminated in high vacuum conditions. Zone T had polycrystalline film with small grains. Zone 2 was composed of a columnar film. Zone 3 of large equiaxed grains was not observed in the temperature range of study. Higher temperatures were not applied since ZnO vaporized above 0.5 T_m. The SEM images of the films in the three zones are presented in Fig. 1.23., and the proposed structure-zone *matrix* is given in Fig. 1.24. Based on the measurements of the grain sizes in each zone, the authors calculated the activation energy of surface diffusion of ZnO as ~60 kJ/mol.

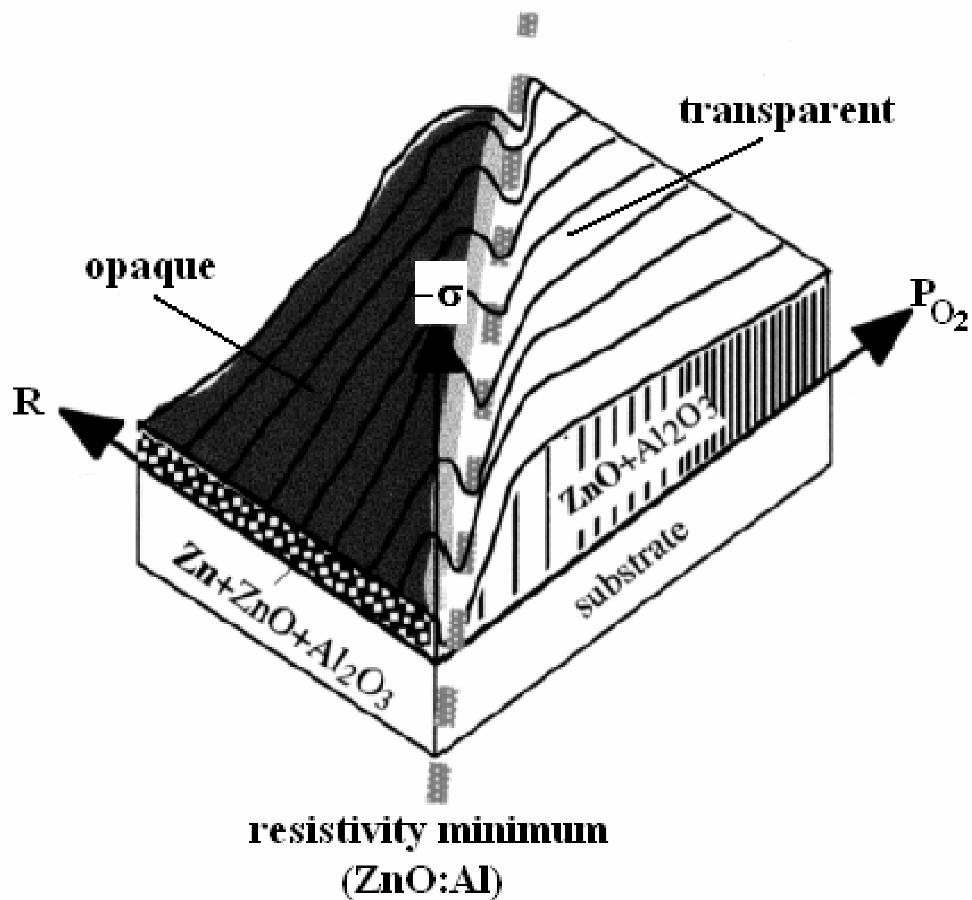

Figure 1.22. The structure-phase zone model with the residual stress effect. The independent parameters are the oxygen partial pressure (p_{O_2}) and the deposition rate (R). (Adapted from Ref. [25] with permission from IOP Publishing Ltd.)

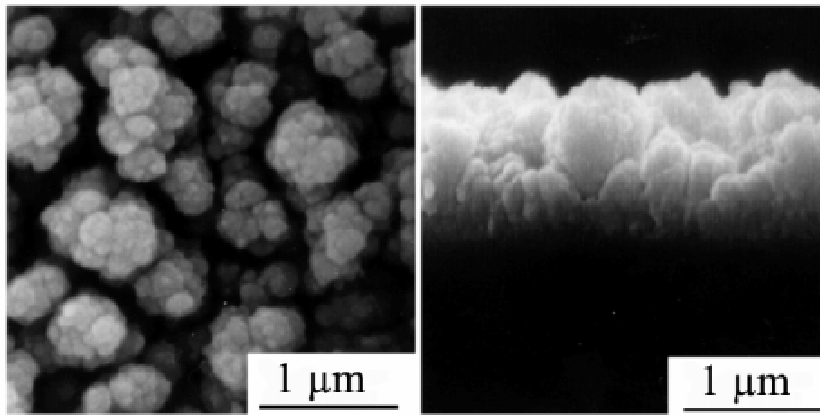

(a)

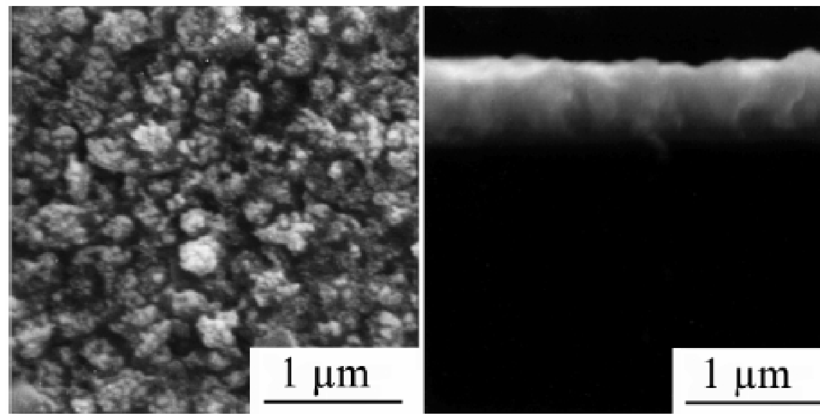

(b)

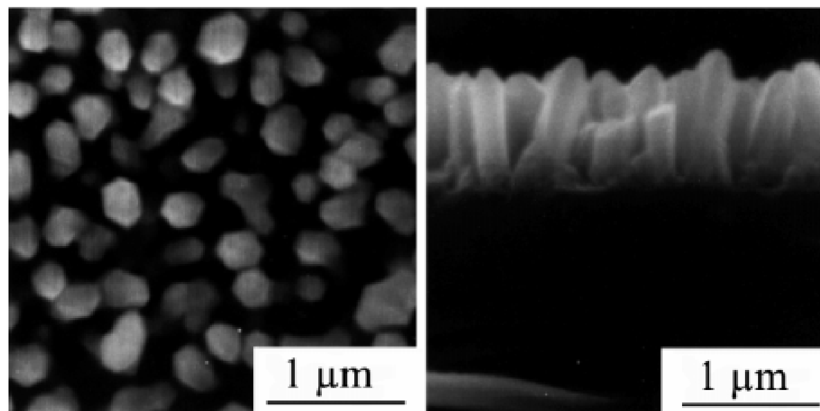

(c)

Figure 1.23. SEM micrographs for the zone matrix developed by Polley and Carter: (a) Zone A microstructure for 0.005 M solution concentration and 0.25 T_m deposition temperature in plane (left) and cross-sectional (right) views; (b) Zone T microstructure for 0.01 M solution concentration and 0.35 T_m deposition temperature in plane (left) and cross-sectional (right) views; (c) Zone 2 microstructure of 0.005 M solution concentration and 0.45 T_m deposition temperature in plane (left) and cross-sectional (right) view. (Reprinted from Ref. [135] with permission from Elsevier Publishing Ltd.)

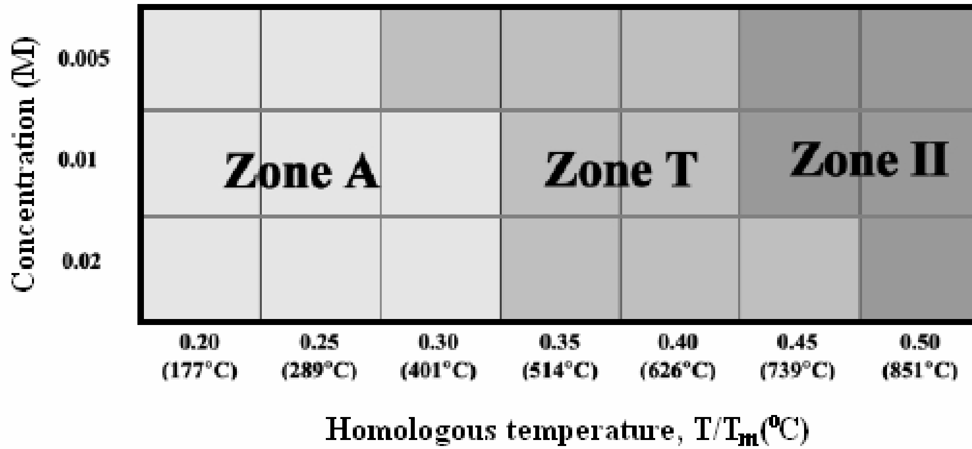

Figure 1.24. Structure-zone matrix for ZnO films deposited by combustion chemical deposition. (Adapted from Ref. [135] with permission from Elsevier Publishing Ltd.)

Another more recent model ZnO films was proposed by Mirica *et al.* [136, 137]. They pointed the difference in morphological development between metal and metal oxide films; hence the differences in the structure zone models. In their model, the formation of previously defined high-temperature structures was achieved at lower homologous temperatures because of the effect of high-energy particles. Increasing substrate temperature decreased shadowing effect and increased surface diffusion. Therefore, the transition zone was eliminated by substrate heating (Fig. 1.25). They described two sub-zones within Zone 2. Zone 2a was composed of a film with faceted columns and a rough surface. Films in Zone 2b were smoother, denser, and highly textured. However, the columns had pitted tops, owing to the limited surface diffusion.

As stated repeatedly, ZnO thin films usually had a very pronounced texture along the (002)-direction. However, there were some cases where other orientations have been reported. In a study by Cebulla *et al.*, the appearance of the (101)-reflection, among the (001)-reflection was mentioned [25, 138]. This orientation was observed in both the XRD 2θ scans (Bragg-Brentano configuration) and the texture distribution (pole figures). This peak was only observed in the pure ZnO films and not in the Al-doped films. The intensity of this peak increased with thickness (Fig. 1.26). Aluminum was proposed to be acting as a mineralizer or surfactant that improves the texture of the layers during growth. Minami *et al.* also observed (101)-reflections from Al-doped ZnO

films thicker than 1 μm at high sputtering pressures and/or high substrate temperatures [139]. Those films had a low visible transmittance with a milky appearance. Sayago *et al.* examined the ZnO films deposited on SiO_2/Si(100) substrates with RF powers of 50, 100, 150, and 200 W [133]. They found that the intensity of the (002)-peak increased with increasing oxygen content. Among the (002)-peak, weak reflections from the (100) and (110)-planes were observed in the XRD scans, for RF powers higher than 50 W. Lim and Lee examined ZnO thin films sputtered from a Zn target on Ru/Si(100) and Al/Si(100) substrates [140]. The films on Al/Si substrates had a mixture of small and large grains with large amount of voids. The films on the Ru/Si substrates were very dense and the grain shapes were hard to detect. For the films on Ru/Si substrates, only the (002)-reflection was observed. For those films, the grain size was 33.4 nm. In the films deposited on Al/Si substrate, the XRD intensity of the (002)-peak decreased to 1/5 of the previous case. At the same time, additional reflections from the (100), (101), and (102)-planes appeared. In that case, there was a slight decrease in grain size to 31.3 nm.

The significance of a pre-deposited thin ZnO buffer layer before the actual deposition was emphasized in a few studies. Buffer layers with different thicknesses (50-500 Å) were sputtered on (0001)-oriented sapphire substrates at 200 °C [141]. After annealing of these layers in the chamber at 350 °C for 10 min, further film deposition was carried at this temperature. The 100-Å thick buffer layer had the roughest surface with a root-mean-square (rms) roughness of ~25.1 Å, presumably due to three-dimensional island formation. As the thickness of the layer increased, the roughness dropped, presumably due to island coalescence. On the other hand, ZnO films deposited on a 100 Å-thick buffer layer had the smoothest surface and most intense (002)-peak among all the samples (Fig. 1.27 and 1.28). In another study, the effect of the pre-deposited buffer layer on the structural properties of the ZnO films deposited by metal-organic chemical vapor deposition (MOCVD) on SiO_2/Si substrates was examined [142]. In the XRD scans, (100), (002), and (101)-peaks were observed. A buffer layer was deposited at 470-490 °C deposited for 1-5 min. This layer provided a template for improved crystalline structure for further film growth at lower temperatures (300–330 °C). These films had a predominant (002)-texture with a very smooth surface (rms roughness = 7 nm.). The residual stress concept was not discussed in either of those studies on the effects of the buffer layer.

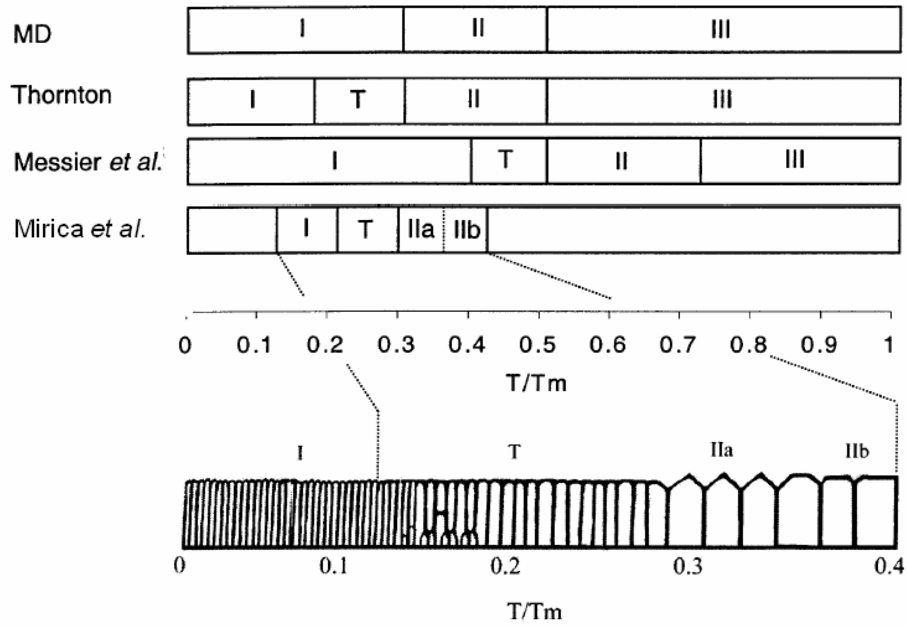

Figure 1.25. Comparison of various structure zone models Reprinted from Ref. [136]; published with permission from the authors.).

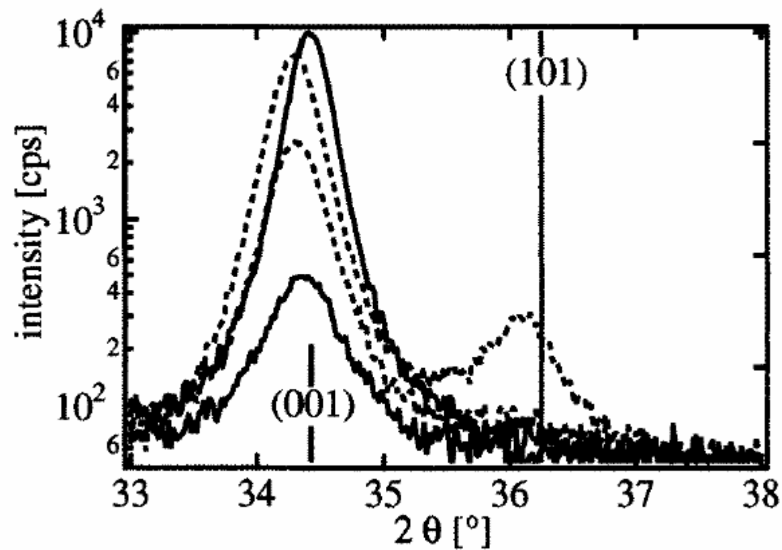

Figure 1.26. XRD spectra of RF-sputtered ZnO (---) and ZnO:Al (—) films of different thicknesses. From bottom to top the films were 170 and 370 nm (ZnO) and 40 and 360 nm (ZnO:Al) thick. The vertical bars display the diffraction pattern of zincite powder (JCPDS-No. 36-1451) [25, 138]. (Reprinted from Ref. [25] with permission from IOP Publishing Ltd.).

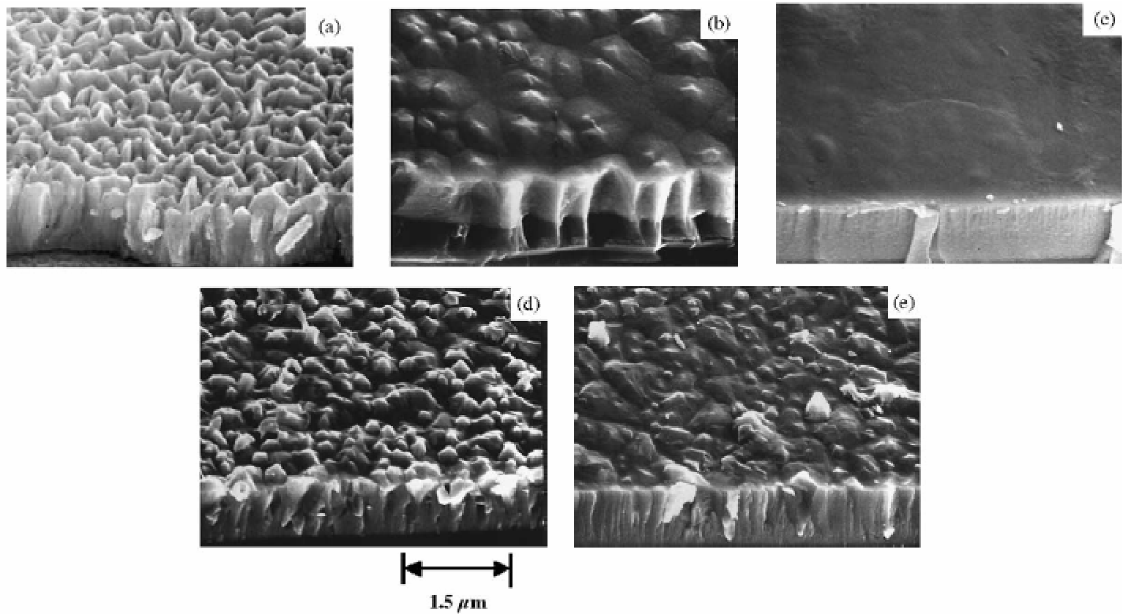

Figure 1.27. SEM images of the surfaces of ZnO films deposited on different buffer layer thicknesses: (a) no buffer layer; (b) 50-Å thick; (c) 100-Å thick; (d) 200-Å thick; (e) 500-Å thick. (Adapted from Ref. [141] with permission from Elsevier Publishing Ltd.).

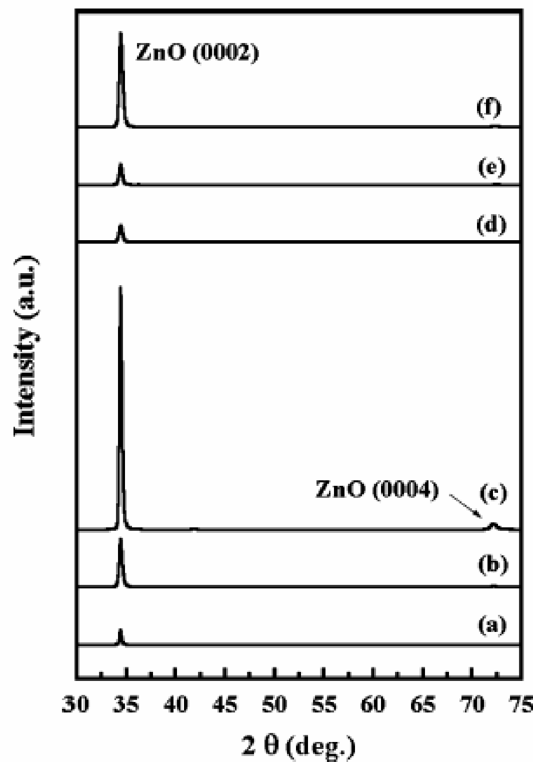

Figure 1.28. XRD spectra of ZnO films deposited on different buffer layer thicknesses: (a) no buffer layer; (b) 50-Å thick; (c) 100-Å thick; (d) 200-Å thick; (e) 300-Å thick; (f) 500-Å thick. (The indices (0002) and (0004) correspond to the indices (002) and (004) in our study, respectively.) (Reprinted from Ref. [141] with permission from Elsevier Publishing Ltd.).

1.3.2. Mechanical Properties and Residual Stresses

There are very limited number of studies on ZnO thin films that related the residual stresses to mechanical properties and the film integrity. These studies concentrated mostly on hardness and elasticity of the ZnO films, and these properties were compared to the bulk ZnO values.

The anisotropy in hardness of ZnO thin films on *a*-axis and *c*-axis oriented sapphire was reported by Coleman *et al.*, and the values were compared to the values for bulk ZnO [143] (Table 1.5). The films were harder than their bulk ZnO counterpart. In addition, *pop-in events* during nanoindentation were observed in the bulk ZnO only, and not in the films. In single crystal bulk materials, the pop-in events were attributed to the slip along the basal or pyramidal planes. The relative hardness of the ZnO epilayers and the absence of pop-in events were proposed to be due to the pre-existing defects. These defects were thought to be inhibiting the slip of the planes by strain compensation. (In nanoindentation, a discontinuity in the load vs. depth curve was commonly referred to as a *pop-in event* [144, 145]. It was an indication of a sudden yielding of a material under load. It was associated with the onset of plasticity, and it is common in crystalline materials. A similar discontinuity during unloading was called a *pop-out event*.) The high hardness of the sapphire substrate was also proposed to be an inhibitor for this slip. Presumably, the high lattice mismatch provided a high dislocation density.

Navamathavan *et al.* [146] reported the mechanical deformation behavior of epitaxial ZnO thin films grown on (0001) oriented sapphire substrates. The films were grown by magnetron sputtering with thicknesses of 400 and 800 nm. By nano-indentation studies, the average elastic modulus and hardness were evaluated as 154±5 and 8.7±0.2 GPa, respectively. These values were slightly higher than the bulk ZnO values, and this was proposed to be due to the residual compressive stresses within the film. In contrast to the observations reported by Coleman *et al.* [143], the authors observed *pop-in events* in the indentation depth vs. load curves. These discontinuities pointed to plastic deformation of the films. This plastic deformation was attributed to sudden propagation of dislocations, which had been pinned down by pre-existing defects.

Table 1.5. Hardness and elastic modulus for bulk and epitaxial ZnO measured by nano-indentation [143].

Orientation	Sample type	Hardness (GPa)	Elastic Modulus (GPa)
a	epitaxial	6.6 ± 1.2	318 ± 50
c	epitaxial	5.75 ± 0.8	310 ± 40
a	bulk	2 ± 0.2	163 ± 6
c	bulk	4.8 ± 0.2	143 ± 6

In a study by Rossington *et al.*, the adherence of ZnO films on Si substrates were studied [147]. The films were deposited by reactive magnetron sputtering from a Zn target with a thickness of 5–10 μm. The thermally grown oxide layer on the Si substrate was 0.1 μm-thick. The 5 μm-thick films deposited under 100% O_2 at 350 °C had 730±70 MPa of residual compressive stress, as measured by substrate bending. The stress was 580±90 MPa for the 10 μm-thick film. Decreasing the oxygen content to 60% eliminated the stress completely. The substrate bending was measured by the optical interference fringes on the film. The elliptic shape of the fringes revealed that the biaxial strain in the film was not isotropic. In this study, the influence of buckling on the cracking of the compressed films was examined. In stress-free samples, the cracks propagated along the interface, with a very smooth fracture surface. In the stressed films, the nature of the cracks depended on the load and film thickness. The thinner film (5 μm) cracked *along the interface* under low loads (1–3 N). For higher loads, the cracks propagated *within the film, adjacent to the interface*. The latter behavior was observed in the thicker films for the whole range of loading. The transition in the fracture path in the thinner film was attributed to the onset of buckling and consequent deflection of the crack towards the surface. Once the cracks were created within the film, they were confined in a plane parallel to the substrate. The critical loads for buckling of stress-free samples were outside the loading range and they were consistent with the quantitative predictions. However, the predictions were inconsistent with the data for stressed films. This was attributed to the bending of the sample under the influence of residual stress, and consequent decrease in the buckling load. These results were summarized in Fig. 1.29. In the same study, the fracture toughness (G_c) was calculated as 16 ± 7 J/m^2 and 13 ± 4 J/m^2 for the 10 μm-thick and 5 μm-thick films, respectively.

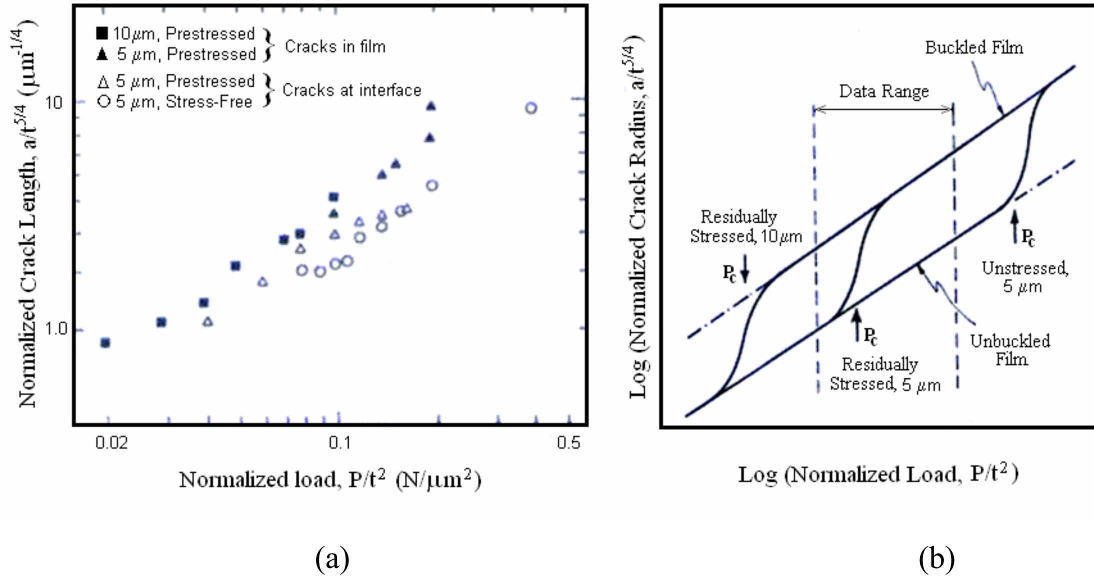

(a) (b)

Figure 1.29. (a) Normalized crack length as a function of normalized load. (b) Critical buckling loads (P_c) in relation with buckling (Reprinted from Ref. [147]; published with permission from AIP.).

In a study by Huang *et al.*, ZnO films with a thickness of 202–1535 nm were deposited on Si(100) substrates by magnetron sputtering [148]. The applied load was in the 10 mN–2.0 N range. The films thinner than 554 nm experienced only indentation-induced radial *cracking*. Those films contained about 387 MPa residual compressive stress. When the film thickness exceeded 832 nm, for low indentation loads, only indentation-induced *delamination* was observed. For the same samples under higher loads, *radial cracking* accompanied delamination. Two types of interfacial fracture energies were calculated depending on whether the delaminated film was *buckled* or not. That value was 12.2 J/m^2 for buckled films and 9.2–11.7 J/m^2 for unbuckled films.

Residual compressive stresses have been observed in ZnO thin films in many studies [25, 95, 96, 99, 102, 111, 112]. These stresses were manifested in a shift of the x-ray diffraction (XRD) peaks to lower diffraction angle (2θ) when compared to powder data. This behavior will be explained in more detail in Chapter 3. As mentioned in Section 1.2.3, there were several factors for residual stress formation in thin films. For example, thermal stresses in films were caused by the thermal expansion mismatch between the film and the substrate material. If the thermal expansion coefficient of the substrate material was lower than that of ZnO, as in the case of Si substrate, the films

were under tensile thermal stress in the axial direction [95], resulting in higher Bragg reflection angles (2θ) than that of the powder. The reverse holds for substrates with a higher thermal expansion coefficient than that of ZnO, such as glass or polymers.

Several studies reported on the intrinsic component of the residual stresses in the films. These stresses were proposed to be arising from the oxygen deficiencies and several imperfections in the crystal lattice of the films formed during film growth. Some of the studies associate the residual stresses to entrapped argon or oxygen, but only very few authors actually measured the entrapped gas amount in the films. For example, Bachari *et al.* found about 0.5 at.% argon in the RF magnetron-sputtered ZnO films by Rutherford back-scattering (RBS) measurements. Maniv *et al.* discussed the pressure and angle-of-incidence effects on the residual compressive stresses in ZnO films [149]. The films were deposited on Corning 7059 glass substrates by reactive magnetron sputtering from a Zn target on thermally oxidized Si wafers. The residual stress varied from -8 GPa to zero, and decreased by one order of magnitude as the pressure was increased from 0.4 to 4.7 Pa. This was proposed to be due to the decreased mean free path of the adatoms and the consequent weakening of the *atomic peening effect.* At low pressures, the films had a dense structure. Increasing the pressure promoted column formation. The *c*-axis orientation of the grains decreased by increased rotation of the substrate. When the film thickness exceeded 3 μm, the glass substrate bent. The films thicker than 6 μm cracked and detached from the substrate.

Other than the aforementioned factors (oxygen deficiency, argon entrapment, and thermal expansion mismatch between the substrate and the film), lattice mismatch is also a factor in stress formation. For example, differences between stresses in ZnO films sputtered on Si and GaAs could not be explained solely by thermal expansion mismatch [98] between the film and the substrate. Since GaAs and Si both have lower thermal expansion coefficients than ZnO, the thermal mismatch effect would cause the ZnO film to shrink more than the substrate when cooling down after deposition on both substrates. Thus, a residual tensile stress in the film would be expected, and that stress would increase with the increasing substrate temperature. However, the observations were contradictory; the residual stresses were compressive and increased with increasing substrate temperature. This contradiction was associated with the affects of the lattice structure on the residual stresses.

Increasing the substrate temperature (from room temperature to 300 °C) was observed to decrease the residual compressive stresses [95, 98]. This result was attributed to the increased mobility of the atoms, ions, and molecules reaching the surface. The residual stresses could be eliminated or turned from compressive into tensile by a separate post-deposition annealing in air at a suitable temperature for a suitable time period [95, 96, 150-154]. In all cases, the annealing led to a decrease in the residual compressive stresses. In some studies, an optimum annealing temperature for annealing ZnO in air was found to eliminate these stresses. This optimum annealing temperature ranged from 480 °C [154] to 600 °C [95]. Annealing at that optimized temperature often led to the strongest texture, the largest grain size, and the maximum XRD peak intensity. One study showed that performing the annealing in a single step or in the form of consecutive annealing cycles did not change the resulting stresses [155].

Lim and Lee examined ZnO thin films sputtered from a Zn target on Ru/Si(100) and Al/Si(100) substrates [140]. The films on two different substrates had very different residual stresses, with accompanying differences in the microstructure and texture. The films on the Ru/Si substrates were very dense and the grain shapes were hard to detect. For the films on Ru/Si substrates, only the (002) reflection was observed. For those films, the grain size was 33.4 nm and the residual compressive stress was -0.137 GPa. The films on Al/Si substrates had a mixture of small and large grains with large amount of voids. XRD intensity of the (002)-peak on these substrates was $1/5^{th}$ of the previous case. At the same time, additional reflections from the (100), (101), and (102) planes appeared. In that case, there was a slight decrease in grain size to 31.3 nm, and a huge increase in the residual stress to -0.986 GPa.

Cimpoiasu *et al.* discussed the ways of decreasing the residual compressive stresses by adjusting the deposition parameters [156]. ZnO thin films were reactively deposited by DC sputtering on Si(100), $Al_{(111)}$/Si, and $Al_{(111)}/SiO_2$/Si, substrates. The distribution of the *c*-axis orientation in the films depended on the additional layer on the Si substrate as in Table 1.6. The residual compressive stress was much larger in the films grown directly on the Si substrate. This was attributed to the lesser number of defects present in the films on Al substrates than those on Si substrates (Fig. 1.30). In addition, the stress on highly (111)-textured Al substrates was less than that on poorly (111)-textured Al. The minimum stress (about -50 MPa) was obtained at 6 mTorr, 100% O_2, and 375 °C. The stress was higher both below and above 6 mTorr, regardless of the

other parameters. A lower pressure led to an increase in adatom energy, damaging the film and the substrate, whereas a higher pressure caused a decrease in the adatom energy and mobility, owing to high number of collisions on their way to the substrate. Both of these effects promote increased residual stresses. The stress increased to -300 MPa by decreasing the temperature to 225 °C. At about 3.0 A of sputter current, the stress changed from compressive to tensile. Since Si has a lower thermal expansion coefficient than that of ZnO, tensile lateral stresses formed at the film-substrate interface upon cooling down to room temperature after deposition. At the point of sign change of the stress, the compressive intrinsic stress was thought to be of the same order of magnitude as the tensile thermal stress, resulting in a zero residual stress. In all cases, the stresses were eliminated by thermal annealing at 280–400 °C. Thermal treatment was believed to eliminate boundary defects and improve *c*-axis orientation.

Table 1.6. Distribution of *c*-axis orientation of zinc oxide films grown on different substrates [156].

Substrate material	*c*-axis distribution
Si	±15°
$Al_{(111)}/SiO_2/Si$	±6°
$Al_{(111)}/Si$	±3°
$Al_{(low(111)orientation)}/Si$	±8°

As mentioned earlier, Ellmer proposed a structure-phase zone model for Al-doped ZnO thin films [25]. The residual compressive stress was one of the variables in this model. The residual compressive stress values that were used in this model were reported in a previous study, and they varied from 0.8 to 2.8 GPa [138]. The residual stress decreased upon Al-doping. The thickest (350 nm) Al-doped films were nearly stress-free. They also observed that the stress in RF-sputtered films were lower than those in DC-sputtered films. For both ZnO and ZnO:Al films, the stress increased with increasing ratio of DC power (P_{DC}) over RF power (P_{RF}), while the grain size remained relatively constant (Fig. 1.31). This result was explained by the more intense ion bombardment of the films by the RF discharge than the DC discharge. As will be discussed in Sec. 1.3.3, RF discharges could provide a more energetic plasma with higher ion density.

Ellmer also calculated the thermal strain arising from the differences in thermal expansion coefficients of ZnO and the glass substrate to be less than $5x10^{-4}$ [25]. Thus, the thermal contribution to the residual compressive stress was insignificant. At the same time, both the Rutherford back-scattering (RBS) analysis and the transport of ions in matter (TRIM) simulations revealed that the films were free of implanted argon for the range of deposition parameters used (50 eV Ar ions). Thus, it was concluded that the major part of the stress was created by other factors during growth.

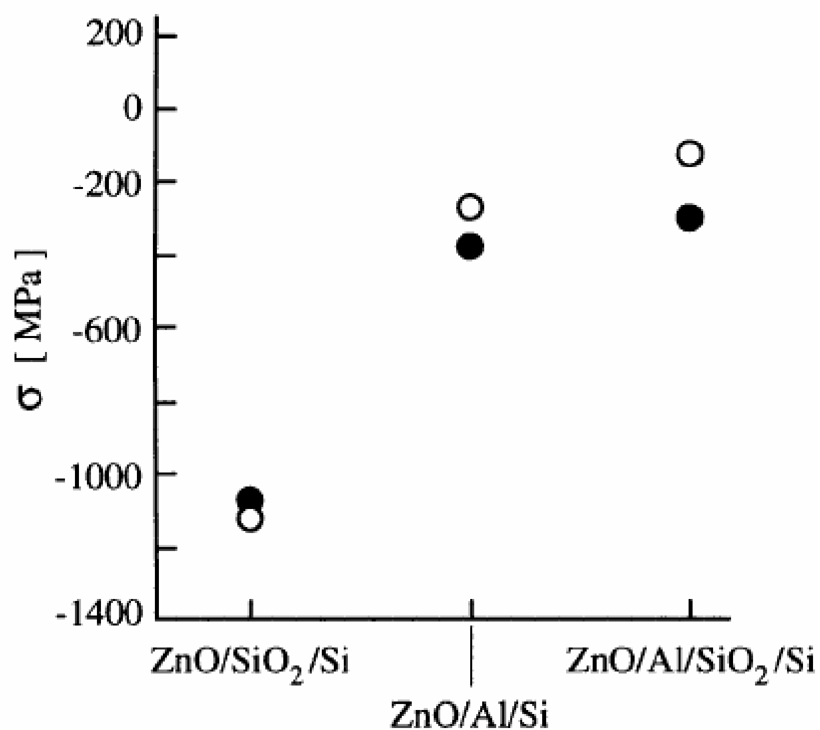

Figure 1.30. The total stress in a zinc oxide film calculated from the deflection measurements (open symbols) and the x-ray diffraction measurements (full symbols). (Reprinted from Ref. [156] with permission from IOP Publishing Ltd.).

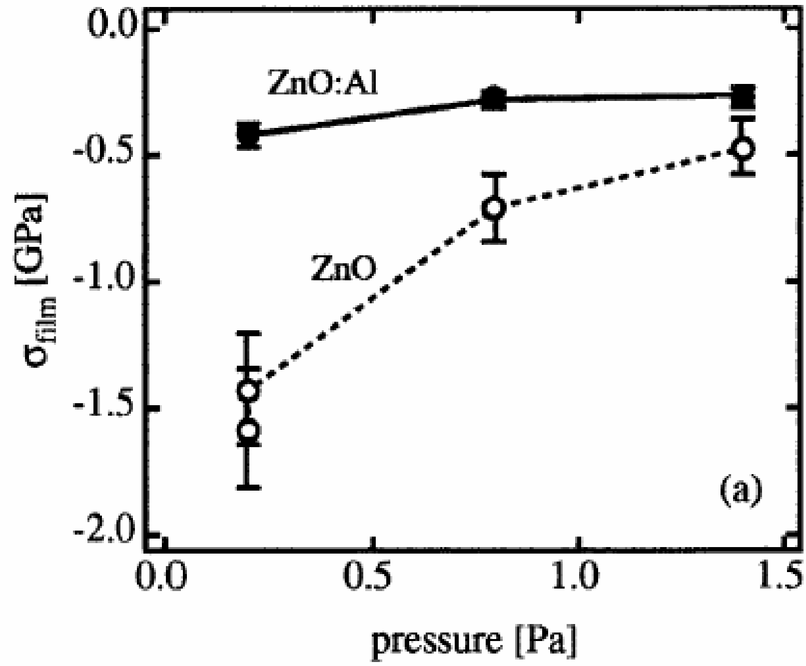

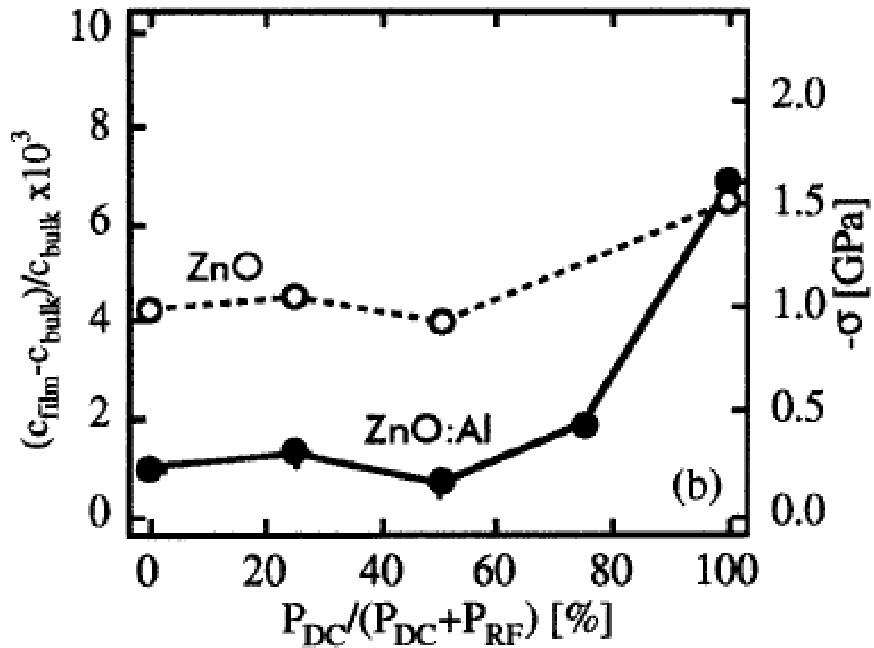

Figure 1.31. (a) Dependence of the film stress on the sputtering pressure for ZnO and ZnO:Al films with sputtering parameters: P_{RF} = 30 W, h_{ZnO} = 120 nm, $h_{ZnO:Al}$ = 350 nm [138]. (b) Strain (left) and stress (right) of ZnO and ZnO:Al films depending on the $P_{DC}/(P_{DC} + P_{RF})$ ratio with sputtering parameters $P_{DC} + P_{RF}$ = 80 W and p_{Ar} = 0.8 Pa [25, 138]. (Reprinted from Ref. [25] with permission from IOP Publishing Ltd.).

1.3.3. Optical and Electrical Properties

Like the other properties, the optical properties of ZnO films depend on the deposition parameters and the consequent microstructure: RF or DC magnetron-sputtered ZnO thin films exhibit a transparency greater than 80% in the visible region [101, 106, 109, 111, 113]. For sputtered films, the transmittance is found to increase with the increasing oxygen partial pressure and the total pressure. This result was associated with an improvement of the structural homogeneity and the stoichiometry of the films [115] and an accompanying decrease in the light scattering loss [96]. In accordance to that, the extinction coefficient decreases with increasing total and oxygen partial pressures, within the range of 400 to 800 nm irradiation [96]. On the other hand, with increasing RF power could provide denser films that more strongly reflect the incident radiation, causing a slight decrease in optical transmittance [96]. Increasing the substrate temperature during deposition causes more scattering of incident light with consequent decrease of the transmittance [113].

The band-gap of ZnO films changes according to the crystal structure. By photoluminescence measurements on pulsed laser deposited films, the difference in band gap of the wurtzite and zinc blende type ZnO was estimated to be 0.10 eV, which was in good agreement with the theoretically calculated value [19]. Some band gap measurement results for RF magnetron-sputtered films on various substrates are as follows: 3.22 eV for silicon [106], 3.27 eV [109] and 3.3 eV [111] for glass, and 2.95–3.2 eV for polymer substrate [99]. DC magnetron sputtering yielded a band gap of 3.38 eV on glass substrate [113]. The stoichiometry of the films, in other words the oxygen content, also influences the band-gap [107]. High pressure and low RF power [99] as well as high substrate temperature [113] promote wider band gap.

In all cases, independent of the pressure, more homogeneous and denser films had higher refractive indices. The refractive indices of thin films were calculated based on transmittance measurements in the UV–VIS range. They were seen to depend on the microstructure, which is influenced by the coating parameters. For example, increasing RF power also increases the refractive index, due to a denser film [96, 102, 105]. Pressure must also be controlled during deposition. Increasing total pressure may decrease [96, 102] or increase [115] the refractive index, depending on the contribution of oxygen partial pressure. For DC sputtered films on glass, substrate temperature did

not have a significant effect on the refractive index, where the index ranged from 2.03 to 1.87 in the wavelength range of 400 to 1000 nm [113]. On the same type of substrate, an index of 1.95 is reported at 632.8 nm for RF magnetron-sputtered ZnO film [111]. (It should be noted that, optical indices calculated from the ellipsometry results may vary according to the method used for fitting the data; hence the assumptions about the microstructure must be done very carefully for accurate results [109].)

Most of the studies on ZnO thin films focused on the effects of deposition parameters on the optical properties of the films. On the other hand, electrical properties are also strongly influenced by the deposition conditions. Literature results on the electrical resistivity, charge carrier density and mobility in ZnO thin films can be found in an excellent review by Ellmer [25]. It is possible to tune the transparent oxide's electrical resistivity by varying the dopant concentration. The most studied dopant for ZnO is Al. Some other dopants for ZnO films are also studied in literature (B, Ga, In, Si).

Both the carrier concentration and mobility exhibit a strong dependence on the degree of crystallinity and on the grain size, which are influenced by the coating conditions such as the RF power, substrate temperature and chamber pressure, as stated previously. The minimum resistivity (ρ) obtained for magnetron-sputtered polycrystalline Al-doped ZnO thin films was 1.9×10^{-4} Ω-cm [25, 157, 158]. For single crystal substrates, even a lower resistivity of 1.4×10^{-4} Ω-cm was achieved by depositing epitaxial ZnO on sapphire [25, 159]. The films had a charge carrier concentration (N) of 1.5×10^{21} cm^{-3} and Hall mobility (μ) of 34 cm^2/V-s. This resistivity was comparable to that of ITO. For those films, as the deposition rate increased, the residual compressive stresses also increased. These stresses damaged the crystallinity of the film. Consequently, the mobility of charge carriers decreased, and the resistivity passed through a minimum. The mobility was lower than the theoretical limit value for TCOs, calculated by Bellingham *et al.*, by *ionized impurity scattering* model (90 cm^2V/s) [25, 160].

A charge carrier concentration of 1.5×10^{21} cm^{-3} means that 60% of the doped Al is electrically active [25]. Ellmer studied the dependence of electrical resistivity on the oxygen partial pressure in ZnO thin films, sputtered from a metallic target by DC discharge [25, 161]. With increasing p_{O_2}, N decreased drastically upon formation of Al_2O_3 and hence loss of electrically active Al. Increasing p_{O_2} from 0.04 to 0.1 Pa caused

two orders of magnitude decrease in N. When the oxygen partial pressure was lower than 0.06 Pa, the films lost transparency due to increased oxygen deficiency. Incomplete oxidation of zinc causes metallic zinc to build up in the films, causing opacity. For p_{O_2} greater than 0.06 Pa, the number of charge carriers continued decreasing. At a total pressure of 0.5 Pa and an oxygen partial pressure of 0.06, the films had maximum Hall mobility. After that point, mobility also started decreasing, due to increased grain boundary barrier on electron transport.

Most TCOs are polycrystalline and the maximum efficiency cannot be reached due to scattering from the grain boundaries and defects [162]. The number of charge carriers cannot be increased infinitely due to absorption of free charge carriers in the infrared [25]. This also decreases transmittance in that region. Increasing the mobility of the ions could be advantageous. Improving the crystallinity of the material by grain growth, or decreasing the mechanical stresses in the material, could be effective in increasing the mobility. As the degree of crystallinity improves, resistivity would decrease.

1.4. Thin Film Deposition

As mentioned before, RF magnetron sputtering is one of the most commonly used techniques for ZnO thin film growth [25, 95-112]. Some other methods such as molecular beam epitaxy [119-121], pulsed laser deposition [101, 122], and chemical vapor deposition [30, 123] have also been applied to deposit ZnO thin films. Comparison of various methods for ZnO deposition can be found in the review by Özgür *et al.* [13]. In sputtering, a sintered ZnO ceramic target with high purity is used as the source. Argon is used as the ionizing gas and oxygen is used to improve the stoichiometry. The growth is usually performed in a O_2:Ar gas mixture with the oxygen ratio ranging from 0% to 100%. In reactive sputtering, metallic Zn target is used as the Zn source. The sputtered Zn particles react with oxygen, and condense as ZnO on the substrate surface.

Another method for ZnO deposition is molecular-beam epitaxy (MBE) [13]. To deposit ZnO by MBE, Zn metal and oxygen gas are used. The Zn metal is evaporated

from an effusion cell. The cell temperature determines the Zn flux, and it is an important parameter on the film growth rate. An oxygen radical beam is produced by a plasma source. This beam is directed on the film surface to provide oxidation of Zn into ZnO. To maintain epitaxy, usually (0001)-oriented sapphire substrates are used.

Pulsed laser deposition (PLD) takes advantage of the high-power laser pulses to evaporate material from a target surface. The evaporated jet of particles arrives at the substrate surface, with a strong forward-directed velocity distribution. Stoichiometry is preserved during film growth. Typical substrate temperature and gas pressure are 200–800 °C and 10^{-5}–10^{-1} Torr, respectively. In ZnO deposition, cylindrical ZnO targets of packed ZnO powder are used as targets. The film properties depend on the substrate temperature, oxygen pressure, and laser intensity.

In chemical vapor deposition (CVD), a solid material is deposited from vapor phase precursors onto a substrate [13]. A reaction chamber with a temperature profile is designed such that a carrier gas carries the gaseous species onto the vicinity of the substrate. The solid-state reactions take place on the substrate, which is heated to the desired temperature. When metal-organic precursors are used, this technique is called metal-organic chemical vapor deposition (MOCVD), metal-organic vapor-phase epitaxy (MOVPE), or organometallic vapor-phase epitaxy (OMVPE). For ZnO deposition, typical organometallic precursors are $(CH_3)_2Zn$ (dimethyl zinc) and $(C_2H_5)_2Zn$. However, these materials are very reactive towards oxygen, which makes the control of the reaction harder, leading to films with poor quality. Studies on less-reactive precursors are continuing [13]. As a carrier gas, typically argon or nitrogen is used, together with oxygen. This method is suitable for large-scale film production.

To understand the stress evolution in thin films and its relation to the microstructure, it would de useful to understand the physical fundamentals of the deposition technique. For this purpose, RF magnetron sputtering, which is the deposition method used in this study, is presented in detail in the next section.

1.4.1. Radio Frequency Magnetron Sputtering

Sputtering is a glow discharge process and a physical deposition technique that is used to grow thin films on substrates for a wide variety of commercial and scientific purposes [1, 163]. It is based on the interaction of the target surface with the high-energy bombarding particles. The typical deposition rates are about one monolayer per second, or 50–500 Å/min [1]. For an atom of about 3 Å diameter, this corresponds to about 200 Å/min, if one monolayer is assumed to contain about 10^{15} atoms/cm^2.

When an energetic ion hits a solid surface, the following phenomena may take place [1]:

i) The ion may be reflected (*ion scattering*).

ii) The target could emit a *secondary electron*.

iii) The ion may be trapped inside the solid (*ion implantation)*.

iv) The solid structure may be modified and lattice defects may be created owing to the energetic interactions with the incoming ion (*radiation damage*).

v) Atoms of the solid material could be ejected because of the momentum transfer from the incident ion (*sputtering*) (Fig. 1.32).

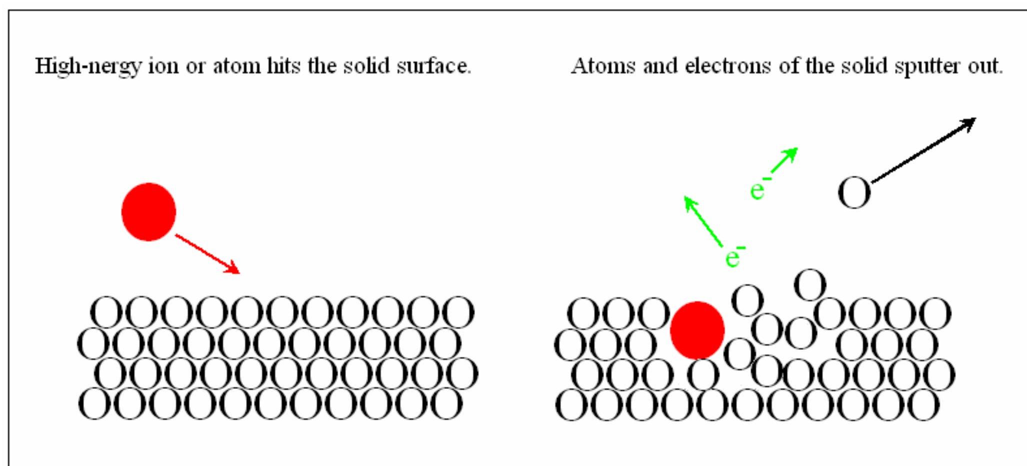

Figure 1.32. The impact of an atom or ion on a surface produces sputtering from the surface as a result of momentum transfer from the incoming particle. No melting of the material occurs, unlike many other deposition techniques.

A partially ionized gas consisting of equal number of positive and negative charges is called a *plasma* [1]. The portion of ionized material in the plasma that is used in glow discharge processes are is on the order of 10^{-4} and thus the sputtering gas is mostly neutral. The temperature of ions in the sputtering medium is around 500 K. The electrons on the other hand, have energy around 2 eV, which correspond to a temperature of 23200 K. However, this high a temperature does not affect the system due to the very low heat capacity of electrons.

During sputtering, the substrate and the target (material to be deposited onto the substrate) are placed inside a chamber of low-pressure inert gas (usually argon). If necessary, reactive gases (usually oxygen or nitrogen) could be mixed with argon. A high voltage is applied between the anode (substrate side) and the cathode (target side) to ionize and energize the gaseous molecules and create a plasma, which consists of electrons and gas ions in a high-energy state (Fig. 1.33). The ones whose energy is high enough to reach the substrate and low enough to be adsorbed on the substrate condense into a film. For deposition of dielectric films, an additional radio frequency source is used to prevent a charge build-up on the non-conducting target surface. This method was first introduced in the 1960s [164-166].

During the course of glow discharge, the plasma is under the influence of the *plasma potential*, also known as the *space potential* (V_p) [1]. The substrate, on the other hand, has a *floating potential* (V_f). The electrons in the vicinity of the substrate are repelled by a voltage barrier of $V_p – V_f$. Therefore, the substrate has a net positive charge around it, known as the *space charge* or *sheath*. The electron density decreases along this sheath. The atoms that have been excited by the electron impact goes under *relaxation* and because of this, the discharge *glows* (Fig. 1.34). The glow density depends on the density of excited atoms, hence the density of electrons. Thus, the glow is much dimmer within the sheath and the sheath creates a *dark space* on every surface that is in contact with the plasma.

The problem of charge-build up during deposition of dielectric materials can be better understood considering the following discussion. When the dielectric target material is placed in a DC discharge, its surface will be charged, forming a *sheath*, until it reaches the *floating potential* [1]. That point onwards the ion flux and the electron flux on the material surface are equal. These electrons and ions recombine at the surface, leaving it with zero net current. The magnitude of a DC plasma density is

around 10^{10}/cm^3, and the *sheath voltage*s of insulating materials are around 10–20 volts. In these circumstances, the rate of electron-ion recombination could be lower than what is required to maintain the zero current on the surface. This causes a charge build-up on the target material, which is a problem in DC-sputtering of dielectric materials. This situation could be demonstrated more clearly, if both the insulating target and the glow discharge are represented by equivalent *capacitors*. Considering the below equations,

$$C = Q/V \tag{1.20}$$

$$Q = \int I \, dt, \tag{1.21}$$

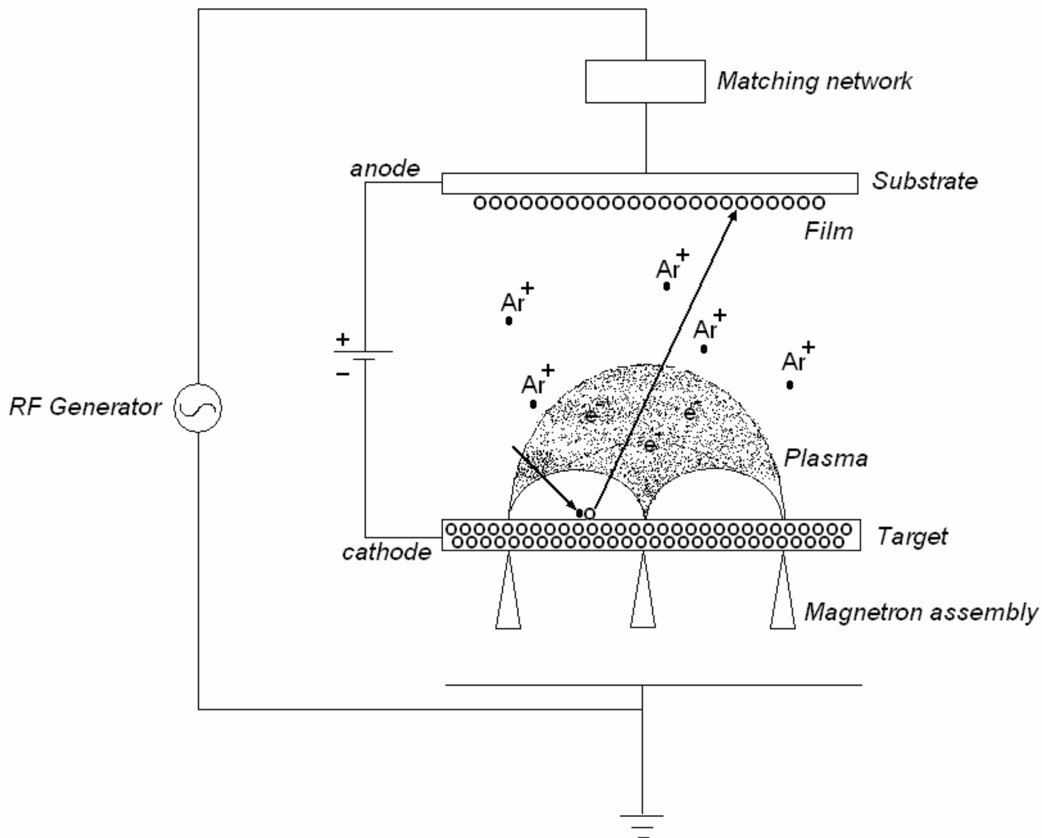

Figure 1.33. Schematics for the RF magnetron sputtering method. The substrate is placed in a low-pressure chamber between two electrodes. The electrons are driven by an RF power source, which generates a plasma and ionizes the gas (*e.g.*, Ar) between the electrodes. A DC potential drives the ions towards the target, knocks atoms off the target, and condenses them on the substrate surface. A strong magnetic field is applied to contain the plasma surface of the target to increase the deposition rate.

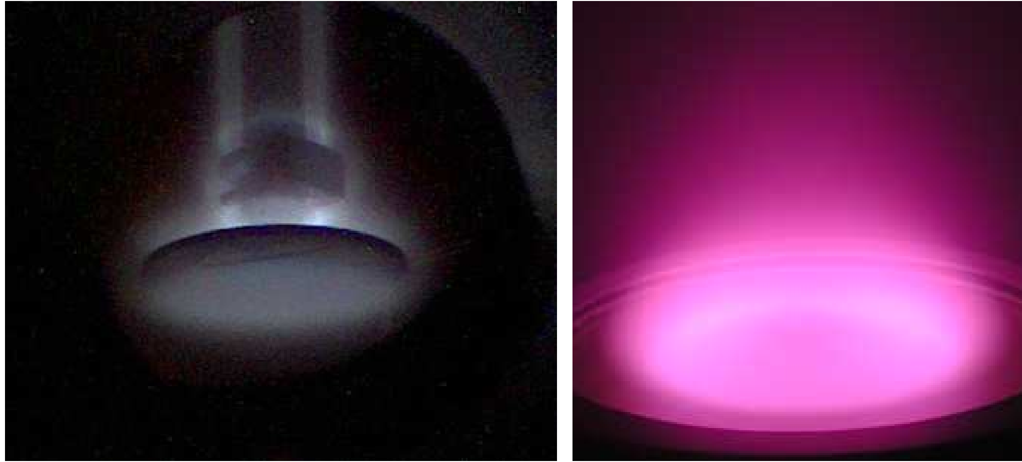

Figure 1.34. Plasma glow (a) around the substrate holder and the holder arm (present study), (b) around the target [167].

(where C is the capacitance, Q is the stored charge, V is the applied voltage, I is the current and t is time), it is obvious that the voltage across a capacitance cannot be changed instantaneously. Once the circuit is closed, the voltage at surface of the insulator will be at $-V_s$, the supply voltage, instantaneously. When the glow discharge is initiated, the insulating surface starts loosing electrons due to the combination with the positively charged gas ions bombarding its surface. Then, the negatively biased target surface will start to charge positively. Consequently, the voltage on the surface will start rising exponentially, from $-V_s$ towards 0. When it passes the discharge-sustaining limit, the plasma will be lost. To overcome this problem, one solution has been proposed to use an alternating current (AC) discharge, by bombarding the target surface with positive ions and electrons in an alternating fashion. The AC-frequency that has been conventionally used is 50 Hz. If the charging time of the insulating surface is much less than half the period of the AC source, then the plasma would be off for a significant amount of time. Thus, the AC discharge has not been a very useful solution to the charge build up problem on the insulating surface [1].

As an alternative, radio-frequency (RF) sources are being used. Average RF and DC ion currents are similar to each other (~1 mA/cm^2). For a quartz substrate with a typical capacitance of 1 pF/cm^2 and for an applied voltage of 1000 V and a current density of 1 mA/cm^2, t would be equal to ~1 μs. Thus, a continuous discharge can be maintained at frequencies above 1 MHz. In RF sputtering, the target is alternatively

bombarded with ions and electrons, by the voltage supply alternating at the set frequency in the RF range [1]. The conventional RF-discharge equipments operate at a frequency of 13.56 MHz. An RF discharge is more efficient in using the electron impact ionization than a DC discharge. For this reason, the minimum operating pressure could be decreased to 1 mTorr (0.0013 mbar). Therefore, the scattering of the sputtered target atoms by the gas medium is decreased. Another problem for glow discharges is the *arc formation* caused by the dirt particles on the target surface. In RF systems, it is more difficult for the arc to be sustained owing to the fast alternating field.

The sputtering gas should be inert to maintain chemical purity of the coating and heavy enough to provide the momentum necessary to eject the target atoms [1]. Among the noble gases, argon ($Z = 18$) is the generally preferred one. It is cheap and available, not radioactive like radon ($Z = 86$), and has a high sputtering yield comparable to that of xenon ($Z = 54$). The minimum operating pressure is limited by the DC glow discharge requirements (generally about 30 mTorr): there should be enough gas ions inside the chamber to provide a significant sputtering rate [1]. On the other hand, at high pressures, the probability of collision between the sputtered target atoms and the gas ions increase, decreasing the energy and distorting the line-of-sight of the particles incident on the substrate surface, and thereby decreasing the deposition rate. Thus, the maximum operating pressure is also limited (generally about 100 mTorr). In addition, there is a specific voltage-current relationship for each target material–sputtering gas pair. To maintain a glow discharge with a current density of 0.1–2.0 mA/cm^2, the applied voltage should be in the 500–5000 V range.

A *pre-sputtering* step is performed to clean the target surface from any contamination that would decrease the deposition performance [1]. During this step, the target surface is covered with a *shutter*. However, care should be taken for the contamination of the shutter itself after deposition.

The power efficiency in sputtering is very low and there is excessive amount of heating of the target (up to 400 °C) [1]. This amount of heating could damage the target-backing electrode bonding or other parts of the system. For this reason, a cooling system is used, usually by running water underneath the target.

Another important parameter in sputtering is the substrate temperature. It dictates the mobility of the species on the substrate surface, which is the basic factor in thin film

formation mechanisms [1]. It also effects the gas incorporation into the film. The substrates are usually heated by hot-liquid circulation or electrical resistance. The temperature is measured by a thermocouple in contact with the substrate or positioned nearby it. However, it should be kept in mind that the exact temperature at the substrate surface is usually different from its bulk due to the heat input from the glow discharge by the energetic ions. Thus, the value measured by the thermocouple could be erroneous. The use of infrared thermocouples is a solution, if the appropriate calibration is applied.

Magnetic fields are used in sputtering systems to increase the deposition rate and reduce electron bombardment onto the substrate and maintain greater structural homogeneity of the film [1]. The energetic efficiency for electron/gas molecule collision is increased, and higher deposition rate is achieved compared to simple RF sputtering [163, 168]. With magnetic field assistance, deposition rates greater than 1 μm/min could be achieved [1]. Consider a particle that is charged by an amount Q, moving with a velocity of v. The magnetic field (**B**) applied perpendicular to the velocity vector (**v**) of this particle creates a force vector (**F**) that is perpendicular to both **B** and **v**:

$$\mathbf{F} = Q\,\mathbf{v} \times \mathbf{B}. \tag{1.22}$$

Therefore, the particle is accelerated by:

$$\mathbf{a} = \mathbf{F}/m. \tag{1.23}$$

The typical magnetic fields that are used in sputtering are around 100 Gauss, which is enough to accelerate the electrons but not the ions. The more electrons are accelerated towards the target, the more ionization takes place. Without this boosting effect, most of the electrons are neutralized by their collisions with the chamber walls. There are two different configurations to apply magnetic fields in sputtering systems: *axial magnetic fields* and *magnetrons*. In the first case, the magnetic field is applied parallel to the glow discharge direction. The electrons moving along this direction are unaffected from this applied field. However, an electron moving with an angle θ to that direction would experience a force of magnitude ($BeV\sin\theta$), with a direction

perpendicular to the applied magnetic field. Therefore, the electron travels in a helical path, its net velocity reducing to zero when it is close to the walls. At the same time owing to the increased path length, more collisions with the gas atoms and more ionization take place. In the magnetron systems, there is an electric and a magnetic field applied perpendicular to each other, the magnetic filed being parallel to the target surface. In addition to the similar helical route, the electron is *forced* to fall back onto the target, if it has not been already used by a collision on its way. Consequently, the electrons would be *magnetically confined* near the target surface, further increasing the electron density hence the number of collisions in that region. Although the use of magnetic fields to assist glow discharge processes had been proposed much earlier [169], they have widely been in practical use only for the last couple of decades.

There are two disadvantages of magnetron systems [1]:

i) localized erosion of the target (causes inconstant deposition rates and necessitates frequent replacement of the target),

ii) arcing, (more common for magnetron sputtering systems than the other types of sputtering systems).

In overall, sputtering is advantageous over other deposition techniques by not requiring the melting of the target material. Thus, high melting point dielectric materials can be deposited at low temperatures. In addition, it enables reactive deposition of a wide range of materials including mixed oxides, nitrides, *etc.* [51]. Also, the energy provided by the plasma enables control of the film structure [25]. The energy transfer to the adatoms provides good adhesion and thickness uniformity. It is a suitable method to coat large areas for a lower cost than many other deposition methods [25]. On the other hand, it is not a desirable deposition system for organic solids since these solids degrade under the ion bombardment and the temperature rise (polytetrafluoroethylene being an exception) [1]. It is also not suitable for volatile materials due to the vacuum requirements to create the plasma.

1.5. Measurement of Residual Stresses in Thin Films

The measurement of the tensile stresses in an anisotropic material is based on the three-dimensional Hooke's Law [149, 170]:

$$\begin{Bmatrix} \sigma_x \\ \sigma_y \\ \sigma_z \end{Bmatrix} = \begin{bmatrix} C_{11} & C_{12} & C_{13} \\ C_{12} & C_{11} & C_{13} \\ C_{13} & C_{13} & C_{33} \end{bmatrix} \begin{Bmatrix} \varepsilon_x \\ \varepsilon_y \\ \varepsilon_z \end{Bmatrix} \tag{1.24}$$

Here, σ_i and ε_i are the tensile stress and strain in the corresponding directions, respectively. C_{ij} are the elastic constants and they form the stiffness matrix $[C_{ij}]$. In this matrix, there are four independent elastic constants: C_{11}, C_{12}, C_{13}, and C_{33}. (The stiffness constants C_{44} and C_{66} are used for calculating the shear stresses. In hexagonal crystals, due to symmetry, C_{66} is not independent; $C_{66} = (C_{11}\text{-}C_{12})/2$ [13].) The use of this equation is given in more detail in Chapter 3.

The accuracy of the stress calculation depends on the accurate measurement of the stiffness constants and the strains. Various values reported in the literature that have been collected by Özgür *et al.* [13] are given in Table 1.3. Another aspect of the stress determination is the accurate measurement of the strains. As stated earlier, the origins of the misfit in the film-substrate system could be thermal, mechanical, arising from plastic deformation, *etc.* [76]. Thus, the appropriate measurement method should be selected for the correct measurement of the stress among the methods developed so far. The early methods depended on the bending of the substrate upon stress, measured by the superposition of coherent light beams [74]. For a film thickness of t and a total sample thickness of h, the radius of curvature (ρ) is related to the residual compressive film stress (σ_c) as follows [147, 171]:

$$\rho = [E_s h^2 / 6\sigma_c t\,(1\text{-}v_s)][(1+t/h)(1\text{-}4t/h)] \tag{1.25}$$

Here E_s and v_s are the elastic modulus and Poisson's ratio of the substrate.

Texture is a serious obstacle in stress analysis, and the measurement of residual stresses in textured samples is still an evolving field. The texture existing in the films complicates the stress analysis because of the following factors [49]:

i) The restricted range of tilt angles due to the nonrandom distribution of the crystal orientation (*"A reliable regression of the measured strain distribution may thus become impossible."*) Then the intensity of the diffracted beams is a function of the inclination angle, ψ, and at low intensities, the d-spacing measurement could become erroneous or even impossible.

ii) Due to the texture, the elastic properties become anisotropic and the calculation of the diffraction elastic constants become inadequate.

Intrinsic stresses are hard to quantify due to the complex kinetics of film growth. On the other hand, the portions of the residual stresses in thin films that are caused by the so-called extrinsic factors are more easily quantified. The thermal stresses are proportional to the thermal expansion coefficient difference of the film and the substrate as [49]:

$$\sigma_{th} \sim (T_s - T)\,\Delta\alpha, \qquad (1.26)$$

where σ_{th} is the thermal stress, T_s is the substrate temperature during deposition, T is the equilibrium temperature after deposition (room temperature), and $\Delta\alpha$ is thermal expansion coefficient difference of the film and the substrate. The proportionality constant is the effective elastic modulus of the textured film. For large $\Delta\alpha$ or ΔT, the thermal stress is reduced by a plastic strain factor where the film stress exceeds the yield point of the film material. Some values of α_{ZnO} that were used to calculate the thermal stresses in ZnO thin films are given in Table 1.7.

The lattice-misfit stress is related to the lattice parameters of the two materials as follows [49]:

$$\sigma_m \sim 2(a_f - a_s) / (a_f + a_s), \qquad (1.27)$$

where σ_m is the lattice-misfit stress, a_f and a_s are the lattice constants of the thin film and the substrate, respectively. Here the bending effect of the substrate on the misfit dislocations is not taken into account.

Table 1.7. Some values for the thermal expansion coefficient (α) of ZnO used in the literature.

α (x10^6/°C)	**Direction**	**Temperature (°C)**	**Reference**
5–8		25–400	[172]
4.75	*a*	23	[25]
2.92	*c*		
6–8	*a*	300–800	[173]
3.5–4.5	*c*		
6.05	*a*	0	[174]
3.53	*c*		
3.2	*a*	40	
3.9	*c*		
4			[138]

The method that is used in this study to evaluate residual stresses in the ZnO thin films is presented explicitly in Chapter 3. The relevance of the background information provided in this chapter is presented in Chapter 2. Some other methods for stress measurement in thin films are x-ray diffraction with experimentally calculated x-ray elastic constants ($\sin^2\psi$ method) [175-177], nanoindentation [178, 179], two-dimensional XRD [180], and Raman spectroscopy [181-183]. Table 1.8 prepared by Welzel *et al.* [184] shows some of the critical review articles on stress measurements in thin films. More information on different techniques could be found on other texts such as [49, 50, 178, 185, 186].

Table 1.8. Review articles on diffraction stress analysis with a short description of the contents according to various categories [184].

Reference	[189]	[188]	[187]	[76]
Focus	Stress analysis by X-ray diffraction; polycrystalline specimens	Stress analysis by X-ray and neutron diffraction; polycrystalline specimens	Stress analysis by X-ray diffraction; poly- and single-crystalline specimens	Thin-film stress analysis by X-ray diffraction; polycrystalline and epitaxial films
Fundamentals	Brief introduction and brief historical review	Brief introduction	Historical review; types of residual stresses (macro versus micro)	Origins of stress; types of residual stresses (macro versus micro); stress states of thin films
Instrumentation	-	Brief introduction	Detailed treatment of laboratory (Bragg-Brentano) and portable diffractometers	Brief treatment of traditional (Bragg–Brentano, Seeman–Bohlin) and high-resolution diffractometers; microbeam diffraction
Analysis of gradients	Effect of a stress gradient on a $\sin^2$ analysis is discussed	Brief introduction	-	Grazing/glancing incidence diffraction
Elastically quasi-isotropic case	Full treatment; calculation of X-ray elastic constants	Brief introduction	Full treatment; calculation of X-ray elastic constants	Basic treatment
Elastically anisotropic case (case of texture)	Simplified treatment (assuming a Reusstype grain interaction)	Only mentioned; no details	-	-
Comments		In German	Sequence of four publications in German; introduction with historical review	Also covered: stress from curvature measurements, reflectometry for determination of film thickness and composition

CHAPTER 2

AIM AND MOTIVATION

As stated previously in Chapter 1, ZnO has many current and potential uses for the industry. It is a promising material for transparent conductive oxide or piezoelectric device applications [5, 13]. The optical and electrical behavior of these films is strongly influenced by the microstructure, which is primarily set by the deposition conditions as well as the substrate structure [101, 106, 109, 111, 113]. Until now, zinc oxide has been grown with various methods on a limited number of substrates. Much research has been done on the effects of deposition parameters for RF magnetron-sputtered ZnO thin films. However, the work on how the film growth parameters determine the microstructure and the final film properties is still incomplete.

The stable crystallographic structure of zinc oxide at room temperature and pressure is the hexagonal wurtzite type [13, 23, 24]. Wurtzite ZnO thin films tend to grow in polycrystalline form, with a very strong (002) texture [137, 190]. In a few studies, some other orientations, such as (100), (101), and (102) were reported [25, 133, 138-140]. However, the consequences of this variation from the (002) texture were not reported in detail.

The structure of the grains and the strength of texture depend on the deposition parameters. In a broad sense, the affects of the deposition parameters on the film growth can be summarized as follows:

i) Increasing the substrate temperature generally induced an increase in the adatom mobility and improved structural homogeneity. However, T_s should also be optimized for strongest texture (presumably due to microcrack formation above 400 °C [111]) or minimum roughness (due to grain over-growth above 300 °C [95]).

ii) The number of collisions increased between the gas molecules and sputtered atoms by increasing total pressure, effectively reducing the energy of the particles adsorbing on the substrate. Therefore, the mobility of the adatoms decreased. On the other hand, deposition rate and film stoichiometry (O/Zn ratio) decreased with increasing pressure. For example, optimum p for maximum deposition rate, maximum O/Zn ratio, and minimum *FWHM* in XRD was 1 Pa = 0.1 mbar in Ref. [96]. In another study for DC-magnetron sputtered ZnO films, the deposition rate increased for p = 0.2–3.0 Pa (0.002–0.03 mbar), while the p range for maximum structural homogeneity and the highest crystallinity was only in the 0.6–0.8 Pa (0.006–0.008 mbar) range [115].

iii) Other than the total gas pressure, the effects varying the partial oxygen pressure during reactive sputtering had been studied. Since ZnO tended to grow with oxygen vacancies and zinc interstitials, providing extra oxygen was beneficial for maintaining stoichiometry [99]. However, the oxygen content should be optimized for the best film quality. For example, optimum p_{O_2} was 0.01 Pa (0.0001 mbar; 10% O_2 in Ar) for the maximum XRD peak intensity [96], and 40% O_2 in Ar resulted in minimum film roughness [95] and minimum *FWHM* in XRD with maximum peak intensity [111].

iv) A similar discussion held for the RF power as with the chamber pressure, however the two had adverse effects. Increasing the RF power increased the energy of the particles incident on the substrate surface. Therefore, the adatom mobility increased. The film crystallinity improved; a denser film and better–oriented grains were obtained (*e.g.*, in the 1.28–1.90 W/cm^2 [96, 99], or 300–600 W [112] ranges). However, very high RF powers could have been disadvantageous for the film's crystal structure. The sputtering yield and the deposition rate increased with the increasing RF power (*e.g.*, deposition rate increased six-fold in the 25–100 W P_{RF} range [102]) However, the deposition rate should be optimized to allow the adatoms enough time to seek minimum energy positions, before subsequent adatoms arrived at the surface. Therefore, there was an optimum P_{RF} value for the highest peak intensity and minimum *FWHM* in the XRD spectra (*e.g.* optimum P_{RF} = 600 W in Ref. [112]), or maximum grain size (*e.g.*, grain size decreased rapidly for $P_{RF} > 50$ W in Ref. [102]).

It should be noted that, all of these parameters should be optimized for the desired microstructure and the consequent electronic properties.

The microstructure of thin films has been investigated under the topic of *structure zone models* (SZM) for several decades [51]. These models basically discuss the changes in the grain shapes depending on the homologous temperature (ratio of the substrate temperature, T, to the melting temperature of the film material, T_m) and the working pressure [54-58, 63]. A few studies included the adatom energy and the film thickness as a parameter [59, 60]. However, these models were developed based on the studies of metallic films. Most ceramics have much more complicated and more anisotropic crystal structures. They also have more than one type of ions. Therefore, oxide films could have very different growth dynamics compared to metals. For this reason, previously developed SZMs were not directly applicable to ZnO thin films. In addition, these models did not cover the entire spectrum of deposition parameters, and there remains a need for studying the morphological evolution of ZnO films under a wide range of deposition parameters [137]. For ZnO, a few structure zone models have been developed. One study examined the effect of T/T_m and the precursor concentration for chemically deposited ZnO thin films [135]. For magnetron-sputtered ZnO thin films, one study showed that the structures achieved for metallic thin films in the conventional models could be reached at lower homologous temperatures [136]. One study discussed the effects of deposition rate and oxygen content on the structure zones of Al-doped and magnetron-sputtered ZnO films, providing a technological window of low stress and high transparency [25]. In a few studies, the effect of a thin buffer layer between the film and the substrate on the structure of the films has been investigated [141, 142].

RF magnetron-sputtered ZnO thin films possessed residual compressive stresses [25, 95, 96, 99, 102, 111, 112]. Thermal annealing has been widely applied to relax those stresses [95, 96, 150-155]. The residual stresses might originate from the coating method itself: sputter deposition is known to produce highly dense, close-packed microstructure films with compressive stresses that varied as a function of the coating parameters such as the working-gas pressure, the gas discharge current, and the angle of incidence of the coating material atoms. In most cases, the stresses were attributed to the thermal expansion mismatch between ZnO and the substrate material [156]. However, the thermal contribution to the overall stress is very insignificant for the deposition temperatures of interest [25]. A few studies mentioned the creation of stresses upon argon implantation into the film during deposition and consequent peening mechanism. However, the actual argon content in the films has been measured

in only a few studies and the films contained a few atomic percentage of argon [96]. Some studies emphasized the effect of substrate morphology and the lattice mismatch between the film and the substrate [98, 140, 156]. On the other hand, a significant amount of residual compressive stress has been observed on amorphous substrates as well. These were attributed to the so-called *growth stresses*, although the mechanisms yielding these growth stresses have not been clearly described. Therefore, there was no clear distinction between the intrinsic and the extrinsic contributions to the residual stresses in ZnO thin films. It has been reported in many studies that these residual stresses affect the functional properties of the films. Thus, mechanisms behind the formation of these stresses should be elaborated to be able to tailor these functional properties.

The mechanical integrity of thin films is very important for the stability of the functional properties and device lifetime. In the majority of the studies on zinc oxide, although electrical and optical properties of the thin films were examined; the thermal and mechanical stability were not investigated in detail. There have been some studies on the hardness of ZnO thin films [143]. There have also been a much more limited number of studies on the mechanisms during mechanical failure of these films [146, 148] as well as on the adhesion control of the films on different substrates [147].

Combining the above statements, the need becomes clear for investigating the microstructural evolution, residual stress evolution, and the relaxation of these stresses in ZnO thin films in one comprehensive study. This study will discuss, as the title implies, the mechanisms behind residual stress formation, how they affect the film's structure, and the mechanisms behind stress relaxation. The aim is to take the thin film or microstructure growth one step further than just experimental observations. Once the above problems have been addressed, it would be possible to design the optimal conditions for the highest performance films with maximum stability and mechanical integrity. The results could be used not only for zinc oxide but also for other materials of interest for the demands of optics and electronics industry. The methods used, the results obtained, and the conclusions arrived are presented in the following chapters.

CHAPTER 3

EXPERIMENTAL PROCEDURES

In this chapter, the procedures for thin film deposition and characterization are presented. First, the sample preparation and RF magnetron-sputtering for thin film deposition are described. The sample characterization methods include x-ray diffraction (XRD) for stress analysis, scanning electron microscopy (SEM) for microstructure study, and dilatometry for measurement of the thermal expansion coefficients of the substrates. Additional experiments for the measurement of optical transmittance in the UV–VIS range and their results are provided in the Appendix E.

3.1. Substrate Preparation

Substrate selection and preparation are very crucial in determining the final film structure and properties [2, 191-200]. In this study, three types of substrates are used: glass microscope slides, single crystal silicon wafers, and single crystal mica sheets. The surface preparation methods and material specifics for each substrate type are given below.

Amorphous glass microscope slides (Temas, Germany) with a thickness of 2 mm and cover slides (Isolab, Germany) with dimensions of 20x20x0.16 mm^3 were used as glass substrates. The microscope slides were cut by a diamond scribe to obtain pieces of ~20x20-mm^2 size. Two different preparation methods were used for each of the two groups of those glass slides. The first group of slides was cleaned under ultrasonic vibration with the following steps ("alcohol cleaning"):

i) Acetone bath (room temperature, 10–15 min),

ii) Methanol bath (80 °C, 10–15 min),

iii) Ethanol bath (80 °C, 10–15 min),

iv) Distilled water rinse (room temperature),

v) Wetting test (see Appendix A),

vi) Drying under nitrogen jet (99.998% v/v, max 5 ppm humidity, max 5 ppm O_2).

The pieces in the second group were first annealed in air atmosphere at 450 °C for 2 hours to diminish any possible residual stress that might be formed during cutting. This step was followed by a special surface cleaning method, to achieve the surface of pure SiO_2 as close as possible ("acid cleaning" [199]). This method involved rinsing under ultrasonic vibration, with the following steps:

i) Detergent bath (H_2O:detergent = 30:1 v/v, T = 80 °C, 10 min),

ii) Distilled water rinse x 3 (10 min each),

iii) Acid–peroxide bath (H_2SO_4:H_2O_2 = 2:1 v/v, T = 80 °C, 10 min),

iv) Distilled water rinse x 3 (80 °C, 10 min each),

v) Wetting test (see Appendix A),

vi) Drying under nitrogen jet (99.998% v/v, max 5 ppm humidity, max 5 ppm O_2).

Single crystal, (100)-oriented, phosphorus-doped silicon (Si) wafer pieces (Silicon Materials, Inc., Glenshaw, PA, USA), and high quality single crystal mica ($KAl_2(AlSi_3O_{10})(F, OH)_2$; potassium aluminum silicate hydroxide fluoride) sheets (Ted Pella Inc., Redding, CA, USA) were used as crystalline substrates. The Si wafer pieces were of various surface areas (about 2–6 cm^2), all with a thickness of 508±20 μm. Mica sheets had a similar surface area, and a thickness of 0.23 mm. Silicon has a face-centered cubic structure. The mica sheets were of the monoclinic muscovite class ("Muscovite has a layered structure of aluminum silicate sheets weakly bonded together by layers of potassium ions [201]"). The data obtained from the Joint Committee on Powder Diffraction Standards (JCPDS) and the XRD spectra of each of the crystalline

substrates are provided in the Appendices B and C, respectively. Prior to deposition, these substrates were cleaned with the "alcohol-cleaning" described above.

During preparation stages, the substrates were handled with Teflon tweezers to prevent scratches. More detail on the crucial points of the cleaning method is provided in the Appendix A.

3.2. Film Deposition

ZnO films were deposited on various substrates by a 13 MHz-radio frequency magnetron sputtering system (Teknoplazma, Ankara, Turkey) (Fig. 3.1 and Fig. 3.2). Pure (99.999%) ZnO was used as the sputtering target (Kurt J. Lesker, Clairton, PA, USA). Target diameter and thickness were 50.8 and 3.175 mm, respectively.

Film depositions with different materials in the chamber produce metal and oxide residues in the chamber. The chamber was cleaned from the remains of the previous depositions with a vacuum cleaner, acetone, and alcohol prior to the ZnO depositions. The stainless steel target shutters, the target housing rings, and the substrate holder were further cleaned in an acid bath $HCl:H_2SO_4$ (55:45 v/v) [202]. Prior to ZnO depositions, the chamber was initially evacuated to 10^{-6}–10^{-5} mbar. For further preparation of the target surface, the target was subjected to argon-ion plasma cleaning for 5 min with the shutters closed, immediately before the film depositions. High-purity argon gas (Karbogaz; 99.999% v/v, max 1 ppm humidity, max 4 ppm O_2) was used for generating the plasma.

The ZnO target was placed on one of the three magnetrons on the bottom of the main chamber (Fig. 3.3). The substrate holder was placed above the magnetron set. The substrate-to-target distance was fixed at 14 cm. The substrates were placed on a 10 cm-diameter stainless steel holder with polyimide tape, which was stable under vacuum and high temperature. To maintain the thickness uniformity of the film across different samples, the useful area of the holder was restricted to a diameter of 7 cm maximum, with one control sample at the center of the holder, encircled by 4–5 others (Fig. 3.4). To improve homogeneity further, the holder was spun around its axis by a spindler with a speed of 3 rpm.

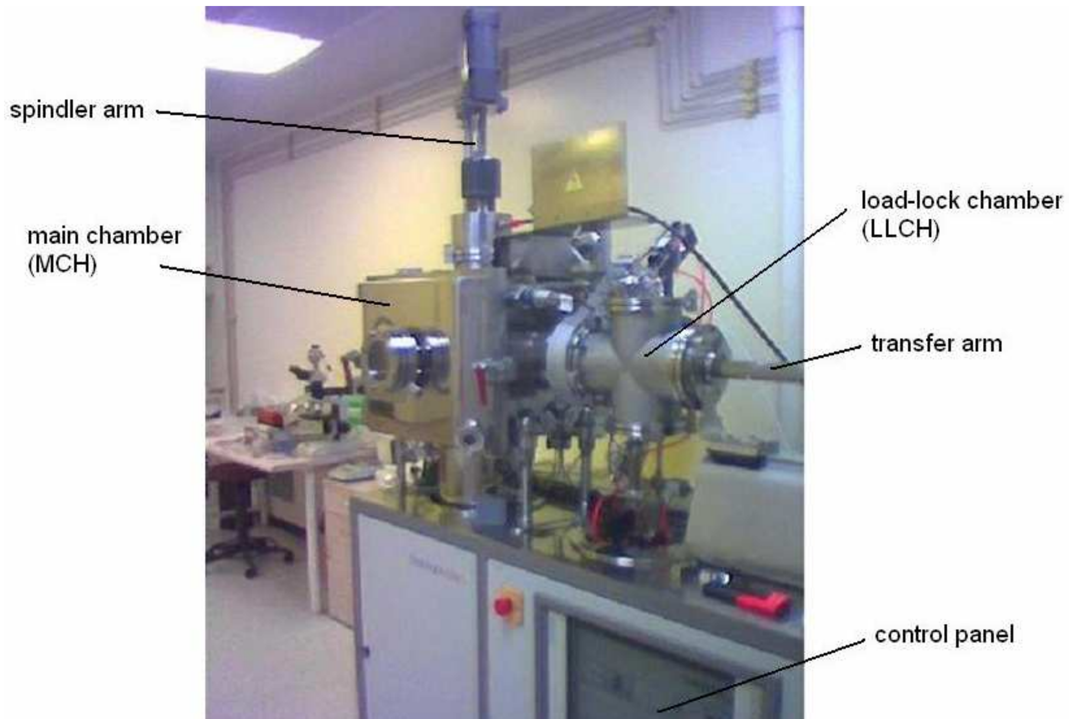

Figure 3.1. The radio frequency magnetron sputtering (RFMS) system placed in a Class–1000 clean room.

The film deposition parameters are given in Table 3.1 and Table 3.2. The depositions were performed under a pure argon atmosphere with a pressure (p) range of 0.009–0.4 mbar, 35 cm^3/min Ar gas flow (V), 100–150 W RF power (P_{RF}), 30 W DC power (P_{DC}), 85–90 kHz DC bias frequency. The chamber was heated by an electronically controlled halogen lamp placed inside the chamber (Fig. 3.3). The following substrate temperatures (T_S) were used for different groups of samples:

i) Substrates were initially heated to 200 °C. No heating was performed during deposition and the depositions were done under a decreasing temperature. The final temperature was measured to be ~63 °C.

ii) Substrates were heated to 200 °C and held at that temperature during deposition.

iii) Initially at room temperature. No heating was performed. The samples were naturally heated by electron and ion bombardment from the plasma (presumably to around 70–80 °C; see Fig. D.1.1 and Ref. [155, 203]). The final temperature at the end of deposition was measured as 39 °C by the thermocouple.

iv) Initially at room temperature. Heating and deposition started at the same time, and the final temperature at the end of the deposition was 195 °C.

From this point forward in the text, for the depositions where no heating was performed, the deposition temperature is indicated to be as *room temperature* (RT). Considering the deposition temperatures (20–200 °C = 293–473 K) and the melting point of ZnO (1975 °C = 2248 K), the homologous temperature during film growth was between 0.13 and 0.21. The temperature was monitored by irreversible temperature strips (Palmer Wahl, USA) stuck to the substrate surfaces and the empty substrate holder surface (Fig. 3.4). In addition, a thermocouple was also placed near the sample holder (Fig. 3.3). For the depositions at 200 °C, the system was allowed 1 hour for temperature stabilization prior to deposition (see Fig. D.2.1 for the temperature calibration between the thermocouple and the temperature strips during heating).

After the deposition was completed, one set of samples was held under vacuum at 200 °C for two hours inside the chamber (Set 10). Similarly, one set of samples (Set 11 in Table 3.1) was held at 200 °C for two hours under mixed O_2:Ar flow (2:5 v/v; O_2: Karbogaz, 99.6% v/v, max 5 ppm humidity). The total gas flow rate was fixed at 35 cm^3/min, to provide consistency with other depositions. Unless otherwise stated, all the other samples were cooled in the chamber down to room temperature under vacuum, argon or nitrogen flow (Karbogaz, 99.998% v/v, max 5 ppm humidity, max 5 ppm O_2) after the deposition was completed (see Fig. D.2.2 for the cooling curve of the chamber).

In order to elucidate the effect of a pre-deposited ZnO buffer layer on the further film growth, a set of films was deposited on ZnO buffer layers. All the buffer layers were deposited at T_s = 200 °C, P_{RF} = 125 W, and p = 0.2 mbar for 10 min on glass substrates (see Set12 in Table 3.1). Prior to the buffer layer deposition, two of these substrates were cleaned with the acid-cleaning procedure described in Section 3.1 (12A and 12B). Two of them were taken directly from the package and were not cleaned (fresh substrates) (12C and 12D). After buffer layer deposition for 10 min, the samples were kept inside the chamber until they cooled down. Two of the buffer-deposited substrates (12B and 12D) were annealed in air at 600 °C for 2 hours. All four samples were used for further film growth, under the same conditions used for buffer layer deposition. The remaining deposition time was 50 min, to allow a film of the same thickness as the other control sets.

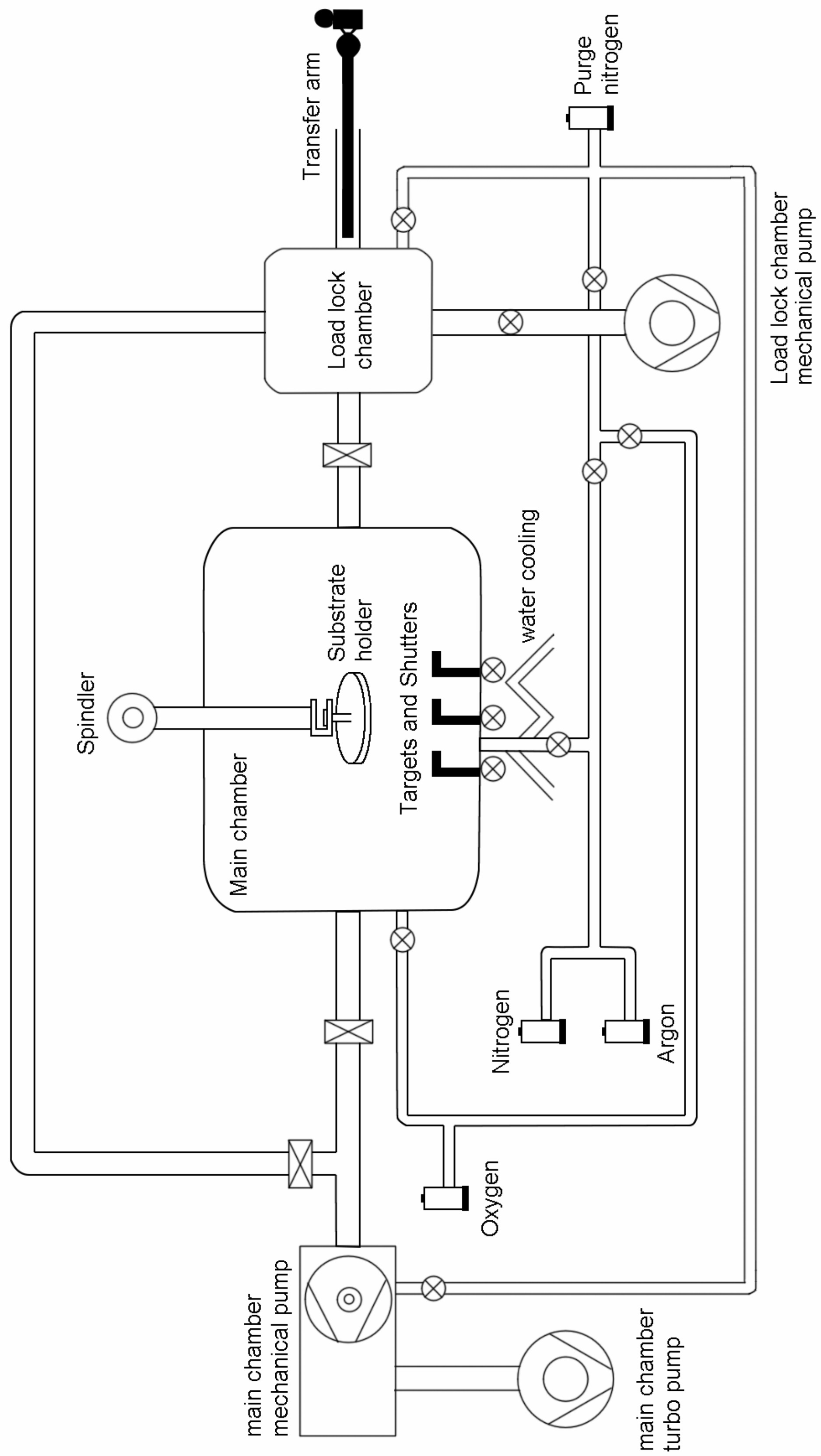

Figure 3.2. Schematics of the RFMS deposition system.

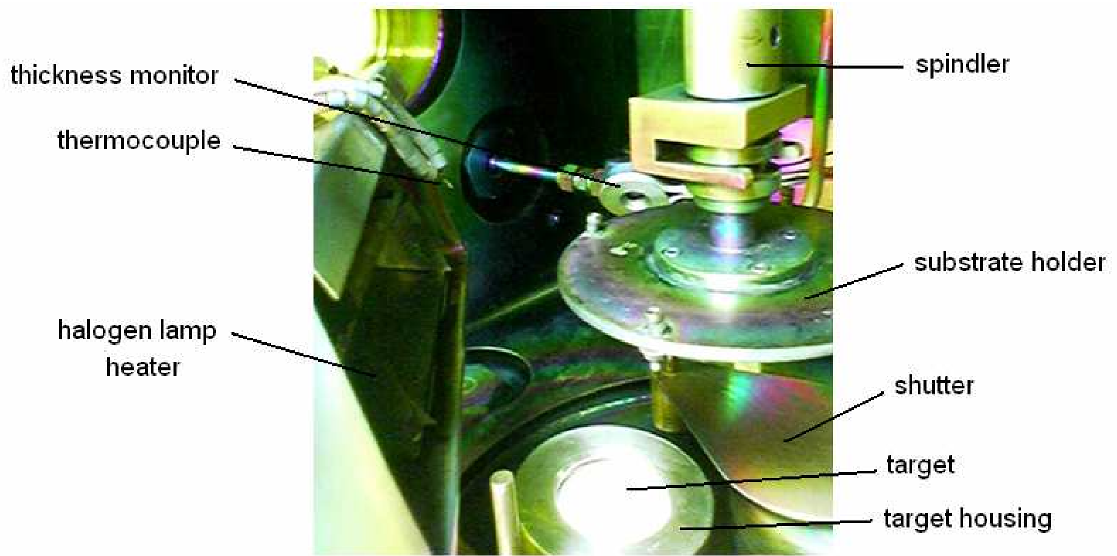

Figure 3.3. A close look at the main chamber.

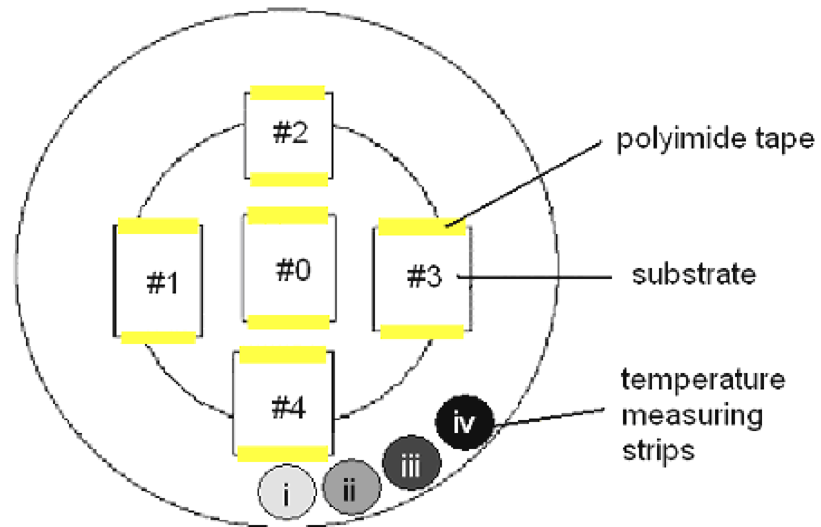

Figure 3.4 The positions and the indices of the substrates on the holder. The gray circles represent the temperature measuring strips. The measurable temperatures are: i) 43–54 °C, ii) 60–93 °C, iii) 93–126 °C, iv) 132–148 °C.

Table 3.1. ZnO thin film deposition variables. Unless otherwise stated, all substrates were prepared by the acid cleaning method described in Section 3.1. DC power was 30 W for all depositions.

Set no	Substrate	RF power, P_{RF} (W)	Chamber pressure, p (mbar)	Substrate temperature, T_s (°C)	Duration, t (min)	Note
1	Glass	100	0.4	200	20	*
2	Glass	100	0.4	200	60	*
3	Glass	100	0.4	RT	60	*
4	Glass	125	0.4	RT	60	*
5	Glass	125	0.4	200	60	*, §
6	Glass	125	0.2	200	60	*, §§
7	Glass	125	0.2	RT	60	*
8	Glass	125	0.2	200	60	*
9	Glass	125	0.02	200	60	*
10	Glass	100	0.2	200	60	**
11	Glass	125	0.2	200	60	***
12	Glass	125	0.2	200	10	****
13	Glass	125	0.2	200	50	*****
16	Glass, Mica, Si(100)	100	0.02	200–63	65	§§§
17	Glass, Mica, Si(100)	100	0.009–0.02	RT	97	§§§
18	Glass, Mica, Si(100)	100	0.43	115–67	45	*, §§§
19	Glass	100	0.025	RT	60	*, §§§
20	Glass	100	0.05–0.033	RT	30	*, §§§

*	Cooled to room temperature inside the chamber after deposition.
**	Kept under vacuum inside the chamber at 200 °C for 30 min. after deposition. Cooled to room temperature inside the chamber after deposition.
***	Kept under O_2:Ar (2:5 v/v) flow inside the chamber at 200 °C for 30 min. after deposition. Cooled to room temperature inside the chamber after deposition.
****	Cooled to room temperature inside the chamber after deposition. Some samples were annealed in air after deposition at 600 °C for 2 h. Used as buffer layer for Set13. (See Table 3.2.)
*****	See Table 3.2 for the substrates. Cooled to room temperature inside the chamber after deposition.
§	For comparison, one of the samples was cleaned with alcohol. (See Sec.3.1)
§§	No substrate cleaning.
§§§	Alcohol cleaning. (See Sec.3.1)

Table 3.2. Substrate details about Set13. Four different samples were prepared to elucidate the effects of the pre-deposited ZnO layer on the residual stress. See Section 3.1 for the substrate cleaning method.

Sample	Pre-deposition (Substrate cleaning and buffer layer)
13A	Acid-cleaned substrate; Buffer layer 12A.
13B	Acid-cleaned substrate; Buffer layer 12B annealed in air.
13C	Fresh substrate; Buffer layer 12C.
13D	Fresh substrate; Buffer layer 12D annealed in air.
13E	Alcohol-cleaned substrate; No buffer layer.
13F	Acid-cleaned substrate; No buffer layer.

3.3. Post-deposition Treatments

Several post-deposition treatments have been applied to the ZnO thin films after deposition. The corresponding experimental procedures are presented in the following sections.

3.3.1. Thermal Annealing

In order to alter the residual stresses, the films were subjected to thermal annealing. Two different atmospheres were used to observe the differences in results depending on the oxygen content provided: air and argon. Air annealing was performed under normal ambient air atmosphere in a heated box furnace (Thermolyne 48000). High-purity (99.999% v/v) argon gas was used in the argon-annealing, with a maximum oxygen content of 1 ppm and a maximum humidity value of 4 ppm (Karbogaz). Argon-annealing was performed in a tube furnace (Protherm; Alser Teknik). For the argon-annealing, the alumina tube inside the furnace was sealed from both ends. Argon gas with a flow of 50 ml/min was attached to the inlet. The air inside the tube was suctioned for 30 min with a pump and then flushed with Argon for another 30 min. The pump operated throughout the annealing period. The heating and cooling curves of the two furnaces are given in Fig. 3.5.

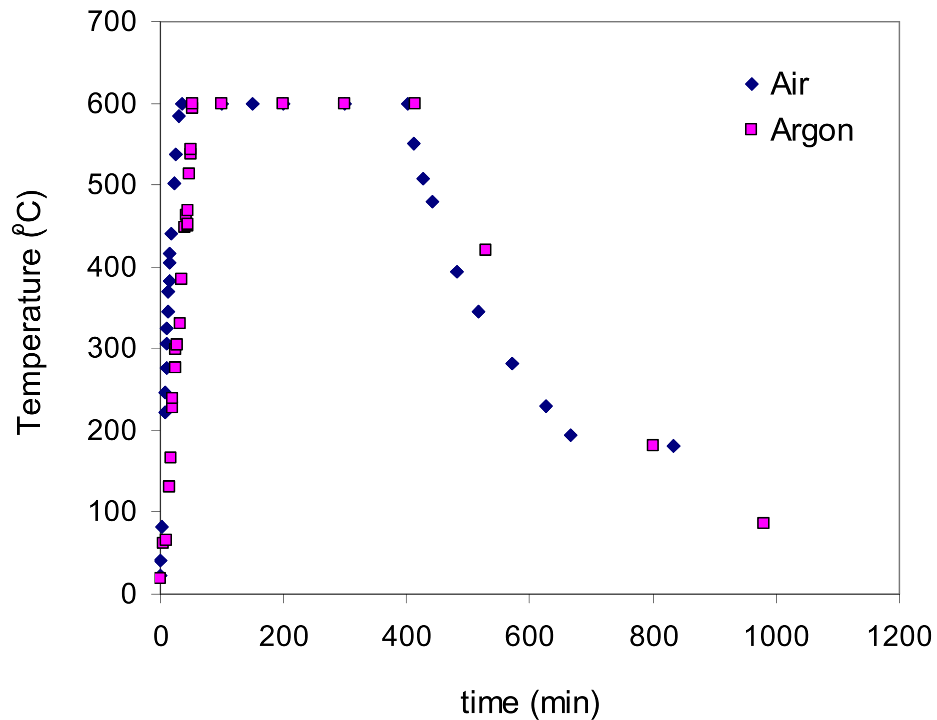

Figure 3.5. Heating and cooling curves for the annealing furnaces.

3.3.2. Aging

The samples were stored to monitor the time-dependent changes in the microstructure and the residual stresses. Sets 1–15 were stored under vacuum for 2 months and Sets 16–18 were stored under ambient conditions for 12–28 months.

3.4. Material Characterization

The ZnO thin films have been characterized in terms of their microstructure, texture, and residual stresses. Film characterization has been applied after both the film deposition and the post-deposition treatments. The corresponding procedures are presented in the following sections.

3.4.1. Microstructure

Film thickness and microstructure was characterized by SEM (Zeiss–Leo Supra 35VP, Oberkochen Germany). For film thickness measurements and cross-sectional microstructure examination, the samples were broken by the help of a diamond scribe. A metal support tool was used during cutting such that the edge touched the sample only along the cutting line to minimize damage to the film surface (Fig. 3.6). The samples were coated with carbon (Emitech K950X Carbon Vacuum Evaporator) to maintain a conductive layer on the surface to prevent charging due to electron build-up during scanning. Elemental analysis was performed with the energy-dispersive x-ray spectrometer (EDX) attached to the SEM, with an accelerating voltage of 20 keV.

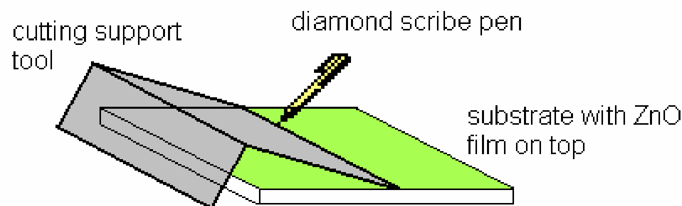

Figure 3.6. Sample cutting for cross-sectional SEM analysis.

The gun chamber pressure was about 10^{-10} mbar. The base pressure of the sample chamber was on the order of and 10^{-6} mbar. The column was equipped with a secondary electron detector, a back-scattered electron detector, a special in-lens detector for annular secondary electron detection. The extractor voltage was set to 5.2 keV, and the accelerating voltage used was in the 2–20 keV range. Elemental analysis was done by an energy-dispersive x-ray spectrometer (EDX) attached to the SEM, with a working distance of 8 mm.

3.4.2. Crystal Structure and Residual Stress Analysis

3.4.2.1. Phase analysis and strain measurement

Crystalline phases were examined with an x-ray diffractometer (Bruker AXS GmbH–D8 Advance, Karlsruhe, Germany). The x-ray source was fixed while the sample and the detector were allowed to rotate along a goniometer circle on the source-sample-detector plane, the sample being at the center of this circle (Fig. 3.7). Cu-K_{α_1} radiation with a wavelength of 1.5406 Å was used for diffraction. The x-ray generator voltage and current were held at 40 kV and 40 mA, respectively.

For phase analysis, the *locked-couple* mode (*i.e.* θ–2θ geometry) was used. In this mode, the sample rotates around an axis perpendicular to its normal. Simultaneously, the detector rotates along a circular *goniometer* with the sample at the center, spanning an angle of 2θ (Fig. 3.7). The reflection angle 2θ was varied continuously from 10° to 90° with a step size of 0.02°/step and a signal time of 0.5 s/step. For the peak shift analysis, the scanning range was narrowed down to 32°–37° to focus on the peaks of interest, and the acquisition time (time per step) was increased to 3 or 5 s/step depending on the peak intensities and the noise—higher acquisition times were used in order to reduce noise for small peaks. For very low-intensity peaks, the scans were repeated and merged, such that the total acquisition time would be 30–270 s/step. For planar homogeneity, the locked-couple scans were repeated for different ϕ angles (0–360°), around the surface normal of the sample (Fig. 3.7). In this study, the ZnO standard with the JCPDS number of 36-1451 was taken as the reference during XRD measurements. Nevertheless, the θ–2θ measurement was repeated for a commercial ZnO powder sample (Merck, Darmstadt, Germany) for comparison.

A Göbel mirror was also positioned between the source and the sample holder, to maintain parallel incident beams on the sample surface at all times. This way, the errors in peak shifts created by the differences in sample heights were minimized. To decrease this error further, the samples were positioned on the holder such that the film surface was always aligned with the holder surface. The sample was placed inside the gap of a Plexiglas frame and taped from above the frame. The frame was then placed inside the holder, aligned with the holder surface with the help of a spring and a plate placed

underneath (Fig. 3.8). To narrow the beam, and to decrease anti-parallel scattering, three slits were positioned along the beam path: a 0.2-mm wide slit at the exit of the Göbel mirror, a 0.6-mm computer-controlled automatic anti-scatter slit and a 0.2-mm detector slit in front of the detector.

To account for the changes in the crystal structure during high-temperature deposition or annealing, some samples were investigated by variable-temperature XRD. The samples were heated by a hot-air gun, and the increasing temperature was monitored by a laser pyrometer (Fig. 3.9). The temperature range obtained was 20–170 °C. After reaching 170 °C, the sample was allowed to cool to room temperature and another scan was performed. During these measurements, the ϕ angle was held constant at all times.

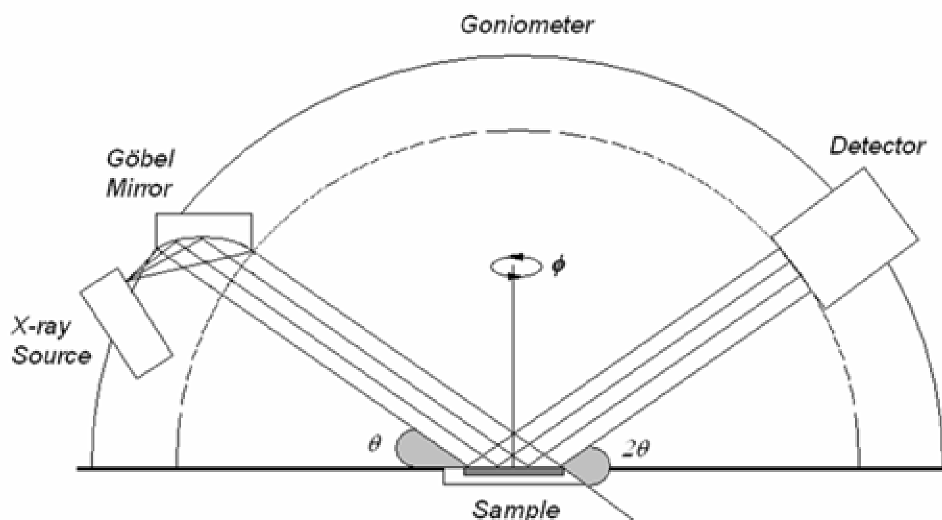

Figure 3.7. XRD measurement configuration. (Adapted from Ref. [108].)

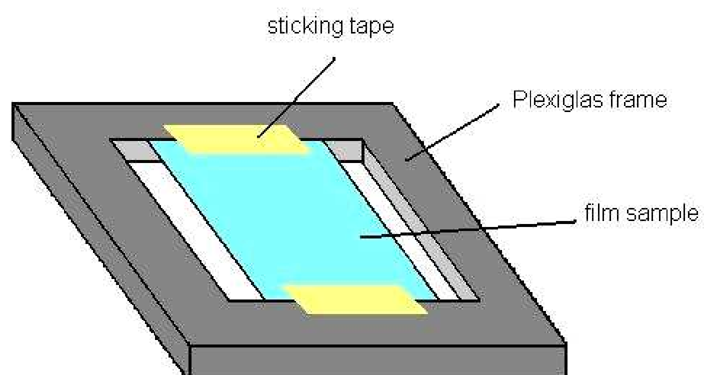

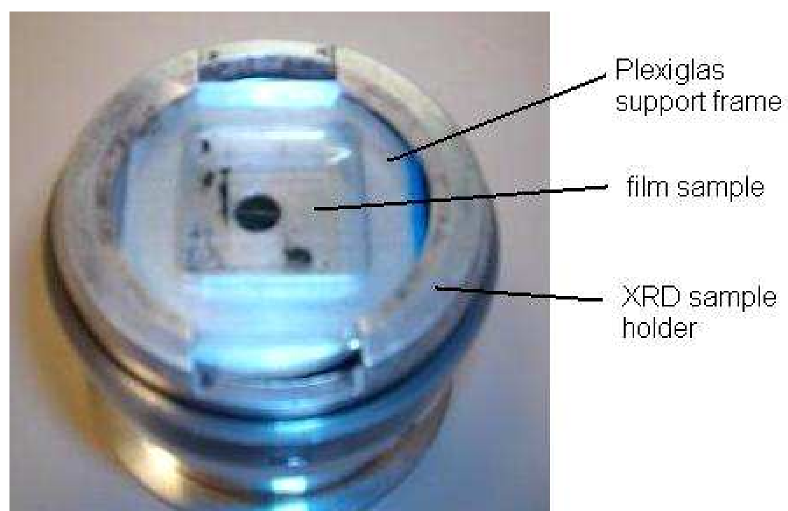

Figure 3.8. Sample placement configuration for XRD measurements.

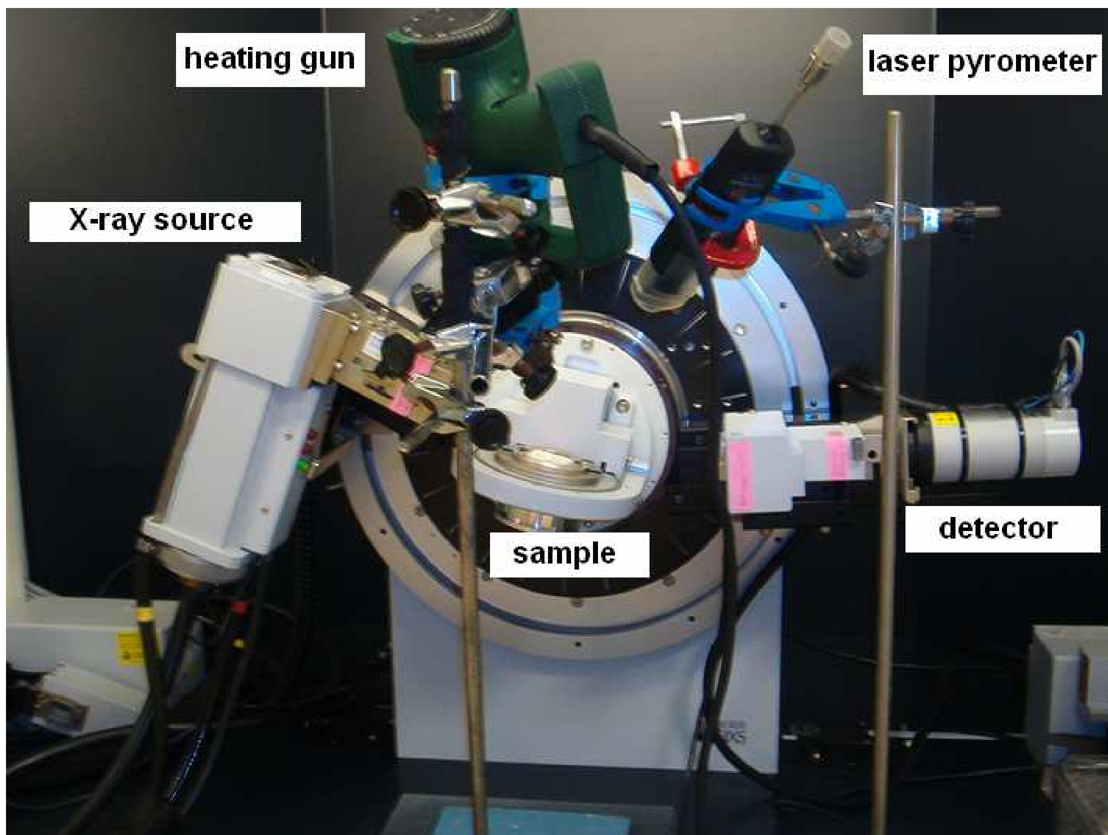

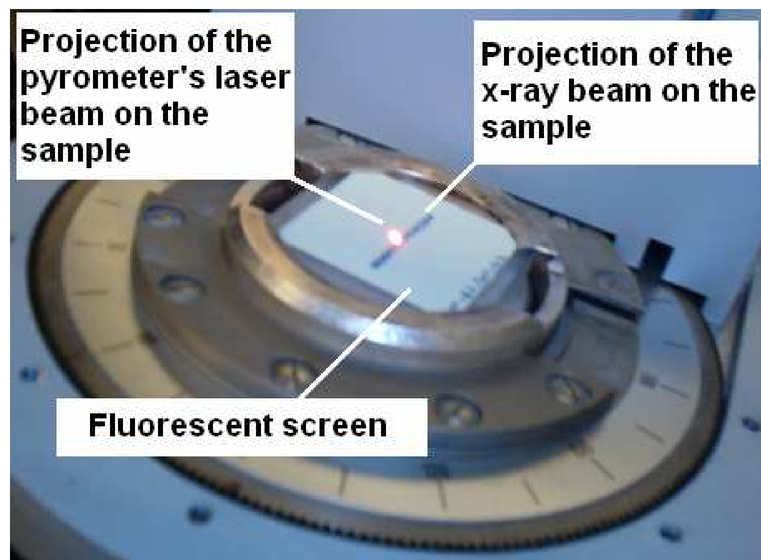

Figure 3.9. Variable-temperature XRD set-up.

3.4.2.2. Calculation of the average residual stress

According to Braggs's Law, reflected beams from the crystal planes will interfere constructively, hence producing a signal of non-zero intensity in the XRD scans, only if the following condition is satisfied:

$$\lambda = 2d\sin\theta, \tag{3.1}$$

$$d = \lambda/2\sin\theta. \tag{3.2}$$

where λ is the x-ray beam wavelength, d is the lattice spacing of the diffracting planes, and θ is the (Bragg) angle between the incident beam and the diffracting plane (Fig. 3.10). The beam wavelength is an instrument property and is equal to 1.5406 Å for the Cu-K_{α_1} radiation of the diffractometer used in this study. The lattice spacing, d, is a material property, and the d values for ZnO crystallographic planes (JCPDS no. 36-1451) are given in Table3.3.

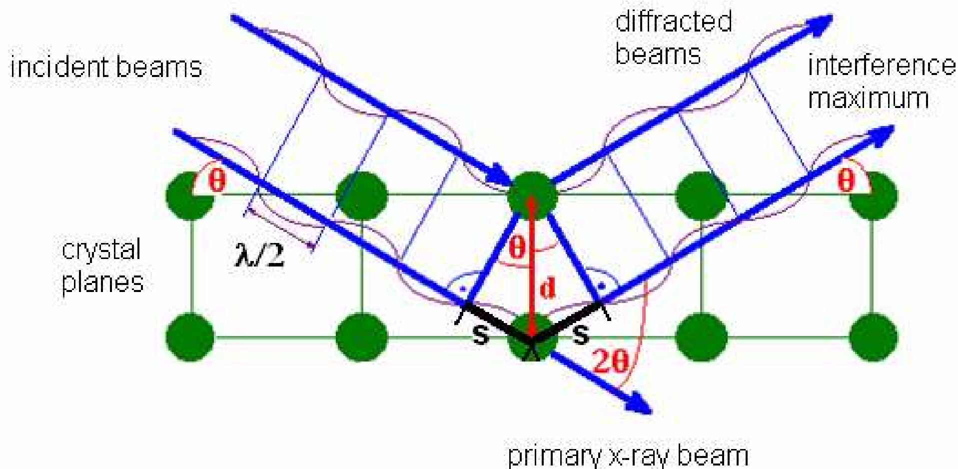

Figure 3.10. Demonstration of Bragg's Law. Only the reflections that have the required angle of incidence interfere constructively and yield an XRD peak. (Adapted from Ref. [204].)

Table 3.3. Lattice spacings and the corresponding diffraction angles of the stress-free powder standard JCPDS-No. 36-1451 [205].

Peak (*h k l*)	**Intensity (normalized)**	**2θ (°)**	***d* (Å)**
1 0 0	57	31.770	2.81430
0 0 2	**44**	**34.422**	**2.60332**
1 0 1	**100**	**36.253**	**2.47592**
1 0 2	23	47.539	1.91114
1 1 0	32	56.603	1.62472
1 0 3	29	62.864	1.47712
2 0 0	4	66.380	1.40715
1 1 2	23	67.963	1.37818
2 0 1	11	69.100	1.35825
0 0 4	2	72.562	1.30174
2 0 2	4	76.955	1.23801
1 0 4	1	81.370	1.18162
2 0 3	7	89.607	1.09312
2 1 0	3	92.784	1.06384
2 1 1	6	95.304	1.04226
1 1 4	4	98.613	1.01595
2 1 2	2	102.946	0.98464
1 0 5	5	104.134	0.97663
2 0 4	1	107.430	0.95561
3 0 0	3	110.392	0.93812
2 1 3	8	116.279	0.90694
3 0 2	4	121.572	0.88256
0 0 6	1	125.188	0.86768
2 0 5	3	133.932	0.83703
1 0 6	1	136.520	0.82928
2 1 4	2	138.513	0.82370
2 2 0	3	142.918	0.81247

For a stress-free sample, the Bragg condition for ZnO is satisfied for the values given in Table 3.3, and the diffraction peaks for the given planes will be seen at the corresponding 2θ values as the detector scans the whole 2θ range. However, for the stressed crystals, the lattice spacings could deviate from their original values, depending on the direction of stress. For compressive planar stress, the crystal would shrink in the lateral direction (*i.e.*, in the direction of the residual stress). Poisson's ratio indicates that

there must be a corresponding elongation along the axial direction. The case is reversed for tensile planar stress. Therefore, the lattice parameters of the samples either increase or decrease. Accordingly, the 2θ angle to satisfy the Bragg condition shifts to lower values for compressive planar stress and to higher values for tensile planar stress (Fig. 3.11). The amount of this shift is measured in order to calculate the transverse strain (ε_z) and is used in calculating the amount of residual stress in the longitudinal direction (σ_x or σ_y).

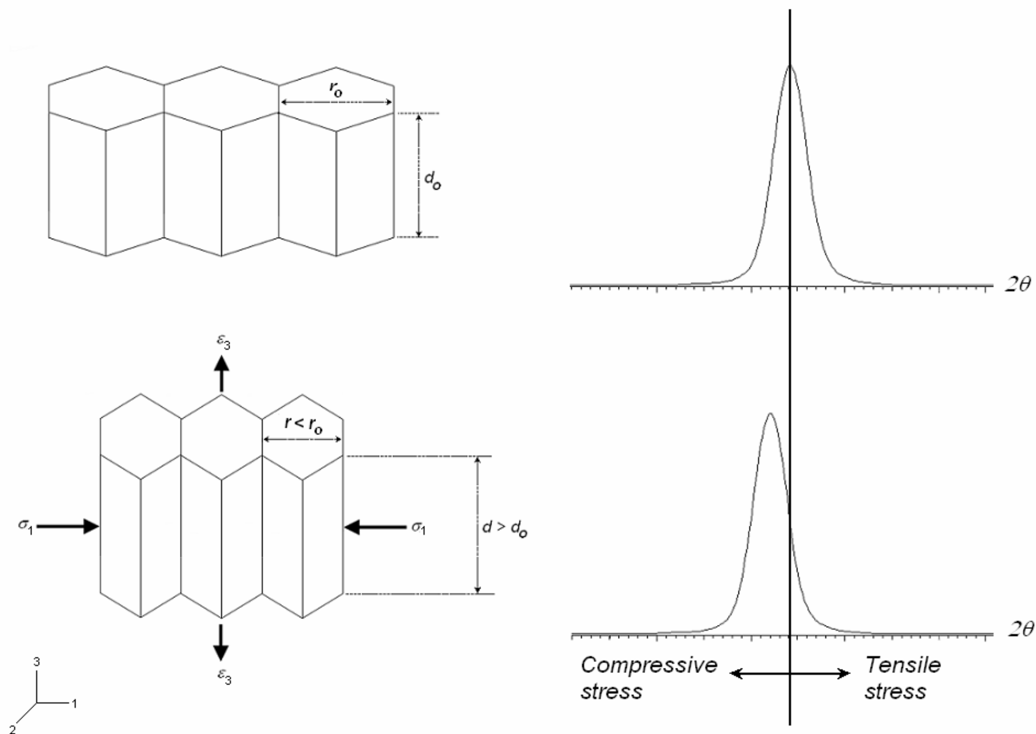

Figure 3.11. Determining compressive and tensile stresses via the shift in the x-ray diffraction peaks (for the biaxial strain model, the stress along the direction 3 is zero, and equal amounts of stresses are present in along directions 1 and 2. For clarity, only the stress in the direction 1 is shown in the figure).

In the elastic regime, the stress is directly proportional to strain, and the strains are small. In this regime, Young's modulus (elastic modulus; E) defines the ratio of the *tensile stress* and the resulting strain in direction *i* through Hooke's Law:

$$\varepsilon_i = \sigma_i / E \qquad (3.3)$$

Poisson's ratio (v) defines the ratio of strain along transverse strain to the longitudinal strain along direction of the applied stress:

$$\nu = -(\varepsilon_3 / \varepsilon_1) \tag{3.4}$$

If the strain field is three dimensional and E is isotropic, Eq. 3.3 expands into the following:

$$\begin{aligned} \varepsilon_1 &= \frac{1}{E}\left[\sigma_1 - \nu(\sigma_2 + \sigma_3)\right] \\ \varepsilon_2 &= \frac{1}{E}\left[\sigma_2 - \nu(\sigma_1 + \sigma_3)\right] \\ \varepsilon_3 &= \frac{1}{E}\left[\sigma_3 - \nu(\sigma_1 + \sigma_2)\right] \end{aligned} \tag{3.5}$$

In order to deduce the stresses from the measured strains, Eq. (3.5) should be written in terms of the stresses. It should be considered that, for a hexagonal crystal, E is no longer isotropic. Moreover, for constrained samples such as thin films deposited on substrates, the sample is not free for the full Poisson's effect to be observed. Instead, a stress tensor with the elastic stiffness constants, [C_{ij}] is defined. For a hexagonal symmetry, the corresponding Hook's law is as follows [149, 170]:

$$\begin{Bmatrix} \sigma_1 \\ \sigma_2 \\ \sigma_3 \end{Bmatrix} = \begin{bmatrix} C_{11} & C_{12} & C_{13} \\ C_{12} & C_{11} & C_{13} \\ C_{13} & C_{13} & C_{33} \end{bmatrix} \begin{Bmatrix} \varepsilon_1 \\ \varepsilon_2 \\ \varepsilon_3 \end{Bmatrix}, \tag{3.6}$$

or,

$$\sigma_1 = C_{11}\varepsilon_1 + C_{12}\varepsilon_2 + C_{13}\varepsilon_3 \tag{3.7a}$$

$$\sigma_2 = C_{12}\varepsilon_1 + C_{11}\varepsilon_2 + C_{13}\varepsilon_3 \tag{3.7b}$$

$$\sigma_3 = C_{13}\varepsilon_1 + C_{13}\varepsilon_2 + C_{33}\varepsilon_3 \tag{3.7c}$$

In this study, the stresses are calculated by the *biaxial strain model* for thin films [149]. This model assumes that the strains along x and y directions are equal to each other and the axial stress is zero except very close to the edges. This assumption was shown to be valid in thin films [170], and it is reasonable for the films with the thickness values in this study (100–500 nm). Thus,

$$\sigma_1 = \sigma_2, \tag{3.8a}$$

and

$$\sigma_3 = 0. \tag{3.8b}$$

If the biaxial compressive stress, σ_c,is defined as $\sigma_c = \sigma_1 + \sigma_2$, then adding Eq.(3.7a) and Eq.(3.7b) yields:

$$\sigma_1 + \sigma_2 = C_{11}\varepsilon_1 + C_{12}\varepsilon_2 + C_{13}\varepsilon_3 + C_{12}\varepsilon_1 + C_{11}\varepsilon_2 + C_{13}\varepsilon_3, \tag{3.9}$$

$$\sigma_c = (C_{11} + C_{12})(\varepsilon_1 + \varepsilon_2) + 2C_{13}\varepsilon_3. \tag{3.10}$$

From Eq.(3.7c) and Eq.(3.8b), it follows that:

$$\varepsilon_3 = -C_{13}(\varepsilon_1 + \varepsilon_2)/C_{33}, \tag{3.11}$$

$$\varepsilon_1 + \varepsilon_2 = -(C_{33}/C_{13})\,\varepsilon_3. \tag{3.12}$$

Inserting Eq.(3.12) into Eq.(3.10) yields:

$$\sigma_c = -(C_{11} + C_{12})(C_{33}/C_{13})\varepsilon_3 + 2C_{13}\varepsilon_3, \tag{3.13}$$

$$\sigma_c = [C_{13} - (C_{11} + C_{12})C_{33}/C_{13}]\varepsilon_3. \tag{3.14a}$$

On the other hand, if we define σ_c as $\sigma_c = \sigma_1 = \sigma_2$, then the term in brackets is halved, and:

$$\sigma_c = [C_{13} - (C_{11} + C_{12})C_{33}/2C_{13}]\varepsilon_3. \quad (3.14b)$$

Comparing to Hooke's Law (Eq. 3.3), it is reasonable to call the term in the brackets in Eq. 3.14b as the *film elastic modulus*, E_f. Obviously, this value depends on the measured elastic stiffness constants, $C_{ij.}$ Inserting the stiffness constants (Table 3.4) gives:

$$\left| C_{13} - (C_{11} + C_{12})\, C_{33}/C_{13} \right| = 450 \text{ GPa} \quad (3.15a)$$

and

$$E_f = 450 / 2 = 225 \text{ GPa}. \quad (3.15b)$$

Note that this value is almost twice the elastic modulus given for bulk ZnO in Table 1.3. Then; if σ_c is defined as $\sigma_c = \sigma_1 + \sigma_2$,

$$\sigma_c = -450\ \varepsilon_3\ (\text{GPa}), \quad (3.16a)$$

and if σ_c is defined as $\sigma_c = \sigma_1 = \sigma_2$,

$$\sigma_c = -225\ \varepsilon_3\ (\text{GPa}), \quad (3.16b)$$

By convention, a compressive stress has a negative value. Thus, a negative sign is included in Eq. 3.16.

Table 3.4. Elastic stiffness constants of ZnO [149, 206, 207].

Symbol	Value (GPa)
C_{11}	210
C_{12}	120
C_{13}	105
C_{33}	210

The tensile strain, which is along the normal of the substrate, is:

$$\varepsilon_3 = (c\text{-}c_o)/c_o. \tag{3.17a}$$

Here c_o and c are the axial lattice parameters of the stress-free and stressed ZnO, respectively. In terms of the plane spacing (d), Eq.(3.17) could also be written as:

$$\varepsilon_3 = (d\text{-}d_o)/d_o. \tag{3.18b}$$

Alternatively, the percent strain can be written as:

$$\%\varepsilon_3 = \varepsilon_3 \text{ x}100 = [(c\text{-}c_o)/c_o] \text{ x } 100 = [(d\text{-}d_o)/d_o] \text{ x } 100. \tag{3.19}$$

For each sample, d is calculated from the (002)-peak position, via Eq.(3.2). Table 3.3 lists d_o for stress-free powder standard (JCPDS-No. 36-1451). Then, ε_3 is calculated by Eq.3.18, and σ_c is calculated by inserting that result into Eq.3.16.

Some variations of this equation have been used in literature to calculate the residual stresses in ZnO thin films. First of all, there are different reported values for the elastic stiffness constants of ZnO in literature, which change the value of the stiffness matrix and the film elastic modulus. Some of these values were given in Table 1.3. For example, Lim and Lee [140], and Fang *et al.* [154] used Eq.3.16a, but with a proportionality constant of 453.6 GPa (then, E_f = 226.8 GPa). Hong *et al.* used Eq.3.16b with different stiffness constants [150]. Therefore, their film elastic constant was E_f = 233 GPa. These E_f values used in literature to calculate the residual stresses in ZnO thin films differ from the one that is used in our study in a range from –9.3% to 6,8%. In addition to these, the reference value of the lattice parameter of the unstressed powder ZnO (c_o) varies in different studies.

Another variation in the model arises from the modifications in the film elastic constants due to the constraints and the stresses in the film. Zhenxing *et al.* pointed out that, due to the strong (002) texture and the distortion of the lattice, the elastic constants of single crystal ZnO were not appropriate to use directly for ZnO thin films [208]. They recalculated the stiffness constant, C_{33}, of a textured crystal as:

$$C_{33}' = 0.99C_{33.} \tag{3.20}$$

In addition, the stiffness constants were modified according to the *effective directions*; C_{33} was assumed to be inversely proportional to the fourth power of the lattice constant.

Gupta and Mansingh [151], as well as Water and Chu [95], used the same elastic stiffness constants as those used in this study [149, 206, 207]. However, they took into account the modifications stated by Zhenxing *et al.* [208], and used the following the following term inserted into Eq.3.15 instead of C_{33}:

$$C_{33}'' = 0.99C_{33}/(1-\varepsilon_3)^4. \tag{3.21}$$

Therefore, E_f is also a function of the strain in the z direction. Inserting the value of C_{33} from Table 3.4:

$$E_f = 210 - 3{,}14 \text{ x } C_{33}'' = 210 - 652.806/(1-\varepsilon_3)^4 \text{ (GPa)} \tag{3.22}$$

and

$$\sigma_c' = [210 - 652.806/(1-\varepsilon_3)^4]\ \varepsilon_3 \text{ (GPa)}. \tag{3.23}$$

Inserting the expression for ε_3 (Eq.3.18) and the value for d_o from Table 3.3 into Eq.3.23, σ_c' can be calculated. The results of the theoretical calculations of σ_c and σ_c' for a 2θ range of 0–2.5° are given in Fig. 3.12, and indicate that the correction for σ_c is significant only at high strain values. (For example, for an offset ($\Delta 2\theta$) of 0.1°, $\sigma = 1.27$, and $\sigma_c' = 1.23$ GPa. This corresponds to a difference of 3.2%. For $\Delta 2\theta = 2.5°$, $\sigma = 34.22$ GPa, and $\sigma_c' = 21.09$ GPa. This corresponds to a difference of 38.4%.) Moreover, this correction takes into account only the modification in C_{33}, but not the other stiffness constants. Hence, it is incomplete. For these reasons, in this study, Eq. 3.16 is used to calculate the residual stresses in the ZnO thin films.

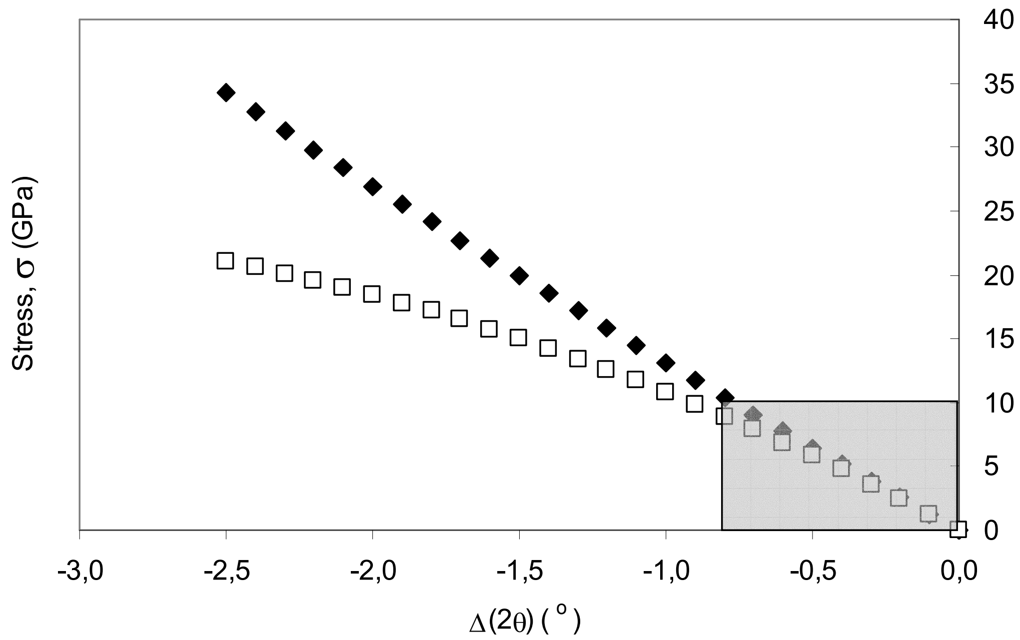

Figure 3.12. Theoretical compressive stress as a function of left-shift of the (002)-peak of the ZnO crystallites, calculated by the biaxial strain model. $\Delta(2\theta) = 2\theta_{sample} - 2\theta_{standard}$. ♦ = σ, = σ'.

In these calculations, care must be taken for the factors that may cause a peak-shift, other than the residual stress in the sample. Instrument misalignment or goniometer offset, and error in sample positioning (height and tilt) may also cause peak shift, and these factors should be minimized [209]. In our study, the instrument was calibrated using a polycrystalline quartz standard and the error in peak shifts occurring from the goniometer offset was within ±0.03°, corresponding to σ = 0.38 GPa. The error from sample positioning was minimized by the method described above in Sec 3.4.2.1. The maximum amount of error originating from sample positioning, *i.e.*, the maximum deviation between two successive measurements of the same sample was observed to be ±0.04° (corresponding to σ = ±0.51 GPa). For most measurements, the error range was smaller. The errors in the corresponding stress values were taken into account in the interpretation of the results, and indicated for each result in Chapter 4.

3.4.2.3. Calculation of the thermal stresses

Consider a rod of length l, whose temperature is reduced from T_0 to T. During cooling, the rod would shrinks with an amount determined by its linear thermal expansion coefficient, α [50]. For a rod-shaped sample with an initial length of l_0 and a final length of l, this elongation is equal to:

$$l - l_0 = \alpha\,(T - T_0)l_0, \tag{3.24}$$

and the associated strain, ε, is:

$$\varepsilon = \alpha\,(T - T_0) = \alpha\Delta T. \tag{3.25}$$

However, if the rod is constrained from both ends, it is under a stress of σ, determined by the Hooke's Law (Eq. 3.3). Then:

$$\sigma = E\alpha\Delta T. \tag{3.26}$$

Likewise, when a film is deposited on a substrate at an elevated temperature, thermal strains are induced both in the film and in the substrate material [50]:

$$\varepsilon_f = \sigma_f\,\Delta T + F\,(1 - \nu_f)\,/\,E_f\,t_f\,w_f, \tag{3.27}$$

$$\varepsilon_s = \sigma_s\,\Delta T + F\,(1 - \nu_s)\,/\,E_s\,t_s\,w_s. \tag{3.28}$$

Here, the subscripts f and s denote the film and the substrate, respectively. F is the thermal mismatch force between the film and the substrate, t is the thickness, and w is the width of the material:

$$\sigma = F/A = F\,/\,(t\,w) \tag{3.29}$$

In the film-substrate system, if all the substrate area is used, $w_f = w_s$. Also, compatibility requires $\varepsilon_f = \varepsilon_s$. Thus, the thermal mismatch force is [50]:

$$F = \frac{w(\alpha_s - \alpha_f)\Delta T}{((1-\nu_f)/t_f E_f) + ((1-\nu_s)/t_s E_s)}. \tag{3.30}$$

If the substrate is of relatively infinite thickness with respect to the film, then $t_s E_s /(1-\nu_s) >> t_s E_s /(1-\nu_s)$, and:

$$F \cong \frac{w(\alpha_s - \alpha_f)\Delta T}{(1-\nu_f)/t_f E_f} = \frac{w t_f (\alpha_s - \alpha_f)\Delta T E_f}{(1-\nu_f)}. \tag{3.31}$$

Since the thermal stress in the film is the thermal mismatch force divided by the films cross-sectional area (wt_f), it is equal to [50, 156]:

$$\sigma_{th} = - (\alpha_s - \alpha_f)\Delta T\, E_f / (1 - \nu_f). \tag{3.32}$$

According to this relation, a film on a substrate cooled from T_0 to T will be residually compressed if $\alpha_s > \alpha_f$, where the substrate tends to shrink more than the film. If the adhesion between the film and the substrate is maintained, the two are forced to shrink by equal amounts. In that case, the film experiences a compressive stress, and the substrate will experience a tensile stress along its plane. In the opposite case, when $\alpha_s < \alpha_f$, the film tends to shrink more than the substrate, and it is under residual tensile stress along the film plane. By convention, in the literature, a compressive stress value is negative. Thus, a minus sign is included in Eq.3.32 in front of the (α_s - α_f) term.

In Eq.3.32, there are four constants: the thermal expansion coefficients of the film and the substrate, the film elastic modulus, and the film's Poisson's ratio. For consistency, instead of using the E_f value for bulk ZnO directly, the film elastic constant (Eq.3.15) was used to calculate σ_{th}. For a hexagonal crystal, with isotropic approximation, the Poisson's ratio is given in terms of the stiffness constants as [13]:

$$\nu = C_{13} / (C_{11}+C_{13}). \tag{3.33}$$

Inserting the C_{ij} values from Table 3.4, $\nu_{ZnO} = 0.318$.

The in-plane thermal expansion coefficients (TEC; α) for several substrates were measured in the direction parallel to the substrate plane by a dilatometer (Netzsch Gerätebau GmbH–DIL 409PC, Selb, Germany) (Fig. 3.13). For sample preparation, three pieces of each sample was cut into rectangular shapes and attached to each other with double-sided adhesive carbon tape. Because all the pieces were cut randomly, there was no preferred measurement direction in the substrate plane for the mica substrates: that result should be considered as the average planar TEC of mica. For Si (cubic), the measured TEC is in the [100]-direction. The three-layer laminate was placed in a steel mold and the two tips were polished to have two edges perfectly parallel to each other. The laminate was further anchored with aluminum wire wrapped around it (Fig. 3.14). The temperature range was 20–300 °C and the heating rate was 2 K/min. A calibration standard of polycrystalline alumina was used (Al_2O_3, sapphire, NBS SRM 732, DIN 51045). A baseline correction for the equipment expansion under the same parameters as the sample measurement was constructed prior to the sample measurement:

$$\Delta l_{\text{system}} = \Delta l_{\text{standard table}} - \Delta l_{\text{standard measured}}, \tag{3.34}$$

$$\Delta l_{\text{sample}} = \Delta l_{\text{sample measured}} + \Delta l_{\text{system}}, \tag{3.35}$$

where:

Δl_{system} = correction curve for the expansion of the measuring system,

$\Delta l_{\text{standard table}}$ = tabulated reference values for the expansion of the standard,

$\Delta l_{\text{standard measured}}$ = measured, uncorrected expansion of the standard,

Δl_{sample} = true expansion of the specimen under investigation,

$\Delta l_{\text{sample measured}}$ = measured, uncorrected expansion of the specimen.

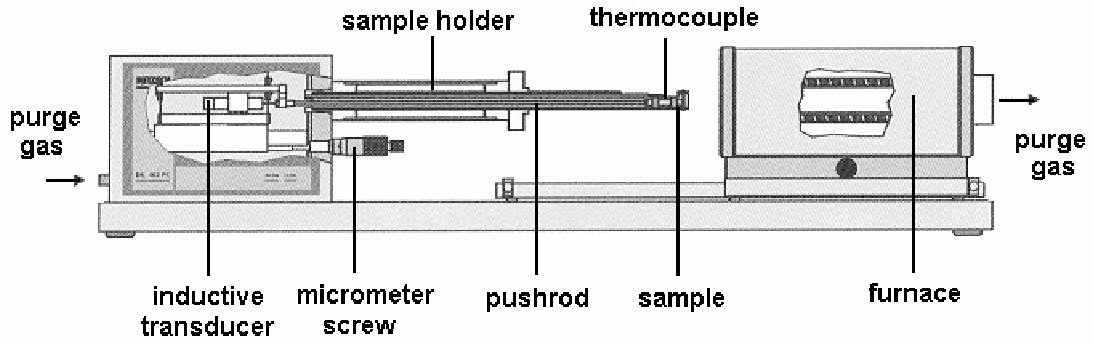

Figure 3.13. Configuration of the dilatometer system. The sample is placed into the holder inside the furnace. As the sample expands, it pushes the pushrod and the effect is transferred onto the inductive transducer. The pressure signal is converted to a strain value based on the instrument calibration and monitored by the software.

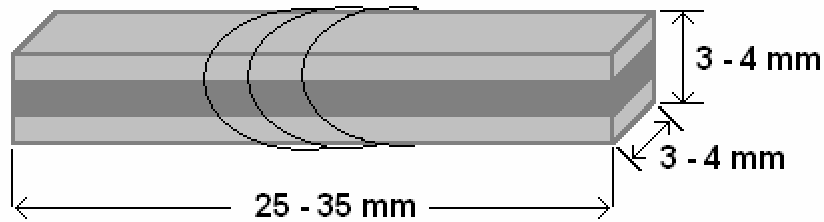

Figure 3.14. The configuration of the substrate laminate sample. The three layers were attached to each other with double-sided adhesive carbon tapes and an aluminum wire.

Then, the mean coefficient of thermal expansion (α_m) within the T_1–T_2 temperature range is:

$$\alpha_m = \frac{1}{L_0}\frac{l_{T_1} - l_{T_2}}{T_1 - T_2} = \frac{1}{L_0}\frac{\Delta l}{\Delta T}, \tag{3.36}$$

where:

l_o = specimen length at room temperature,

$l(T_2)$, $l(T_1)$ = specimen length at temperatures T_2, T_1,

Δl = change of specimen length between temperatures T_2, T_1.

The sample length at room temperature was measured with a caliper of 0.01 mm resolution. For comparison, the same measurement was repeated for compact polycrystalline ZnO powder (Merck, Darmstadt, Germany).

3.4.2.4. Calculation of grain size

For some samples, the grain size was calculated by Scherrer's formula [209]:

$$t = (0.9\, \lambda) / (FWHM \cos\theta), \quad (3.37)$$

where t is the crystallite size (in nm), λ is the x-ray wavelength (in nm), *FWHM* (or *B*; breadth) is the 2θ at the full width at half maximum of the XRD peak (in radians), and θ is the Bragg angle (in radians).

The grain size calculated from XRD-*FWHM* is in the direction normal to the film plane, and this value is indicated as GS_{XRD} later in the text. The grain size was also measured along the lateral direction with respect to the film surface by SEM, and this value is indicated as GS_{SEM} in the text. The column widths and heights were also measured by SEM, and the results are presented accordingly.

CHAPTER 4

RESULTS

In this chapter, the results of the experimental work on ZnO thin film production and characterization are presented. The results are grouped under five sub-headings: *i)* the general structure of the as-deposited films, *ii)* residual stresses, *iii)* effects of deposition parameters on microstructure and texture, *iv)* effects of the buffer layer on stress, structure and texture, and *v)* stress relaxation by annealing or aging.

4.1. General Structure of the As-deposited ZnO Thin Films

RF magnetron-sputtered ZnO films grew in a carpet-like morphology on various types of substrates (Fig. 4.1). The films had a uniform thickness (*h*) of 200–500 nm range throughout the substrate. The films had *columnar* grains that were aligned with their axial direction perpendicular to the substrate surface. An example of the variation of grain size (*GS*) or column width (*w*), through the film thickness can be seen in Fig. 4.1. For the glass substrate, some *equiaxed* grains could be seen at the film-substrate interface with a grain size of 10–40 nm. Columnar growth dominated as the film grew in thickness, with the column thickness varying between 25–55 nm at the top of the film. The variation of the grain size or column thickness was not very pronounced for the films grown at the same conditions on the Si(100) substrates (Fig. 4.2). The columns in those samples had a uniform thickness of about 46 nm. Other changes in the microstructure of the films depending on the deposition conditions are presented in Sec. 4.3.

XRD measurements revealed that these films had a highly *c*-axis oriented hexagonal lattice, giving a single diffraction peak from the (002) plane (Fig. 4.3). In thicker films, the reflection from the (004) plane could also be observed, which is parallel to the (002) plane. In some special cases, the reflection from the (101) plane was also observed. (The details will be discussed in the forthcoming sections.)

The elemental analysis by EDX showed that there was no detectable argon inside the film (Fig. 4. 4) (the K_{α_1} emission of Ar is at 2.958 keV). The Si, Na, Al, and K peaks originate from the glass substrate.

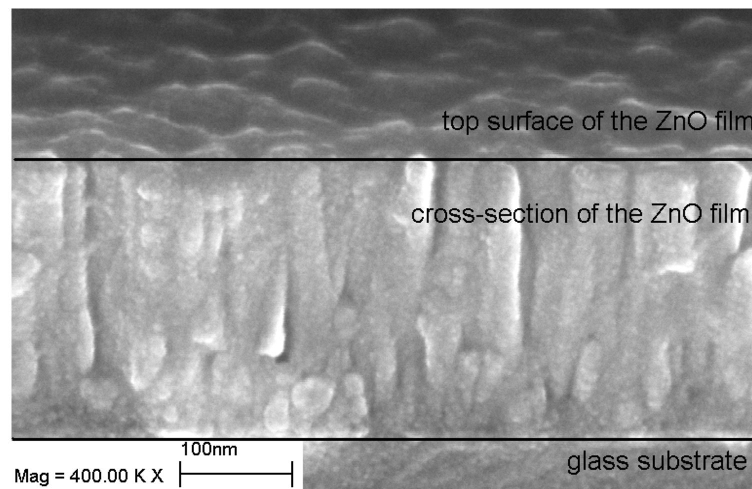

(a)

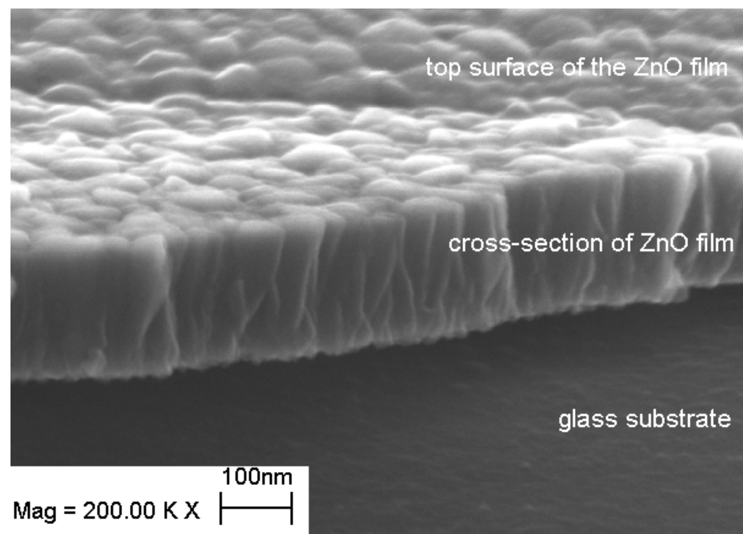

(b)

Figure 4.1. The columnar structure of a ZnO film sample on a glass substrate: (a) T_s = RT (Set 17 in Table 3.1; $h \approx 458$ nm, $w_{bottom} \approx 10$–40 nm, $w_{top} \approx 25$–55 nm), (b) $T_s = 200$ °C (Set 16 in Table 3.1; $h \approx 200$ nm, $w_{bottom} \approx 4$–10 nm, $w_{top} \approx 40$–93 nm).

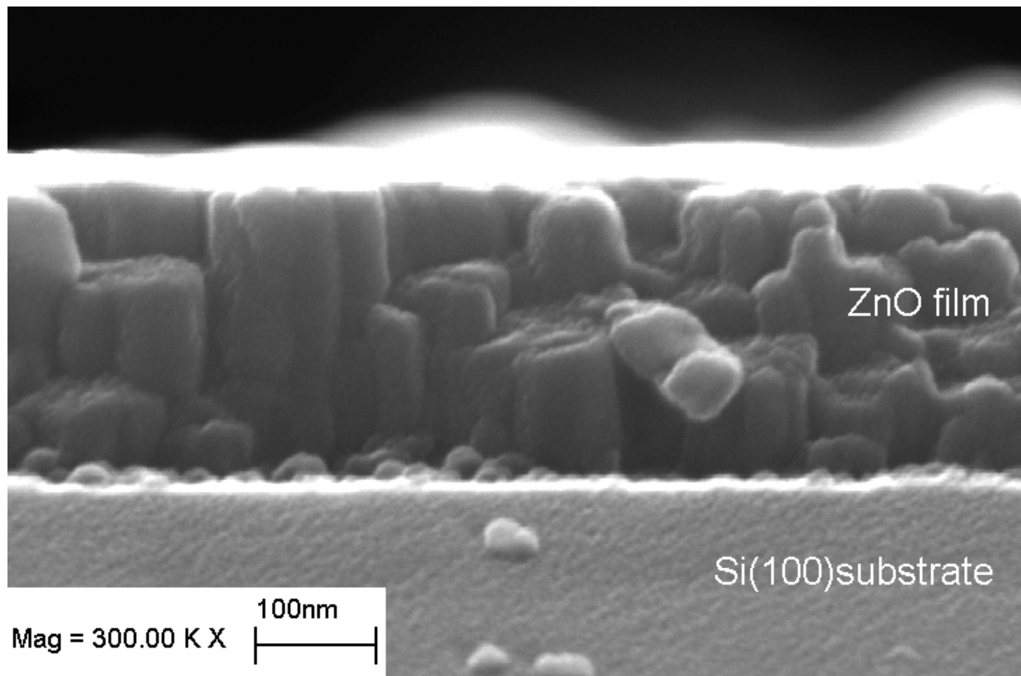

(a)

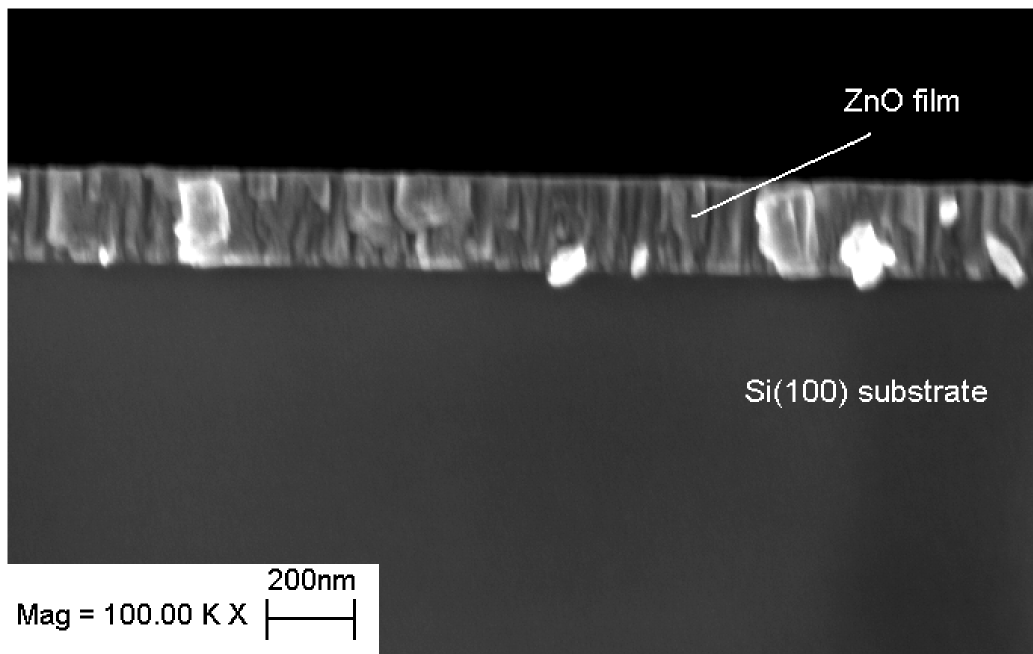

(b)

Figure 4.2. The columnar structure of a ZnO film sample on a Si(100) substrate: (a) T_s = RT (Set 17 in Table 3.1; $h \approx 237$ nm, $w \approx 79$ nm), (b) T_s = 200 °C (Set 16 in Table 3.1; $h \approx 246$ nm, $w \approx 46$ nm).

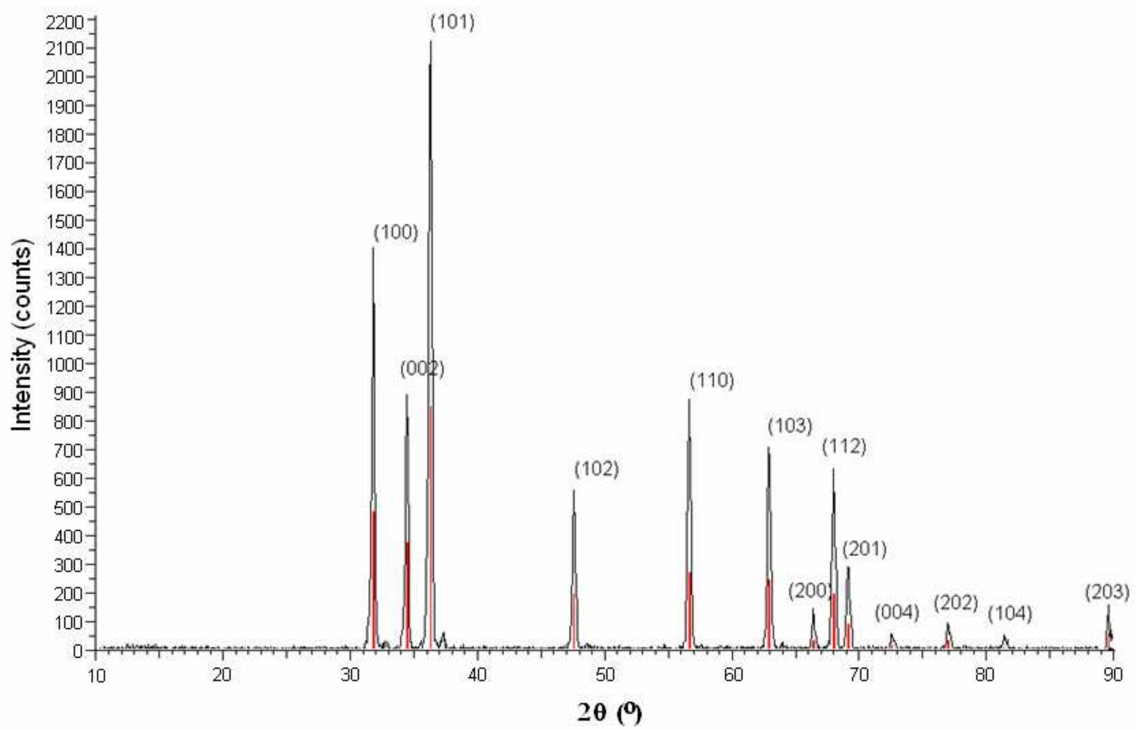

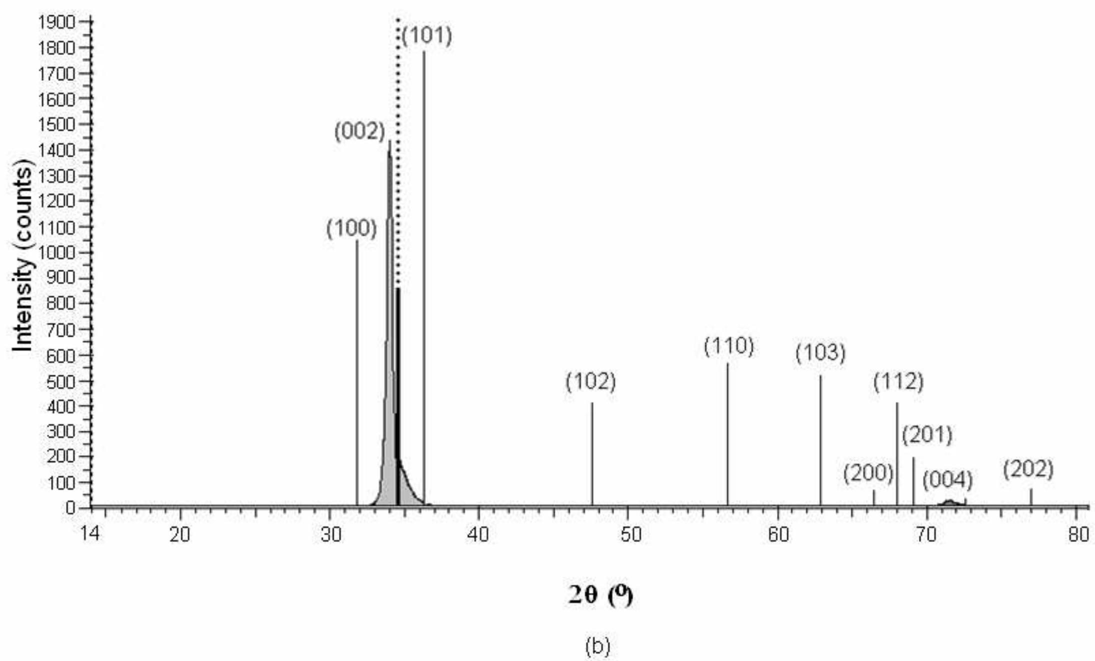

Figure 4.3. XRD analysis of (a) commercial ZnO powder, and (b) a representative example of a ZnO film grown on glass at RT (Set 17 in Table 3.1). The vertical bars represent the peak positions of a stress-free reference powder (JCPDS-No. 36-1451). The ZnO thin film possesses only the (002)-peak, and its multiple, the (004)-peak.

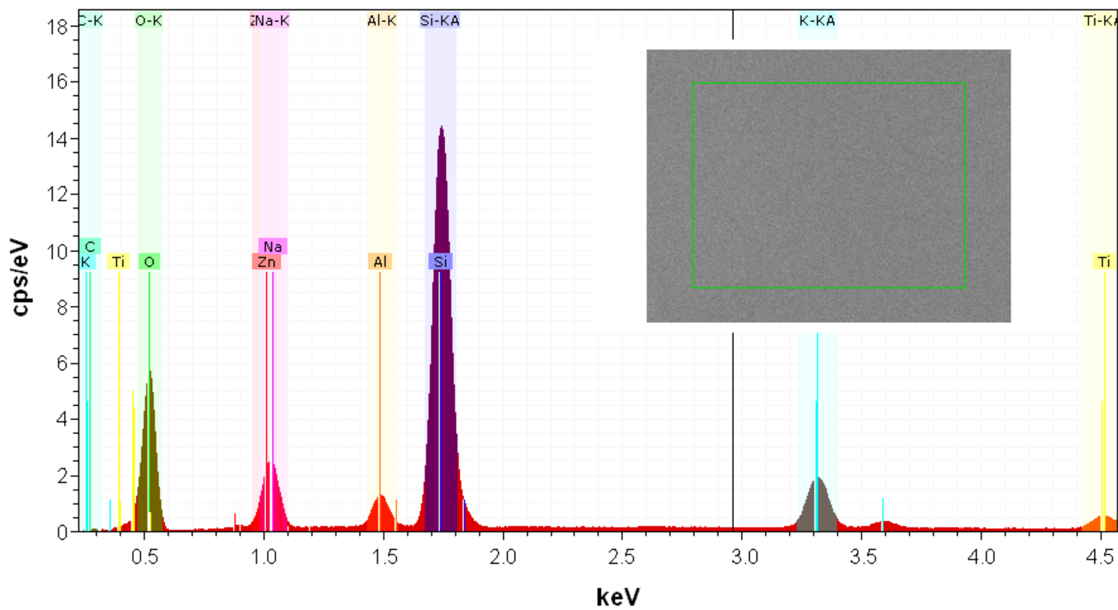

Figure 4.4. EDX profile of a ZnO film sample on glass substrate, deposited at T_s = 200 °C (Set 16 in Table 3.1). The accelerating voltage was 20 keV, and the count rate was 3.1 kcps. The graph shows a close-view between 0 and 4.5 keV. Insert is the SEM image of the scanned film portion (13x9 μm^2). No argon peak could be detected at these conditions (K_{α_1}(Ar) = 2.958 keV). The signals other than those of oxygen and zinc arise from the glass substrate.

4.2. Residual Stresses in ZnO Thin Films

In this section, the effects of substrate material, substrate temperature, chamber pressure, and RF power on the residual stresses of the as-deposited ZnO films are presented. In addition, the contribution of the thermal mismatch force between the film and the substrate to the total residual stress is elaborated.

4.2.1. Substrate Effects on the Residual Stress

All the ZnO films grew with residual stresses, the value of which determined by the substrate type and the deposition conditions. It was seen that the ZnO thin film-glass substrate (alcohol-cleaned microscope cover slides; see Sec. 3.1.) laminate was warped after deposition (Fig. 4.5). In those samples, the ZnO film thickness was about 400 nm,

and the substrate thickness was about 160 μm. The residual compressive stress after the film deposition was -5.47 GPa in that sample. Warping in the other substrates could not be seen by naked eye, and no bending measurements (see Sec. 1.3.2, 1.5, and 5.2 for examples of bending measurements) were performed on those samples to measure the stress. (The thickness of the mica and the Si(100) substrates were about 230 and 508 μm, respectively.) Instead, the residual stresses were calculated by the XRD method described in Sec. 3.4.2.

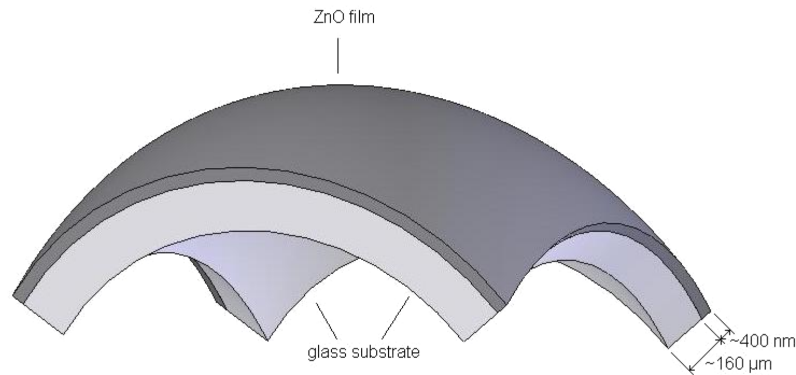

Figure 4.5. Warping of ZnO-glass system after deposition (not to scale; Set 17 in Table 3.1). The film thickness is ~400 nm, and the substrate is ~160 μm-thick. σ_c = -5.46 GPa.

In the XRD analysis, the (002)-peaks of all the films appeared at lower 2θ values than that of the stress-free powder specimen, regardless of substrate type (Fig. 4.6). These peak shifts indicated an increase in the axial lattice parameter (c) of the hexagonal unit cell of the films in comparison to the strain-stress free powder ZnO unit cell, as described in Sec 3.4.2. Based on this increase, the percent strain in the direction normal to the film plane ($\%\varepsilon_Z$) was calculated for each sample. The peak widths at half-maximum intensity (*FWHM*) were measured, and the grain sizes (GS_{XRD}) were calculated by Eq. 3.37. Stretching along the axial direction was associated with a contraction in the basal plane, giving rise to a planar compressive stress component (σ_{c_1}). The residual stress, σ_{c_1}, was calculated by Eq. 3.16.b. It was also calculated with Eq. 3.16a (σ_{c_2}), to enable comparison with some of the literature. Eq. 3.16.a gave half of the value of σ_{c_1}. From this point onward in the text, σ_{c_1} will be assumed as the total amount of residual stress, and it will be designated as σ_c. The results for $\%\varepsilon_Z$, *FWHM*, GS_{XRD}, and σ_c are given in Table 4.1. For a substrate temperature of 200 °C, the (002)-peak of the film deposited on Si(100) wafer was significantly asymmetric and broad (*FWHM* = 0.928°). That sample also had the highest amount of residual compressive

stress (σ_c = -6.69 GPa). Moreover, at that temperature, the films with the narrowest and the most symmetric (002)-peak were those deposited on glass microscope slides (*FWHM* = 0.347°, σ_c = -5.46 GPa), while the films with the least amount of residual stress were those deposited on mica substrates (*FWHM* = 0.433°, σ_c = -3.54 GPa).

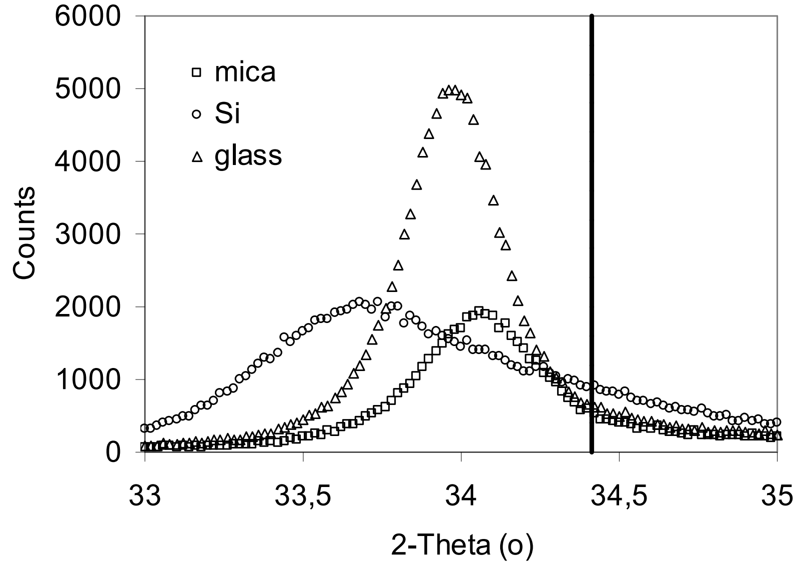

Figure 4.6. Position of the (002)-peak in as-deposited ZnO films depending on the substrate type. The initial substrate temperature was 200 °C (Set 16 in Table 3.1).

Table 4.1. Variation of lattice parameter (c), XRD peak width at half-intensity (*FWHM*), percent tensile strain ($\%\varepsilon_Z$), grain size (GS_{XRD}), and total compressive stress (σ_c) of as-deposited (0) ZnO films on glass (G), mica (M), and Si(100) (S) substrates for an initial substrate temperature of 200 °C (Set 16). The XRD data belongs to the (002)-peak. The reference lattice constant for the unstressed ZnO (c_o) is taken from JCPDS - No. 36-1451. The error range in σ_c is ±0.26 GPa, due to equipment offset.

Substrate	c_o (Å)	c (Å)	*FWHM* (2θ °)	$\%\varepsilon_Z$* (%)	GS_{XRD}** (nm)	σ_{c_1}*** (GPa)	σ_{c_2}**** (GPa)
G0	5.20664	5.26980	0.347	1.21	23.94	-5.46	-2.73
M0		5.24752	0.433	0.79	19.20	-3.54	-1.77
S0		5.28402	0.928	1.49	8.95	-6.69	-3.35

* Calculated from Eq.3.19.
** Calculated from Eq.3.37.
*** Calculated from Eq. 3.16a.
**** Calculated from Eq. 3.16b.

4.2.2. Contribution of Thermal Mismatch Strain on the Residual Stress

As described before, there are several factors contributing to the total amount of residual stress in the thin film samples. Mismatch in the thermal expansion coefficient value of the substrate and the film material is one of them. For high-temperature depositions, the film and the substrate expand by the same amount to maintain stress and strain continuity. However, when cooling down, they shrink by different amounts, depending on their own TEC value, resulting in thermal residual stresses and bending of the composite. In order to elucidate the portion of thermal stress among the total amount of stress, the TEC values for three different substrate materials were measured, and the results are given in Table 4.2 and Fig. 4.7. The TEC values were compared to those of the stress-free polycrystalline ZnO powder. Depending on those TEC values, the thermal stresses were calculated as described in the previous chapter. The results are given in Table 4.3 as σ_{th} and plotted in Fig. 4.8. The calculated σ_{th} values were 5.4–11.1% of the total stress, depending on the sample. The percent contribution of σ_{th} to σ_c is given in Table 4.3. The remaining amount of stress was named as the *intrinsic stress*, σ_{int} (see Sec. 1.2.3). It should be noted that, since the TEC of Si is lower than that of ZnO, σ_{th} of ZnO on Si had a positive value (*i.e., tensile* stress on the film plane). Thus, σ_{int} was higher than σ_c, and the $\%\sigma_{th}$ for ZnO on Si was calculated over the *absolute* values of stress.

Table 4.2. TEC values (α) measured by dilatometry the substrates along the planar direction of the substrate, as described in Section 3.4.2.3. The same measurement was repeated for the ZnO powder (Merck, Darmstadt, Germany).

Material	**α x10^{-6} (ΔC^{-1})**	
	at 50 °C	**at 200 °C**
ZnO	5.8	7.4
Glass	7.4	9.9
Mica	7.0	10.7
Si(100)	2.5	4.1

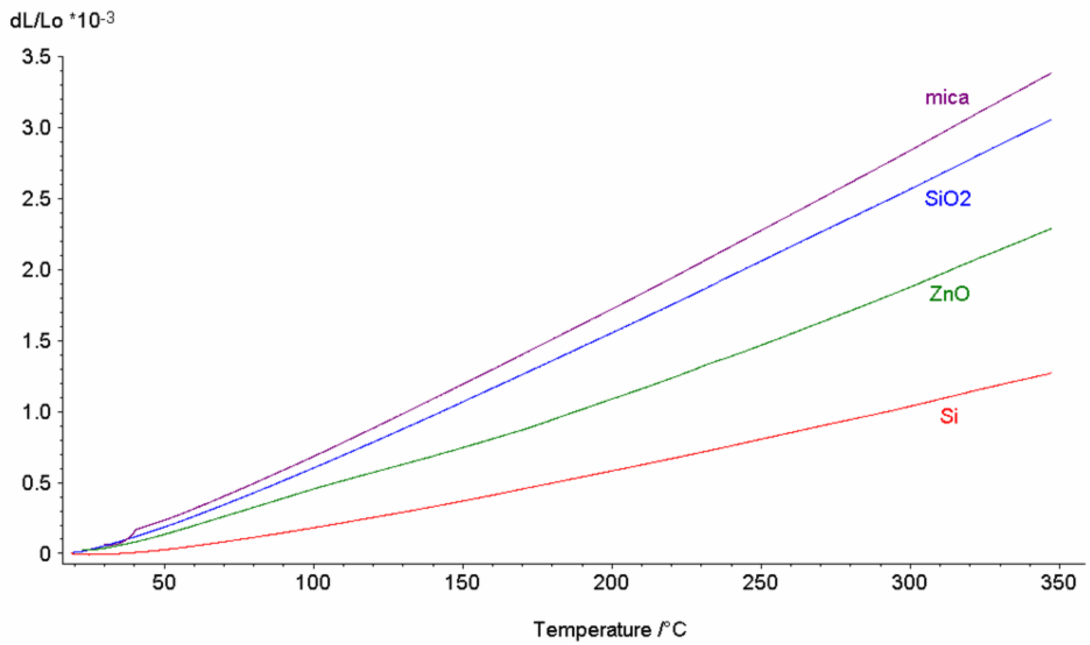

(a)

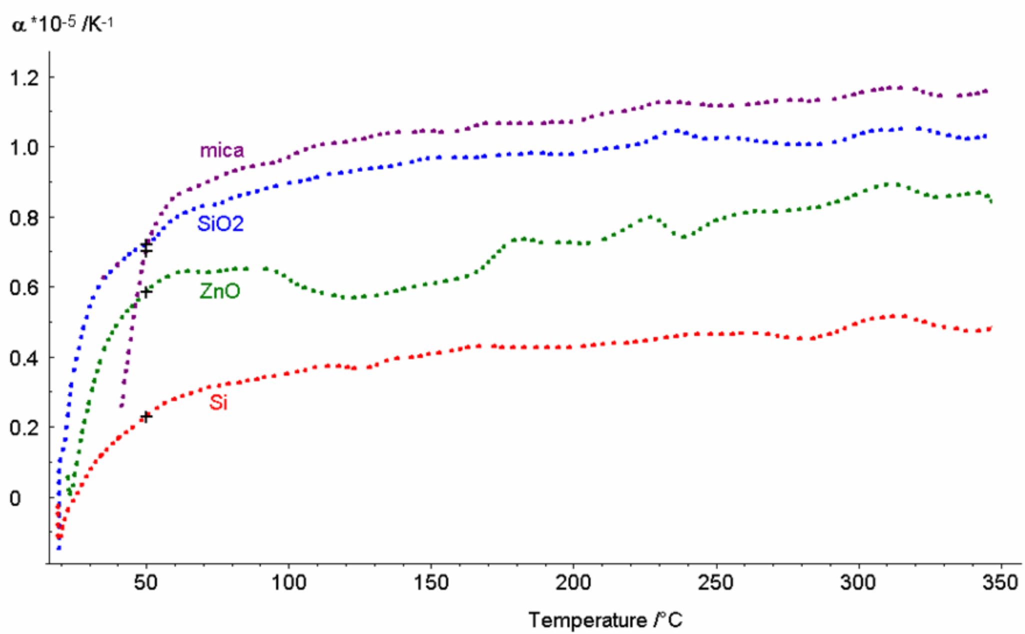

(b)

Figure 4.7. (a) Strain (dL/L_o) and (b) TEC values (α) for ZnO, mica, silica glass, and Si(100), in the temperature range of 20–350 °C in the substrate plane direction. Details on the measurement method were presented in Section 3.4.2.3.

Table 4.3. Comparison of the total (σ_c), thermal (σ_{th}), and the remaining intrinsic stress (σ_{int}) of as-deposited (0) ZnO films on glass (G), mica (M), and Si(100) (S) substrates, deposited at an initial substrate temperature of 200 °C (Set 16). The XRD data belongs to the (002)-peak. σ_c is calculated by Eq. 3.16a, and σ_{th} is calculated from Eq.3.32. σ_{int} the difference between σ_c and σ_{th}. The error range in σ_c due to equipment offset is ±0.26 GPa.

T_o (°C)	T_o (°C)	ΔT (Δ°C)	Sample	σ_c* (GPa)	σ_{th}** (GPa)	σ_{int}*** (GPa)	$\%\sigma_{th}$
			G0	-5.46	-0.296	-5.17	5.42
200	20	180	M0	-3.54	-0.393	-3.14	11.1
			S0	-6.69	0.388	-7.08	5.80

* Calculated from Eq. 3.16a.
** Calculated from Eq. 3.32.
*** $\sigma_{int} = \sigma_c - \sigma_{th}$.

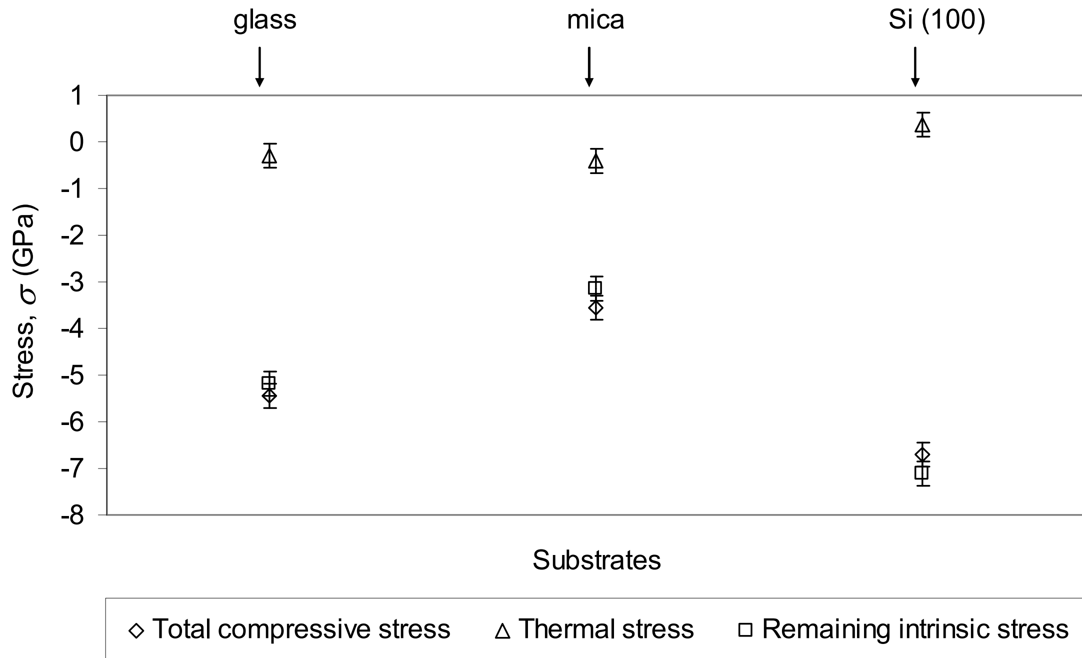

Figure 4.8. Total (σ_c) vs. thermal stress (σ_{th}) as a function of the substrate material for T_s = 200 °C, p = 0.02 mbar, P_{RF} = 100 W (Set 16 in Table 3.1). Thermal stresses were due to the mismatch between the TEC of ZnO and the substrates. The remaining amount of stress among the total is called the *intrinsic stress* (σ_{int}).

4.2.3. Effects of the Deposition Parameters on Residual Stresses

As discussed in Chapter 1, the deposition conditions significantly affect the residual stresses in thin films. To elucidate these effects, the deposition parameters were systematically varied, and the resulting stresses were compared. Table 4.4 and Fig. 4.9 give the stress results including all the control sets, to allow a general comparison of the films on glass substrates.

These results could be grouped separately for the variables T_s, p, and P_{RF}:

i) The effect of chamber pressure (p) at constant substrate temperature (T_s) and RF power (P_{RF}), for three different pairs of T_s and P_{RF} is presented in Table 4.5 and Fig. 4.10. It can be seen that, for all the pairs, increasing P led to higher residual compressive stress. Among these results, the minimum value (σ_c = -1.89 GPa) was obtained at T_s = 200 °C, P_{RF} = 100 W, and p = 0.2 mbar. The maximum residual stress value (σ_c = -7.59 GPa) was at T_s = RT, P_{RF} = 125 W, and p = 0.4 mbar (see Sec. 3.2 for the indication of room temperature for T_s and the use of label RT).

ii) The effect of T_s at constant p and P_{RF}, for three different pairs of p and P_{RF} is presented in Table 4.6 and Fig. 4.11. It can be seen that, for all the pairs, increasing T_s led to lower residual compressive stress. Among these results, the minimum value (σ_c = -3.32 GPa) was obtained at T_s = 200 °C, P_{RF} = 125 W, and p = 0.2 mbar. The maximum residual stress value (σ_c = -7.59 GPa) was at T_s = RT, P_{RF} = 125 W, and p = 0.4 mbar.

iii) The effect of P_{RF} at constant T_s and p, for three different pairs of T_s and p is presented in Table 4.7 and Fig. 4.12. It can be seen that, for all the pairs, increasing P_{RF} led to higher residual compressive stress. Among these results, the minimum value (σ_c = -1.89 GPa) was obtained at T_s = 200 °C, P_{RF} = 100 W, and p = 0.2 mbar. The maximum residual stress value (σ_c = -7.59 GPa) was at T_s = RT, P_{RF} = 125 W, and p = 0.4 mbar.

Table 4.4. Variation of residual stress in the (002) plane depending on the deposition conditions for ZnO films on glass substrate. See Table 3.1 for sample labels. For ease of comparison, the compressive stresses were listed in decreasing order. $\sigma_{c,ave}$ was calculated from Eq. 3.16a with the data from the (002) XRD peak for each sample. The error range is ±0.55 GPa.

Sample	T_s (°C)	P_{RF} (W)	p (mbar)	$\sigma_{c,ave}$ (GPa)
Set4	RT	125	0.4	-7.59
Set3	RT	100	0.4	-6.78
Set5	200	125	0.4	-5.39
Set2	200	100	0.4	-4.25
Set7	RT	125	0.2	-3.83
Set8	200	125	0.2	-3.32
Set6§	200	125	0.2	-2.88
Set9	200	125	0.02	-2.68
Set11*	200	125	0.2	-2.23
Set10**	200	100	0.2	-1.89

§ No substrate cleaning.
* 30 min annealing at 200 °C in O_2:Ar (2:5 v/v) in the chamber.
** 30 min annealing at 200 °C under vacuum in the chamber.

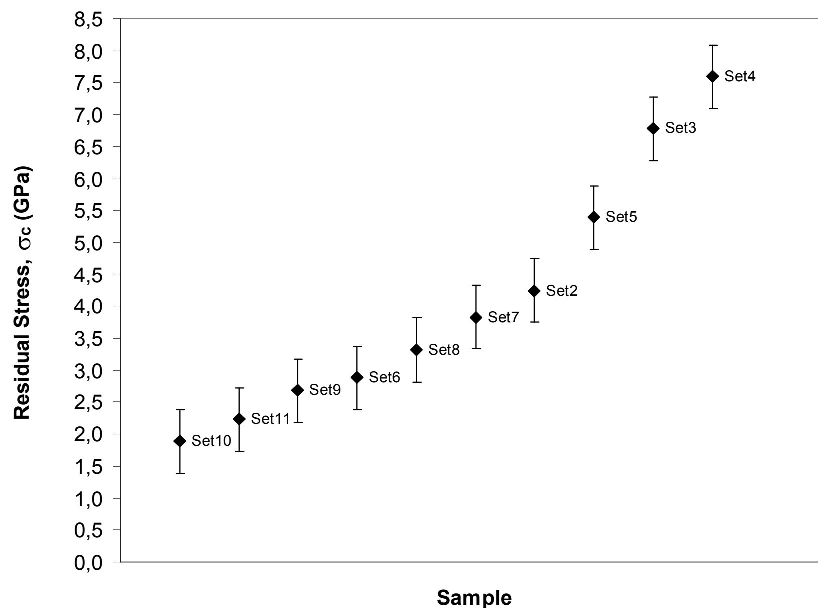

Figure 4.9. Variation of residual planar compressive stress (σ_c) in the (002) plane, depending on the deposition conditions for ZnO films on glass substrate (Set 2–Set 11 in Table 3.1). By convention, a compressive residual stress has a negative value. In the figure, the absolute value of σ_c is given for ease of comparison. See Fig. 4.10–4.12 for the separate effects of the deposition parameters on σ_c.

Table 4.5. Effect of chamber pressure (p) on the residual compressive stress at constant substrate temperature (T_s) and RF power (P_{RF}), for three different pairs of T_s and P_{RF} on glass substrate. $\sigma_{c,ave}$ was calculated from Eq. 3.16a with the data from the (002) XRD peak for each sample. The error range is ±0.55 GPa.

Sample	**p (mbar)**	**$\sigma_{c,ave}$ (GPa)**		
		T_s = 200 C, P_{RF} = 100 W	**T_s = 200 °C, P_{RF} = 125 W**	**T_s = RT, P_{RF} = 125 W**
Set10*	0.2	-1.89		
Set2	0.4	-4.25		
Set9	0.02		-2.68	
Set8	0.2		-3.32	
Set5	0.4		-5.39	
Set7	0.2			-3.83
Set4	0.4			-7.59

* 30 min annealing at 200 °C under vacuum in the chamber.

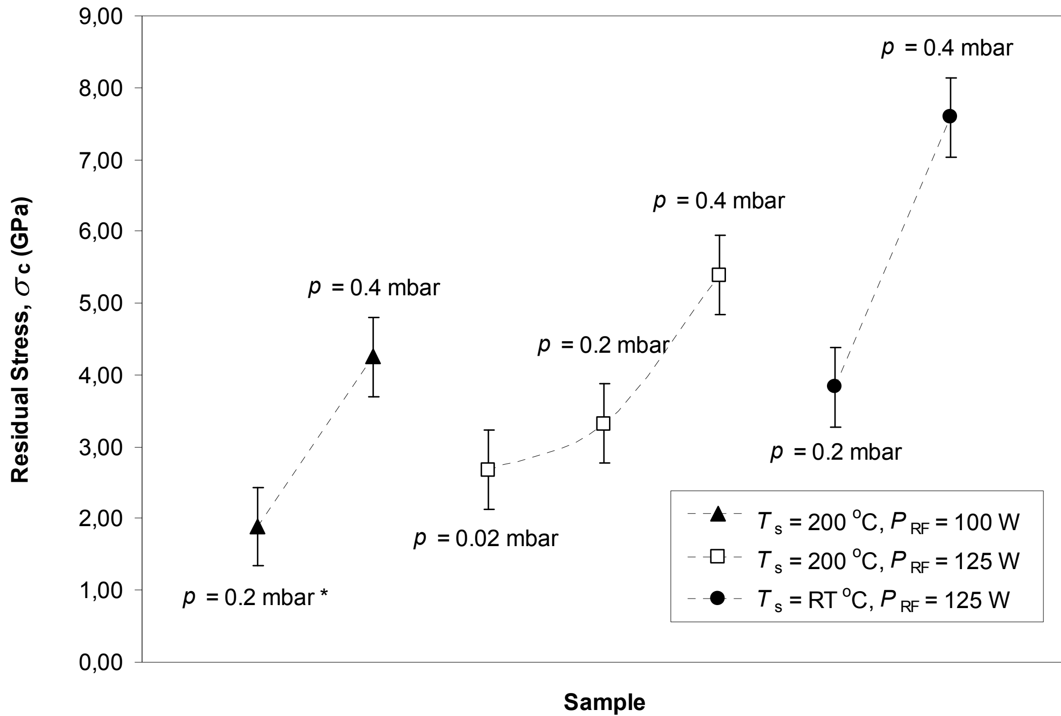

Figure 4.10. Effect of chamber pressure (p) on the residual compressive stress (σ_c) at constant substrate temperature (T_s) and RF power (P_{RF}), for three different pairs of T_s and P_{RF}. By convention, a compressive residual stress has a negative value. In the figure, the absolute value of σ_c is given for ease of comparison. (Refer to Table 4.5 for sample labels.) (*:30 min annealing at 200 °C under vacuum in the chamber.)

Table 4.6. Effect of substrate temperature (T_S) on the residual compressive stress at constant chamber pressure (p) and RF power (P_{RF}), for three different pairs of p and P_{RF}. $\sigma_{c,ave}$ was calculated from Eq. 3.16a with the data from the (002) XRD peak for each sample. The error range is ±0.55 GPa.

Sample	T_s (°C)	$\sigma_{c,ave}$ (GPa)		
		p = 0.2 mbar P_{RF} = 125 W	p = 0.4 mbar P_{RF} = 125 W	p = 0.4 mbar P_{RF} = 100 W
Set6	200	-2.88		
Set7	RT	-3.83		
Set5	200		-5.39	
Set4	RT		-7.59	
Set2	200			-4.25
Set3	RT			-6.78

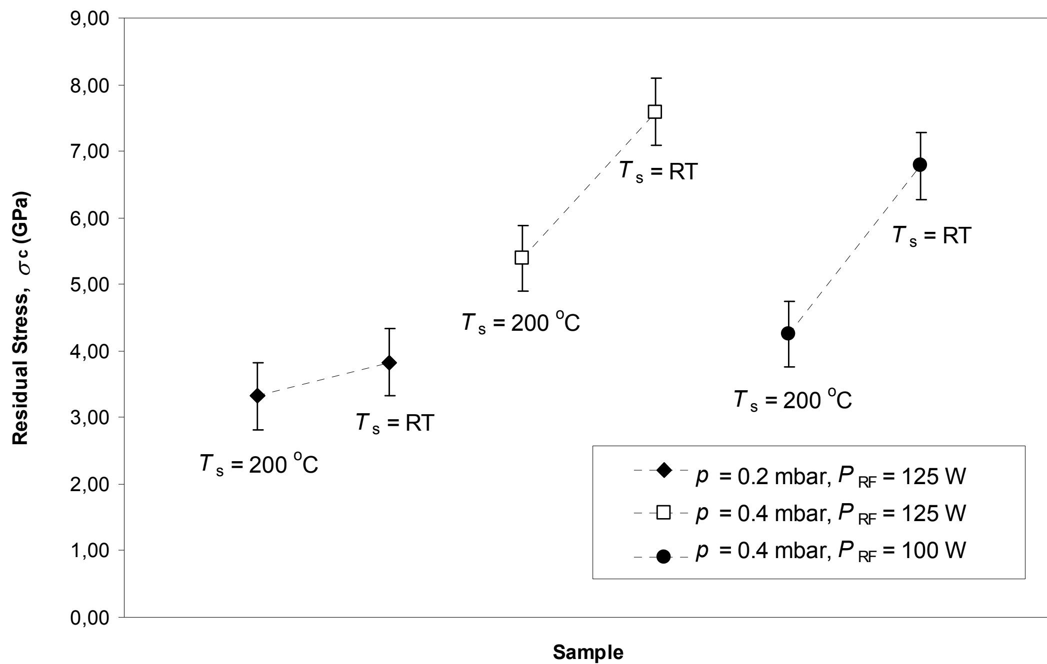

Figure 4.11. Effect of substrate temperature (T_s) on the residual compressive stress (σ_c), at constant chamber pressure (p) and RF power (P_{RF}), for three different pairs of p and P_{RF}. By convention, a compressive residual stress has a negative value. In the figure, the absolute value of σ_c is given for ease of comparison. (Refer to Table 4.6 for sample labels.)

Table 4.7. Effect of RF power (P_{RF}) on the residual compressive stress at constant substrate temperature (T_s) and chamber pressure (p), for three different pairs of T_s and p. $\sigma_{c,ave}$ was calculated from Eq. 3.16a with the data from the (002) XRD peak for each sample. The error range is ±0.55 GPa.

Sample	**P_{RF} (W)**	**$\sigma_{c,ave}$ (GPa)**		
		T_s = 200 °C, p = 0.2 mbar	**T_s = 200 °C, p = 0.4 mbar**	**T_s = RT, p = 0.4 mbar**
Set10*	100	-1.89		
Set8	125	-3.32		
Set2	100		-4.25	
Set5	125		-5.39	
Set3	100			-6.78
Set4	125			-7.59

* 30 min annealing at 200 °C under vacuum in the chamber.

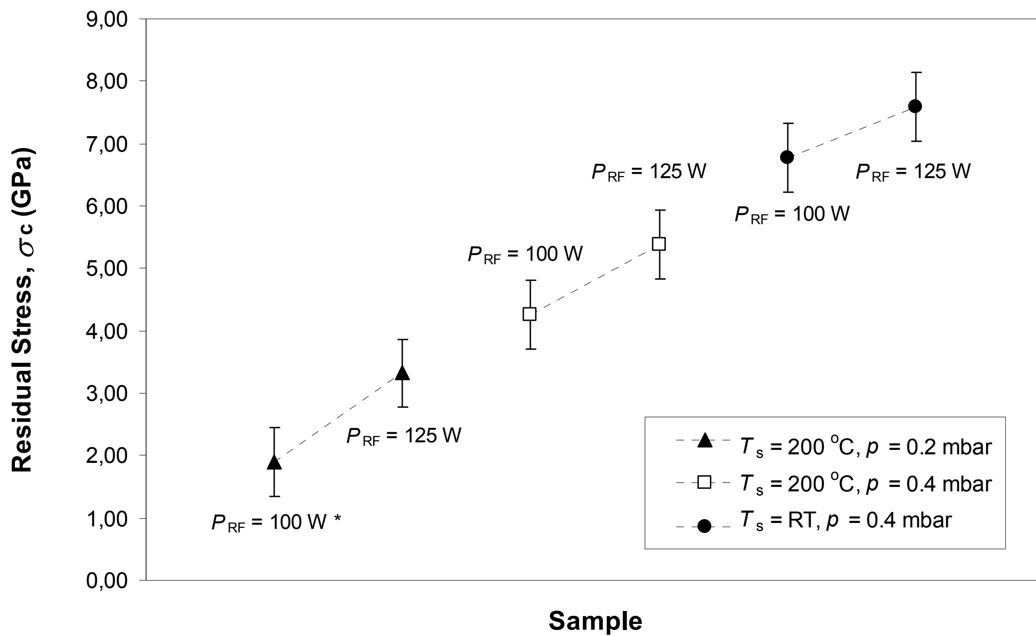

Figure 4.12. Effect of RF power (P_{RF}) on the residual compressive stress (σ_c), at constant substrate temperature (T_s) and chamber pressure (p), for three different pairs of T_s and p. By convention, a compressive residual stress has a negative value. In the figure, the absolute value of σ_c is given for ease of comparison. (Refer to Table 4.7 for sample labels.) (*:30 min annealing at 200 °C under vacuum in the chamber.)

4.3. Effects of the Deposition Parameters on the Film Microstructure

Changes in the microstructure were observed in the films depending on the deposition parameters (Fig. 4.13–4.17). In Fig. 4.13, ZnO films with different microstructures are presented in decreasing order of σ_c. At low T_s (RT) and low p (0.2 mbar), the films had *cylindrical* or *hexagonal-prismatic* columnar grains with hexagonal cross-sections, with some inter-columnar voids (Fig. 4.14). When the pressure was increased to 0.4 mbar and RF power was decreased to 100 W, the column width and the grain size (GS_{SEM}) at the surface increased (Fig. 4.15). Again at low p (0.2 mbar) and high P_{RF} (125 W), when the substrate temperature was increased from room temperature to 200 °C, the grain shape changed from cylindrical continuous columns to *distorted hexagonal* or *diamond-shaped* grains with smaller, *equiaxed* grains between them (Fig. 4.16 and 4.17). These latter type of films had the least amount of residual compressive stress, when compared to the other structure types.

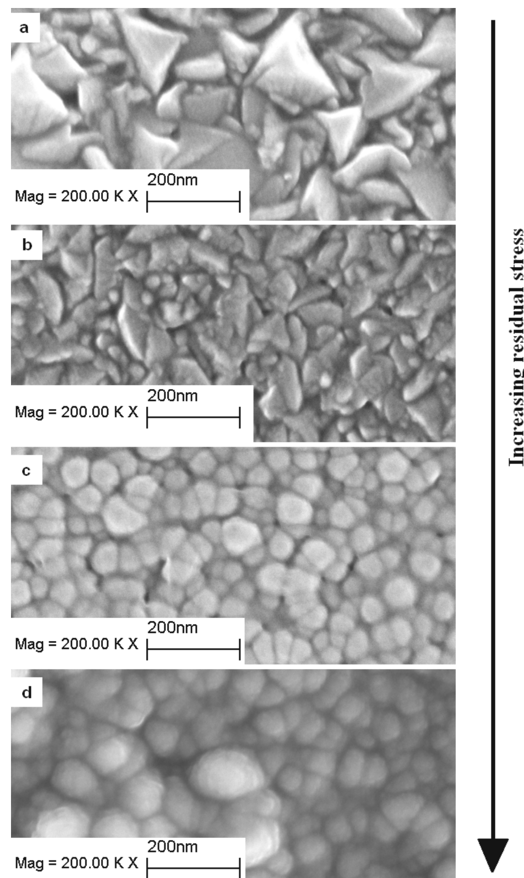

Figure 4.13. Microstructure of the as-deposited films, ordered in increasing residual stress (see Table 3.1 for sample labels). (a) Set 6, (b) Set 8, (c) Set 7, (d) Set 3.

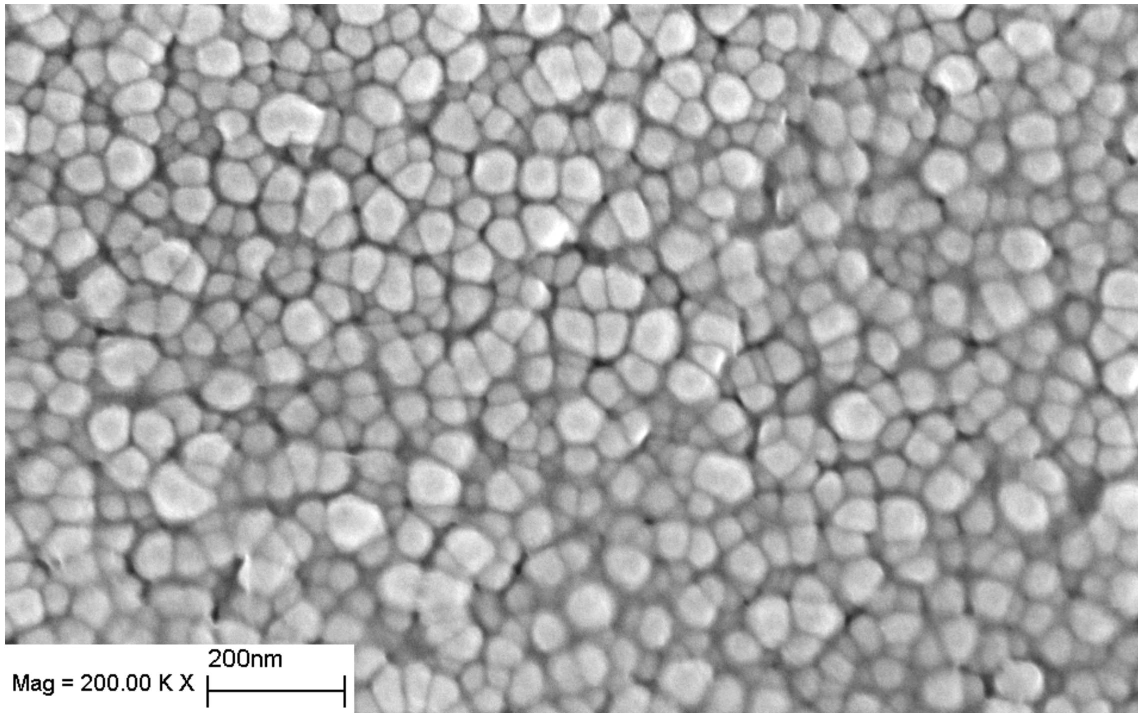

(a)

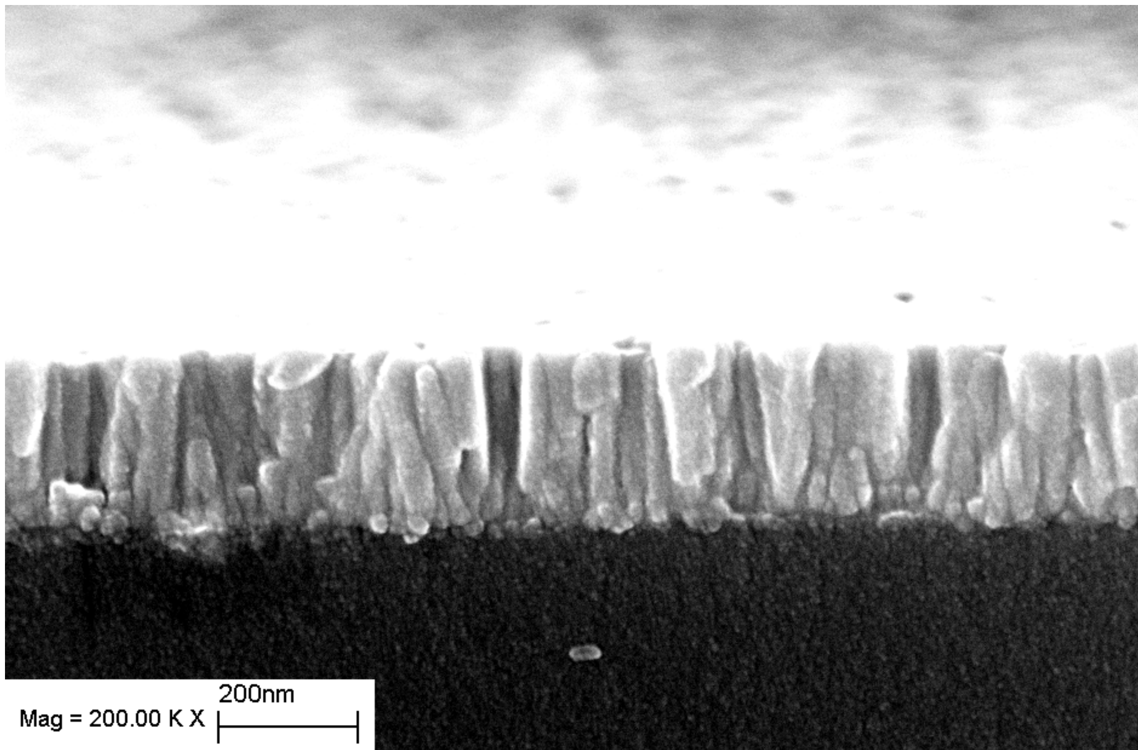

(b)

Figure 4.14. SEM images of the ZnO film grown on glass at T_s = RT, p = 0.2 mbar, P_{RF} = 125 W (Set 7 in Table 3.1): (a) top surface (GS_{SEM} ≈ 56 nm), (b) cross-section (h ≈ 278 nm, w ≈ 44 nm).

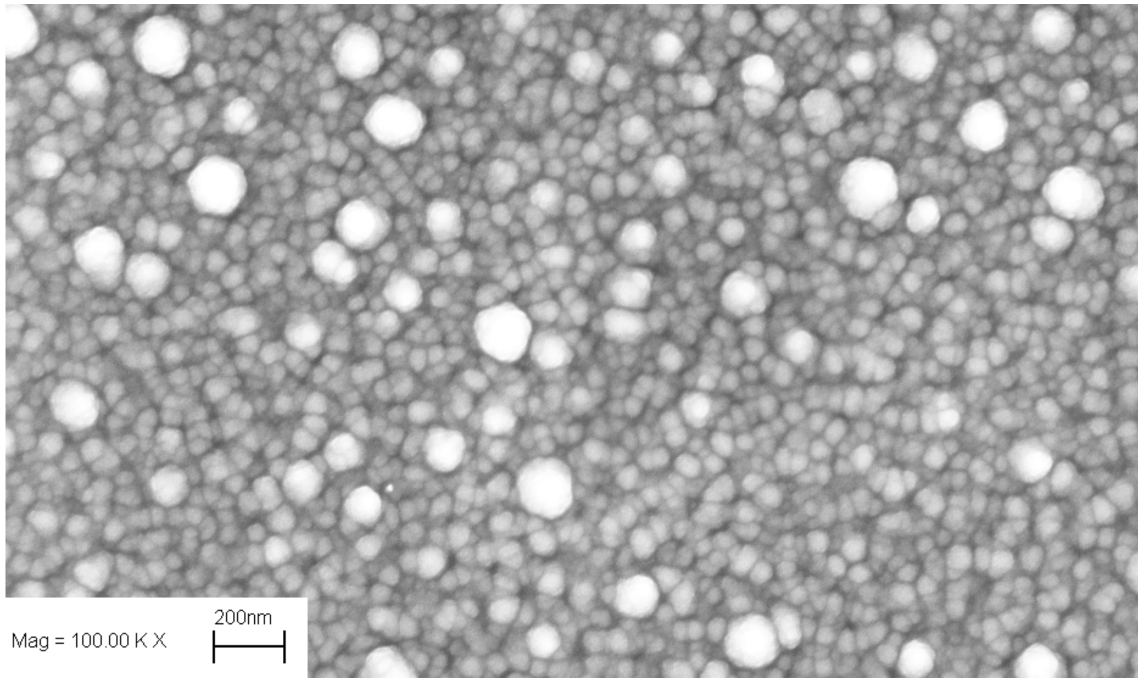

(a)

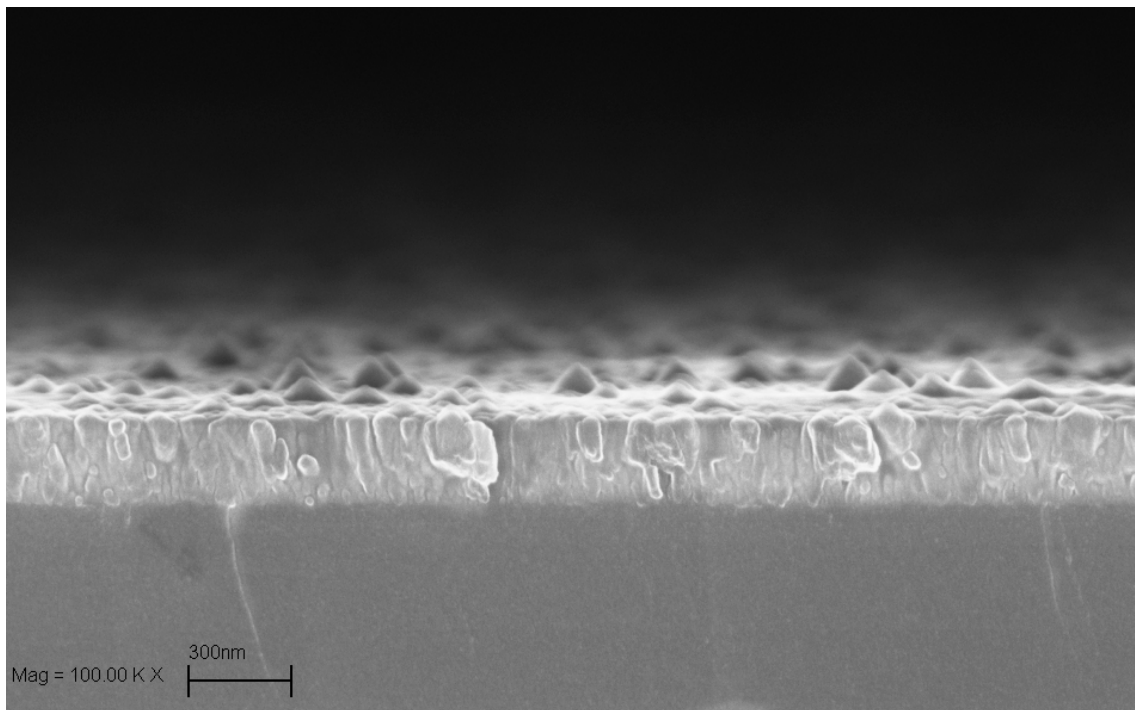

(b)

Figure 4.15. SEM images of the ZnO film grown on glass at T_s = RT, p = 0.4 mbar, P_{RF} = 100 W (Set 3 in Table 3.1): (a) top surface (GS_{SEM} ≈ 50–150 nm), (b) cross-section (h ≈ 280 nm, w_{bottom} ≈ 40 nm, w_{top} ≈ 120 nm).

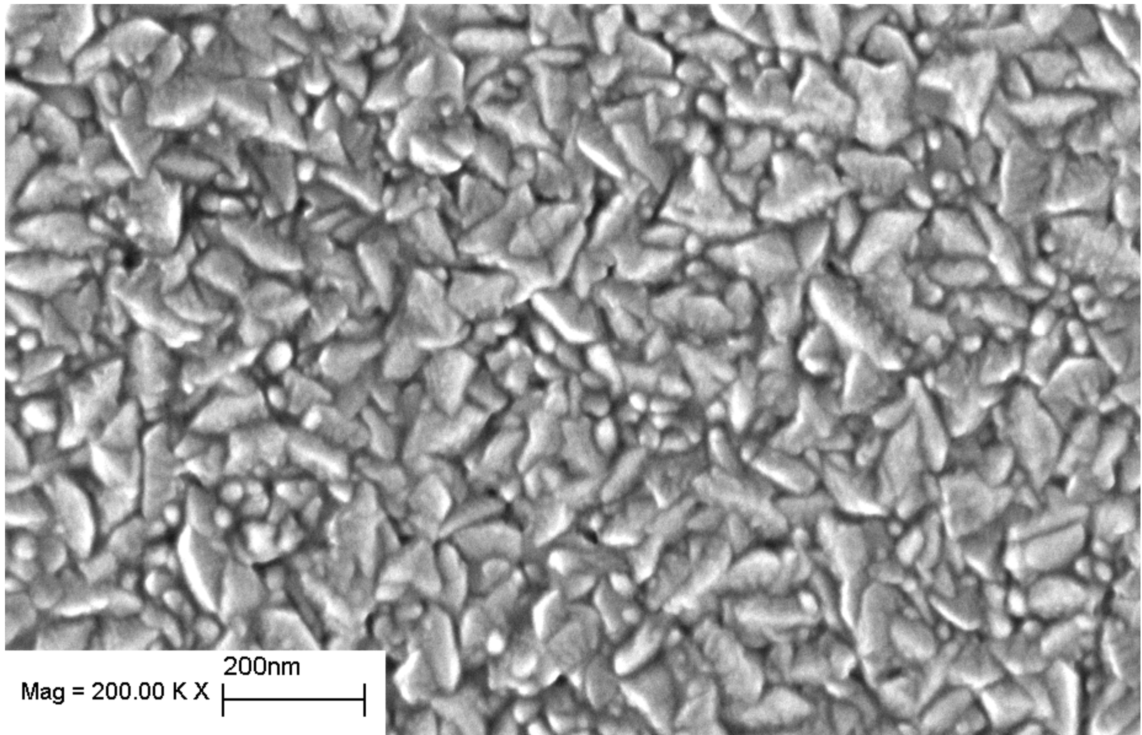

(a)

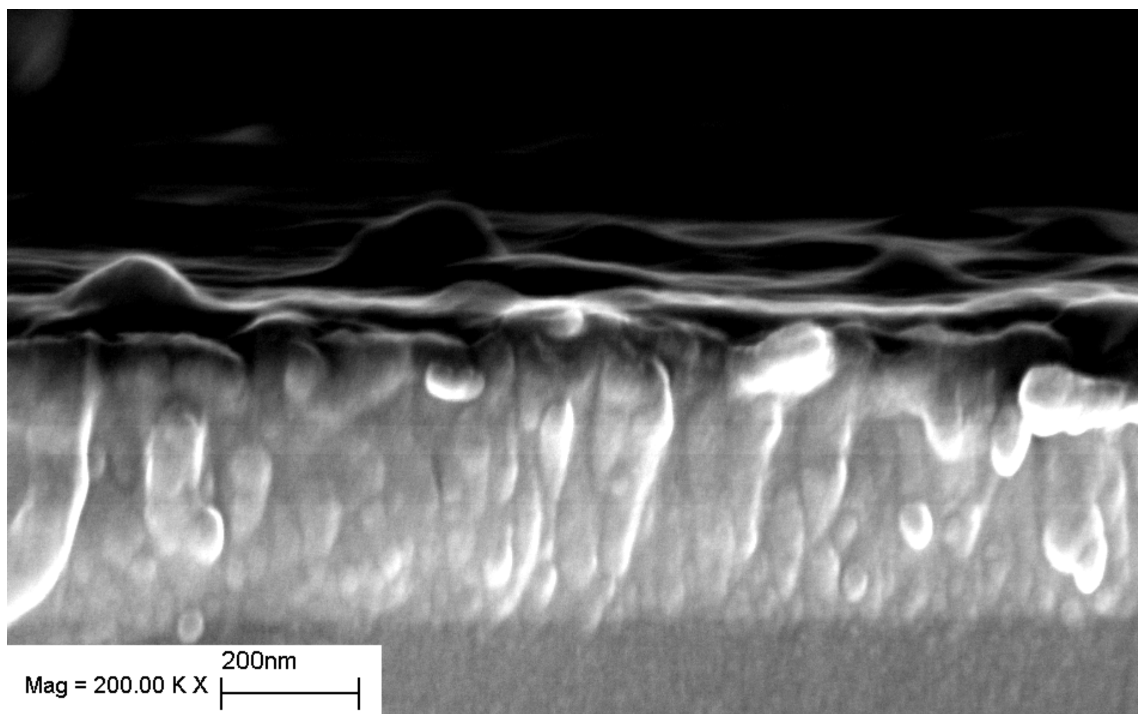

(b)

Figure 4.16. SEM image of the ZnO film grown on glass at T_s = 200 °C, p = 0.2 mbar, P_{RF} = 125 W (Set 8 in Table 3.1): ($GS_{SEM,equiaxed}$ ≈ 21–32 nm, $GS_{SEM,diamond}$, (b) cross-section (h ≈ 400 nm, w_{bottom} ≈ 15–33 nm, w_{top} ≈ 70–80 nm).

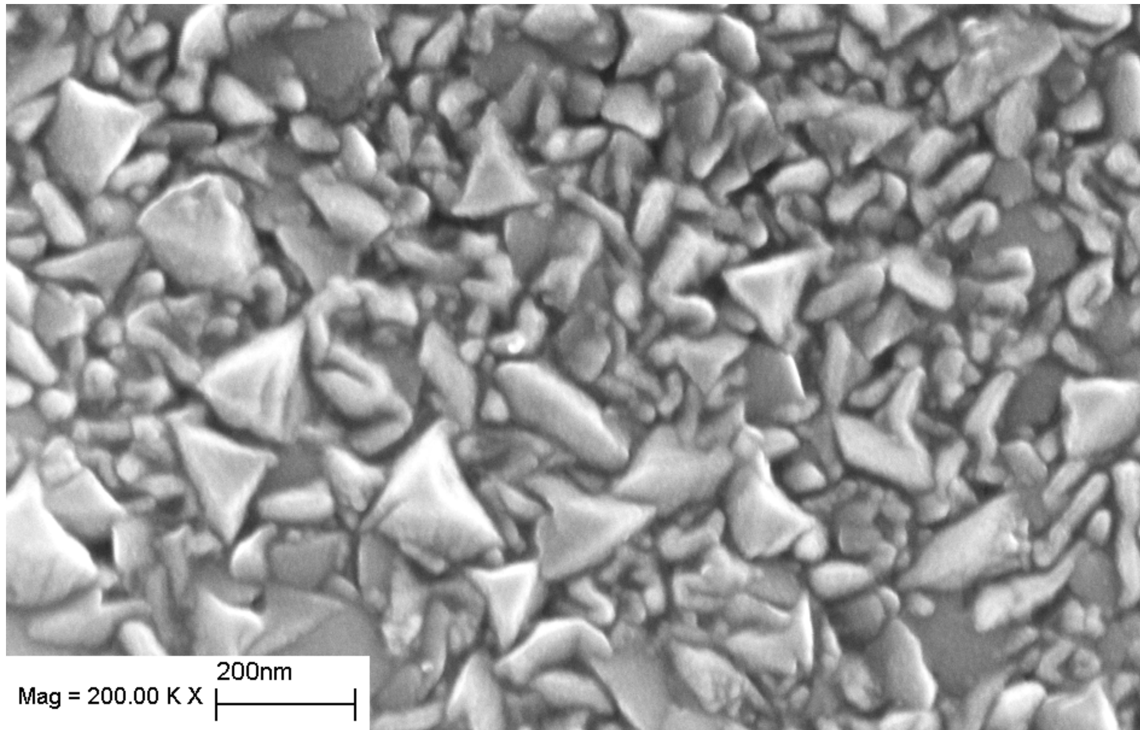

(a)

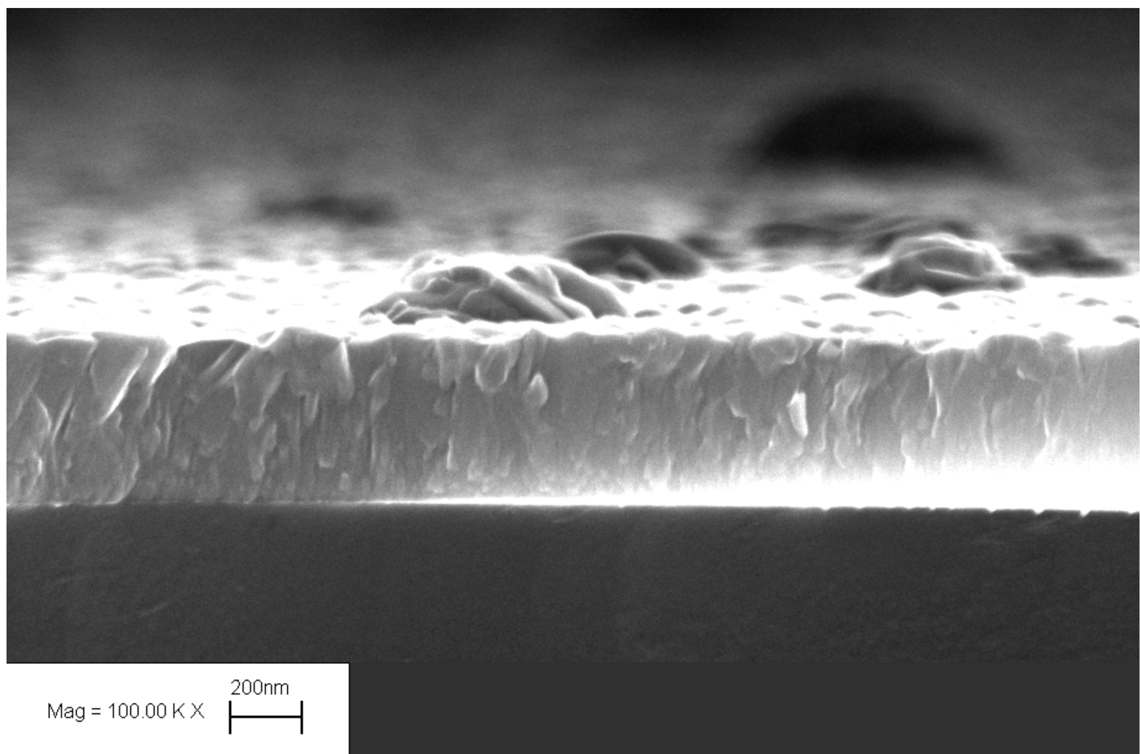

(b)

Figure 4.17. SEM image of the ZnO film grown on glass at T_s = 200 °C, p = 0.2 mbar, P_{RF} = 125 W (Set 6 in Table 3.1): (a) top surface ($GS_{SEM,equiaxed}$ ≈ 20–35 nm, $GS_{SEM,diamond/tringular}$ ≈ 97–216 nm), (b) cross-section (h ≈ 463 nm, w_{bottom} ≈ 28 nm, w_{top} ≈ 84 nm).

4.4. Effects of the Deposition Parameters on the Film Texture

In this section, the variations in the preferred orientation direction of the ZnO crystallites within the thin films are presented. As have been stated in Sec. 4.1, all of the film samples were strongly textured along the (002) direction, on any type of substrate. An example can be seen in Fig. 4.18.a (T_s = 200 °C, p = 0.4 mbar, P_{RF} = 125 W). The (002)-peak with little intensity can be seen on all of the samples of this set.

For a specific set of deposition conditions (T_s = 200 °C, p = 0.2 mbar, P_{RF} = 125 W), additional texture was observed along the (101) direction in some samples, in addition to (002). When the pressure was decreased to 0.2 mbar, the (002)-peak intensity increased (Fig. 4.18.b). At the same time, (101) reflection appeared. The same trend was also observed for the films deposited under those conditions on a fresh glass substrate (Fig. 4.18.c). Thus, that trend was independent of the substrate preparation method (see Table 3.1). The (101)-peak disappeared when either p was further decreased to 0.02 mbar (Fig. 4.18.d), or when p was kept constant, but T_s was decreased to RT (Fig. 4.18.e).

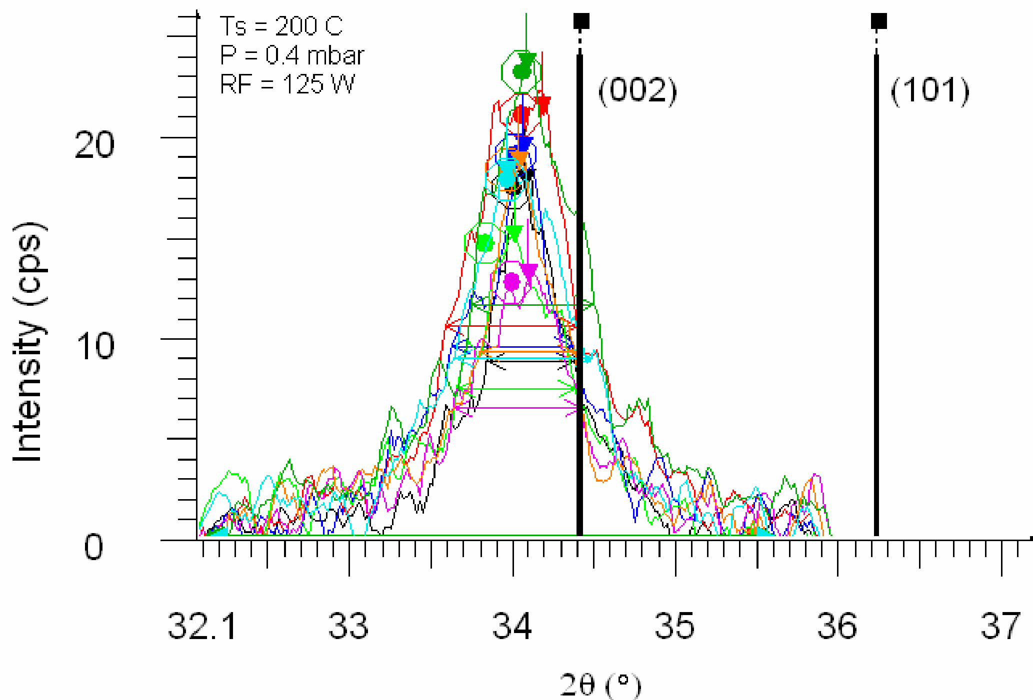

Figure 4.18.a. XRD spectra (θ–2θ) of the ZnO film grown on glass at T_s = 200 °C, p = 0.4 mbar, P_{RF} = 125 W (Set 5 in Table 3.1).

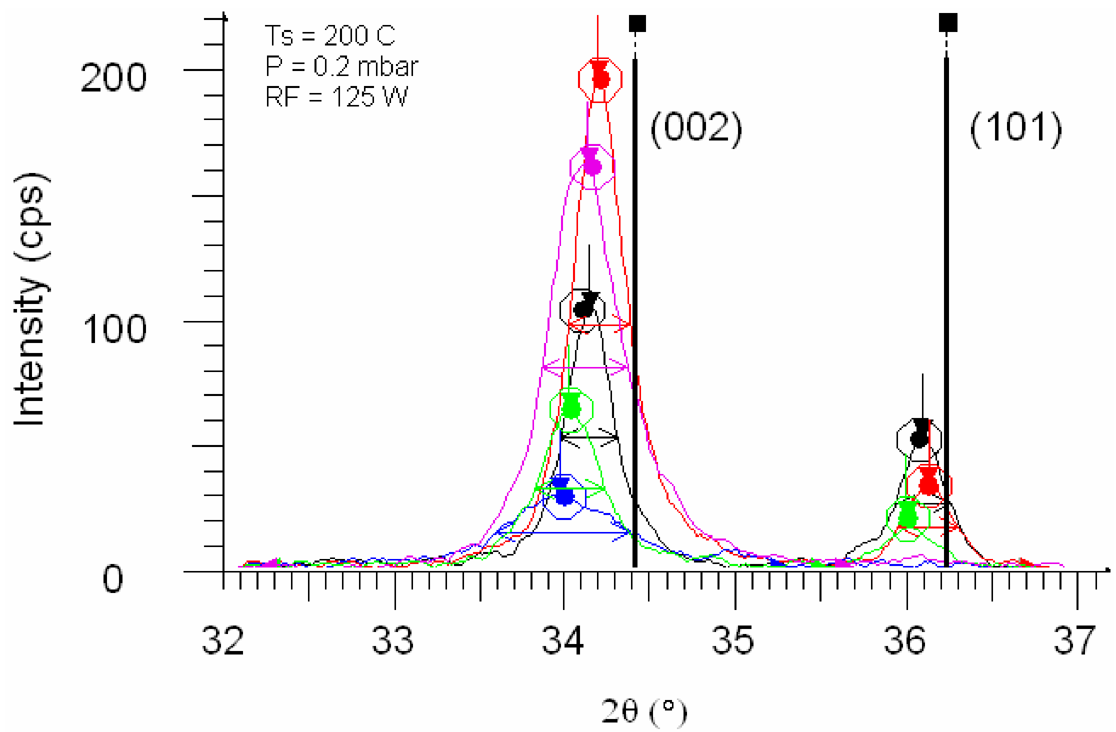

Figure 4.18.b. XRD spectra (θ–2θ) of the ZnO film grown on glass at T_s = 200 °C, p = 0.2 mbar, P_{RF} = 125 W (Set 8 in Table 3.1).

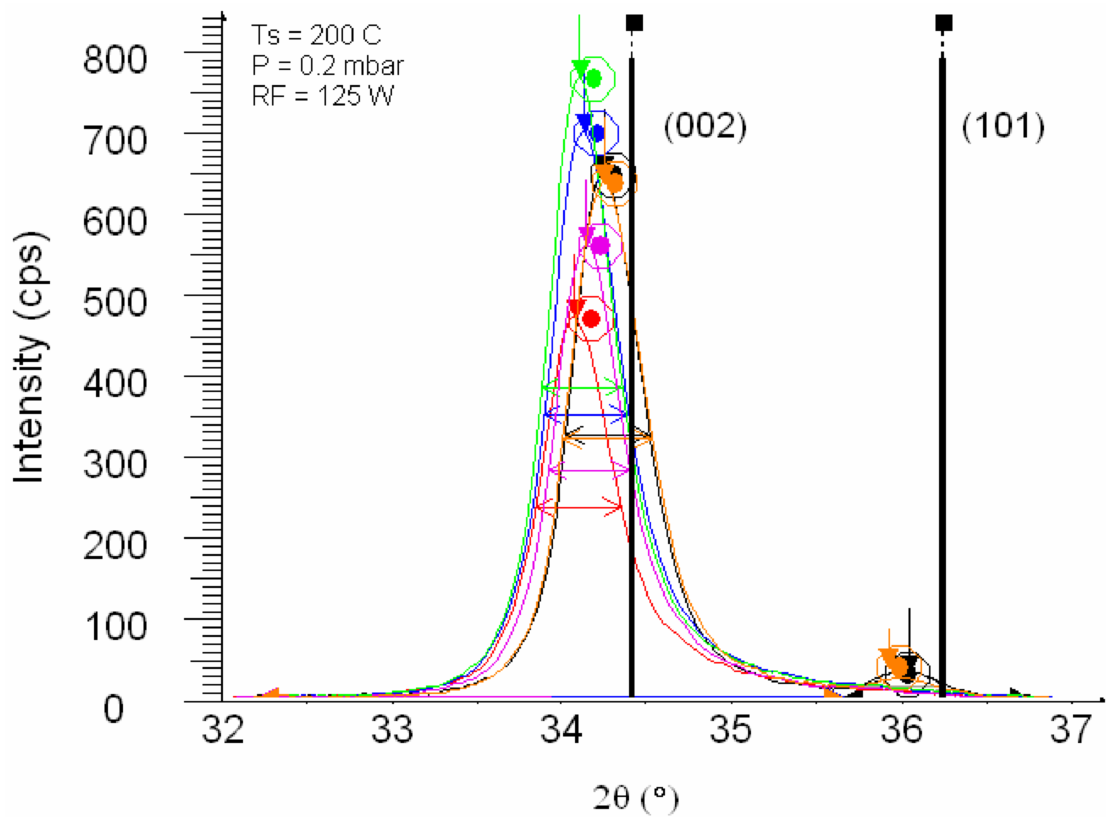

Figure 4.18.c. XRD spectra (θ–2θ) of the ZnO film grown on glass at T_s = 200 °C, p = 0.2 mbar, P_{RF} = 125 W (Set 6 in Table 3.1).

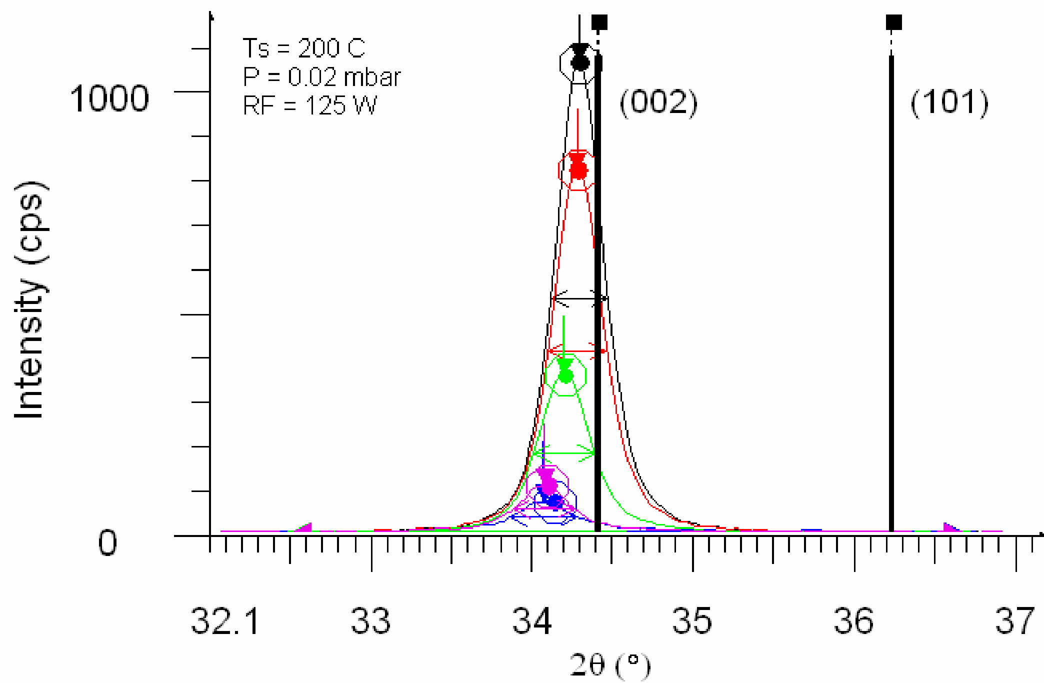

Figure 4.18.d. XRD spectra (θ–2θ) of the ZnO film grown on glass at T_s = 200 °C, p = 0.02 mbar, P_{RF} = 125 W (Set 9 in Table 3.1).

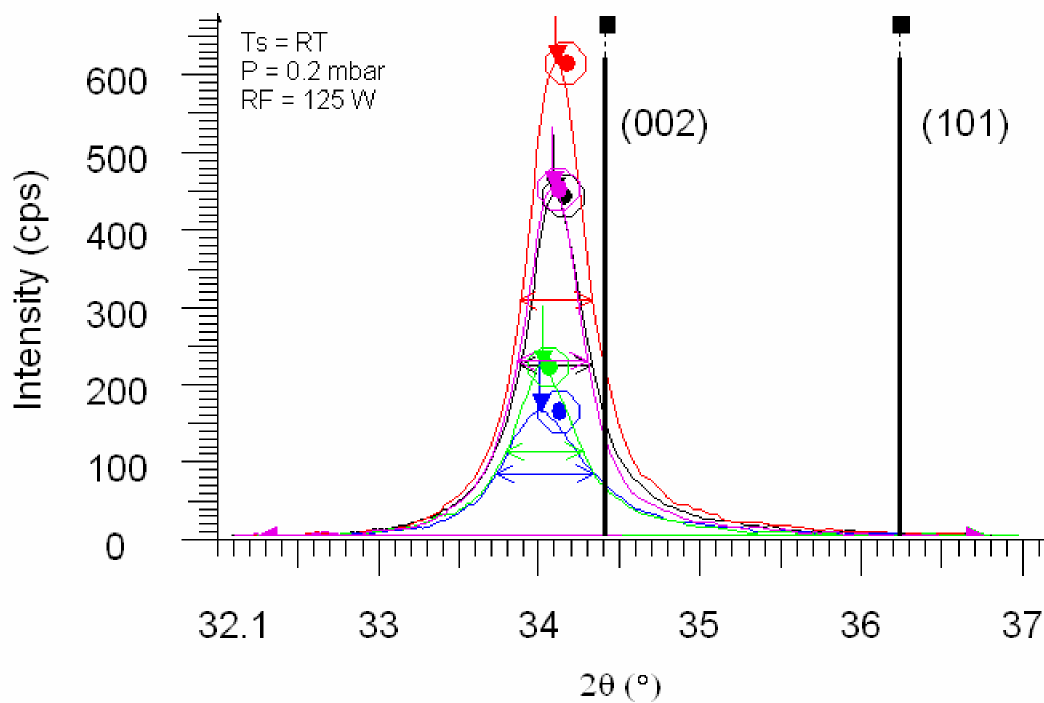

Figure 4.18.e. XRD spectra (θ–2θ) of the ZnO film grown on glass at T_s = RT, p = 0.2 mbar, P_{RF} = 125 W (Set 7 in Table 3.1).

4.5. Effects of the Buffer layer on the Residual Stress, Texture, and Microstructure

In order to elucidate the effect of a pre-deposited ZnO buffer layer on the further film growth, a set of films were deposited on buffer layers with different treatments as described in Chapter 3, with T_s = 200 °C, P_{RF} = 125 W, and p = 0.2 mbar. Like the other sets that have been deposited at the same conditions (Set 6 and 8), these films had a (101) reflection among (002) (Fig. 4.19).

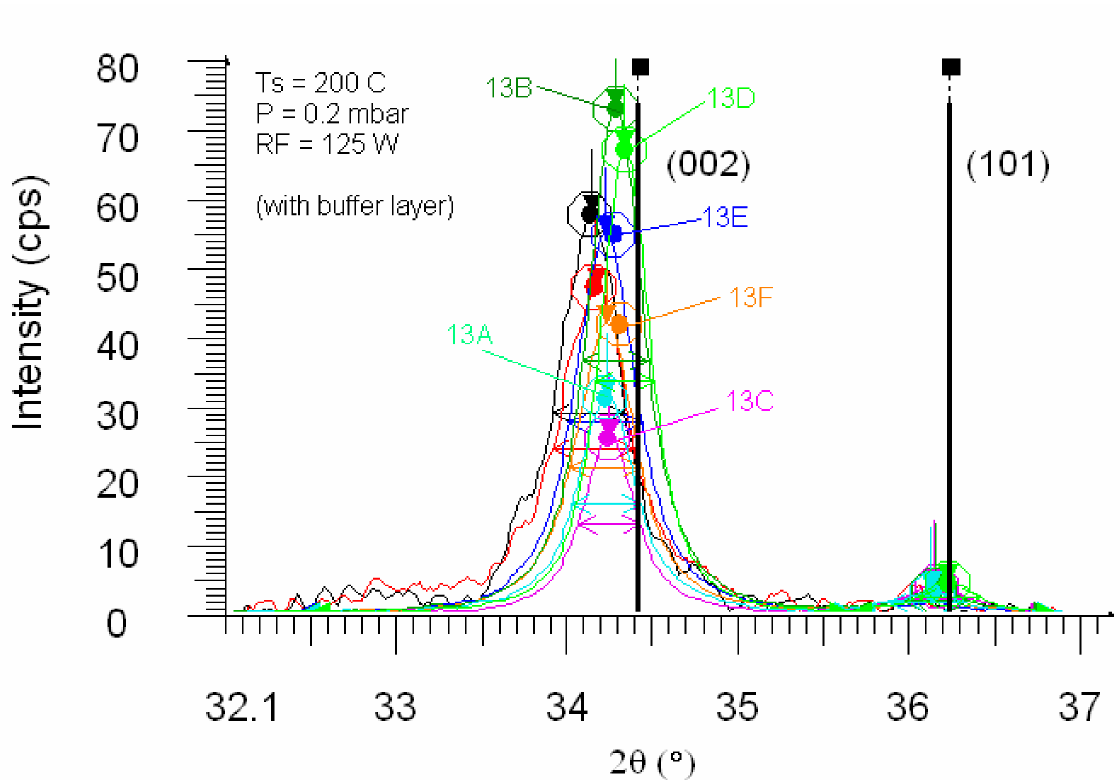

Figure 4.19. XRD spectra (θ–2θ) of the ZnO film grown on glass at T_s = 200 °C, p = 0.2 mbar, P_{RF} = 125 W, with an initial buffer layer (set 13 in Table 3.1; see Table 3.2 for details).

The residual stresses of all of the samples with the (101) texture are compared in Table 4.8. The first column under $\sigma_{c,ave}$ belongs to the (002)-peak of the samples where no (101)-peak was observed. The middle column values were calculated from the (002)-

peaks of the samples which also possessed the (101)-peak. The last column is for the (101)-peaks, when they were observed. Among these samples, the one with the annealed buffer layer on a fresh substrate (13D; see Table 3.1 and 3.2) had the lowest residual stress (-1.09 GPa), while the one with the non-annealed buffer layer on an acid-cleaned substrate (13A) had the highest residual stress (-2.60 GPa) (Fig. 4.20).

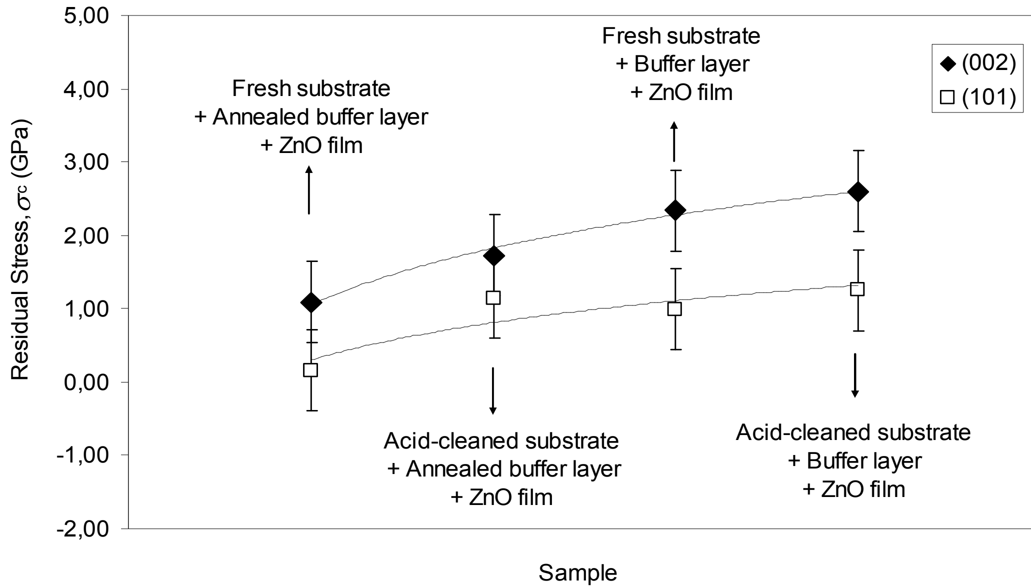

Figure 4.20. Variation of residual stress (σ_c), for ZnO film grown on glass at T_s = 200 °C, p = 0.2 mbar, P_{RF} = 125 W (Set 13), depending on the pre-deposited ZnO buffer layer (Set 12): ZnO film on annealed buffer layer on a fresh substrate (13D), or on an acid-cleaned substrate (13B), and ZnO film on an as-deposited buffer layer on a fresh substrate (13C), or on an acid-cleaned substrate (13A) (see Table 3.1, 3.2, and 4.8 for sample labels and stress values). By convention, a compressive residual stress has a negative value. In the figure, the absolute value of σ_c is given for ease of comparison.

The changes in the microstructure as shown in Fig. 4.21 were due to the influence of a buffer layer. As have been stated before in Sec. 4.3, the films deposited under the aforementioned set of conditions had *distorted hexagonal, diamond-shaped,* or *triangular* grains with interspersed smaller *equiaxed* grains (Fig. 4.21.a and 4.22.a). By depositing a buffer layer with a thickness of a sixth of the total film thickness (about 67 nm), those non-hexagonal grains were eliminated (Fig. 4.21.b and 4.22.b). At the same

time, the residual compressive stress decreased from -3.94 GPa to -2.60 GPa (Table 4.8).

Annealing the buffer layer before further film growth led to further decrease in the residual compressive stress (-1.09 GPa; Table 4.8), without changing the overall grain shape and size significantly (Fig. 4. 21.c and 4.22.d).

Table 4.8. Variation of residual stress for Set 13, depending on the pre-deposited ZnO buffer layer (Set 12). Film deposition conditions were: P_{RF} = 125 W, p = 0.2 mbar, T_s = 200 °C. The error range is ±0.55 GPa.

Sample	**Substrate preparation**	***t* (min)**	**$\sigma_{c,ave}$ (GPa)**		
			(002)*	**(002)****	**(101)*****
Set6	Fresh substrate	60	-2.88	-1.44	-2.73
Set8	Acid-cleaned substrate	60	-3.32	-3.94	-1.96
13D	Fresh substrate; Buffer layer annealed in air (12D).	10 + 50		-1.09	-0.16
13B	Acid-cleaned substrate; Buffer layer annealed in air (12B).	10 + 50		-1.73	-1.14
13C	Fresh substrate; Buffer layer not annealed (12C).	10 + 50		-2.34	-0.99
13A	Acid-cleaned substrate; Buffer layer not annealed (12A).	10 + 50		-2.60	-1.25

* σ value calculated from the (002)-reflection, for those samples in the set, which had only (002)-reflection.

** σ value calculated from the (002)-reflection, for those samples in the set, which had both (002) and (101)-reflections.

*** σ value calculated from the (101)-reflection, for those samples in the set, which had both (002) and (101)-reflections.

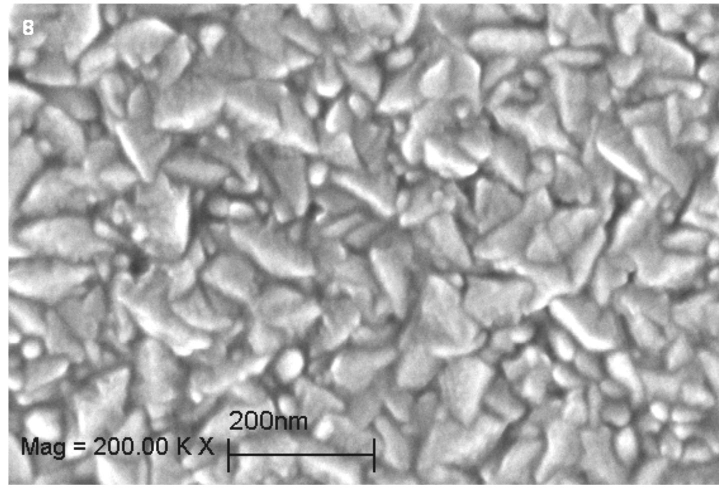

(a)

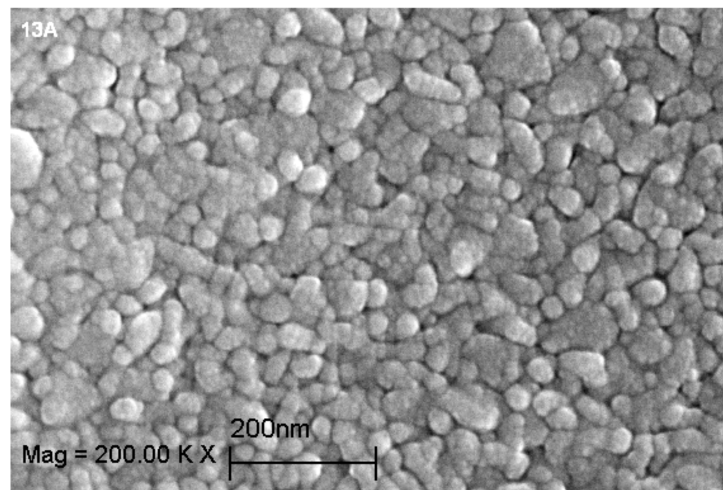

(b)

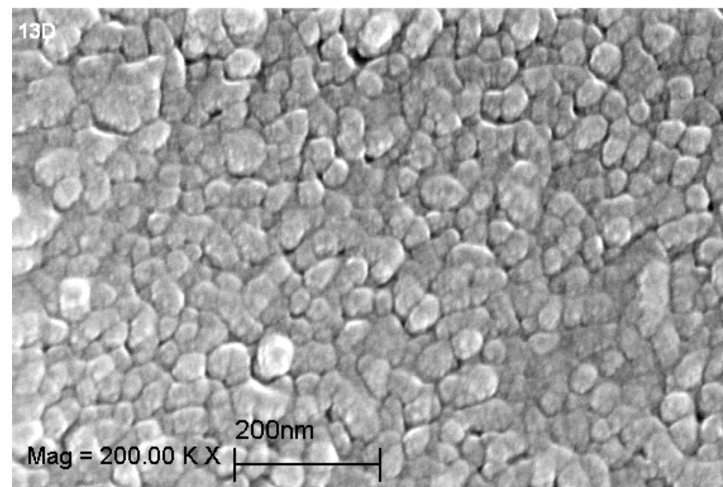

(c)

Figure 4.21. Microstructure of the top surface of the ZnO films grown on glass at T_s = 200 °C, p = 0.2 mbar, P_{RF} = 125 W, ordered in decreasing residual stress. (a) Without a buffer layer (Set 8; σ_c = -3.32 GPa; $GS_{SEM,equiaxed} \approx$ 21–32 nm, $GS_{SEM,diamond} \approx$ 126 nm), (b) with a buffer layer (Sample 13A; σ_c = -2.60 GPa; GS_{SEM} = 19–51 nm), (c) with a pre-annealed buffer layer (sample 13D; σ_c = -1.09 GPa; GS_{SEM} = 19–51 nm; see Table 4.8).

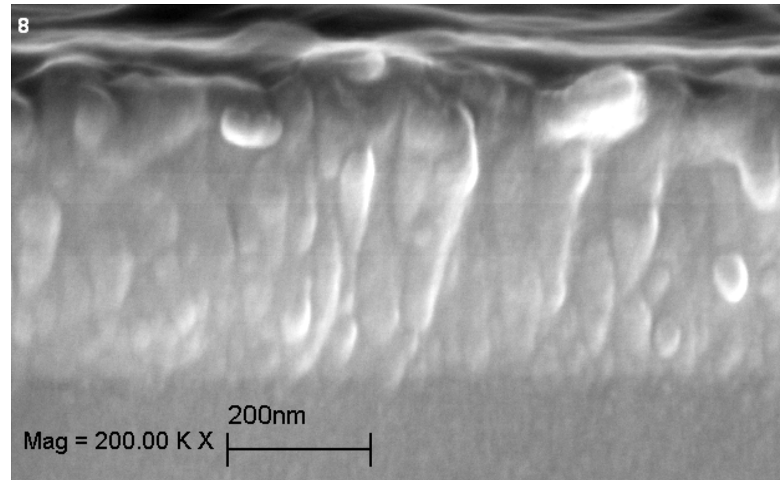

(a)

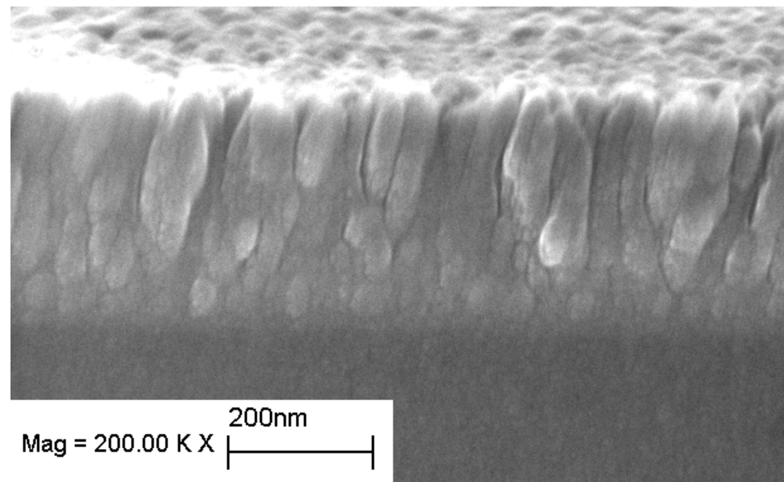

(b)

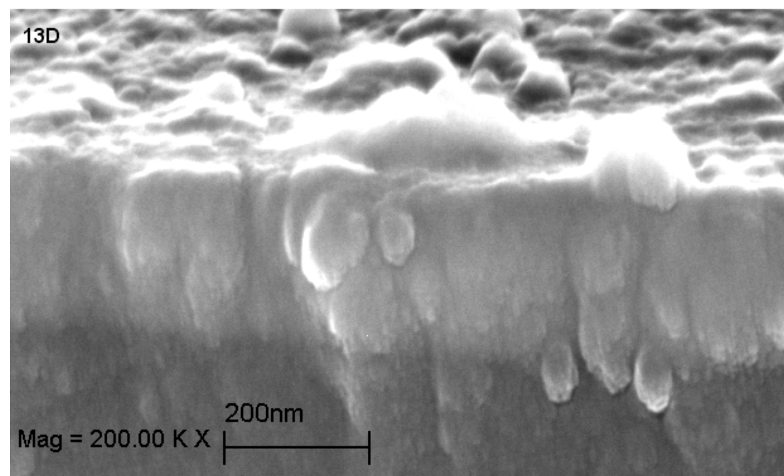

(c)

Figure 4.22. Microstructure of the cross-section of the ZnO films grown on glass at T_s = 200 °C, p = 0.2 mbar, P_{RF} = 125 W, ordered in decreasing residual stress. (a) Without a buffer layer (Set 8; σ_c = -3.32 GPa; $h \approx$ 400 nm, $w_{bottom} \approx$ 15–33 nm, $w_{top} \approx$ 70–80 nm), (b) with a buffer layer (Sample 13A; σ_c = -2.60 GPa; $h \approx$ 314 nm, $w \approx$ 48 nm), (c) with a pre-annealed buffer layer (sample 13D; σ_c = -1.09 GPa; $h \approx$ 248 nm; see Table 4.8).

4.6. Stress Relaxation by Thermal Annealing or Aging

To investigate the effects of post-deposition annealing on the intrinsic stresses, the samples were heated at 600 °C for 1 h or 6 h, in air or argon. As presented in Fig. 4.4, the ZnO-glass laminate warped after deposition. When annealed at 600 °C for 1 h in air, the warping of the ZnO-glass laminate reversed (Fig. 4.23).

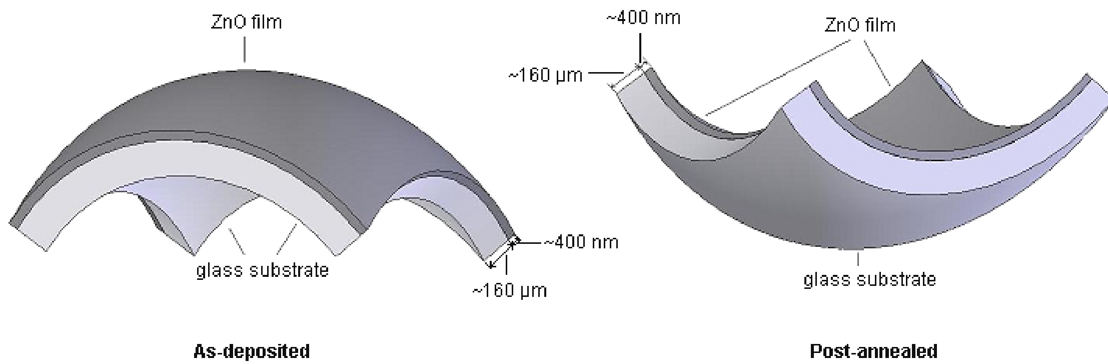

Figure 4.23. Warping of ZnO-glass system after deposition and after annealing (not to scale).

As seen in Fig. 4.24, upon annealing, the (002) diffraction peak of the film shifted closer to (002)-peak of the powder, moving towards lower plane spacing (d) and lower axial strain, which indicated a release of compressive stresses in the plane of the film. At the same time, the XRD peaks became narrower, more symmetrical, and more intense. The planar compressive plane stresses decreased by ~90% for the film on the glass substrate, and ~95% for the film on the mica substrate (Table 4.9 and Fig. 4.25). For the film on the Si(100) substrate, the residual stress changed sign upon annealing, and σ_c was calculated as +0.48 GPa. That value corresponded to 7% of the stress before annealing, when the absolute values were considered. The interpretation of these values will further be discussed in Chapter 5.

The increase in the grain size upon annealing for all samples can be seen in Table 4.9. These grain sizes were calculated from the XRD peak widths, and correspond to the grain size along the normal of the film surface, as described in Sec. 3.4.2.4 (GS_{XRD}). Grain size was also measured along the lateral direction with respect to the film surface (GS_{SEM}), and a similar increase in GS_{SEM} upon annealing could be seen in Fig. 4.26.

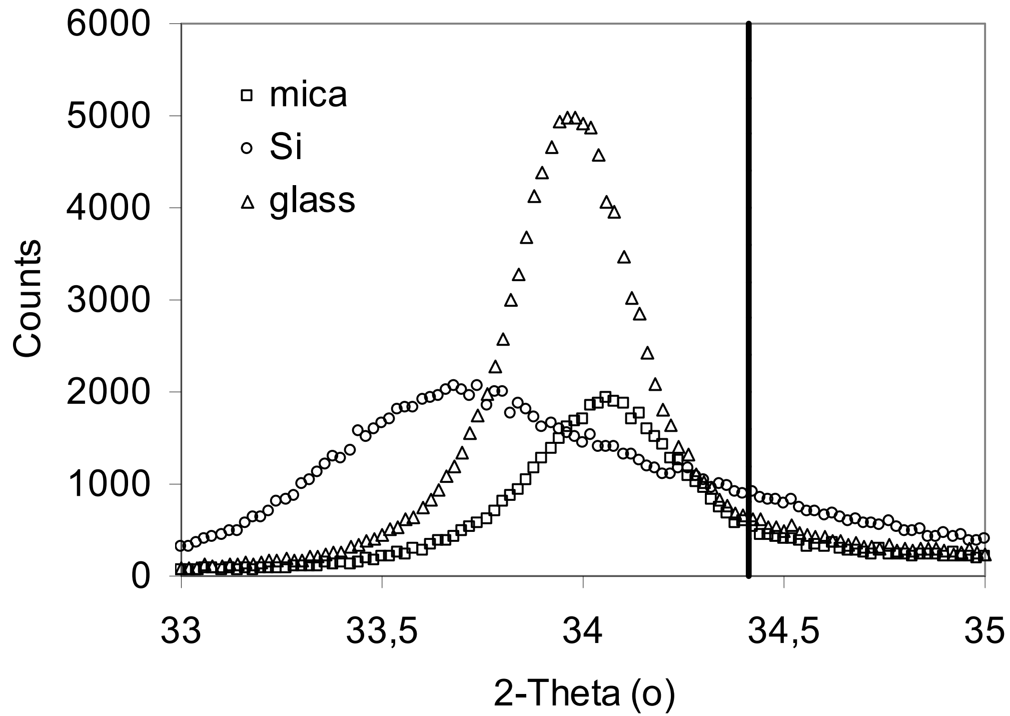

(a)

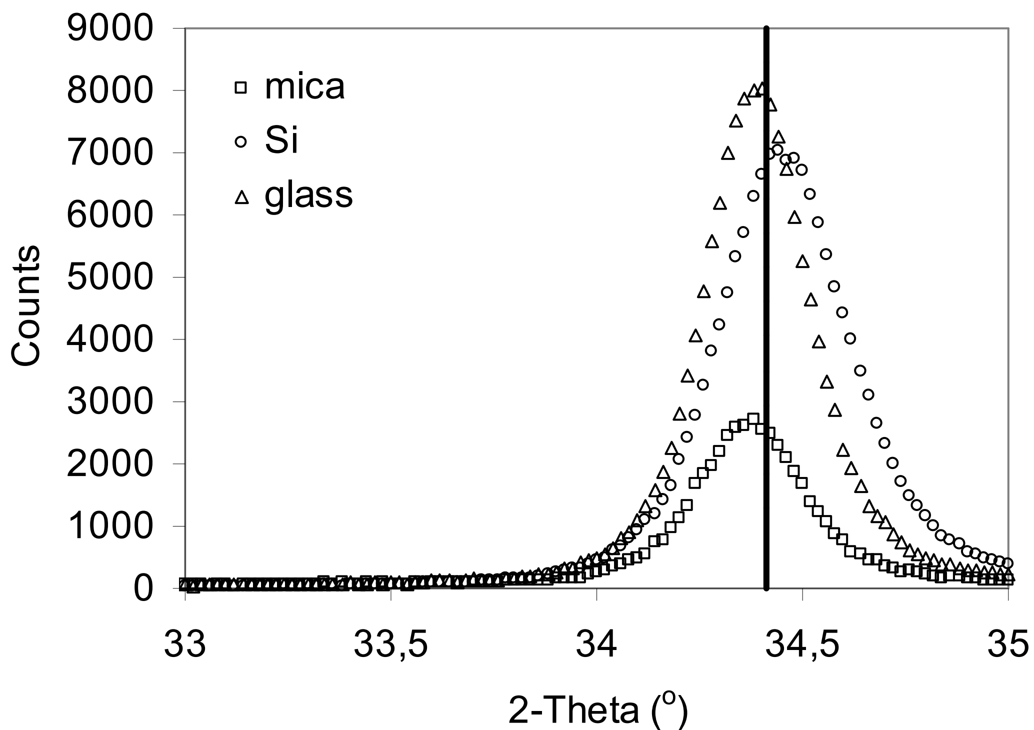

(b)

Figure 4.24. Position of the (002)-peak of the ZnO films with T_{s_0} = 200 °C, depending on the substrate type (Set 16 in Table 3.1): (a) as-deposited, (b) after post-deposition annealing in air for 1 hour at 600 °C. Annealing the films eliminates the stresses.

Table 4.9. Variation of lattice parameter (c), XRD peak width at half-intensity ($FWHM$), percent tensile strain ($\%\varepsilon_Z$), grain size (GS_{XRD}), and total compressive stress (σ_c) of ZnO films on different substrates for an initial substrate temperature of 200 °C (Set 16). The XRD data belongs to the (002)-peak. The reference lattice constant for the unstressed ZnO (c_o) was obtained from JCPDS-No. 36-1451. The results are given for the as-deposited (0) and the thermally annealed (1) films on glass (G), mica (M), and Si(100) (S) substrates. The error range in σ_c due to equipment offset is ±0.26 GPa.

Sample	c_o (Å)	c (Å)	***FWHM*** **(2θ °)**	$\%\varepsilon_Z$* (%)	GS_{XRD}** (nm)	σ_c*** (GPa)
G0	5.20664	5.26980	0.347	-1.21	23.94	-5.46
G1		5.21322	0.293	-0.13	28.38	-0.57
M0		5.24752	0.433	-0.79	19.19	-3.54
M1		5.20880	0.298	-0.04	27.91	-0.19
S0		5.28402	0.928	-1.49	8.95	-6.69
S1		5.20102	0.357	-0.11	23.30	0.48

* Calculated from Eq.3.19.
** Calculated from Eq.3.37.
*** $\sigma_c = \sigma_x + \sigma_y$; Calculated from Eq. 3.16a.

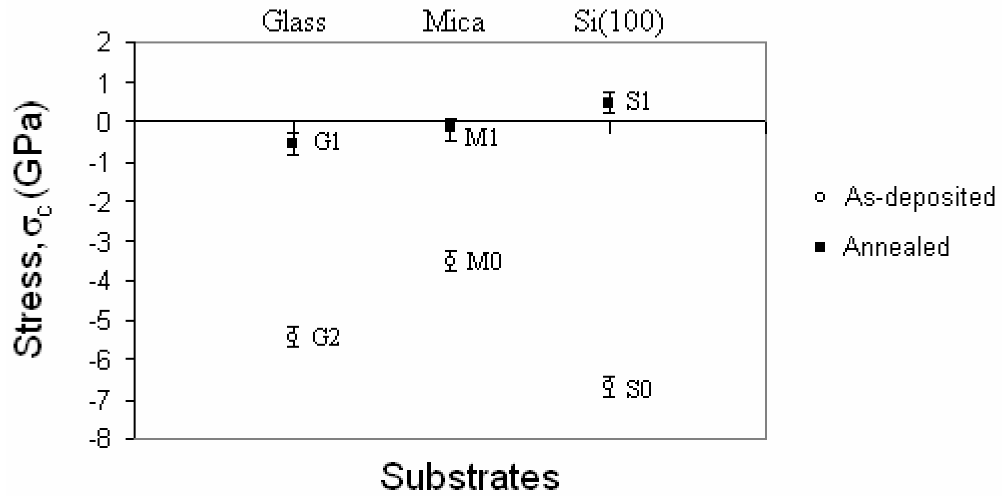

Figure 4.25. Comparison of planar stresses of the ZnO films with T_{s_0} = 200 °C, depending on the substrate type (Set 16 in Table 3.1): as-deposited and after post-deposition annealing in air for 1 hour at 600 °C.

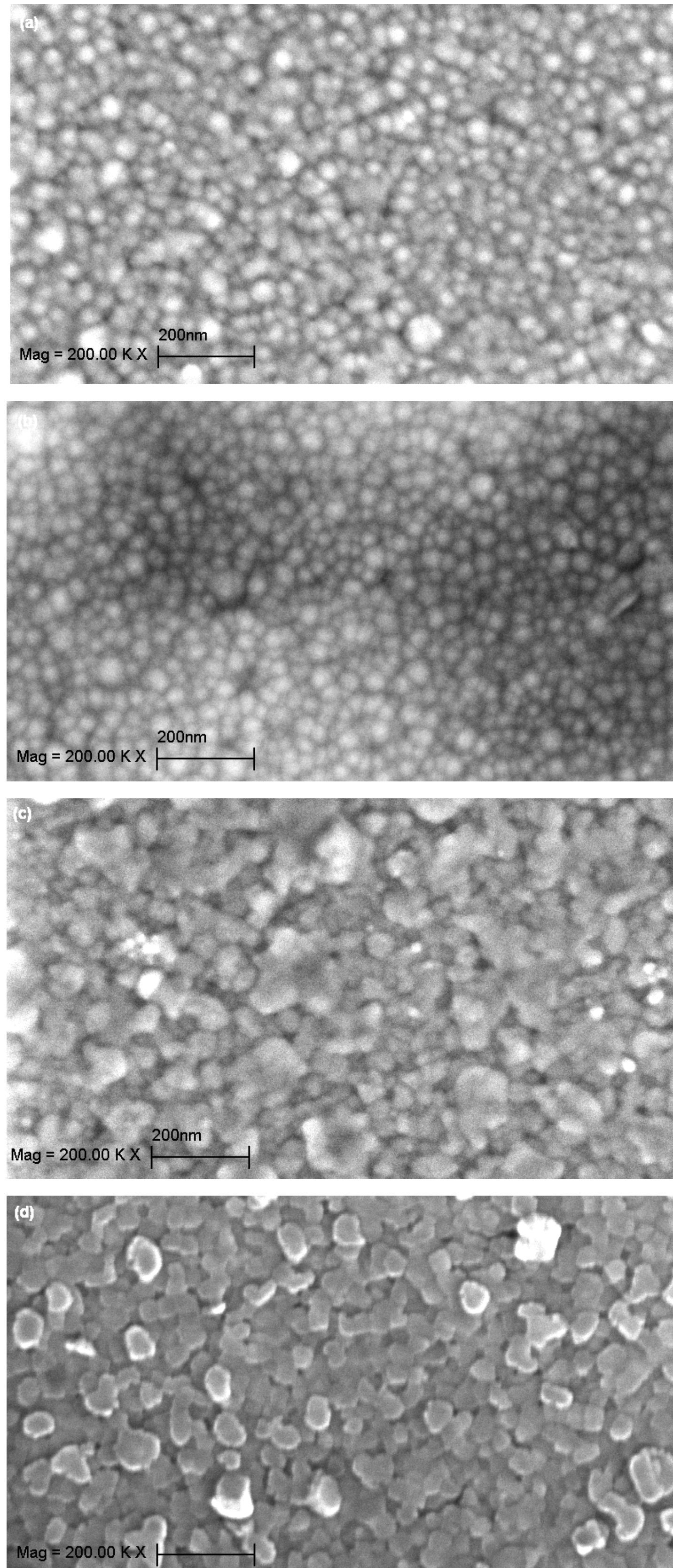

Figure 4.26. SEM images of ZnO on Si(100) with T_{s_0} = 200 °C (Set 17 in Table 3.1). (a) as-deposited (GS_{SEM} ≈ 43 nm), (b) 28 months-old (GS_{SEM} ≈ 42 nm), (c) annealed in air at 600 °C for 1 h (GS_{SEM} ≈ 43–130 nm), (d) 28-months-old film, annealed at 600 °C for 6 h (GS_{SEM} ≈ 57–130 nm).

To understand the mechanism of stress release during annealing better, the XRD spectra of some samples were done obtained under increasing temperature (see Fig. 3.9), and one example is shown in Fig. 4.27. The intensity of the ZnO (002)-peak increased with increasing the temperature from 25 °C to 170 °C, while no change was observed in the peak position. The peak shift with respect to the powder standard was minimized only after cooling down to room temperature. The intensity was also the highest for the cooled-down sample. On the other hand, the intensity of the Si–peak decreased as the temperature was increased, and was minimized at the end of cooling.

If the ZnO films grew with an oxygen deficiency, oxygen diffusion from the air into the film during annealing could be contributing to the reduction of the residual stresses (see Sec. 1.3.2). To understand if this phenomenon was taking place in the samples under study, two identical samples were annealed in air or argon atmospheres, separately at 600 °C for 6 hours. No difference in the results could be observed between the two samples after annealing (Fig. 4.28).

Aging caused a similar decrease in the residual stresses as in annealing, both for glass and the Si(100) substrate (Table 4.10, Fig. 4.29 and 4.30).

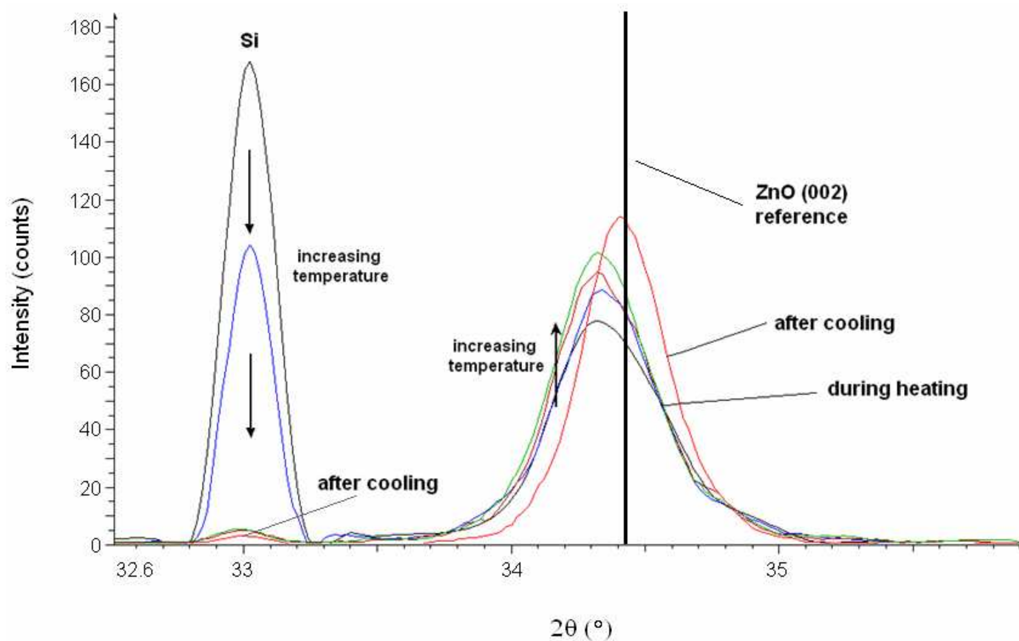

Figure 4.27. Increasing intensity of the (002)-peak of ZnO on Si(100) substrate (Set 18 in Table 3.1), as the temperature was increased from room temperature to 170 °C. All the residual stress was eliminated during cooling, and the sample was stress-free after the heating process.

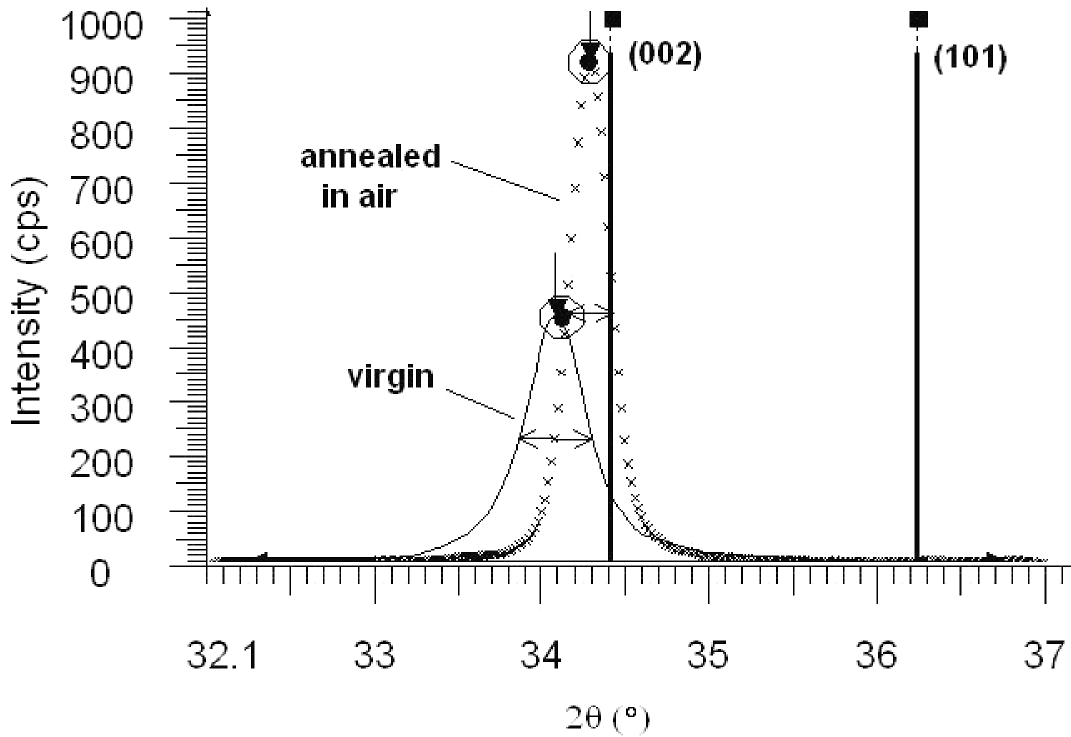

(a)

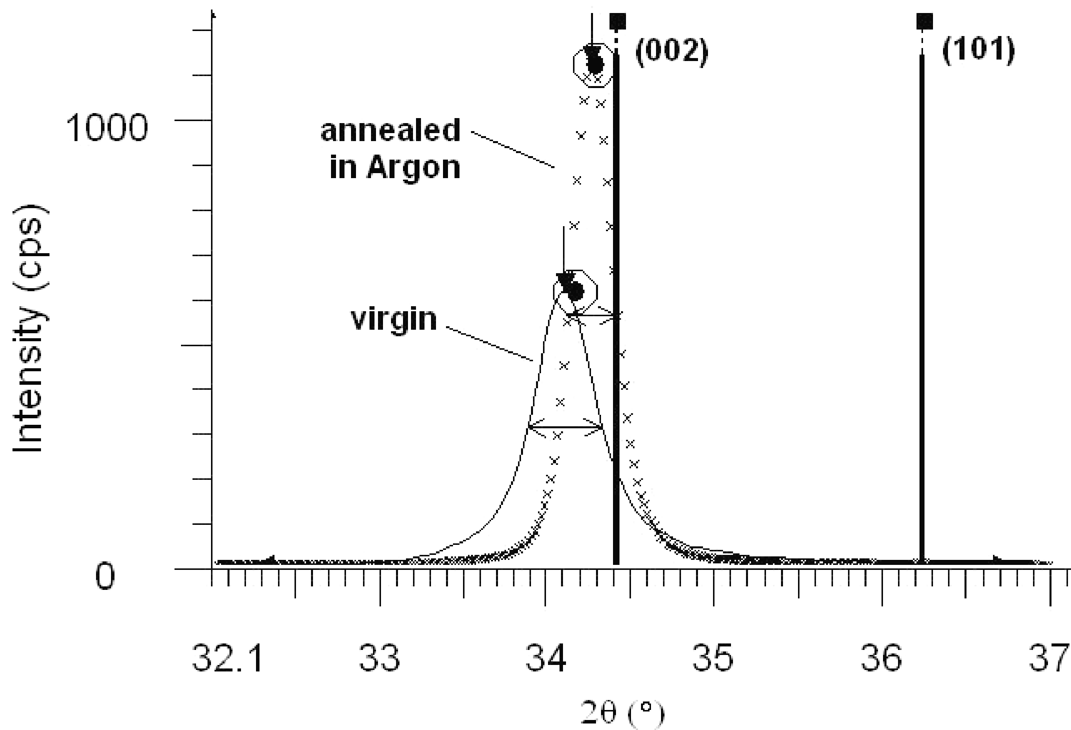

(b)

Figure 4.28. Effect of annealing on the peak position and intensity of the (002)-peak of ZnO films grown on glass at T_s = RT, p = 0.2 mbar, P_{RF} = 125 W (Set 7 on Table 3.1) (a) annealed in argon, (b) annealed in air. No significance difference was observed depending on the annealing atmosphere. Both annealing experiments were performed at 600 °C for 6 hours.

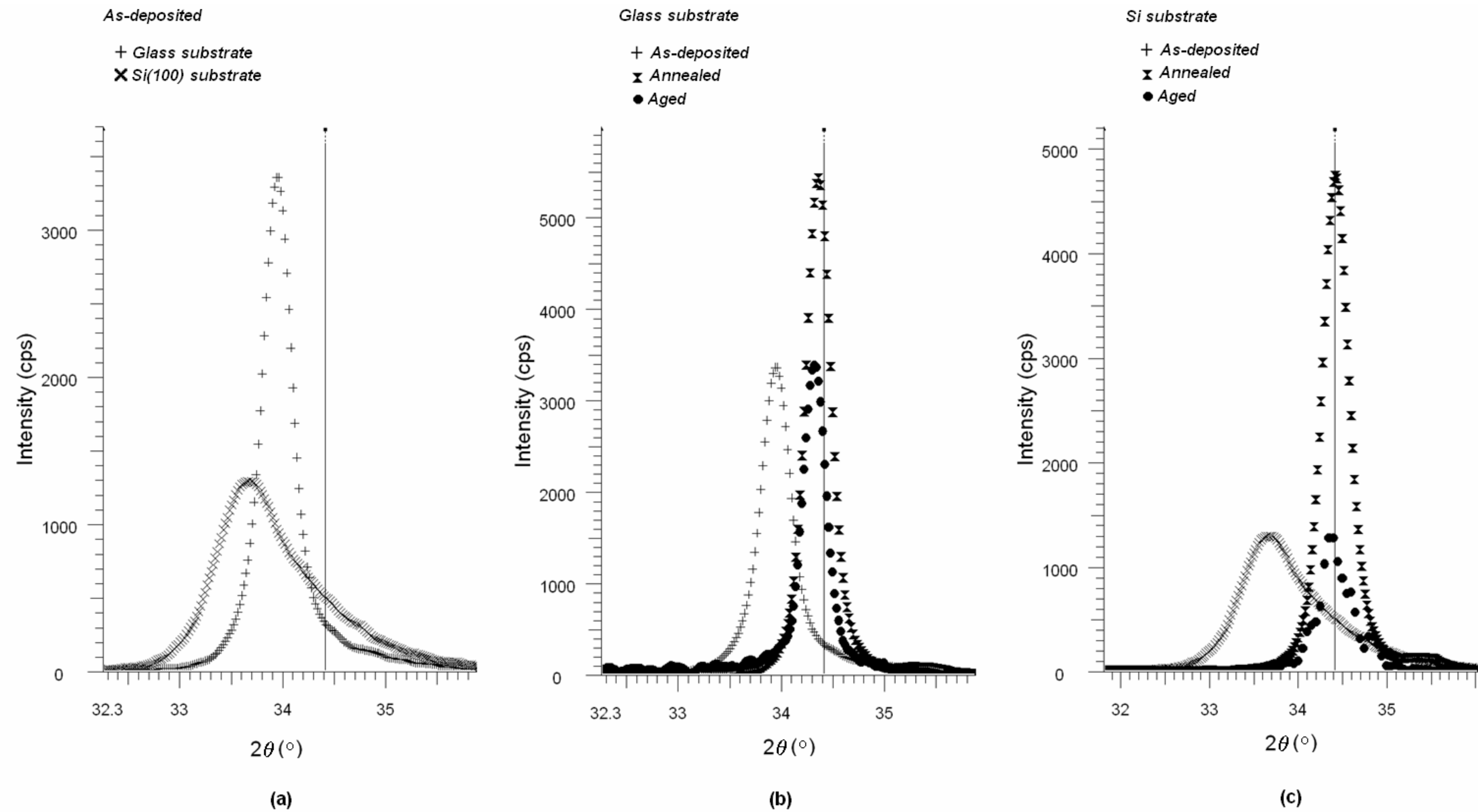

Figure 4.29. Shift of the (002)-peak of ZnO indicating residual stresses. The data shows the effect of a) substrate material, b) aging and annealing of ZnO on the glass substrate, c) aging and annealing on the Si(100) substrate. The vertical line represents the position of the (002)-peak in stress-free ZnO powder JCPDS-No. 36-1451. The (002)-peaks of aged ZnO films were scaled with those of the as-deposited films for comparison (see Table 4.10 and Fig. 4.30 for sample labels and stress values).

Table 4.10. Variation of lattice parameter (c), XRD peak width at half-intensity ($FWHM$), percent tensile strain ($\%\varepsilon_z$), grain size (GS_{XRD}), and total compressive stress (σ_c) of ZnO films on different substrates with an initial substrate temperature of 200 °C (Set 16). The XRD data belongs to the (002)-peak. The reference lattice constant for the unstressed ZnO (c_0) is taken from JCPDS-No. 36-1451. The results are given for the as-deposited (0), the thermally annealed (1), and the aged (2) films on glass (G) and Si(100) (S) substrates. The error range in σ_c due to equipment offset is ±0.26 GPa for the as-deposited and annealed films, and +0.73/-0.66 for the aged films.

Sample	c_o (Å)	c (Å)	$FWHM$ (2θ °)	$\%\varepsilon_z$ * (%)	GS_{XRD} ** (nm)	σ_c *** (GPa)
G0	5.20664	5.26980	0.347	-1.21	23.94	-5.46
G1		5.21322	0.293	-0.13	28.38	-0.57
G2		5.22110	0.266	-0.28	31.36	-1.25
S0		5.28402	0.928	-1.49	8.95	-6.69
S1		5.20102	0.357	-0.11	23.30	0.48
S2		5.20304	0.378	0.07	22.00	0.31

* Calculated from Eq.3.19.
** Calculated from Eq.3.37.
*** $\sigma_c = \sigma_x + \sigma_y$; Calculated from Eq. 3.16a.

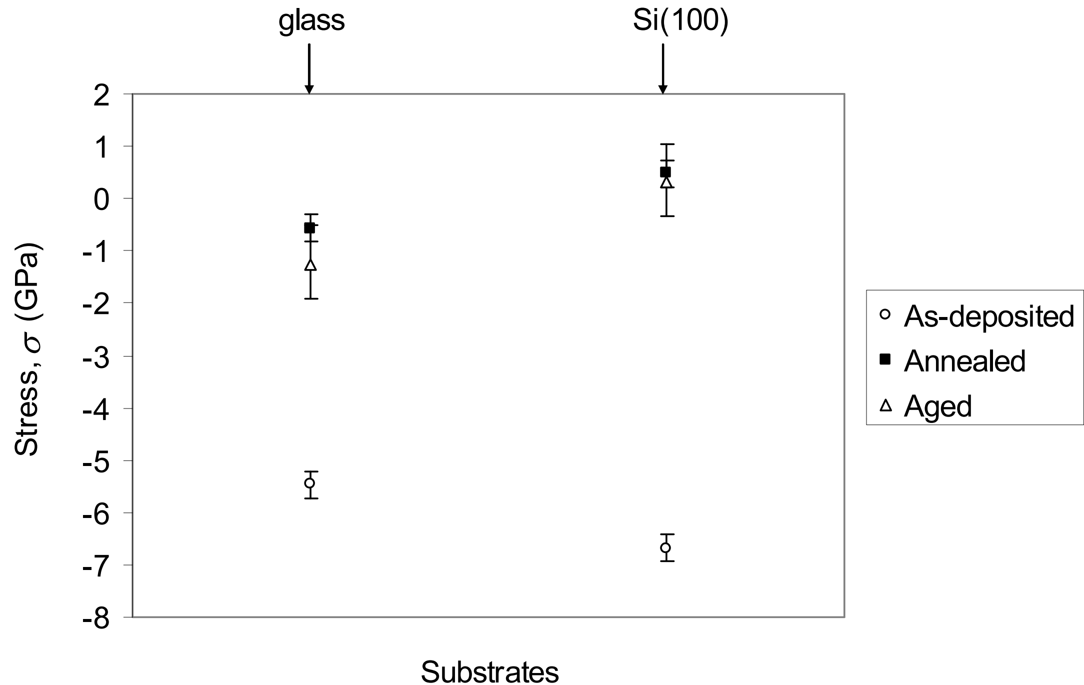

Figure 4.30. Comparison of planar stresses of the ZnO films with T_{s_0} = 200 °C, depending on the substrate type (Set 16 in Table 3.1): as-deposited, after post-deposition annealing in air for 1 hour at 600 °C and aged 28 months.

Apart from these post-deposition treatments, the effect of heat treatment on the samples inside the deposition chamber was also investigated. Among two sets of ZnO film samples that have been deposited at T_s = 200 °C, p = 0.2 mbar, one set was held in vacuum at the deposition temperature for 30 min after the end of deposition (P_{RF} = 100 W; Set 10 in Table 3.1). Another similar set of samples (P_{RF} = 125 W; Set 10 in Table 3.1) was kept at the same deposition temperature for 30 min, under a flow of O_2:Ar (2:5 v/v). Both sets of samples were let cool down after the heat treatment period. The residual stress results of these samples are presented in Table 4.11 and Fig. 4. 31. Heat treament in vacuum, together with the decrease in P_{RF}, led to a decrease in σ_c from -3.32 GPa to -2.23 GPa. (32.8% decrease). With heat treatment under an O_2/Ar flow, σ_c decreased further to -1.89 GPa (43.07% decrease). At the same time, these heat treatments eliminated the (101)-peaks in the XRD scans (Fig. 4.32).

There were simultaneous changes in the microstructure as the stresses were released. SEM examination of the films revealed the formation of porosity in the films upon annealing (Fig. 4.33). The pores formed within the film (Fig. 4.33.a), and/or at the film-substrate interface (Fig. 4.33.b). In some samples, annealing led to the formation of extended voids and consequent damage at the interface (Fig. 4.33.c). In addition to pore formation and pore coalescence, annealing caused cracking in the films. Examining the planar surface of the annealed films revealed the existence of elongated crack-like defects upon pore coalescence on the surface (Fig. 4.34). On the other hand, no pore formation was observed in the films that had been deposited under the same conditions, and those samples were aged, but not annealed (Fig. 4.35). The cracks in those films followed the grain boundaries.

The residual stresses caused buckling and local loss of adhesion of the film, upon either aging (Fig. 4.36), or annealing (Fig. 4.37 and 4.38). Two different buckle types can be seen in Fig. 4.37.a (*flat*-walled) and Fig. 4.37.b (*curved*-walled; δ = 478 nm, b = 666 nm). Protrusions on the annealed ZnO film and consequent cracking of the film on the Si(100) substrate can be seen in Fig. 4.38. Similar behavior was also observed on the aged ZnO film on the glass substrate (Fig. 4.39). Upon further annealing of these aged films, crack propagation and delamination of the film from the substrate was observed (Fig. 4.40).

Another consequence of annealing was the growth of ZnO crystals on the film surface. Fig. 4.41 shows the initial stage of crystal growth on the ZnO film surface upon

annealing. The crystallites in this sample had grown up to 205 nm in diameter. Fig. 4.42 shows further growth of these crystallites on ZnO film on the glass substrate. In some samples, the crystallites grew into *nano-rods*, with the sizes 100 nm in width and 916 nm in height (Fig. 4.42.a). Similar growth was observed on the annealed ZnO film on Si(100) (Fig. 4.42.b). The thickness of the crystallites varied between 82–149 nm, and their height was between 36–174 nm. (Both films were annealed in air at 600 °C for 6h.)

Table 4.11. Variation of residual stress for ZnO films grown on glass substrates at T_s = 200 °C (see Table 3.1). The residual stress decreases by in-chamber annealing at the deposition temperature for 30 min, both in O_2:Ar (2:5 v/v) and in vacuum. $\sigma_{c,ave}$ was calculated from Eq. 3.16a with the data from the (002) XRD peak for each sample. The error range is ±0.55 GPa.

Sample	T_s (°C)	p (mbar)	P_{RF} (W)	$\sigma_{c,ave}$ (GPa)
Set8	200	0.2	125	-3.32
Set10*	200	0.2	100	-1.89
Set11**	200	0.2	125	-2.23

* 30 min annealing at 200 °C under vacuum in the chamber.
** 30 min annealing at 200 °C under O_2:Ar (2:5 v/v) in the chamber.

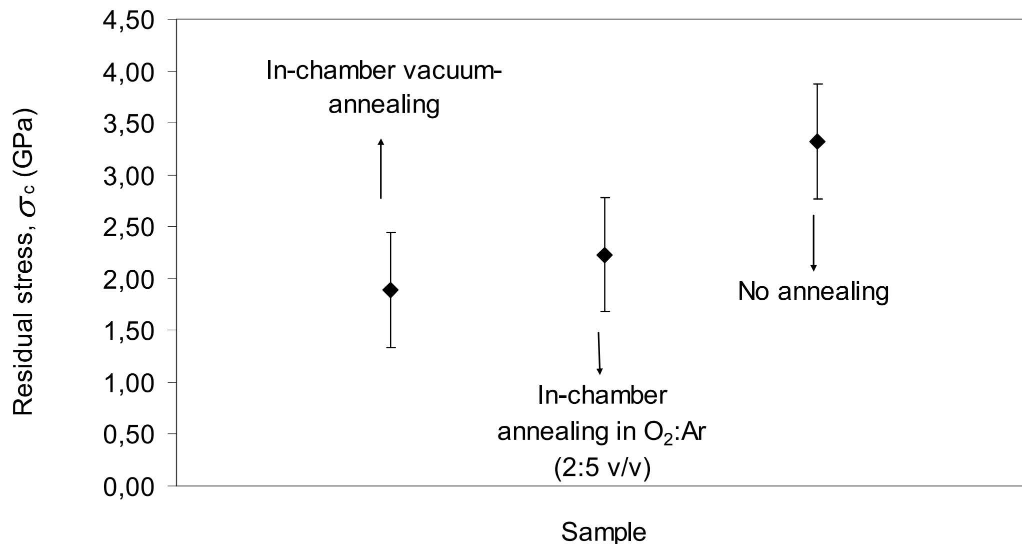

Figure 4.31. Variation of residual stress (σ_c), for ZnO films grown on glass substrates at T_s = 200 °C (see Table 3.1 and 4.9). The residual stress decreases by in-chamber annealing at the deposition temperature for 30 min, both in oxygen (Set 11) and in vacuum (Set 10), with respect to the case with no annealing (Set 8). By convention, a compressive residual stress has a negative value. In the figure, the absolute value of σ_c is given for ease of comparison.

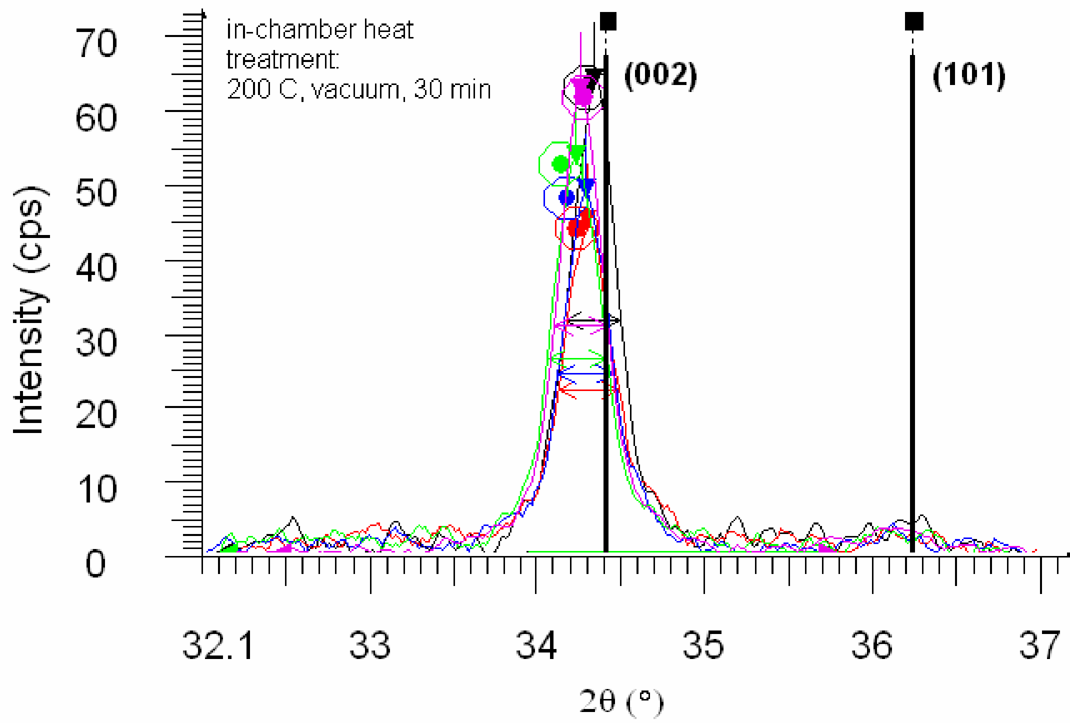

(a)

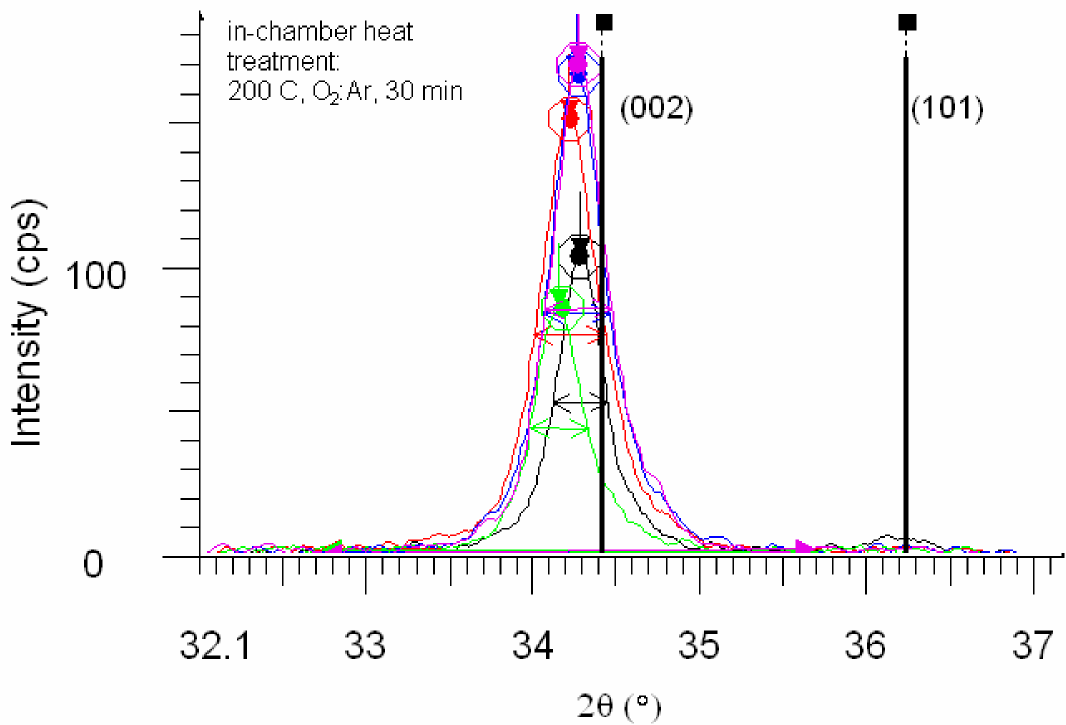

(b)

Figure 4.32. XRD spectra (θ–2θ) of the ZnO films grown on glass at T_s = 200 °C, p = 0.2 mbar; (a) P_{RF} = 100 W, 30 min vacuum annealing in the chamber at 200 °C (Set 10 in Table 3.1); (b) P_{RF} = 125 W, 30 min annealing in O_2:Ar (2:5 v/v) inside the chamber at 200 °C (Set 11 in Table 3.1).

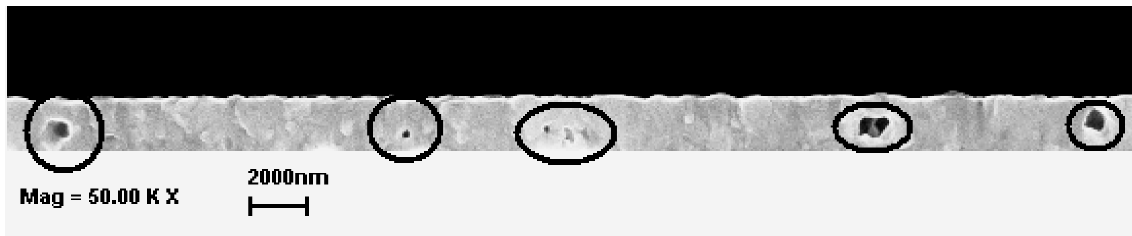

(a)

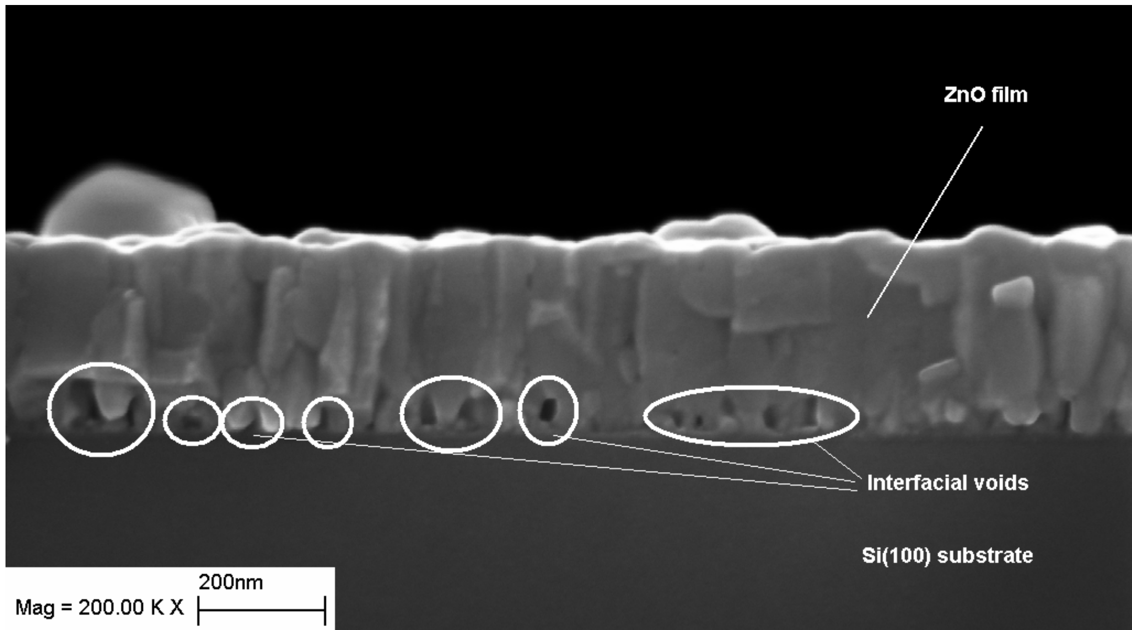

(b)

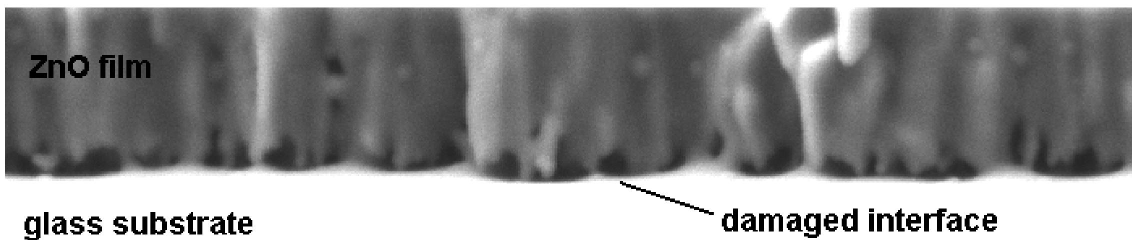

(c)

Figure 4.33. Damage on the films by annealing in air at 600 °C for 6 h: (a) Void formation within the ZnO film on glass (Set 16 in Table 3.1); (b) interfacial damage in the ZnO film on Si(100) (Set 17 in Table 3.1); (c) destroyed interface of the ZnO film on glass (Set 19 in Table 3.1).

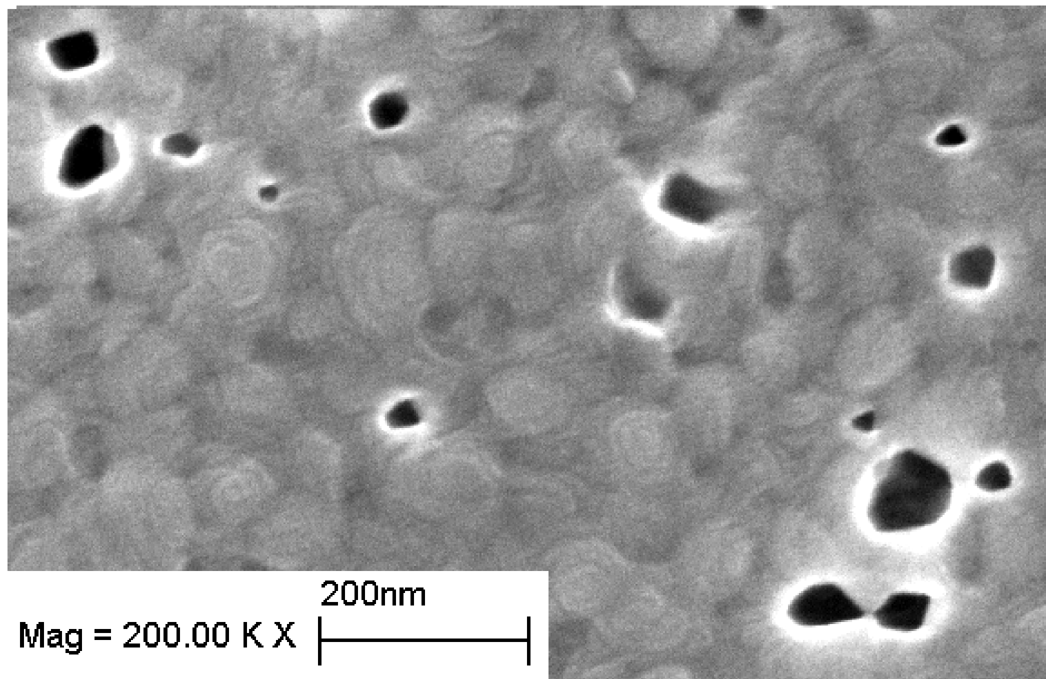

(a)

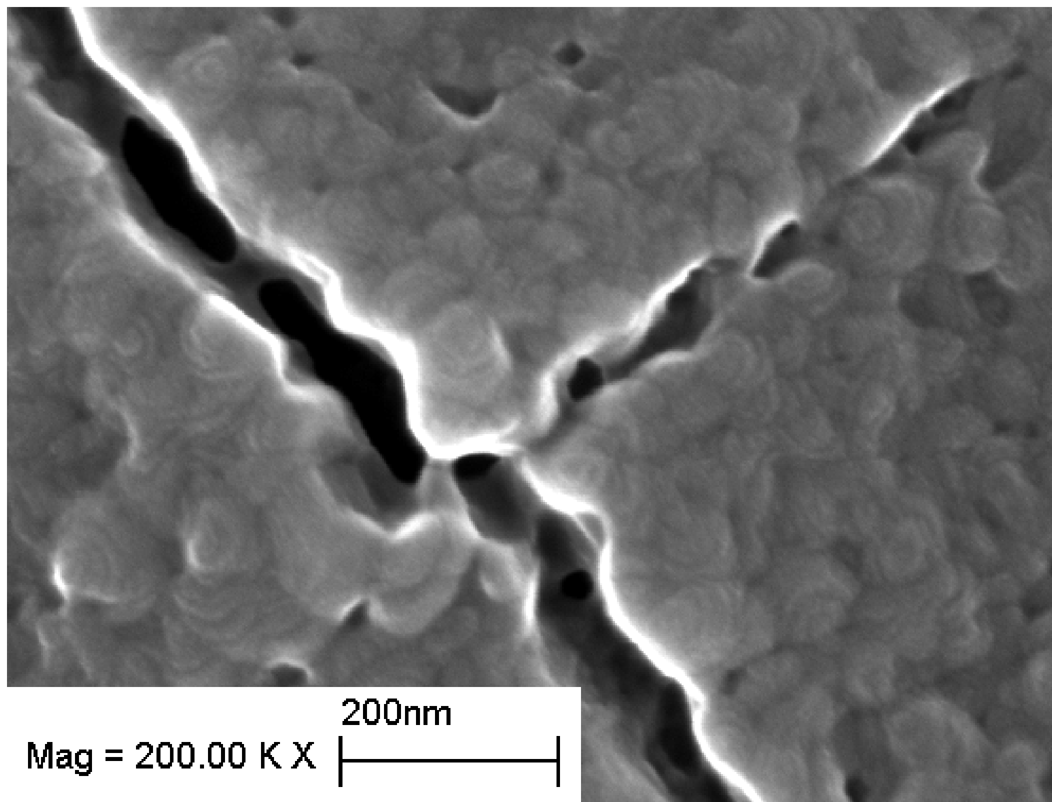

(b)

Figure 4.34. Crack formation on ZnO film on glass substrate (Set 17 in Table 3.1) through pore clustering upon annealing (in air at 600 °C for 6 h).

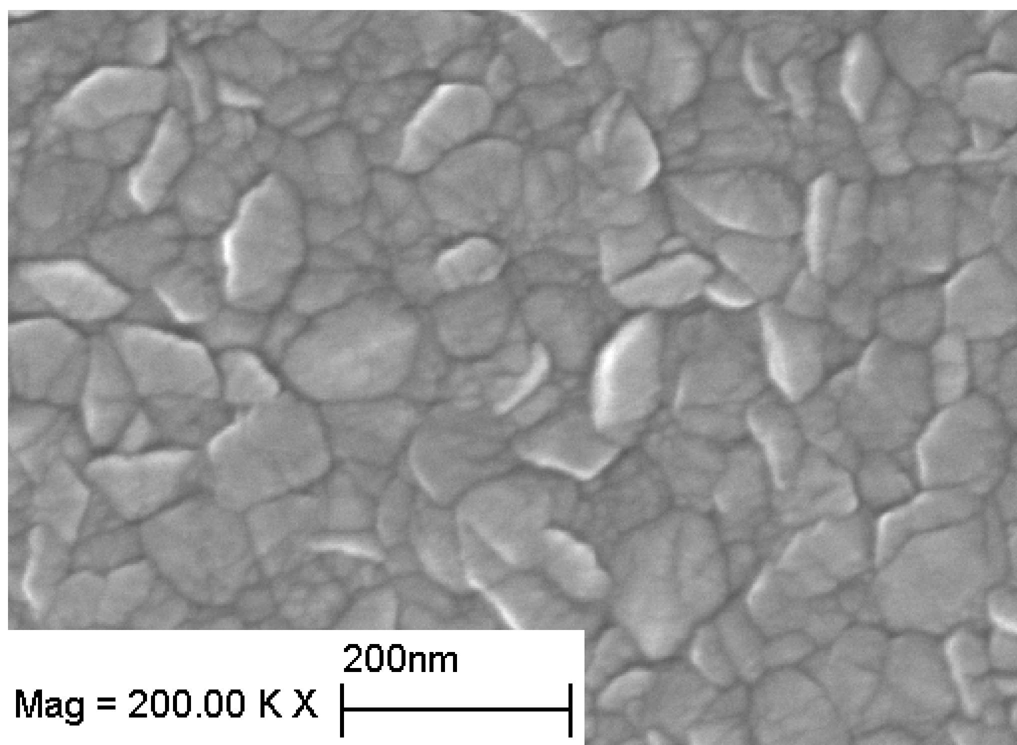

(a)

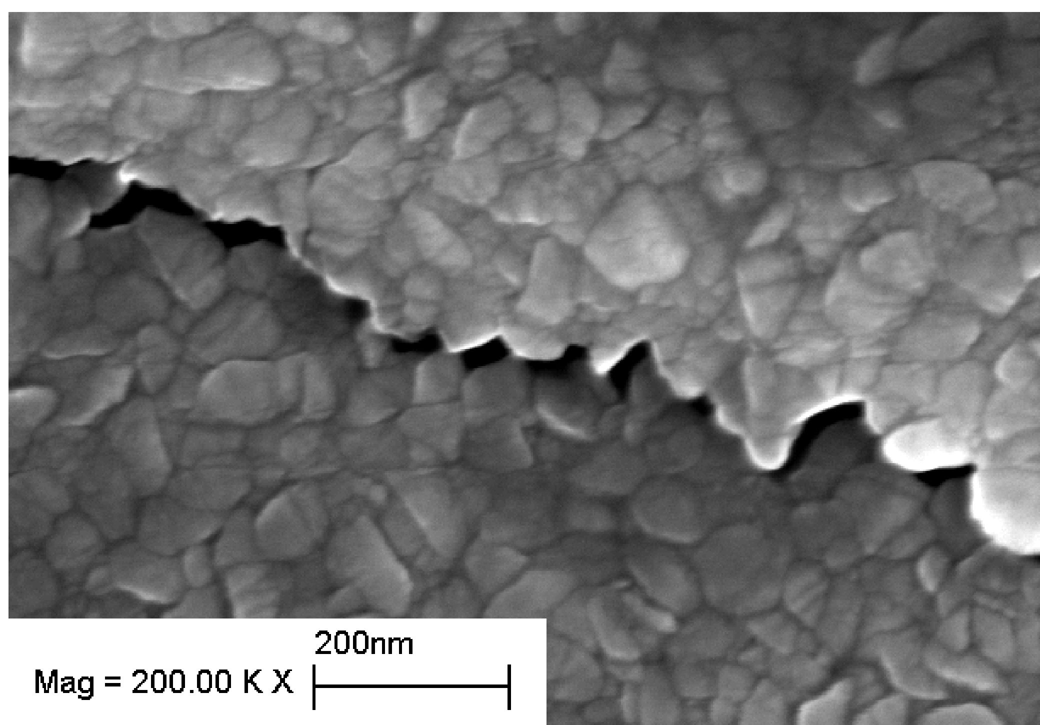

(b)

Figure 4.35. Crack formation on ZnO film on glass substrate (Set 17 in Table 3.1) through grain boundary detachment upon aging (in air for 28 months).

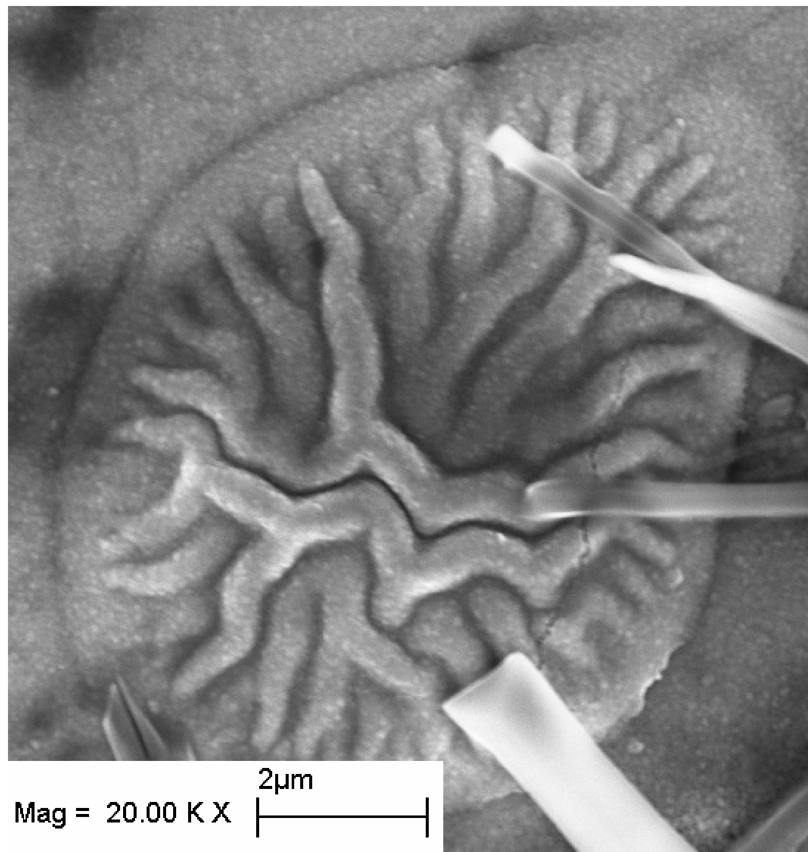

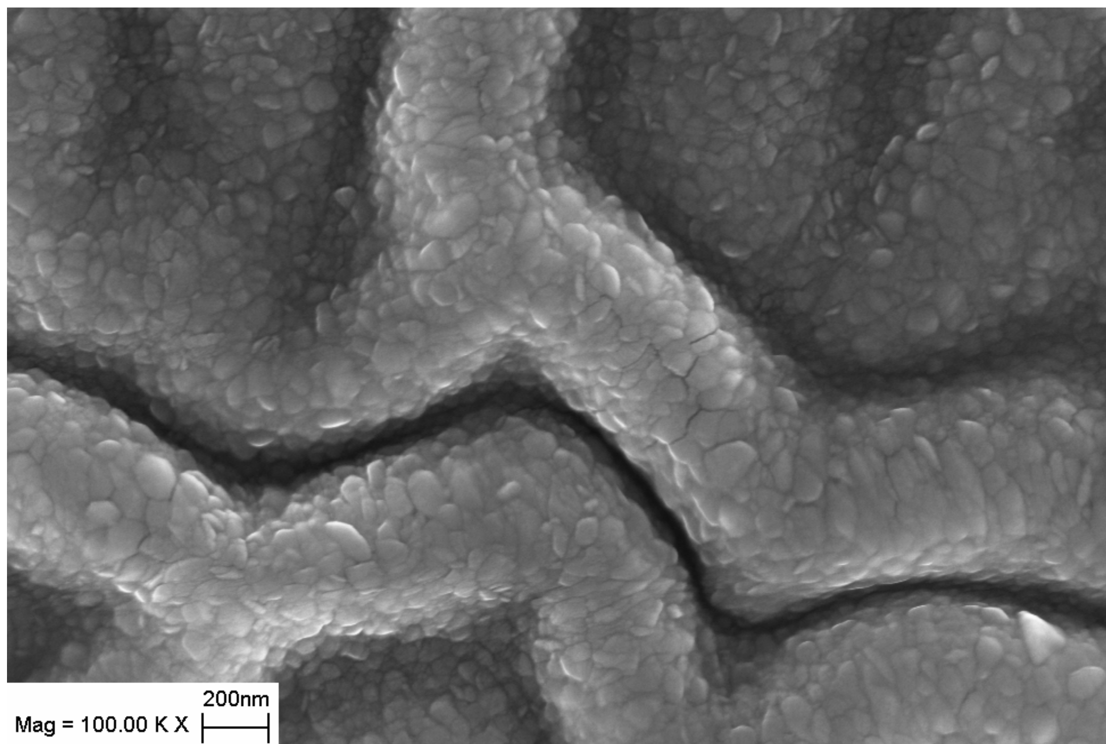

Figure 4.36. Buckling in the ZnO film on glass substrate (Set 16 in Table 3.1; aged 28 months in air), occurred presumably around a pre-existing defect on the substrate.

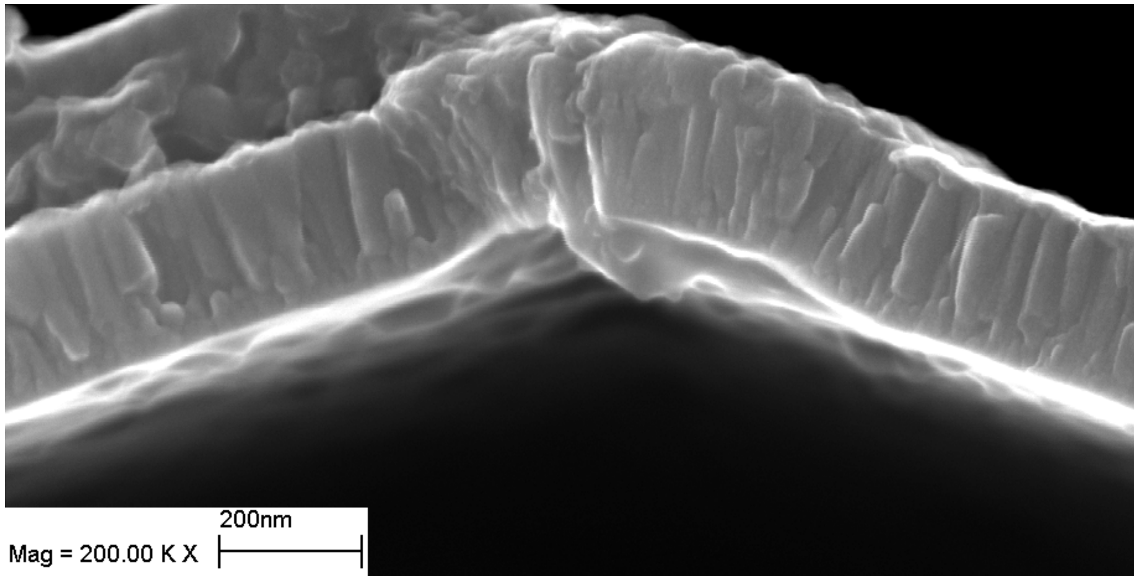

(a)

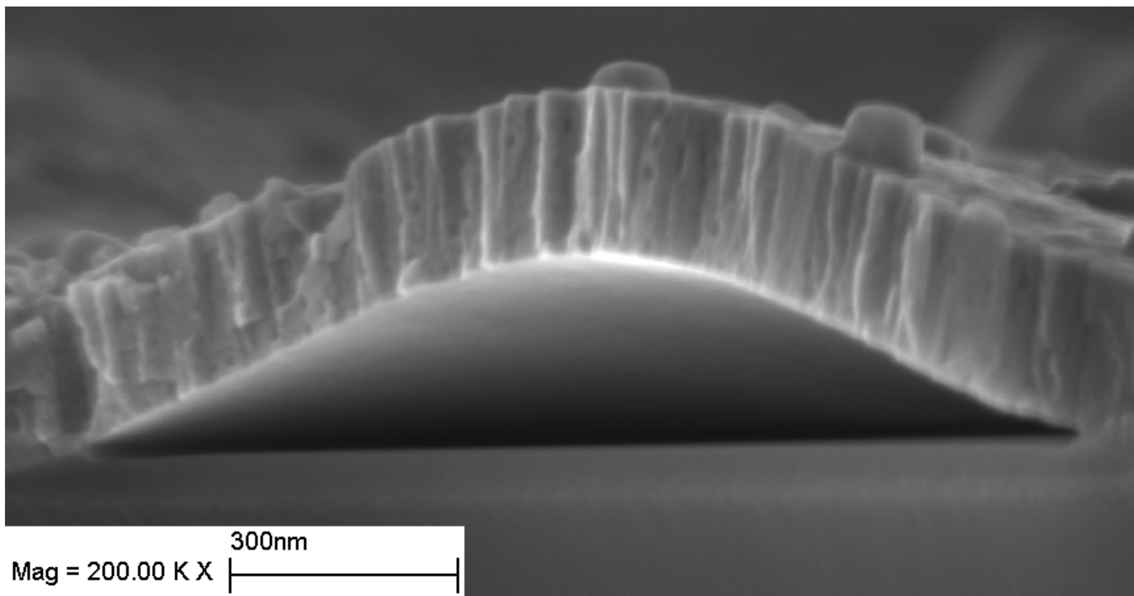

(b)

Figure 4.37. Two different types of buckles: (a) a straight-sided buckle on the ZnO film on glass with T_s = RT (Set 17 in Table 3.1); (b) a curved-sided buckle on the ZnO film on Si(100) with T_s = 200 °C (Set 16 in Table 3.1). Film in (b) was aged 28 months in air. Both films were annealed in air at 600 °C for 6 hours.

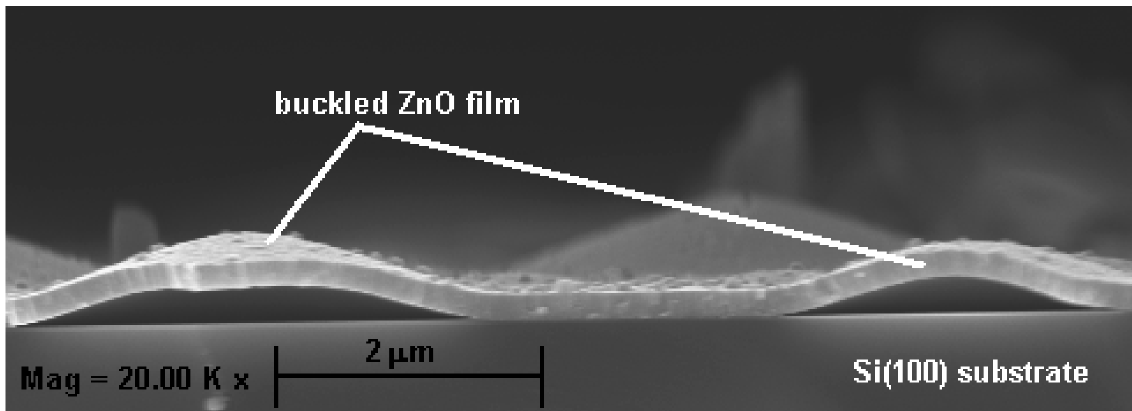

(a)

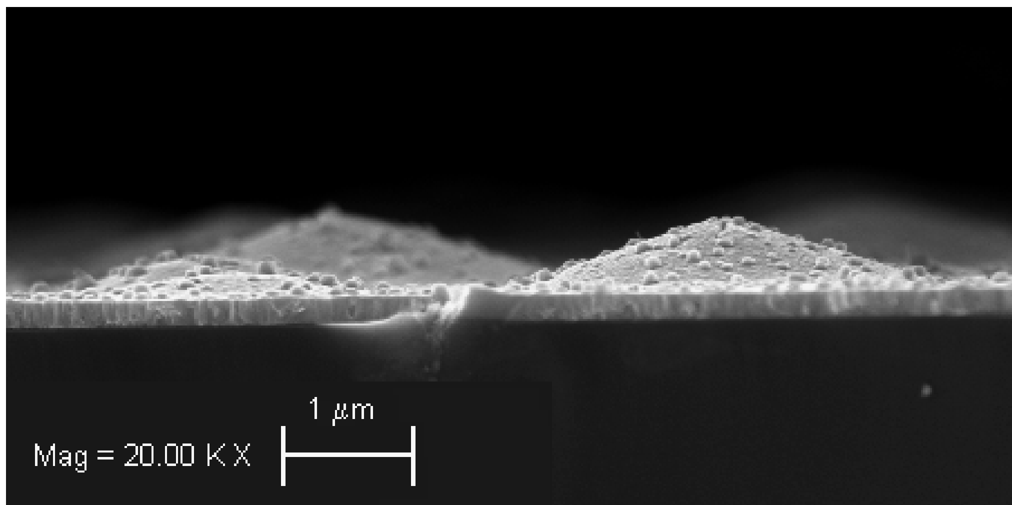

(b)

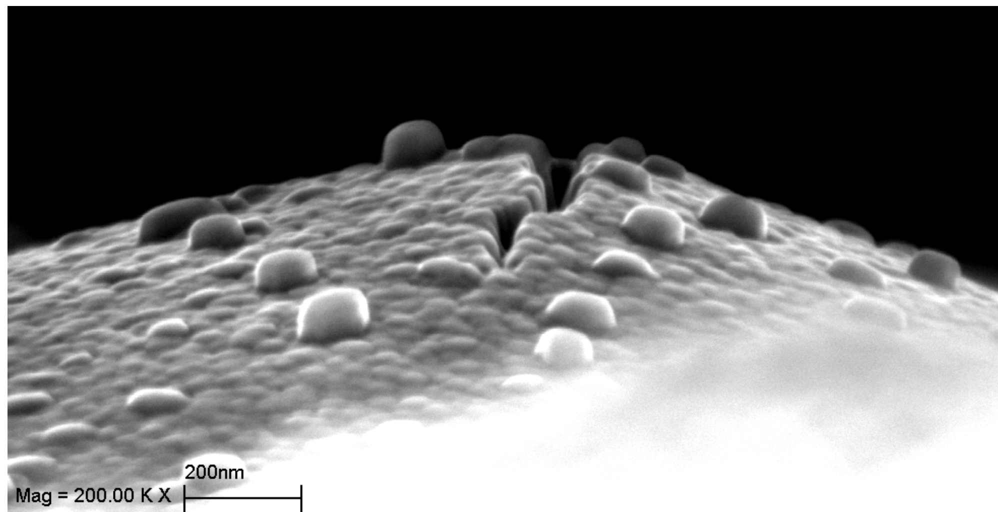

(c)

Figure 4.38. Buckling and local loss of adhesion in the ZnO film upon stress relaxation (Set 16 in Table 3.1; annealed in air at 600 °C for 6h): (a) buckles seen from the side view of the film, (b) protrusions on the film surface, (c) crack at the protrusion center.

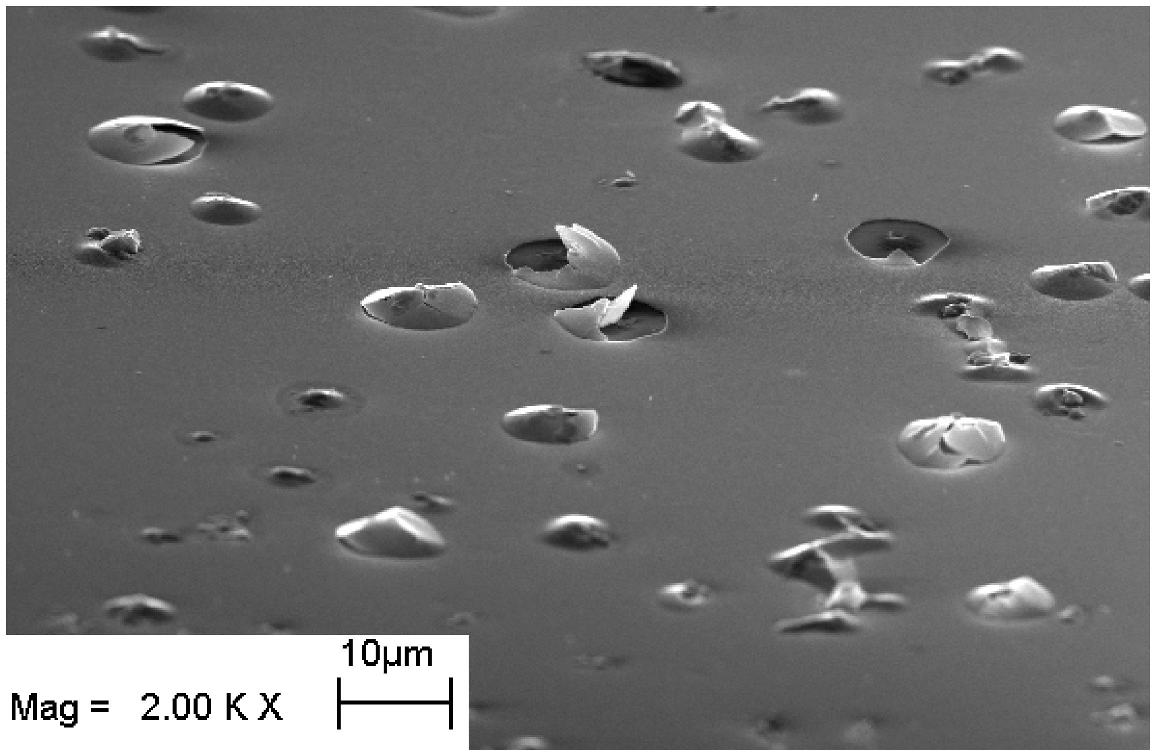

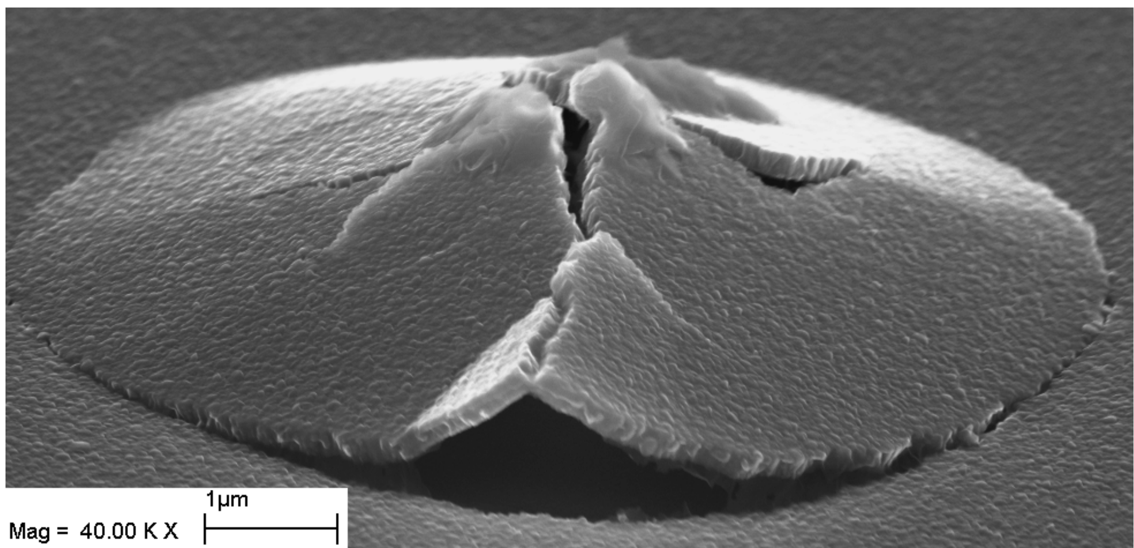

Figure 4.39. Bulging and cracking in the ZnO film on glass upon prolonged aging (Set 16 in Table 3.1; aged 28 months in air).

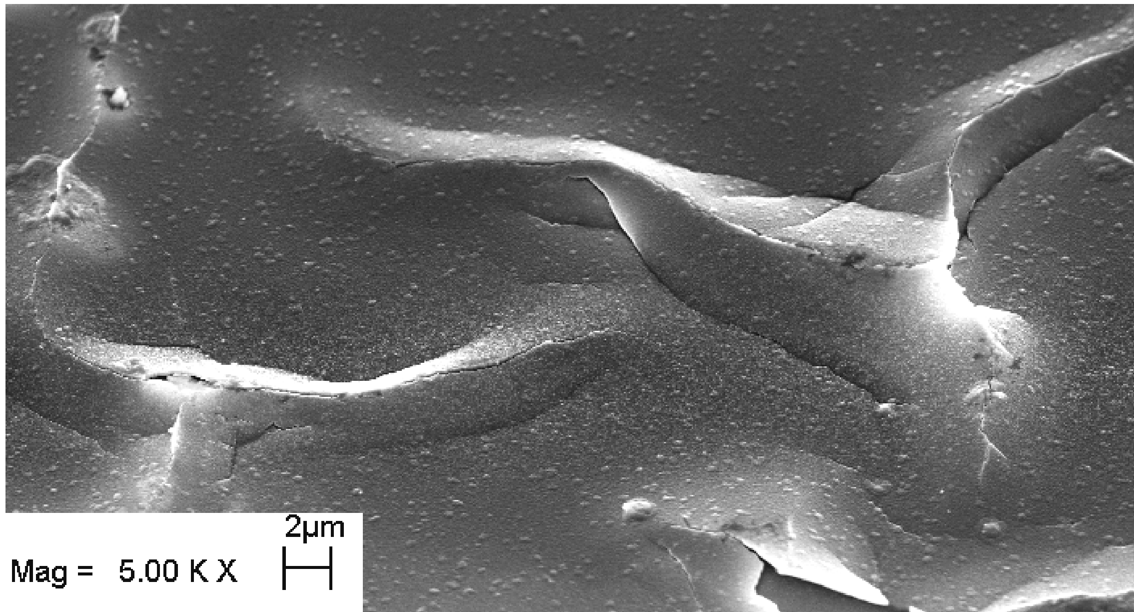

(a)

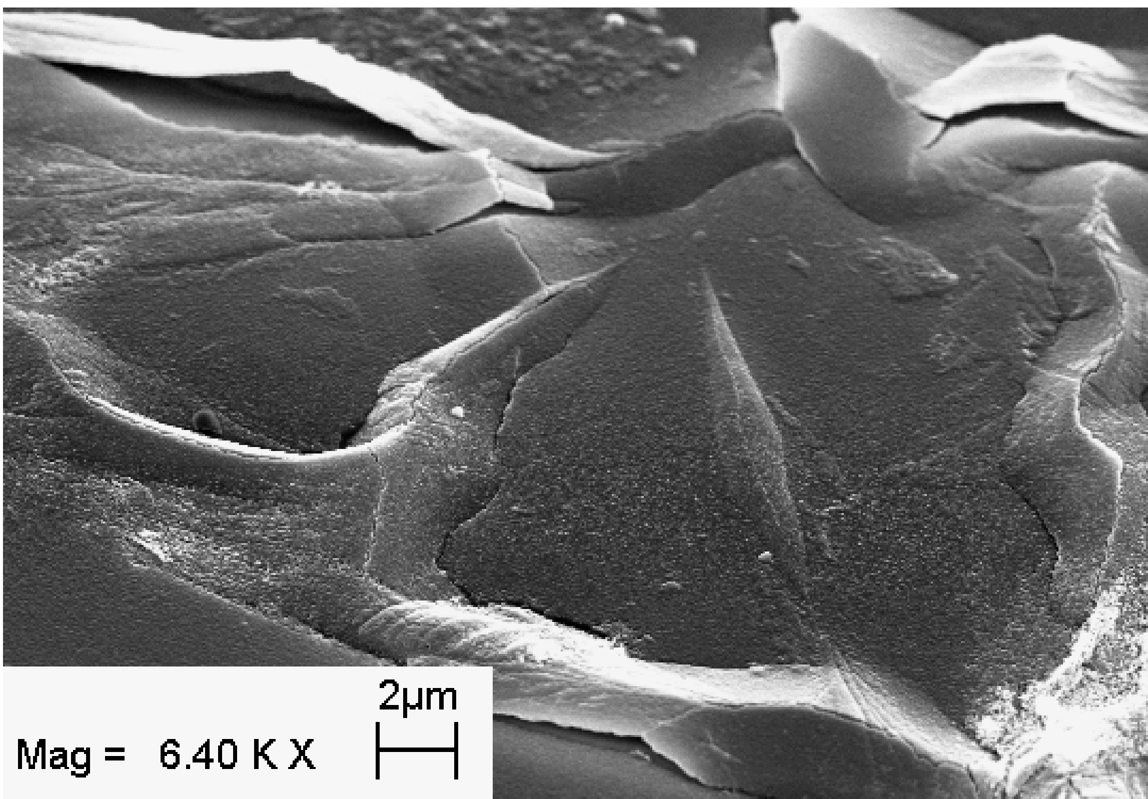

(b)

Figure 4.40. Cracking in the ZnO film on glass upon prolonged aging (28 months), followed by annealing (in air at 600 °C for 6h): (a) Set 17 in Table 3.1; (b) Set 16 in Table 3.1.

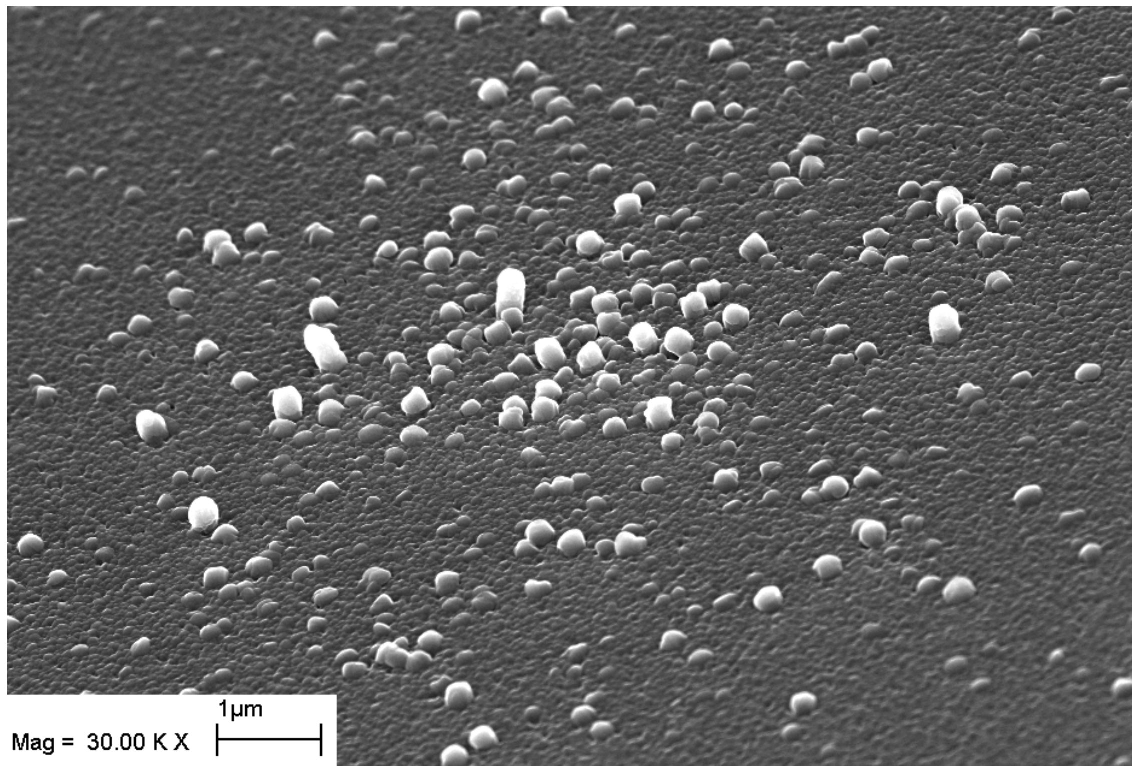

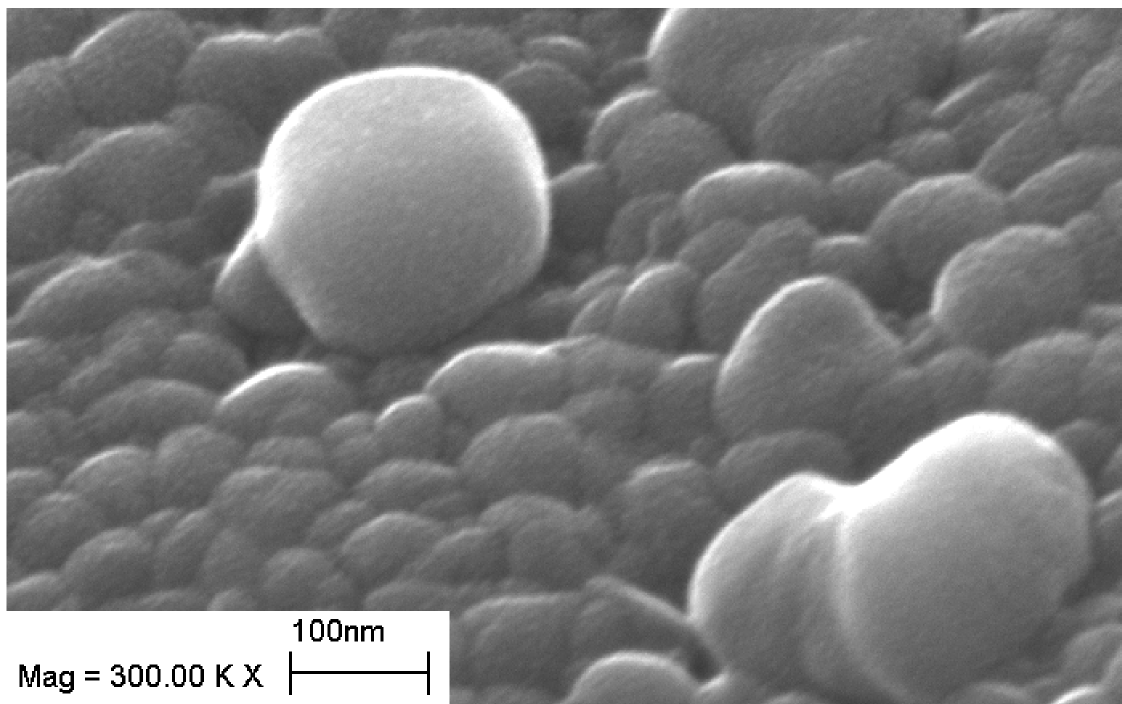

Figure 4.41. Initial stage of crystal growth on the ZnO film surface upon annealing (Set 16 in Table 3.1; annealed in air at 600 °C for 6h). The crystallites in this sample have grown up to 205 nm in diameter.

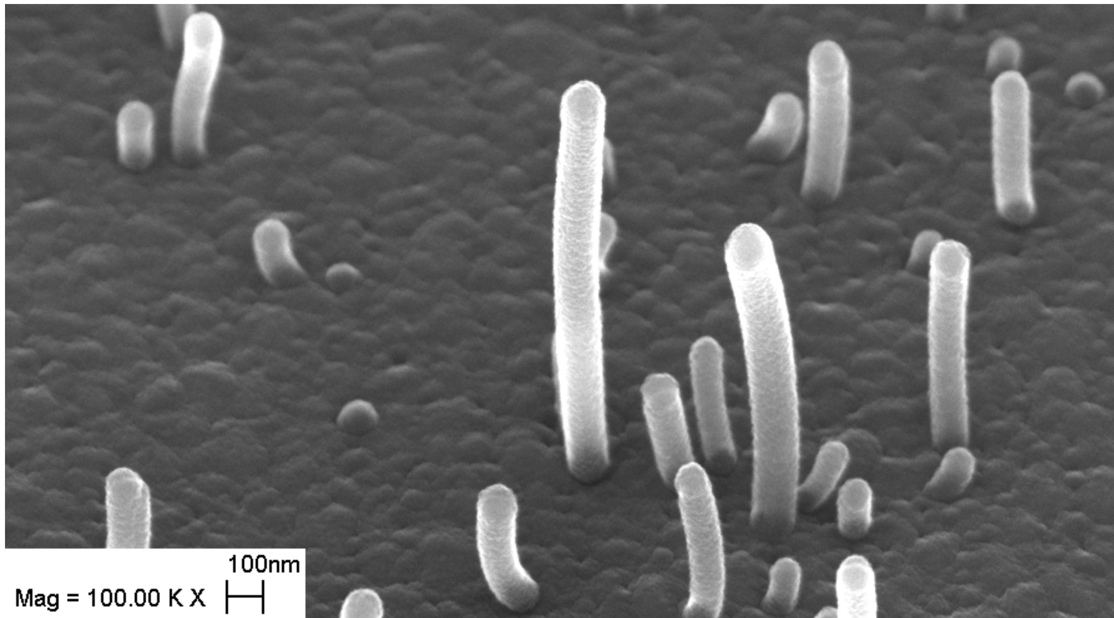

(a)

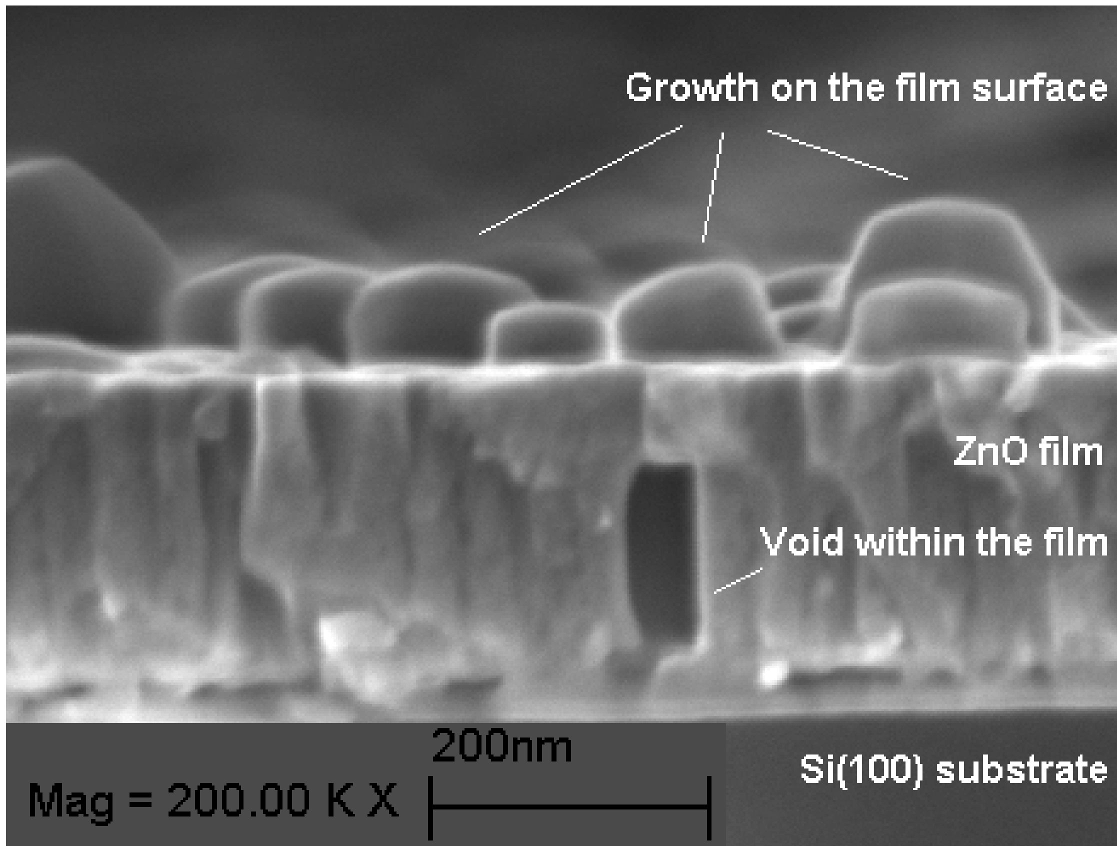

(b)

Figure 4.42. Growth of ZnO crystallites on the film surface upon annealing. (a) ZnO on glass (Set 20 in Table 3.1). The nano-rod thickness was about 100 nm, and the rods elongated up to 916 nm. (b) ZnO on Si(100) (Set 16 in Table 3.1). The thickness of the crystallites is between 82–149 nm, and their height is between 36–174 nm. Both films were annealed in air at 600 °C for 6h.

CHAPTER 5

DISCUSSION

In this chapter, the experimental results that have been presented in Chapter 4 are discussed, and compared with the literature results: *i)* microstructure and texture of ZnO thin films, *ii)* residual stresses and their origins, *iii)* stress relaxation. Some of the results were repeated briefly for ease of discussion.

5.1. Microstructure and Texture of ZnO Thin Films

In Chapter 1, the *structure zone models,* describing the thin film microstructure were presented. The microstructure of thin films in these models depended on the amount of energy and the mobility of the adatoms on the surface [51, 52, 54-57]. The energy and mobility of the adatom were determined by

i) the substrate temperature (T_s), or rather the homologous temperature (T_h) (thermally induced mobility),

ii) the incident ion energy, which was dictated primarily by the chamber pressure (p) and the energetic particle bombardment of the film during deposition (momentum-induced mobility).

A recent updated model summarized the five zones depending on T_h and p [51], and these zones are illustrated in Fig. 5.1:

i) *Zone 1:* This zone was characterized by low adatom mobility. The sticking coefficient (the ratio of the adatoms adsorbed to the overall number of adatoms incident on the surface) was equal to one. The dominating factor is the *shadowing* effect.

Shadowing caused a low number of nuclei and a film with a network of interconnected voids that defined columns of material (*i.e.*, longitudinal porosity). The low adatom mobility also led to columns that competed for growth in a power-law shape, forming hierarchical aggregates and cauliflower type structures, bundles of smaller and equiaxed grains [51, 58-60].

ii) *Zone T:* This was a transition zone between Zone 1 and Zone 2. The increased substrate temperature led to densely packed, fibrous grains with weak grain boundaries. The temperature for the transition zone shifted to higher temperatures with increasing gas pressure.

iii) *Zone 2: Surface diffusion* increased with T_h, due to the increased adatom mobility, giving rise to columnar grains with increased width, increased density, and well-defined grain boundaries. The activation energy for grain growth for metallic films were the same order of magnitude with the activation energy for surface diffusion, and also similar to that of g*rain boundary diffusion* [58]. As the temperature increased, the Zone 2 columns became faceted.

iv) *Zone M:* By increasing the pressure in Zone T, matchstick morphology was obtained. In this zone, the columns were parallel to each other and they contain dome-shaped tops [63].

v) *Zone 3:* Upon increasing T_h further, *bulk diffusion* dominated forming a highly dense film structure composed of equiaxed grains.

Several competing mechanisms of film evolution were proposed. The stages of this process were presented in detail in Sec. 1.2. During the formation of the first few monolayers, there was competition between the *nucleation* and *growth* processes [2, 50-52]. Their relative weight determined the relative amounts of *islands* and the *layers*. When the bonding between the atoms or molecules of the film material was stronger than that of the film-substrate bonding, island-type of growth was observed. The smallest stable cluster of the film material nucleated on the substrate, and grew in three dimensions. In the reverse case, when the atoms of the film material tended to bond more strongly to the substrate than to each other, the stable clusters grew much more rapidly in two-dimensions namely on the substrate surface, and they form layers on the substrate [2, 50-52]. For ZnO films, it was proposed that island formation dominated when the film thickness was less than 100 Å [136]. After the initial stages of nucleation

and growth, the relative weight of the following effects determined the film formation kinetics, and hence, the final film structure. [50, 54]:

i) shadowing and transport of adatoms onto the substrate,

ii) adsorption and surface diffusion,

iii) incorporation of adatoms into the coating or removal by evaporation or desorption,

iv) transport of the adatoms to their final positions by bulk diffusion.

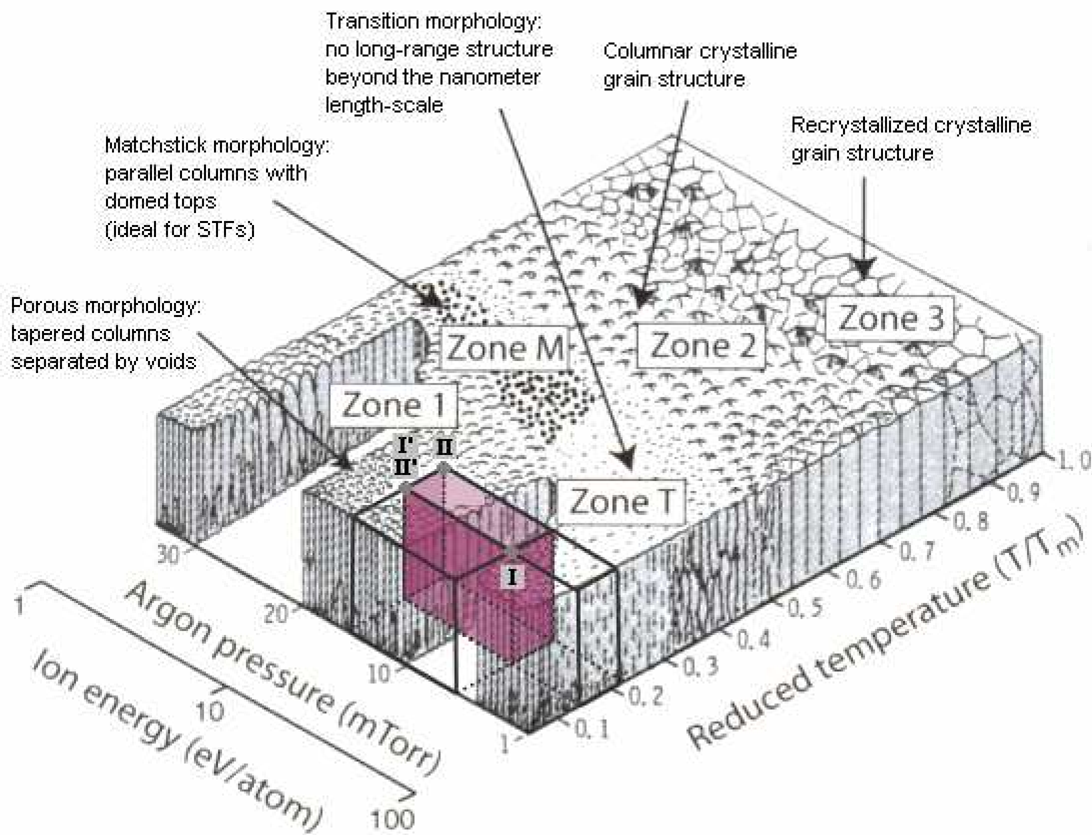

Figure 5.1. A recent structure-zone model developed by Messier and Trolier-McKinstry, also showing the region of operation in part of our study discussed in Sec. 5.1 (T_S = RT–200 °C, p = 6.8–15 mTorr, P_{RF} = 100 W). (Adapted from Ref. [51]; original figure by Ref. [63]; published with permission from SPIE Press and Elsevier Publishing Ltd.).

Due to the *shadowing* effects, not all the atoms incident on the surface had the same line-of-sight [50, 54]. Thus, the adatoms had a limited range of positions on which they can be settled, defining an anisotropic film structure. As the film grew further, the structural anisotropy became more pronounced as a preferred direction was promoted faster over the other crystallographic directions of the material. Here, the film growth had two branches: the growth of the crystal planes, and the growth of the grains [210]. The shadowing effect was controlled mainly by the deposition parameters of the system, such as the system geometry and the gas pressure. On the other hand, the diffusion and adsorption-desorption behavior were mainly dictated by the substrate temperature and the resulting adatom mobility on the surface.

It should be kept in mind that previous structure zone models that have been developed are based primarily on studies of metallic thin films. Most ceramics have much more complicated and more anisotropic crystal structures. They also have more than one type of ions. Therefore, they may have more complicated growth mechanisms than the metals, leading to variations in the previously defined structure zone models. In ZnO, an additional anisotropy comes from the crystal structure itself (see Fig. 1.1 and 1.2). For ZnO thin films, the studies on the relations between several deposition parameters and the resulting thin film structure were summarized in Chapter 1. It would be helpful to the reader to repeat the general affects of deposition parameters on the film growth behavior together with some examples here:

i) Increasing the substrate temperature generally induced an increase in the adatom mobility and improved structural homogeneity. However, T_s should also be optimized for strongest texture (presumably due to microcrack formation above 400 °C [111]) or minimum roughness (due to grain over-growth above 300 °C [95]).

ii) The number of collisions increased between the gas molecules and sputtered atoms by increasing total pressure, effectively reducing the energy of the particles adsorbing on the substrate. Therefore, the mobility of the adatoms decreased. On the other hand, deposition rate and film stoichiometry (O/Zn ratio) decreased with increasing pressure. For example, optimum p for maximum deposition rate, maximum O/Zn ratio, and minimum *FWHM* in XRD was 1 Pa = 0.1 mbar in Ref. [96]. In another study for DC-magnetron sputtered ZnO films, the deposition rate increased for p = 0.2–3.0 Pa (0.002–0.03 mbar), while the p range for maximum structural homogeneity and the highest crystallinity was only in the 0.6–0.8 Pa (0.006–0.008 mbar) range [115].

iii) Other than the total gas pressure, the effects varying the partial oxygen pressure during reactive sputtering had been studied. Since ZnO tended to grow with oxygen vacancies and zinc interstitials, providing extra oxygen was beneficial for maintaining stoichiometry [99]. However, the oxygen content should be optimized for the best film quality. For example, optimum p_{O_2} was 0.01 Pa (0.0001 mbar; 10% O_2 in Ar) for the maximum XRD peak intensity [96], and 40% O_2 in Ar resulted in minimum film roughness [95] and minimum *FWHM* in XRD with maximum peak intensity [111].

iv) A similar discussion held for the RF power as with the chamber pressure; however these two parameters had opposite effects on the adatom energy and consequent microstructure formation. Increasing the RF power increased the energy of the particles incident on the substrate surface. Therefore, the adatom mobility increased. The film crystallinity improved; a denser film and better–oriented grains were obtained (*e.g.*, in the 1.28–1.90 W/cm^2 [96, 99], or 300–600 W [112] ranges). However, increasing the RF powers could have been disadvantageous for the film's crystal structure since the sputtering yield and the deposition rate increased with the increasing RF power (for example, deposition rate increased six-fold in the 25–100 W P_{RF} range [102]). The deposition rate should be optimized to allow the adatoms enough time to seek minimum energy positions, before subsequent adatoms arrived at the surface. Therefore, there was an optimum P_{RF} value for the highest peak intensity and minimum *FWHM* in the XRD spectra (*e.g.* optimum P_{RF} = 600 W in Ref. [112]), or maximum grain size (*e.g.*, grain size decreased rapidly for $P_{RF} > 50$ W in Ref. [102]).

Having repeated the affects of the deposition parameters on the thin film structure in the literature, it is obvious that these parameters should be optimized for the desired film structure which could be represented by a SZM. A recent structure zone model on ZnO films was proposed by Mirica *et al.* [136, 137]. The films were deposited by RFMS at a constant pressure of 0.007 mbar (5.2 mTorr) and substrate temperatures between room temperature and 700 °C. They pointed out the difference in morphological development between metal and metal oxide films and impact of the differences on the structure zone models. In their model, the formation of previously defined high-temperature structures was achieved at lower homologous temperatures, because of the effects of collision between high-energy particles. Increasing the substrate temperature overcame the shadowing effect by increased surface diffusion (the valleys that were created by shadowing were filled with the diffusing atoms). Therefore,

the transition zone was eliminated by substrate heating (Fig. 1.25). They described two sub-zones within Zone 2. Zone 2a was composed of film with faceted columns and a rough surface. Films in Zone 2b were smoother, denser, and highly textured. However, the columns had pitted tops, owing to the limited surface diffusion.

In light of the various factors affecting the microstructure of thin films, our results about ZnO film microstructure will be discussed in Sec. 5.1.1–5.1.4.

5.1.1. Effect of the Substrate Material on the Film Microstructure

The microstructural evolution of the ZnO films in our study was monitored as a function of the substrate material at various conditions. In Fig. 5.1, points I–I′ (p = 0.009–0.02 mbar = 6.8–15 mTorr, T_s = RT; Set 17) and II–II′ (p = 0.02 mbar = 15 mTorr, T_s = 200 °C–RT; Set 16) represent the two sets of film depositions performed to compare the substrate effects. The range of this operation is marked as the shaded area in Fig. 5.1. The homologous temperature ranges of these sets were 0.13–0.14 and 0.21–0.14, respectively. According to Fig. 5.1, a Zone 1 structure (porous morphology with tapered columns separated by voids) was expected for these ranges of deposition parameters.

For the glass substrate, the 0.009–0.02 mbar (6.8–15 mTorr) and RT (T_h = 0.13) conditions resulted in a microstructure (Fig. 4.1.a) that was between Zone T (no long-range structure beyond the nanometer length scale) and Zone 2 (a columnar crystallite grain structure). By increasing both the initial temperature (T_s = 200 °C, T_h = 0.21) and initial pressure (0.02 mbar = 15 mTorr), the grains evolved to a structure similar to that in Zone 1 (Fig. 4.1.b). As explained in detail in Sec. 1.2.1 and summarized above, the chamber pressure and substrate temperature have opposite effects on the energy of the adatoms. Increasing the chamber pressure causes an increase in the number of collisions of the particles along their path to the substrate, hence, decreasing their energy. On the other hand, increasing the substrate temperature provides thermally induced mobility to the adatoms. Between these two competing mechanisms, one might dominate over the other to dictate the final film structure. In the cases described above, the pressure had a more dominant effect than increasing the substrate temperature. Otherwise, a transition to Zone 2 (a columnar crystallite grain structure) would have been observed for the ZnO

films on glass in Fig. 4.1.a (at the conditions from point I to point I′ in Fig. 5.1), when compared to those in Fig. 4.1.b (at the conditions from point II to point II′ in Fig. 5.1).

On the Si(100) substrate, at 0.009–0.02 mbar (6.8–15 mTorr) and RT (T_h = 0.13), the ZnO films had a well-defined columnar structure (Zone 2; Fig. 4.2.a). By increasing both the initial temperature and initial pressure, the grains gained a slightly more tapered structure with inter-columnar voids, like those in Zone 1 (Fig. 4.2.b). These results were consistent with the dominance of the increasing pressure effect (*i.e.*, less energetic adsorbed species) over the increasing temperature effect (*i.e.*, increased adatom mobility at the surface and increased surface or bulk diffusion).

To summarize, at lower T_h and lower p conditions, the SZM showed deviations from the expected Zone 1 structure, depicted by the currently accepted model for metallic films, towards the higher mobility zones for both substrates. This trend of reaching the higher mobility zones at lower T_h values then expected was in accordance with the work of Mirica *et al.* [136, 137]. Considering our results, it could be concluded that at very low mobility conditions for ZnO films, decreasing p was more critical than increasing T_h for the purpose of increasing the adatom mobility.

The effects of deposition parameters on the film microstructure will be discussed in greater detail in Sec. 5.1.2. Some aspects were included here only to emphasize the effects of different substrates. When the effects of the two different substrates are compared, it is evident that the crystallinity of the substrate had an influence on the microstructure of the film. When the substrate was amorphous, many equiaxed grains were seen at the interface, indicating the presence of a randomly oriented layer (Fig. 5.2). Such a structure of fine, equiaxed grains still existed for the films on the Si(100) substrate at the same deposition conditions with the glass substrate, but was considerably less pronounced. In addition, the films grown on this substrate had a better-defined and less tapered columnar grain structure (Zone 2) than the films on the amorphous substrate (Zone T–Zone 2). This improved columnar structure of the film could be related to a more crystalline, more strongly textured (along the *c*-direction), and more densely nucleated interface layer on the Si(100) substrate than the one on the glass substrate (Fig. 5.3).

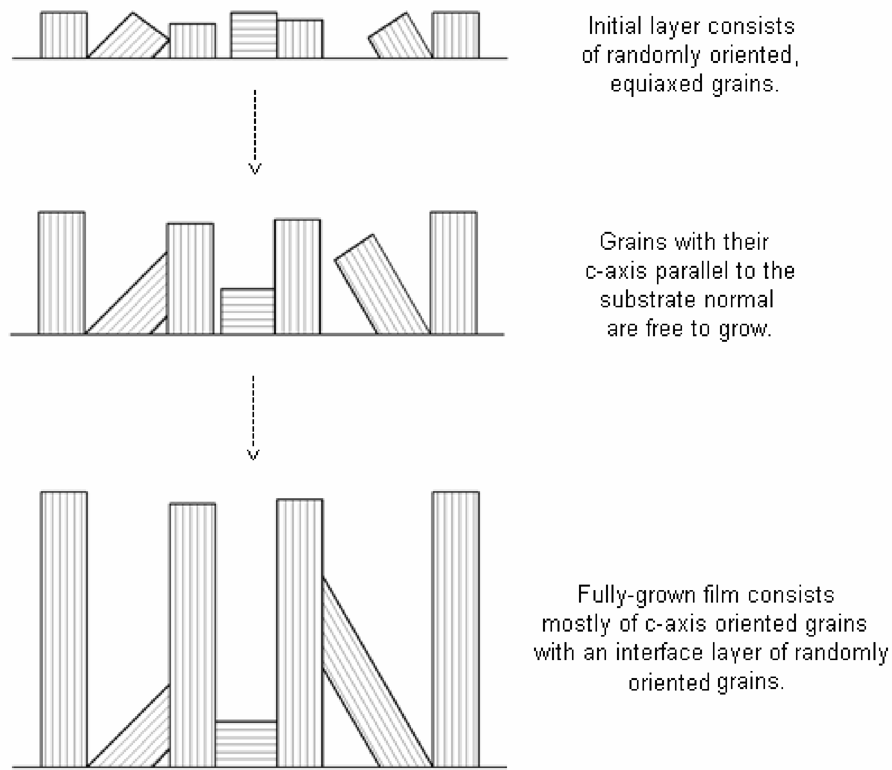

Figure 5.2 A film structure with a randomly-oriented layer at the substrate interface. Only the fastest growing directions survive and form the strongly textured film.

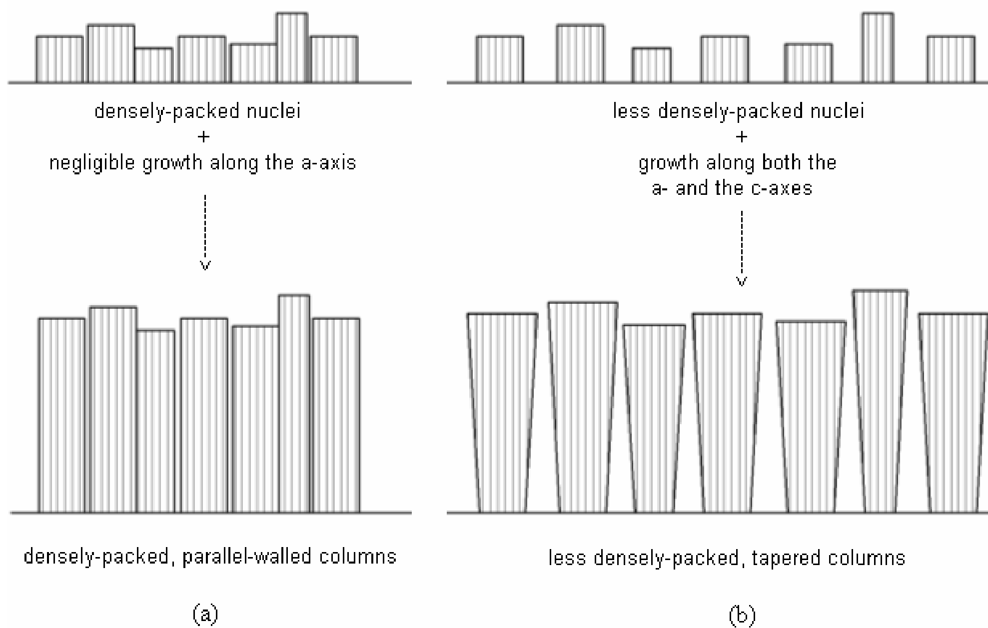

Figure 5.3. Two different growth behaviors on an initial layer of textured nuclei. The nuclei continue to grown in the preferred orientation. The film microstructure depends on the nucleation density and the growth rate of different crystal faces.

The crystalline surface of the Si substrate could provide a better template for ZnO by promoting *preferential nucleation* over *random nucleation* (*"Preferential nucleation is a process in which initial nuclei with a specific crystallographic direction normal to the substrate preferentially nucleates on the substrate. The direction is determined by the surface energy when the interfacial energy between the substrate and the nuclei can be ignored, and therefore preferred orientation becomes the direction with the lowest surface energy plane parallel to the substrate."* [210]). This interpretation would be consistent with observations of ZnO films grown by RFMS on glass, Al, Au, and sapphire substrates [211]. An initially randomly oriented layer upon random nucleation was found at the ZnO film-substrate interface, on both the glass substrates and the Al substrates with a native oxide layer on their surface. The films with the amorphous interface grew with polycrystalline morphology. On the other hand, the films on the Au and sapphire substrates grew epitaxially, without first forming an interface layer [211]. Similarly, the ZnO film grown on (111)-textured Pt by RFMS was free of either an amorphous interface layer or one with equiaxed grains. These films were also more crystalline and more strongly textured than the film grown on Si(100) substrate with a native oxide layer on top [137]. The degree of orientation of the initial layers was at least partially determined by the crystallinity of the substrate—the ZnO films had a better *c*-oriented structure and better defined micro-columns on the crystalline substrate.

To summarize, microstructure shifted to more ordered regions then dictated by the most recent SZM. The effect of increasing p in the 0.009–0.02 mbar range was more effective on the microstructure then increasing T_s from RT to 200 °C. Based on the SEM observations, although the lattice structure of the film and the substrate did not match (*i.e.* non-epitaxial film growth), substrate crystallinity had an impact on the film microstructure—presumably due to preferential nucleation on the crystalline substrate. However, separate texture measurements by XRD and TEM focusing on the interface layer should be conducted to achieve such a conclusion.

5.1.2. Effect of the Deposition Parameters on the Film Microstructure and Texture

The effects of deposition parameters on the microstructure of ZnO thin films were examined on glass substrates. The experiments were performed at RT–200 °C of T_s (T_h = 0.13–0.21), 0.02–0.4 mbar (30–600 mTorr) of p (100% Ar), and 100–125 W of P_{RF}. The pressure range in this study was out of the range of the most recent SZM for thin films, the maximum p value being an order of magnitude higher than the maximum pressure in Fig. 5.1 (~30 mTorr). In those ranges of deposition parameters where the adatoms had much lower kinetic energies than those reported in the previous literature, various grain morphologies of the hexagonal wurtzite ZnO were detected by SEM. For those pressure ranges, the highest homologous temperature was still 0.21. Referring to Fig. 5.1 and extrapolating the zones to higher pressure values, we would expect a Zone 1 structure with enlarged columns for the films grown at those low temperature-high pressure conditions. However, the interpretation of our observations could not be made that straightforwardly.

At this point, it would be useful to introduce various forms of hexagonal crystals. These include the hexagonal pyramid, hexagonal bipyramid, hexagonal trapezohedron, hexagonal prism, hexagonal pyramidal prism, and hexagonal bipyramidal prism (Fig. 5.4). In nature, the *hemimorphic* forms—hexagonal pyramid and hexagonal pyramidal prism—of wurtzite type ZnO are the most common (see also Fig. 1.2). The Miller indices of the family of planes in a hexagonal pyramidal prismatic ZnO crystal are shown in Fig. 5.5.

At p = 0.2 mbar (150 mTorr) and T_h = 0.13–0.14 (no external heating; T_s = RT), the films had a well-defined columnar microstructure with inter-columnar voids and dome-tops (Fig. 4.14; Set 7). Comparing to Fig. 5.1, this structure is between Zone 1 (tapered columns separated by voids) and Zone M (matchstick morphology: parallel-walled columns with dome-shaped tops). The columns were of equal sizes, with cylindrical or hexagonal cross-section (see Fig. 5.6.a), indicating a well-developed wurtzite structure and strong (002)-texture. In addition to these, many equiaxed smaller grains could be seen at the film-substrate interface (Fig. 4.14.b). This microstructure resembles the structure in Fig. 5.2.a, and is presumed to be due to shadowing and low surface diffusion [53] acting together with high growth rate along the c-axis. The

equiaxed grains at the interface point to a large number of randomly-oriented nuclei at the initial stages. Among these grains, the ones with the (002)-orientation grew into the regularly shaped columnar grains perpendicular to the surface. Although no other reflections were detected in the XRD spectra of these films (Fig. 4.18.e), TEM examination is required to definitely determine the orientation of the grains at the interface.

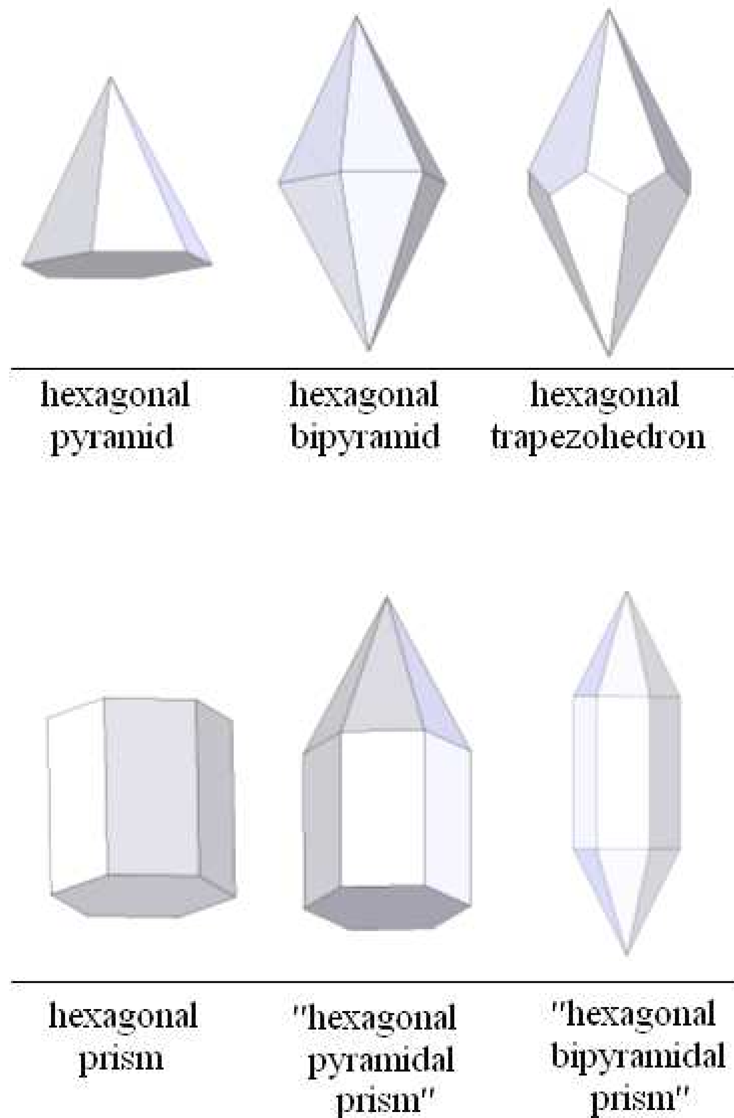

Figure 5.4. Various forms of hexagonal crystal structures. Grains of a hexagonal material could take any of these forms depending on its chemistry and the relative growth rate of different surfaces depending on the growth conditions.

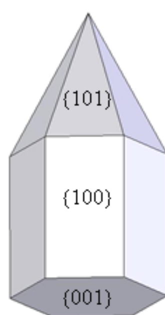

Figure 5.5. Crystal planes and Miller indices of hemimorphic wurtzite-type zinc oxide. The angle between the hexagonal {001} and each triangular {101} surface is 32° [25].

(a) T_s = RT, p = 0.2 mbar, P_{RF} = 125 W, acid-cleaned substrate

(b) T_s = 200 °C, p = 0.2 mbar, P_{RF} = 125 W, acid-cleaned substrate

(c) T_s = 200 °C, p = 0.2 mbar, P_{RF} = 125 W, fresh subtrate

Figure 5.6. SEM images of the ZnO films on glass deposited at low p (0.2 mbar) and high P_{RF}. (125 W) Drawings on the right side illustrate the possible forms of the encircled grains in the SEM images. (a) Set 7 (b) Set 8, (c) Set 6.

At the low T_h condition (0.13–0.14), increasing the pressure from 0.2 mbar (150 mTorr) to 0.4 mbar (300 mTorr) maintained the hexagonal or cylindrical cross-section of the grains (Set 3; Fig. 4.15). However, the columns were much more tapered ($w_{bottom} \approx 40$ nm, $w_{top} \approx 120$ nm) than the lower-p case at the same T_h ($w \approx 44$ nm). There were two distinct groups of grains with different shapes and sizes as seen from the top surface of this (low T_h and high p) film: cauliflower-like large grains (up to 200 nm in diameter) were surrounded by smaller grains (about 50 nm in diameter) (Fig. 4.15.a). Moreover, the columns were not continuous along the thickness, but rather interrupted by either other columns or irregular-shaped grains (Fig. 4.15.b). This implies that there was continuous nucleation during film thickening [53], and it led to void formation within the bulk of the film. Comparing to the films grown under the same T_s (and P_{RF}) conditions (Set 7) we would expect similar thermally induced mobility of the adatoms on the surface. Thus, it is reasonable to expect a similar nucleation behavior to that of Set 7 with randomly oriented nuclei. However, there was a decrease in the momentum-induced mobility, due to increased p and consequent decrease in the energy of the particles incident on the substrate surface. This decrease in energy must have suppressed the growth of any nuclei, and instead promoted more nucleation as the film grew. Thus, the grains were not continuous throughout the thickness. We can thus conclude that increasing p from 0.2 mbar to 0.4 mbar at T_h = 0.13 decreased the adatom mobility such that the microstructure changed from the well-built columnar form to the cauliflower-type.

Increasing T_h from 0.13 to 0.21 at the constant p (0.2 mbar = 150 mTorr) and P_{RF} (125 W) conditions, the microstructure deviated from the previous regular columnar structure (Set 8; see Fig. 4.16 and 4.17). The vertical cross-section of the films (Fig. 4.16.b and 4.17.b) had a structure resembling that of Zone 1. The majority of the grains in those samples were tapered not only along their height but also along their width (Fig. 5.3.b). The smaller equiaxed grains at the film-substrate interface were still present under these conditions, although no longer restricted to the interface. In fact, those equiaxed small grains could also be seen in between the larger grains on the film surface (Fig. 4.16.a and 4.17.a), and throughout the film thickness (Fig. 4.16.b and 4.17.b). This also points out to continuous nucleation during film growth (Fig. 5.7). SEM examination revealed that the planar cross-sections of the grains deviated from the regular hexagon (in Sec. 4.3, these grains were labeled as *diamond-shaped* grains). In

the planar SEM images of the film surfaces, these larger grains appear like the other forms (*i.e.*, with non-basal projection) of the hexagonal crystal illustrated in Fig. 5.4. Based on these forms, the grain shapes and orientations of the samples in Fig. 4.16 and 4.17 (T_h = 0.21) could be deduced. In the majority of the grains in Fig. 5.6.b, it appears as the triangular planes have grown in both ends, forming the pyramidal tops. This structure resembles either a hexagonal bipyramid or a hexagonal (bi)pyramidal prism, oriented horizontal to the substrate surface. In addition, they could be the projections of the incompletely grown (bi)pyramidal grains, as shown with the arrows in Fig. 5.6.b. In Fig. 5.6.c, the shape of the larger grains resembles either a hexagonal pyramid or a hexagonal pyramidal prism with a small aspect ratio of the rectangular faces.

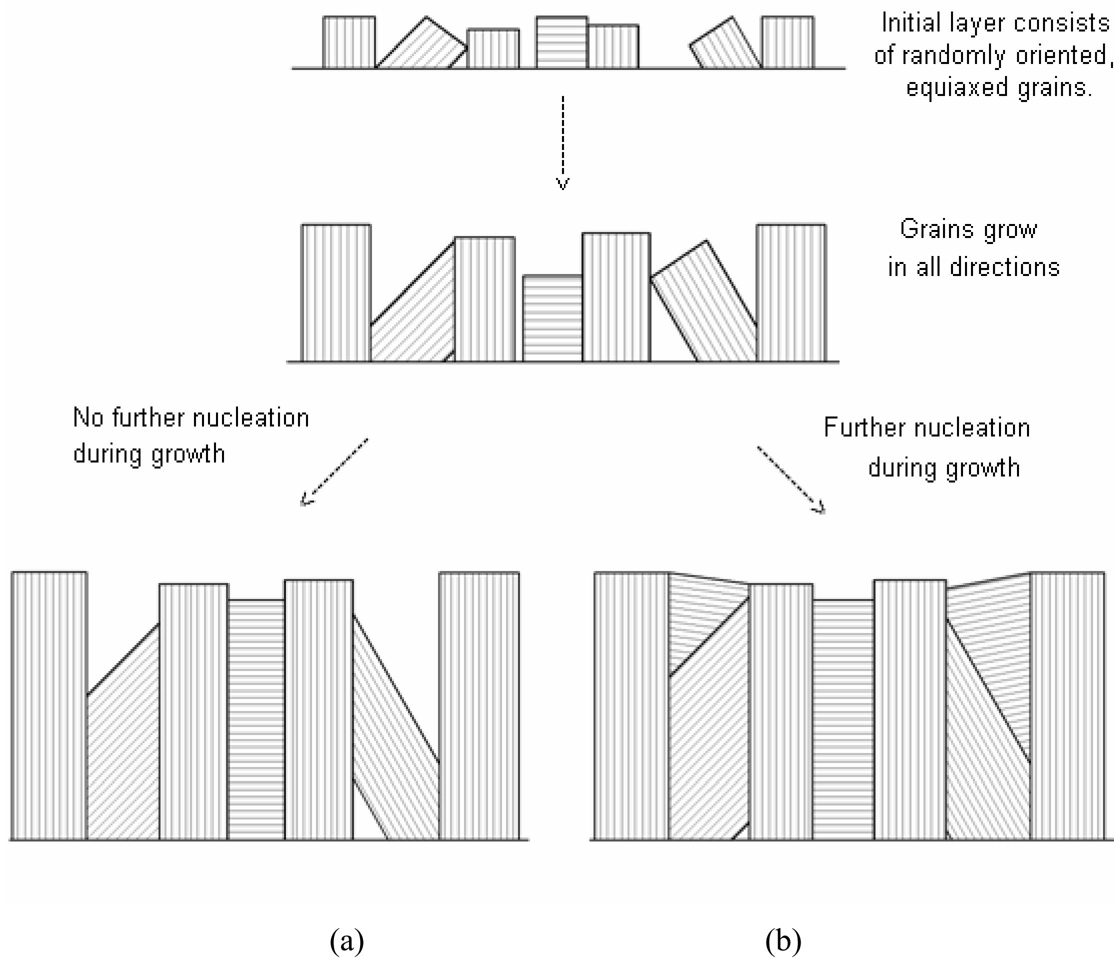

(a) (b)

Figure 5.7. A film structure with a randomly-oriented layer at the substrate interface. The grains are free to grow in all directions. Additional nucleation may take place during growth.

Based on Fig. 5.6, it could be concluded that T_s plays a major role in determining the grain shape and orientation. To understand the evolution of grain morphology seen in Fig. 5.6.b and 5.6.c, the deposition conditions (T_s = 200 °C, p = 0.2 mbar, P_{RF} = 125 W) and the corresponding adatom flux and mobility should be considered. Comparing with the previous lower T_h case (Fig. 5.6.a), the incident atomic flux should be the same, since the p and P_{RF} values were not changed. Thus, a similar initial number of adatoms would be expected on the surface. However, the increasing T_s could have provided increased mobility to those nuclei. It seems reasonable to presume that the nuclei having the similar orientation with each other would coalesce to decrease their surface energy. If there was an orientational distribution of the nuclei, islands with different orientations with each other could be forming on the surface. In the later stages of film growth, each of these islands would grow along their own preferred growth direction. Since under normal conditions the preferred growth direction of ZnO is along its *c*-axis, the nuclei oriented with their *c*-axis parallel to the surface could grow easily into the (002)-oriented columns (Fig. 5.2). For the remaining nuclei, there should have still been room for growth in the vertical direction, and the growth directions other than *c*-axis could have been promoted upon increasing T_s (Fig. 5.6.a). Moreover, these grains in Fig. 4.16 and Fig. 4.17 were not very densely packed; providing another proof that they might have evolved from different nuclei with different orientations (surface area measurements are necessary to elucidate the actual amount of porosity and the extent of contact between separate columns). In addition to growth of the grains in either directions (*a* or *c*), additional nucleation might have occurred during growth (Fig. 5.7.b). This situation could create grains with their *c*-axes tilted with respect to the substrate normal, namely the horizontally placed hexagonal bipyramids/bipyramdal prisms. This might have led to the distinct grain shapes in Fig. 5.6.b and 5.6.c.

In addition to the SEM analysis, we should consider the *texture* in the films revealed by XRD, to better understand the microstructural evolution at T_h = 0.21, p = 150 mTorr, and P_{RF} = 125 W. Comparing Fig. 4.18.b and Fig. 4.18.c (or comparing Fig. 5.8 and 5.9), there is (101)-texturing in addition to (002), at these low T_h–high p conditions. The appearance of an additional texture in our samples suggests the following:

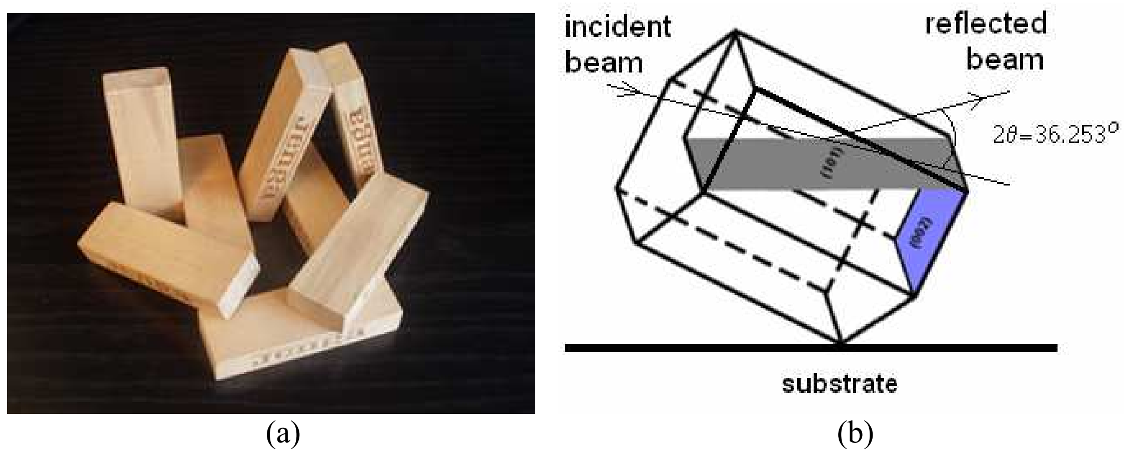

(a) (b)

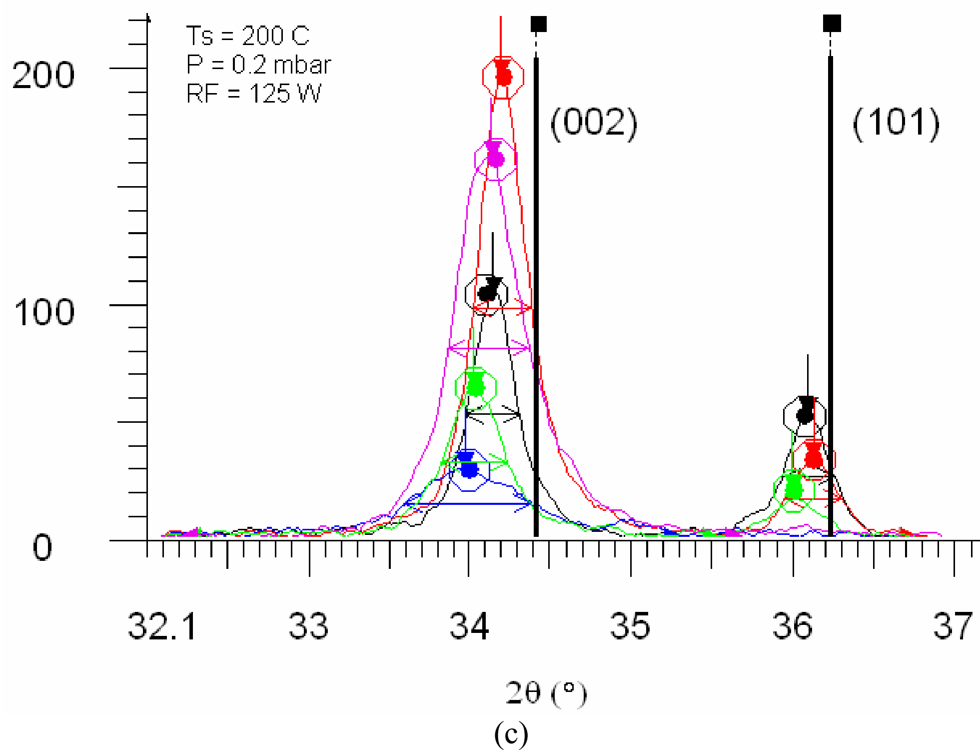

(c)

Figure 5.8. (a) A polycrystalline structure with random texture. (b) The position of a ZnO unit cell with respect to the substrate plane to give a (101)-reflection in the XRD spectra. (c) XRD spectra (θ–2θ) of the ZnO film grown on glass at T_s = 200 °C, p = 0.2 mbar, P_{RF} = 125 W (Set 8 in Table 3.1).

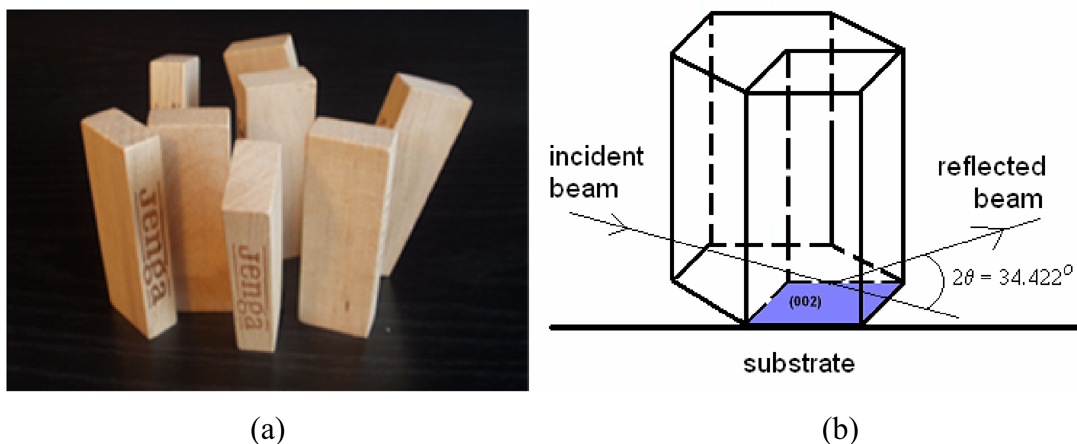

(a) (b)

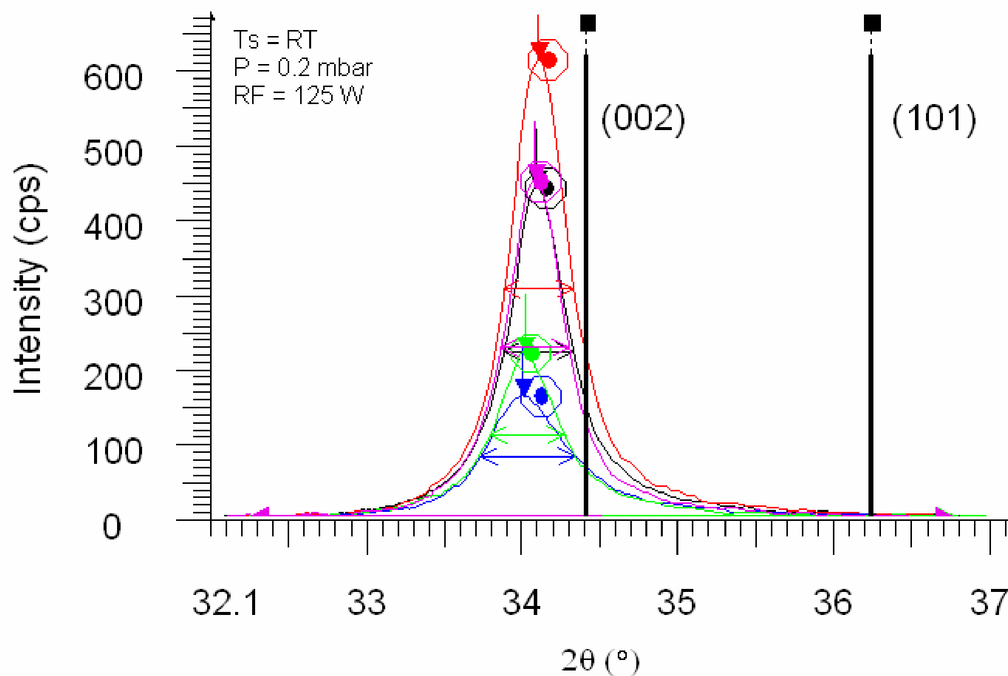

(c)

Figure 5.9. (a) A polycrystalline structure with fiber texture. (b) The position of a ZnO unit cell with respect to the substrate plane to give a (002)-reflection in the XRD spectra. (c) XRD spectra (θ–2θ) of the ZnO film grown on glass at T_s = RT, p = 0.2 mbar, P_{RF} = 125 W (Set 7 in Table 3.1).

i) One column could be made up of multiple grains. To quote from Pulker: *″Columnar microstructure does not always signify well-formed crystallites.″* [2]. Pulker gave two such examples: electron diffraction showed that although both had well-built columns, ThF_4 films had a lot of growth defects, and Al_2O_3 films were even amorphous (page 359 of [2]). Ow-Yang *et al.* have also shown by XRD and TEM columnar amorphous structures of annealed ITO thin films grown under low atom mobility conditions [212]. These films in the study of Ow-Yang *et al.* possessed voids that were distributed through the film thickness, together with equiaxed grains within the columnar network. These observations support that columnar structure did not necessitate the (002)-texture in every case.

ii) The columns were not necessarily perfectly (002)-oriented. There was a relation between the non-cylindrical or non-hexagonal columns and the orientation of the crystals. As stated repeatedly, ZnO thin films have a very pronounced texture along the (002)-direction. However, there are some cases where other orientations have been reported as a function of the substrate material and the deposition conditions. In one study by Cebulla *et al.*, the appearance of the (101)-reflection, among the (001)-reflection was mentioned [25, 138]. This peak was only observed in the pure ZnO films and not in the Al-doped films, and its intensity increased with thickness (Fig. 1.26). Aluminum was proposed to be acting as a mineralizer or surfactant that improved the texture of the layers during growth. Minami *et al.* also observed (101)-reflections from Al-doped ZnO films thicker than 1 μm at high sputtering pressures and/or high substrate temperatures [139]. Sayago *et al.* found that the intensity of the (002)-peak increased with increasing oxygen content in the 50–200 W of P_{RF} range [133].In addition, weak reflections from the (100) and (110)-planes were observed in the XRD spectra for P_{RF} > 50 W. Lim and Lee examined observed that ZnO thin films on Al/Si(100) substrates The films on Al/Si substrates had a mixture of small and large grains with large amount of voids, where the films on the Ru/Si substrates were very dense and the grain shapes were hard to detect; therefore, no grain shape was reported for those films [140]. For the films on Ru/Si substrates, only the (002)-reflection was observed. In the films deposited on Al/Si substrate, the XRD intensity of the (002)-peak decreased to one-fifth of the previous case. At the same time, additional reflections from the (100), (101), and (102)-planes appeared.

These studies showed that the substrate structure was important in the microstructural evolution of the ZnO thin films, although they did not investigate the grain structure in detail. They also indicated that there was a specific set of deposition parameters for the (101)-texture to occur in otherwise highly (002)-textured ZnO thin films. In our studies, this set of deposition parameters to create the additional (101)-texture was limited to T_s = 200 °C, p = 0.2 mbar, and P_{RF} = 125 W. The microstructure of the grains (Fig. 5.6) together with XRD analysis (Fig. 5.8.c and 5.9.c) revealed that the (101)-texture occurred when there were grains that were tilted with respect to the substrate normal as a result of additional nucleation of grains with their *c*-axis oriented with an angle with respect to the substrate normal during film thickening. The film growth rate was presumed to be an important factor in this kind of microstructural evolution. By inspecting the film thicknesses, we can deduce the average growth rates: 6.7 nm/min for Set 8 (T_s = 200 °C; (002) and (101)-textures), and 4.6 nm/min for Set 7 (T_s = RT; only (002)-texture). Thus, at p = 0.2 mbar, the films grew much faster at T_s = 200 °C than those at T_s = RT. At this higher temperature, there were simultaneous mechanisms: increased surface diffusion upon increased T_h, and fast growth along the vertical direction due to increased atomic flux. Thus, overall mobility along the vertical direction should have been higher than in the lateral direction. However, this does not mean that all the grains would be (002)-textured with regular hexagonal prismatic shape—it all depends on the orientation and the density of the interfacial layer of nuclei. Although low adatom mobility is known to give highly anisotropic columnar structures in thin films [59], if the growth was fast, the atoms might not had enough time to rearrange themselves and adhere to the less energetic sites [137]. With the presence of a randomly oriented layer at the interface and a high growth rate, the film grew with a mixture of (002)-textured and, in our case, (101)-textured grains. However, cross-sectional TEM studies are necessary to state the effect of lateral growth and nucleation density definitely. To our knowledge, the irregular-shaped (neither hexagonal nor circular in cross-section) grains in ZnO films at low mobility conditions were not reported in the literature.

To reveal more about the microstructural evolution at low mobility, Fig. 5.10 compares the microstructure of some ZnO film samples, all deposited at the same conditions that proved to produce the tilted grains. As can be seen on Fig. 4.18.b and Fig. 4.18.c, not all of the film samples that were deposited in the same batch showed

diffraction from the (101)-planes. A comparison of the SEM images of a sample that showed (101)-reflection and one that did not might be useful in understanding their diffraction behavior. Fig. 5.10.a shows a SEM image from a ZnO film on a fresh substrate (Set 6) that did not diffract x-rays beams from the (101)-planes. Three types of grains were seen on the film surface: large (up to 200 nm) hexagonal grains with low contrast, triangular grains with similar size to the hexagonal grains, and smaller (20–30 nm) equiaxed grains.

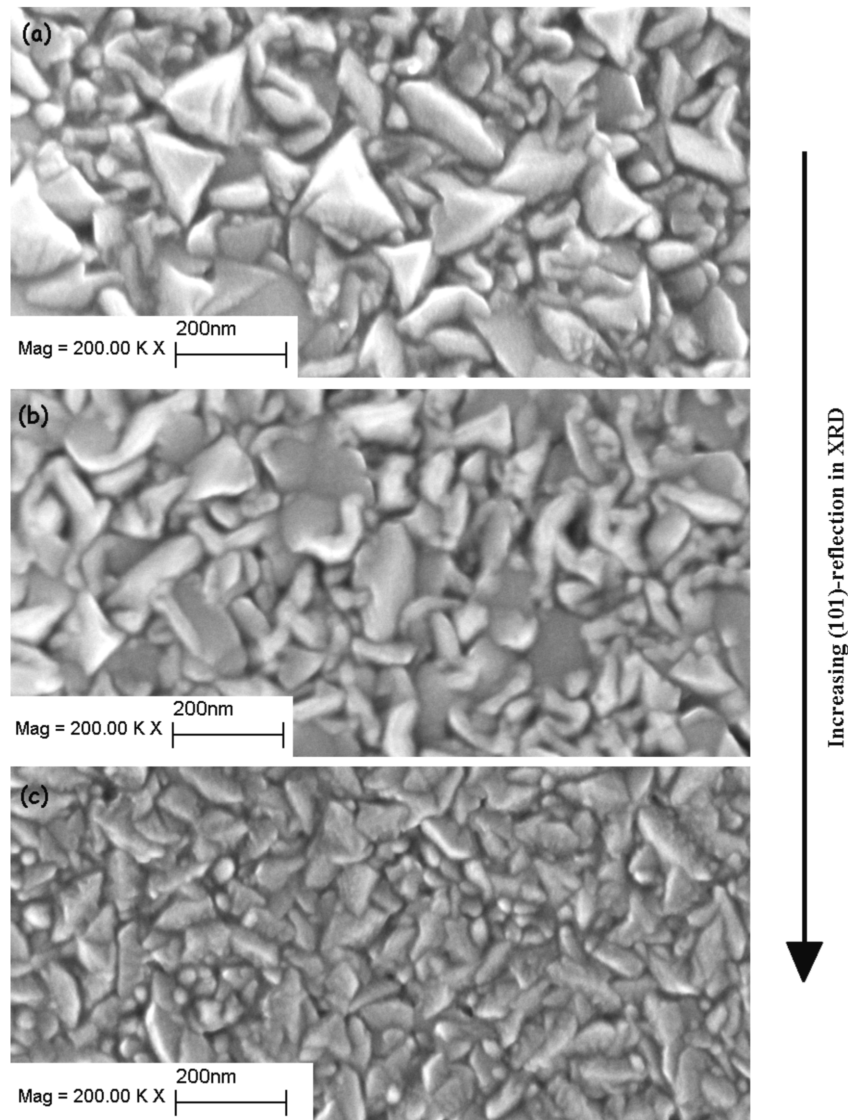

Figure 5.10. SEM images of the ZnO film grown on glass at T_s = 200 °C, p = 0.2 mbar, P_{RF} = 125 W. (a) ZnO on fresh glass substrate (Set 6 in Table 3.1). No (101)-reflection was observed in the XRD spectra from this sample. (b) ZnO on fresh glass substrate (Set 6 in Table 3.1). (101)-reflection was observed in the XRD spectra from this sample. (c) ZnO on acid-cleaned glass substrate (Set 8 in Table 3.1). A more intense (101)-reflection was observed in the XRD spectra from this sample then from the sample in (b).

Fig. 5.10.b shows a sample from the same batch with the previous (Set 6), but one that showed the (101)-reflection. The large hexagonal grains were still present. However, the triangular ones decreased in number and size. Instead of these, there were smaller rectangular or irregularly shaped grains. In the samples with triangular grains, the faces other than the hexagonal and the rectangular faces (see Fig. 5.6) might have grown, but the crystals with the triangular faces might not be tilted enough to satisfy the Bragg's condition (Eq. 3.1). On the other hand, in the samples that did show the (101)-reflection, the crystals might have been tilted enough to satisfy the Bragg condition. With this tilt, the full projection of the triangles might have vanished. Fig. 5.10.c shows an example from a ZnO film on an acid-cleaned substrate (Set 8) with a (101)-reflection that was much stronger than the sample in Fig. 5.10.b. There were again no triangular grains, but rather hexagonal (bi)pyramidal and hexagonal (bi)pyramidal prismatic grains with similar size to the previous triangular grains. That indicated that faces other than (002) have grown, but have been tilted with respect to the substrate plane.

In bulk materials, mainly the surface diffusion determines the crystal growth behavior [137]. The surfaces with the highest energy grow the most slowly, while the surfaces with the lowest energy grow the most rapidly [52]. In ZnO, this mechanism dictates that the fastest growth direction is the [001]-direction [137]. Relative surface diffusion rates on different surfaces determine the relative growth rates of these surfaces. Although surface diffusion is a thermally activated process, momentum-induced mobility could be gained upon momentum transfer from the sputtered gas to the adatoms [137]. Thus, the growth rate of surfaces could be altered not only by varying the temperature, but also by varying the pressure or the sputtering power. [A similar competing mechanism was reported for ZnO films deposited at high P_{RF} (140 W) and high T_s (650 °C), when compared to low P_{RF} (27 W) and low T_s (450 °C) [137]. Growth along the *c*-axis (due to increased P_{RF}, thus, increased atomic flux) must have been faster than the diffusion along the transverse direction (due to high T_s), creating faceted pyramidal surfaces (the surface with the highest energy vanished). There was an optimum combination of T_s and P_{RF} for controlling such faceting.] However, this was not likely to be the case in our study, because the working temperatures were much lower (the maximum T_h = 0.21) and the working pressures were one or two orders of magnitude higher (up to 0.4 mbar) compared to other values in the literature. Thus, the fastest growth direction must still be the [001]-direction. Nevertheless, the additional

(101)-texture occurred at increased temperature and decreased pressure. Therefore, although the [001]-direction was the fastest growing, increase in momentum might still be an effective factor for increasing growth rate of other surfaces.

As discussed in Sec. 5.4.1, the existence of an initially randomly oriented layer could affect the final structure. To enlarge this discussion and adapt to the above cases, several growth scenarios were considered. Let us suppose there was an initial layer with randomly oriented, equiaxed, crystals (Fig. 5.2). Then suppose all of these crystals grew faster in the *c*-direction. These crystals would constrain each other laterally with respect to the growth direction, and only the ones with an exposed (002)-facet would continue to grow. Then, there would be many columns perpendicular to the substrate surface, with a network of inter-columnar voids (Fig. 4.14 and 5.2). Now let us relax the lateral growth constraint and allow the crystals to grow in the *a*-direction as well, which is possible by increasing the substrate temperature (Fig. 5.3). Then there would again be columns that are parallel to each other and perpendicular to the substrate surface, as well as grains that have grown along their basal plane and that are tilted with respect to the substrate normal (Fig. 4.16). If those grains were skewed with respect to the substrate surface at an angle that would satisfy the Bragg diffraction condition (Eq. 3.1) for the (101)-planes, the (101)-peak would also be observed in the XRD spectra (from Fig. 5.8 and 5.9, it is evident that the (101) and (002) reflections cannot come from the same grains).

Finally, consider the case in which there were no randomly oriented grains in the initial layer, but instead all the initial nuclei had a *c*-direction parallel to the substrate normal (Fig. 5.3). Then, the final film would consist almost entirely of columnar grains perpendicular to the substrate surface. In this case, if the initial layer was densely nucleated and the growth along the *c*-axis was much faster than along the *a*-axis, we would expect to have a densely packed structure made of *parallel-walled* columns (Fig. 4.14), with only the (002)-reflection in XRD analysis. If the nucleation was less dense and at the same time growth along *a*-direction would also be allowed, then the final film would consists of a less dense structure, consisting of *tapered columns* plus an extensive network of interconnected voids (Fig. 4.16).

To summarize, in determining the overall structure and texture of a thin film of an anisotropic material like ZnO, there is always a competition between atomic mobility, flux of incoming particles (deposition rate), and the rates of nucleation and growth

[137]. In our results, we observed examples of both thermally induced mobility (increased T_s) and mobility induced by the momentum of the incident particles on the surface (decreased p). In either case, increased mobility led to an increasing diversity of grain shapes observed by SEM, and deviation of texture from the (002)-orientation in XRD. These might be due to the existence of an initial layer with randomly oriented nuclei and subsequent growth of tilted grains with (101)-planes that satisfy the Bragg condition, together with additional nucleation during growth.

5.1.3. Effect of Buffer Layer Deposition on the Film Microstructure

To understand the role of the initial layers in greater depth, the film growth was investigated via two successive separate depositions: a thin buffer layer deposition, followed by growing film with the thickness of interest (Sec. 4.5). The changes in the microstructure upon buffer layer deposition can be seen in Fig. 4.21. By depositing a buffer layer of a sixth of the film thickness (about 67 nm), the hexagonal (bi)pyramidal grains that have been formed at the same deposition conditions were eliminated (Fig. 4.21.b). This result is in agreement with the assumption of the existence of an initially randomly oriented layer. The buffer layer might have acted as a template for further film growth. Although there might be randomly oriented grains in the buffer layer as well, the remaining *c*-axis oriented grains must have acted as templates for further ZnO film growth, enabling only *c*-axis oriented growth through the film thickness. This idea was also supported by the XRD spectra of the films with a buffer layer (Fig. 4.19): the intensity of the (101)-peak was about a sixth of the (101)-peak intensity of a film sample of the same area but without a buffer layer (Fig. 4.18.b).

By annealing the buffer layer at 600 ^{o}C for 6 h prior to further film deposition, the film became denser, without significant change in the grain shape (Fig. 4.21.c and Fig. 4.22.c). This might be explained by the increased number of nucleation sites for the *c*-axis oriented grains upon annealing. This assumption is reasonable when the annealing experiments on the fully-grown films are considered—annealing the films at 600 ^{o}C for 6 h allowed the grain diameter to increase by ~4 times (Fig. 4.26). Increased size of the *c*-axis oriented grains would provide more nucleation sites for similarly oriented grains in subsequent film deposition. For the same reason, there would be fewer grains with

other orientations, which would decrease the amount of voids in the fully developed film, and tapering of the columns. However, there still remains a need for investigation of the growth trend on buffer layers of varying thickness and/or roughness, to fully understand the effect of the initial layers on further film growth [141].

The buffering method has been applied for ZnO thin films in a few earlier studies. For example, when the ZnO films were deposited on the roughest ZnO buffer layer on (0001)-oriented sapphire, they had the smoothest surface and the most intense (002)-peak among all the samples (Fig. 1.27 and 1.28) [141]. In another study, a ZnO buffer layer on SiO_2/Si substrates prevented the (100) and (101)-peaks in the XRD spectra, and strengthened the (002)-texture of the ZnO films [142]. At the same time, the films became smoother, in contrast to the case without a buffer layer. These few studies on the effect of the buffer layer were in agreement with our results and presumption of the buffer layer to provide more textured nucleation as a cause of decrease in the residual stress. [The residual stresses–which will be discussed in relation to the microstructural evolution either with or without a buffer layer in Sec. 5.2–were not investigated in any of these studies.]

Roughness could also be important in determining texture [137], but it was not measured in our present study. Nevertheless, based on the previous literature results summarized above, it could be presumed that the buffer layer is affective on the initial roughness and the microstructure during further film growth. While the ZnO films deposited on the roughest buffer layer had the smoothest surface and the most intense (002)-peak among all the samples in one study [141], a rougher substrate resulted in rougher films in another [137]. Significant surface roughness may create competition between *crystallographic orientation* and *geometrical orientation* [137]. An increasing roughness of the substrate surface increases the number of randomly oriented nucleation sites. Therefore, although there is local texture, the overall orientation would be more random. In our study, the glass surfaces were prepared with acid cleaning (Sec. 3.1). If the acid etched the surface, this might have created roughness, decreasing the initial texturing of ZnO. However, atomic force microscopy (AFM) measurements on the blank substrates are required to check the validity of the argument. It should be kept in mind that the argument of a rougher substrate creating a rougher film was for an amorphous substrate [137], where in the present case the ZnO buffer layer creates an epitaxial ZnO substrate for ZnO film growth, whether rough or not. Thus, different

nucleation and growth behavior should be expected between the two cases, and this might explain the differences in the roughening-smoothening trends between the two.

5.1.4. Grain Size

Before closing the discussion on the film microstructure, the grain size change upon annealing should be mentioned. Fig. 4.26 shows that the grain size of ZnO films on Si(100) substrate grew by up to four times of their original size upon annealing in air at 600 °C for 6 h. The lateral grain size that was measured by SEM (GS_{SEM}) changed from ~40 nm to ~120 nm (four times) by annealing. The change in the vertical direction of the grains upon annealing can be seen by comparing Fig. 4.2.a and Fig. 4.33.b. Annealing at T_h = 0.38 caused a decrease in the grain boundary sharpness, and the columns became harder to distinguish. This result was in agreement with the structure zone model modified by Gupta and Mansingh, where they proposed a transition from Zone 2 to Zone 3 for annealing temperatures of T_h > 0.35, due to grain coalescence [151].

The grain sizes for these samples were also calculated based on XRD measurements and using Scherrer's formula [209] (GS_{XRD}; Sec. 3.4.2.4), and the results were given in Table 4.9. Upon annealing, GS_{XRD} changed from 8.95 nm to 23.3 nm (2.6 times). The relative change in grain size upon annealing measured by XRD was smaller than that measured by SEM. In addition, GS_{XRD} values were much smaller than the average film thickness (220–310 nm). This is another indication that the vertical columns were not necessarily single crystals, but composed of many grains [2]. The relative sizes show that there must be more than one grain throughout the film thickness. (*FWHM* in Eq. 3.37 is essentially zero for t > 100 nm [209].)

The discrepancy between these two values measured by SEM and XRD could be due to several additional factors:

i) The lateral grain size that is measured by SEM could be misleading since it only takes into account the visible grain boundaries but not the actual crystalline regions which are able to diffract coherent x-rays [213]. In addition, XRD peaks arise from a statistically significant average of grain diameters, while SEM allows only

estimating the average grain size from a number of grains that is not statistically representative of the entire film.

ii) The residual stress in thin films contribute to XRD peak broadening; thus the measured grain size is smaller than the real grain size [96, 209]. However, this is probably a less significant factor to cause the discrepancy between GS_{XRD} and GS_{SEM} than the above.

5.1.5. Section Summary

In this section, the development of microstructure of ZnO thin films at deposition conditions which were outside the previously developed SZMs (p > 30 mTorr) was discussed. The proposed effects of these deposition conditions on the ZnO film's microstructure could be summarized as follows:

i) There was an initial layer of random-oriented nuclei at the initial stages of film growth at specific deposition conditions and adatom energy.

ii) Higher RF power, thus high incident flux, resulted in high extent of nucleation.

iii) Lower p and higher T_s enabled greater mobility of the adatoms on the surface, and promoted coalescence of nuclei with the same orientation with each other.

iv) When all three of the above conditions (high P_{RF}, high T_s, low p) were satisfied, the films contained grains of various shapes, and deviation from c-axis orientation was observed. This was proposed to be due to the increased growth rate on every direction (high energy and mobility of adatoms), combined with the limited amount of time between successive layer formations (high flux of adatoms) and additional nucleation during the course of film growth. The conditions for mixed (002) and (101)-texture were determined as T_s = 200 °C, p = 0.2 mbar, and P_{RF} = 125 W.

v) When the surface mobility of the adatoms were lowered (either by decreasing T_s or increasing p), the film structure consisted mainly of columnar grains, with primarily the c-axis orientation.

vi) At the lowest surface mobility and lower adatom flux conditions, the films were close to being amorphous with very low XRD intensities and cauliflower like grains.

vii) The films on crystalline substrates had a better-defined columnar structure. This was attributed to the increased number of nucleation sites for the *c*-axis orientation.

viii) A similar effect as above was observed upon buffer layer deposition prior to the full film growth.

ix) There was always a competition between the growth rate of different crystalline surfaces, the grains, the columns, and the film thickness. The relative domination of these factors determined the film's microstructure.

x) Annealing of the film caused grain growth due to increased bulk and surface diffusion.

These factors will also be used in the discussion about the relations between the film microstructure and the residual stresses.

5.2. Residual Stresses and Their Origins

All the ZnO thin film samples in this study had residual compressive stresses. This phenomenon was manifested both by the warping of the film-substrate laminate system with the thin substrates (Fig. 4.5), and by the XRD peak shifts of the thin film samples with respect to the stress-free ZnO powder peaks (*e.g.*, Fig. 4.6). The warping direction was towards the substrate, confirming the presence of residual compressive stress within the film (see also Fig. 1.14 and Fig. 3.11). In the warped samples, the ZnO film thickness was ~400 nm, and the substrate thickness was ~160 μm. Warping in the other substrates could not be seen by naked eye, possibly due to their higher thickness (the thickness of the mica and the Si(100) substrates were about 230 and 508 μm, respectively).

The total residual stresses were calculated via the *biaxial strain model* [149] (Sec. 3.4.2.2). This model assumes the stress in the direction of the substrate normal is zero. This assumption was shown to be valid for thin films of the thicknesses in this study

(100–500 nm) [170]. The strain values to be used in this model were measured from the shift of the (002)-peak of each film relative to the (002)-peak of the unstressed powder standard JCPDS-No. 36-1451. According to Bragg's Law (Eq. 3.1), the 2θ diffraction angle from the (002)-planes of stress-free ZnO is 34.422° for Cu-K_{α_1} x-rays having a wavelength of 1.5406 Å (Table 3.3). The measurement of strain from the peak shift is known to yield more accurate results for higher 2θ peaks in the spectrum [204, 209]. However, the ZnO thin films in our study were highly textured along their *c*-axis, with only the (002)-reflection in most of the samples, and (101)-reflection in a few samples showing up in the XRD spectra. Thus, no high-angle peaks could have been used to calculate the residual stress.

Another method to measure the stress is the *bending method* (Sec. 1.5). Cimpoiasu *et al.* calculated the residual stress in polycrystalline ZnO thin films on Si and Al/Si substrates, via both the XRD peak shifts and the bending method [156]. They found that the results of the two methods differed by ~10% for low stresses and by up to 50% for high stresses (the highest stress they have measured was 1.2 GPa). In another study, the agreement was found to be about 20%, between the residual compressive stress results obtained by the XRD biaxial stress model and the bending technique, and this value was within the measurement accuracy of both methods [138]. Using the bending technique for ZnO films on Si substrates, Rossington *et al.* found that the biaxial stresses were unequal in the two orthogonal directions with a difference of <25% between the two components, σ_x and σ_y. In our study, these discrepancies were not taken into account, while the error due to equipment misalignment has been included in the results (maximum error = 0.5 GPa within 10 GPa, corresponding to ±5%). Instead, the origins of relative changes in stress were investigated for similar processing conditions, rather than the absolute values of the stresses

The presence of residual compressive stresses in RF magnetron-sputtered ceramic thin films is a commonly observed phenomenon [2, 49]. Many factors have been proposed to play a role in the creation of these stresses [50, 74, 76]:

i) thermal expansion coefficient mismatch between the film and the substrate (extrinsic),

ii) lattice mismatch between the film and the substrate (extrinsic),

iii) incorporation of atoms (residual gas or chemical reaction products) (extrinsic or intrinsic),

iv) variation of inter-atomic spacing with crystal size (intrinsic),

v) recrystallization processes (intrinsic),

vi) microscopic voids and dislocations (intrinsic),

vii) phase transformations (intrinsic).

The nature and magnitude of these stresses varied with the deposition method and post-deposition treatments. Thus, it was not straightforward to decide which of these mechanisms were predominately giving rise to residual stresses, pertaining to a specific film-substrate material pair and specific deposition parameters. In the following sections, the contribution of several factors to the total residual compressive stress will be discussed.

5.2.1. Thermal Expansion Mismatch between ZnO and the Substrate Materials

One of the factors to cause residual stresses in thin films is the mismatch of the TEC of ZnO and the substrate material (Sec. 1.2.3). As can be seen in Fig. 4.6, there are different amounts of shift of the (002)-peak of ZnO films deposited under the same conditions but on different substrates. This fact points to a possible contribution of thermal stresses induced by the mismatch of the thermal expansion coefficients of ZnO and the substrate materials.

To calculate these *thermal stresses* (σ_{th}), the thermal expansion coefficient (α) of both the film and the substrate material should be known (Sec. 1.5 and 3.4.2.3). Some values for α_{ZnO} were presented in Table 1.7. These TEC data in the literature are in agreement with the results in our study: α_{ZnO} was measured as 5.82 x10^{-6}/°C at 50 °C, and as 7.40 x10^{-6}/°C at 200 °C (Table 4.2 and Fig. 4.7). These are the TEC values averaged over all directions, since the measurement sample was polycrystalline powder ZnO. The TEC values were also measured for the substrate materials along the substrate plane (Table 4.2). According to these results, Si had a lower TEC (maximum 4.1 x10^{-6}/°C at 200 °C) than that of ZnO. Mica and glass had similar TEC values to each other (10.7 and 9.9 x10^{-6}/°C, respectively, at 200 °C), which were higher than that of ZnO.

Since the glass substrate was amorphous, there is no directional dependence of the TEC. For mica, no particular orientation could be distinguished in the substrate plane; nevertheless, since the samples were composed of three layers of the same material in each case (Fig. 3.15), the results would belong to the fastest expanding direction. As for the Si substrate, TEC is the same in all directions owing to the cubic structure.

Considering only thermal mismatch effects, we would expect the ZnO films on mica and glass substrates to have residual compressive stresses and the (002)-peaks to shift to smaller angles in the XRD spectra (see Sec. 3.4.2.3 and Eq. 3.32), since these substrates had larger TEC values than ZnO. Mica had a TEC slightly higher than that of glass; hence, the (002)-peak would be expected to show a similar shift to the left of the powder peak with similar strains like those of the films on glass. However, ZnO on mica had the lowest compressive strain among all the samples (Table 4.1). Thus, there must have been other factors contributing to the overall stress amounts. In fact, the σ_{th} amount within the measured total stress, corresponding to the measured TEC values, were calculated to be 11.1% for films on the mica substrate, and 5.42% for films on the glass substrate at the highest T_{s} of 200 °C (Table 4.3 and Fig. 5.11).

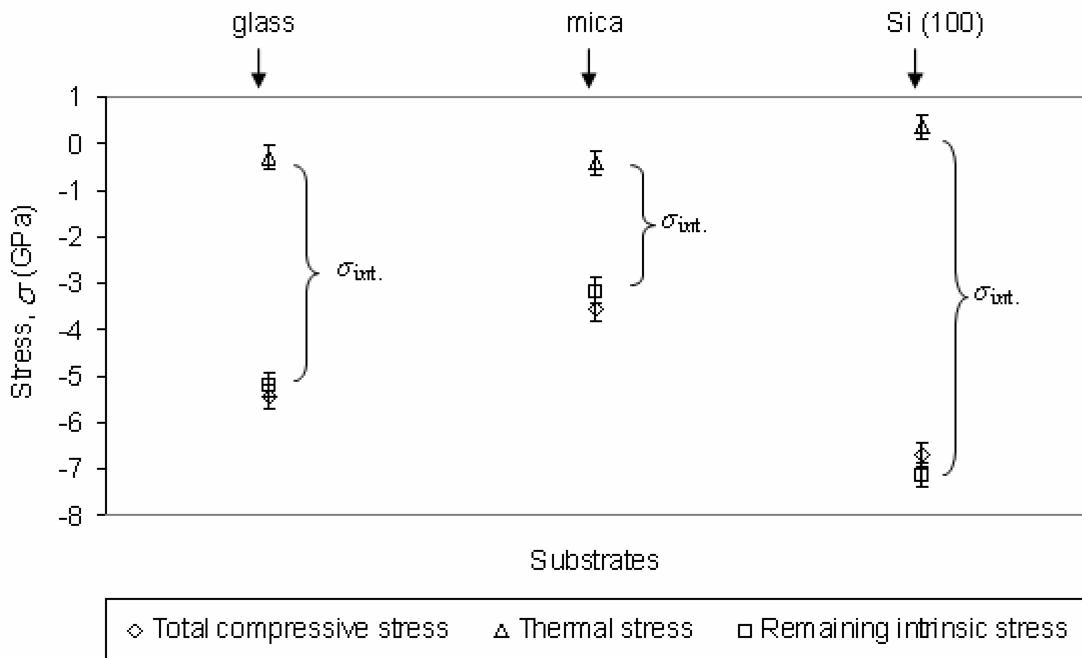

Figure 5.11. Total (σ_{c}) vs. thermal stress (σ_{th}) as a function of the substrate material for T_{s} = 200 °C, p = 0.02 mbar, P_{RF} = 100 W (Set 16 in Table 3.1). Thermal stresses were due to the mismatch between the TEC of ZnO and the substrates. The remaining amount of stress among the total is called the *intrinsic stress* (σ_{int}).

The most critical stress observation was for the ZnO film deposited on the Si(100) wafer. Si had a lower TEC than ZnO, and accordingly, there should have been a residual tensile thermal stress within the ZnO film (and an XRD peak shift to higher diffraction angles). However, the (002)-peak of ZnO on Si(100) was also shifted to even smaller values of 2θ when compared to the films on glass or mica (Fig. 4.6), revealing a much higher positive strain along the *c*-axis (Table 4.1). The theoretical tensile stress of ZnO on Si(100) arising from TEC mismatch was calculated as +0.388 GPa at T_s of 200 °C, which corresponded to 5.8% of the total stress, when the absolute values of the stresses were considered (Table 4.3 and Fig. 5.11). When the overall compressive stress is considered (-6.69 GPa), there is an effective -7.08 GPa of *non-thermal* compressive stress in the ZnO films on Si.

Similar comparisons based on TEC values were done in the literature. Jou *et al.* [98] and Water and Chu [95] compared α_{ZnO} (see Table 1.7, Ref. [174]) and α_{Si} at room temperature (2.5 x10^{-6}/°C). In all cases, although ZnO had a higher TEC than that of Si, in either direction, ZnO films had compressive residual stresses. Jou and Han [98] also found a discrepancy between the residual compressive stress of ZnO films on Si and GaAs with increasing T_s. The stresses in ZnO films on Si substrates were more compressive than those on the GaAs substrates, although the opposite was expected considering the relative TEC values. Moreover, a compressive thermal stress on GaAs was expected to increase with increasing T_s. However, σ_c decreased with increased T_s on both substrates. Based on those observations, the authors concluded that other factors were effective on the evolution of the residual stresses, but did not give alternatives. Cebulla *et al.* calculated that the thermal strain was one order of magnitude smaller than the overall residual strain, considering the relative TEC values of ZnO (see Table 1.7, Ref. [138]) and the glass substrate (9 x10^{-6}/°C). The authors concluded that most of the residual stresses were created by other factors during film growth [138]. Ellmer calculated the thermal strain arising from the differences in thermal expansion coefficients of ZnO and a glass substrate to be less than 5x10^{-4} [25].

To summarize, even at the highest T_s (200 °C), the thermal stresses contributed to the overall amount of stress by only ~5–10%. Thus, the thermal contribution to the residual compressive stress was argued to be insignificant in our samples. In light of these observations, residual stresses in deposited ZnO films cannot be due to only the thermal expansion mismatch between the films and the substrates.

5.2.2. Argon Entrapment inside the Films

Along with the extrinsic causes of residual stresses such as the thermal expansion or the lattice mismatch between the film and the substrate, several studies in literature reported on other causes of residual stresses in thin films, such as atom incorporation, oxygen deficiencies, and other imperfections in the crystal lattice of the films formed during film growth. Some of the studies associated the residual stresses to be entrapped argon or oxygen and the consequent *atomic peening effect* [98, 214]. We also examined this phenomenon in our study.

Fig. 4.4 showed the EDX profile of a ZnO film on a glass substrate, deposited at T_s = 200 °C (Set 16 in Table 3.1). The accelerating voltage was 20 keV (the graph showed a close-view between 0 and 4.5 keV), and the count rate was 3.1 kcps. At these conditions, the Kanaya-Okayama relation (Ref. [215], p.89) estimates an electron interaction volume in ZnO as a semi-sphere with a radius of about 2.3 μm. This value is an order of magnitude higher than the film thickness (250 nm). In addition, the peaks arising from the substrate (*e.g.*, Na, K, Al, Si) could clearly be seen in Fig. 4.4. Thus, the electron excitation volume is representative of the whole film thickness.

The energy for associated with the K_{α_1} radiation of argon is 2.958 keV). The point where the argon peak should have been present is marked with a vertical line on the graph. The values for the accelerating voltage and the count rate were more than required for the detection of the K_{α_1} radiation of argon [215]. However, no argon presence could be detected in this sample. In the mean time, the residual compressive stress was calculated as -5.46 GPa. The EDX signal is integrated over the whole semi-sphere with a radius of about 2.3 μm which is an order of magnitude thicker then the film. Thus, the major part of the elemental signals was obtained from the substrate. For this reason, if the argon content inside the film is small (*e.g.* less than 0.5 at.%), it might be shadowed by the substrate peeks. Nevertheless, the nonexistence of argon in this highly stressed sample could be indicative of *atomic peening* by argon being a minor factor in stress evolution.

Although the role of atomic (Ar) peening was mentioned in stress evolution, only in a very few studies the entrapped gas amount in the films was actually measured. For example, Bachari *et al.* mentioned that sputtered ZnO thin films contain about 0.5 at.%

of argon in general, but did not measure the actual argon content in their ZnO film samples [96]. Maniv *et al.* experienced that the residual stress in ZnO films varied from -8 GPa to zero, and decreased by one order of magnitude as the chamber pressure (100% O_2) was increased from 0.4 to 4.7 Pa (0.004–0.047 mbar) [149]. They proposed this result to be due to the decreased mean free path of the adatoms and the consequent weakening of the atomic peening effect. Hoffman and Thornton discussed the effects of entrapped argon on the residual compressive stress, but in sputtered metallic films [216]. They measured up to 2 at.% of argon inside the films, with the exact value depending on the film material (chrome, stainless steel, molybdenum, and tantalum, in increasing order of trapped %Ar) and the deposition conditions (chamber pressure and angle of incidence). They did not observe a direct correlation between the amounts of residual stress and the amount of entrapped argon inside the films. Cebulla *et al.* showed, by both RBS analysis and TRIM simulations, that the ZnO films were free of implanted argon for the range of deposition parameters used (50 eV Ar ions, p_{Ar} = 0.008 mbar, P_{RF} = 0–150 W, P_{DC} = 0–75 W) [138]. Thus, it was concluded that the major part of the stress was created by other factors during growth (they measured up to -1.6 GPa of compressive stresses). Jou and Han expected more compressive stress in ZnO films on GaAs than on Si, considering the relative thermal mismatch effects—$\alpha_{GaAs} > \alpha_{ZnO} > \alpha_{Si}$ [98]. However, the results were to the contrary. They attributed this discrepancy to the higher amount of peening effect on ZnO films on Si substrates than on GaAs substrates. They claimed that peening effect would be more pronounced on more crystalline films, and both the XRD and SEM results showed that the films on GaAs substrates were less crystalline than those on Si substrates. However, they did not measure the trapped gas content in the films.

Atomic peening was claimed to occur at low deposition pressures and high incidence angles [216, 217], which enable highly energetic gaseous particles to bombard the film surface (Sec. 1.4, [1]). Under such conditions, energetic particles became embedded inside the film, displacing atoms from their equilibrium positions and causing distortion and residual stress [214, 217]. The maximum pressure value in the study of Hoffman and Thornton (5 Pa = 0.05 mbar) [216] was one order of magnitude lower than most of the pressure values in our study (0.2–0.4 mbar). In addition, the total amount of residual stress decreased with decreasing p (see Table 4.5 and Fig. 4.10), where the opposite would be expected if peening effect were playing a

significant role in stress formation. This result showed that argon entrapment was also not a major effect in the evolution of the residual compressive stresses in our study. Nevertheless, TEM/EDX studies on a detached film sample is necessary to more accurately measure the argon content in the films and conclude on the effect of argon entrapment on the residual stresses.

5.2.3. Microstructure-Related Factors: "Growth Stresses"

In the literature, the links between the varying deposition conditions, film microstructure, and the residual stresses are not complete. In examples from the ZnO thin film literature, the amount of stress, which could not be explained by the TEC-mismatch or other intrinsic effects such as atomic peening, was generally referred to as the *growth stresses* (*e.g.*, [218]). In Sec. 5.2.1 and 5.2.2, the contributions of extrinsic factors such as TEC-mismatch and Ar entrapment into the ZnO films on their total residual compressive stresses were discussed. It was shown that these factors did not have significant contribution to the overall stress level in the films. Thus, the so-called *growth stresses* might have a close relationship with the microstructural evolution of the films during growth.

The mechanisms leading to microstructural evolution and the consequent residual stress evolution were not explained in detail in the ZnO thin film literature. Nevertheless, the general understanding on *growth-stresses* in thin films has improved over the last few years in the literature. A recent critical article by Floro *et al.* reviewed and discussed the proposed mechanisms on residual stress formation of high-mobility elemental films (*e.g.*, Ag, Ge, Si, Al) with Volmer–Weber type growth (in other words, *island growth*–see Sec. 1.2.1 for this growth type) [219]. In their paper, the growth-induced stresses were discussed in relation with the highly non-equilibrium nature of the deposition, and the evolution of microstructure and film thickening. Two major factors were claimed to take part in the stress evolution. First one was the s*urface stresses* of the individual grains and the film-substrate and film-surrounding interfaces: whenever atoms in a crystal surface have a different bonding environment than their bulk, the variations in the equilibrium inter-atomic distances resulted in strain within the crystal.

The second but less addresses mechanism was the *particle incorporation into the grain boundaries* [219]. Different from the previously discussed atomic peening model where atoms of the carrier/ionizing gas (*i.e.*, argon) were claimed to be trapped within the bulk of the film, this idea claimed that the atoms of the target material itself preferentially accumulated more at the grain boundaries than the interior of the grains. According to one model, since the atomic flux directed to the film surface during deposition was many orders of magnitude higher than the equilibrium vapor pressure of the film material, the film surface was at a higher chemical potential than it would be under normal conditions. This chemical potential difference acted as a driving force for the incoming atoms to move towards and incorporate at the grain boundaries in the bulk of the film, increasing the average film density and creating compressive stress within the film. For example, in high-mobility Ag films, a compressive strain of 0.1% was measured, which corresponded to one extra atom at the grain boundary per surface layer added during growth.

Floro *et al.* addressed the stress evolution during film formation and thickening under the so-called *CTC behavior*: compressive stress in the discrete island regime, tensile stress in the island coalescence regime, and compressive stress during post-continuity of film thickening [219]:

i) *Compressive stress in the discrete island regime*: For a finite-sized sphere or disc, Hooke's law and the pressure difference on either sides of a curved solid surface surrounded by a vapor phase dictated that the bulk of that solid was in compression compared to its surface.

ii) *Tensile stress in the island coalescence regime*: Upon island coalescence and grain boundary formation, the amount of free surface, hence the total surface energy, decreased. The associated tensile stress was generally at maximum when the film became continuous. If the material was of low mobility, the tensile stress continued to increase after the film became continuous. During this time, the surface shape continued to evolve as the new atoms were adsorbed on the film surface. The short-range interactions of these adatoms created tensile stresses—as if they were forced to stretch. A similar but minor role of grain growth was also considered in tensile stress creation. Since the atomic density at the grain boundary was smaller than in the bulk, grain growth increased the average density of the film. At these circumstances, the film

tended to contract, but was prevented to do so by the substrate constraint, resulting in tensile stress.

iii) *Compressive stress in the film thickening regime*: The evolution of compressive stresses after the establishment of film continuity and during film thickening was less understood than the previous two cases. For a thin circular disc (diameter >> thickness), due to the radial pressure exerted by the positive surface stress, the equilibrium lattice parameter was smaller than that of an infinitely thick slab (*i.e.*, the film is in compression). When the film was stretched to be rigidly bound to a substrate with a larger surface area, it was in a tensile stress state. This situation was representative of the onset of continuity of a Volmer–Weber film. From that point on, as the film thickened, the effect of the substrate constraint, hence the tensile stress, decreased gradually. Depending on the initial amount of tensile stress and the final film thickness, the stress could go to compression (for a small tensile stress at continuity and a large film thickness). The upper limiting value for that film-continuity stress to have a turnover to post-continuity compressive stress depended on the sum of surface stresses at the film-substrate interface (f_t) and at the free film surface, and the film thickness at continuity (h_{cont}). For example, for f_t = 2 N/m and h_{cont} = 100 Å, that limiting value was calculated as 200 MPa. This value was on the order of residual stresses observed in high-mobility metal films during the coalescence stage. For a larger tensile stress at film continuity, upon further film thickening, the residual stress would never go to compression but would asymptotically approach zero.

It should be emphasized that in the work of Floro *et al.*, the so-called CTC behavior was observed and the model of atomic incorporation at the grain boundary creating compressive stress was in accordance with the observations only for high-mobility films [219]. In the discussion of the CTC behavior, low-mobility films were mentioned to have only tensile stresses, where this behavior was interpreted to be a subset of the CTC behavior. In addition, it was reminded that at low T_s, diffusion from the film surface to the grain boundary would be suppressed, and hence the evolution of compressive stresses at the bulk of the film. The possible compressive stress formation at the nucleation stage and the possible tensile stress at film continuity could not be monitored in our study. Moreover, owing to the low working temperatures and the low mobility of our ceramic film material, the aforementioned CTC behavior and the explanatory models could not be directly applied to our study but should rather be

treated with caution. In the following section, we discuss the evolution of the so-called growth stresses in relation to the deposition conditions, the buffer layer, and the resulting microstructural changes.

5.2.3.1. Effects of the deposition parameters on the residual stresses revisited

The discussions on the residual stresses in ZnO thin films in the literature have concentrated on the effects of the deposition conditions. These effects were presented in detail in Sec. 1.3.2 and some examples are summarized below:

i) *Substrate structure:* Lim and Lee observed that the ZnO thin films on Ru/Si(100) and Al/Si(100) substrates had very different residual stresses from each other, with accompanying differences in the microstructure and texture [140]. The films on the Ru/Si substrates had indistinguishable and densely packed grains, only the (002)-reflection in XRD, and a residual compressive stress of -0.137 GPa. The films on the Al/Si substrates had a mixture of small and large grains with large amount of voids, relatively very low (a fifth of the case on Ru/Si) XRD intensity of the (002)-peak, additional reflections from the (100), (101), and (102)-planes, and -0.986 GPa of residual compressive stress. In that latter sample, the average grain size measured by XRD decreased only by ~6%, while the residual stress increased dramatically by ~620%. It was concluded that the lower stress in the films on the Ru/Si substrates was due to a better *c*-axis orientation and a denser structure [140].

Cimpoiasu *et al.* found that among Si(100), Al(111)/Si, and Al(111)/SiO_2/Si substrates, the highest stress was in the films deposited directly onto the Si(100) substrate [156]. The orientation of the columns in these films also had the maximum amount of deviation from the *c*-axis (Table 1.6.). In addition, the stress in films on the highly (111)-textured Al substrates was less than in those on Si(100). This was attributed to the lower defect density present in the films on Al substrates than those on Si substrates (see Fig. 1.30).

ii) *Substrate temperature* (T_s): Increasing the substrate temperature was observed to decrease the residual compressive stresses in ZnO thin films [95, 98, 156]. Water and Chu [95] proposed two possible mechanisms for the decreasing the overall

residual stress (from -14 GPa to -4 GPa) by increasing T_s (from 100 °C to 400 °C) of ZnO films on Si substrates: *i)* out-diffusion of entrapped gas (argon or oxygen) atoms (however, the entrapped gas content was not measured), and *ii)* increased tensile (*positive* portion) stress on the substrate, which was created by the thermal expansion mismatch of Si and ZnO, and which decreased the compressive (*negative* portion) stress. On the other hand, the decrease in the residual stress by increasing T_s was often attributed to the increased mobility of the atoms, ions, and molecules reaching the surface. For example, when the compressive stress decreased from -0.30 GPa to -0.05 GPa by increasing T_s from 225 °C to 375 °C, Cimpoiasu *et al.* ascribed this result to the adatoms settling to the lowest surface energy positions on the film surface [156]. Increasing T_s and decreasing compressive was also often accompanied by an increase in the XRD peak intensity associated with the *c*-axis-orientation (*e.g.*, decreasing σ_c from -2.5 GPa to -0.5 GPa by increasing T_s from 250 °C to 450 °C [95]).

iii) *Chamber pressure* (p): As the density of argon ions inside the chamber increased, sputtered particles encountered a greater energy barrier before reaching the substrate, because more energy was lost due to collisions [1]. When p increased, the mean free path for elastic collisions between the sputtered species and the chamber gas was roughly the distance between the target and the substrate; then, the oblique component of the deposition flux increased, producing a more open Zone 1 structure [52]. When p decreased, the energetic particle bombardment increased, correspondingly increasing the film density [52]. Cimpoiasu *et al.* found an optimum chamber pressure (6 mTorr = 0.008 mbar) for minimum compressive stress (about -50 MPa) [156] proposing that a lower pressure led to an increase in the energy of the adatoms and damaged the film and the substrate. A higher pressure, on the other hand, caused a decrease in the adatom energy and mobility, owing to the higher number of collisions on their way to the substrate.

iv) *RF power* (P_{RF}): High RF power led to high deposition rates and high energy adatoms [156]. Increasing P_{RF} resulted in build-up of compressive stresses [96, 99, 102] (*e.g.*, σ_c increased from -0.4 GPa to -1.4 GPa as P_{RF} increased from 0.2 W/cm^2 to 1.3 W/cm^2 [99]), presumably because the adsorbed atoms could not settle to the lowest energy sites before succeeding atoms were adsorbed, which resulted in stress build-up [156]. For both ZnO and Al-doped ZnO films, the stress increased with increasing DC power, *i.e.*, the P_{DC} /(P_{RF} + P_{DC}) ratio, while the grain size remained

relatively constant (Fig. 1.31) [25]. This result was attributed to the more intense ion bombardment of the films by the RF discharge than by the DC discharge.

To summarize, in the literature, when the *c*-axis orientation, the stoichiometry, and the density of the ZnO films were improved either by the use of suitable templates or by increasing the mobility of the adatoms (*e.g.*, by increasing T_s), the *intrinsic* part of the residual compressive stresses decreased. The *extrinsic* contribution could already be eliminated either by the use of substrates with matching TEC with ZnO or by preventing atom incorporation inside the films upon optimized p and P_{RF}. Our residual stress results and their correlation with the film microstructure will be discussed in light of these findings.

First of all, although the film growth in our study was not epitaxial, the nature of the substrate material was still important. When samples on silica glass, mica, and Si(100) were compared, it was seen that a crystalline ZnO film grew with strong texturing on all of the substrates, but with varying degrees of residual compressive stress (Fig. 4.6 and Table 4.1). The nature of the substrate material might be affecting the residual stresses in the film by influencing the microstructure of the first nucleated layers. The crystalline substrates might promote *preferential nucleation* over *random nucleation*; therefore, determine the crystallinity of the initial layers (see Sec. 5.11).

Comparing the films on various substrates, the highest stress was found in the films on the Si substrate. In this particular case, the crystalline nature of the substrate could also be disadvantageous when minimum stress is desired. The incompatibility of the film and substrate crystal structure (*e.g.* the hexagonal ZnO and cubic Si) might create lattice defects during the initial stages of film growth [156]. It is necessary to actually measure the number of defects on the ZnO films as a function of the substrate material to verify this hypothesis. In this respect, mica could be a better template for ZnO films than Si(100), by providing more nucleation sites, as in the case of Al [156] or Ru [140] substrates. Compared to the Si(100) substrate, the films on mica had less residual compressive stress (-3.54 GPa vs. -6.69 GPa) and larger grain size (19.2 vs. 8.95 nm) at 0.02 mbar with T_{s_0} = 200 °C (see Table 4.1). No records on the residual stresses of ZnO films on mica substrates could be found in literature. In our study, mica has been shown to be a more suitable substrate for sputtered ZnO films than Si, when low residual stress and large grain size are desired. However, TEM studies are required

to account for the presumably improved interfacial microstructure and the consequent decrease in the compressive stress in ZnO films on mica.

Although the crystallinity of the substrate might be affective in stress evolution, the growth of strongly textured and highly stressed films on amorphous substrates indicated that the contribution of lattice mismatch was a minor effect. For the glass substrates, any possible preferential nucleation was eliminated, since the surface did not have long-range structural order. This enabled the investigation of the effects of T_s, p, and P_{RF} on residual stress. The residual stress decreased as T_s was increased at all p and P_{RF} values, and increased with increasing p and P_{RF} for all T_s values (Table 4.5, 4.6, 4.7 and Fig. 4.10, 4.11, 4.12). Among all the ZnO film samples (single layered and without any post-deposition treatment), the highest stress (-7.59 GPa) was produced under the low T_s (RT) and high p (0.4 mbar), conditions, whereas the minimum as-deposited film stress (-2.68 GPa) was generated under high T_s (200 ^{o}C) and low p (0.02 mbar) conditions (Table 4.4 and Fig. 4.9; see also point II in Fig. 5.1). As discussed earlier in this section, the increased mobility of the adatoms upon increasing T_s could be relieving the stress by allowing more nuclei to form with the orientation resulting with the minimum stress [156]. When the substrate temperature was constant, both increased pressure (Table 4.4 and Fig. 4.9) and increased RF power (Table 4.5 and Fig. 4.10) increased the compressive residual stress independently. Increasing pressure must have lowered the energy of the adatoms [1, 52]. This had a similar effect with decreasing the substrate temperature. Finally, when the RF power increased, the ejection energy might have also increased for particles sputtered from the target [1, 156]. These results of decreasing stress with increasing T_s and decreasing p and P_{RF} were consistent with previous work in the literature [1, 25, 52, 95, 98, 156].

Having considered the possible influences of the substrate material and the relative effects of the deposition conditions on the film microstructure and the residual stresses, an explanation of the active mechanisms that created the residual stresses is still incomplete. None of the theories presented in Sec. 1.3.2, Sec. 5.2.1, or Sec. 5.2.2 could satisfactorily explain the evolution of such high residual compressive stresses in our study. At this stage, it might be complementary to consider the non-equilibrium nature of the deposition process. For instance, adatom movement might not necessarily be frozen at the sub-layers of the thin film as the new layers were formed. There might still be rearrangements within the film during the course of growth, towards improving

crystallinity. Although the substrates were not heated externally, the local temperature upon ion impact could reach as high as 80 °C [155, 203]. Thus, there could be local driving force for energy transfer from the film surface down to the bulk. At any given time, the driving force for crystallization would be higher in layers closer to the film surface than in layers closer to the substrate. This would lead to a gradient in strain energy through the film thickness, generating a residual stress.

From the XRD results, it is clear that the *texture* in the film and the measured film stresses are interrelated. [As discussed in Sec. 5.1.2, in most cases, only the (002)-texture was observed in the ZnO films (*e.g.* Fig. 4.18.d and 4.18.e); however, the (101)-reflection was also observed in all sample sets with the deposition conditions of 125 W RF power, 0.2 mbar of argon pressure, and 200 °C substrate temperature (Fig. 4.18.b, 4.18.c, 4.19), and these conditions produced films containing a mixture of hexagonal prismatic and (bi)pyramidal hexagonal prismatic grains, with some having a *c*-axis parallel to the surface normal and others tilted such that a group of (101)-planes met the Bragg condition (see Fig. 5.6 and Fig. 5.7).] In these XRD spectra, the presence of the (101)-peak correlated with the amount of shift of the (002)-peak. For the ZnO film on fresh glass substrate (Set 6), when there was a (101)-peak, the amount of left-shift of the (002)-peak in that sample was less (Fig. 4.18.c). In other words, the presence of tilted grains decreased the amount of compressive stress in the columns perpendicular to the substrates. The average amount of residual compressive stress in those tilted grains were calculated from the shift in the (101) peaks as -2.73 GPa. For the ZnO film on acid-cleaned glass substrate (Set 8) and the ZnO film on ZnO buffer layer (Set 13), as the strain in the (101)-plane decreased, the strain in the (002)-plane decreased as well (Fig. 4.18.b, 4.19, 4.20, and Table 4.8).

In Fig. 5.12, ZnO films with different microstructures were compared as a function of σ_c, regardless of the deposition conditions. The first two samples have the *tilted* grains (triangular prismatic or (bi)pyramidal hexagonal prismatic). The films with the triangular prismatic grains had the least amount of residual compressive stress, when compared to the other morphological types (Fig. 5.12.a; σ_c = -2.88 GPa). These films were deposited on untreated glass substrates at high T_s, low p, and low P_{RF} conditions (Table 1.3). In comparison, the films deposited under the same conditions on acid-cleaned substrates had (bi)pyramidal hexagonal prismatic grains and a slightly higher residual stress (Fig. 5.12.b; σ_c = -3.32 GPa). Between the two, increasing (101)-

reflection in the XRD increased the residual stress (nevertheless, it should be kept in mind that the difference between the two values is close to the error range of ±0.55 GPa—see also Fig. 5.6).

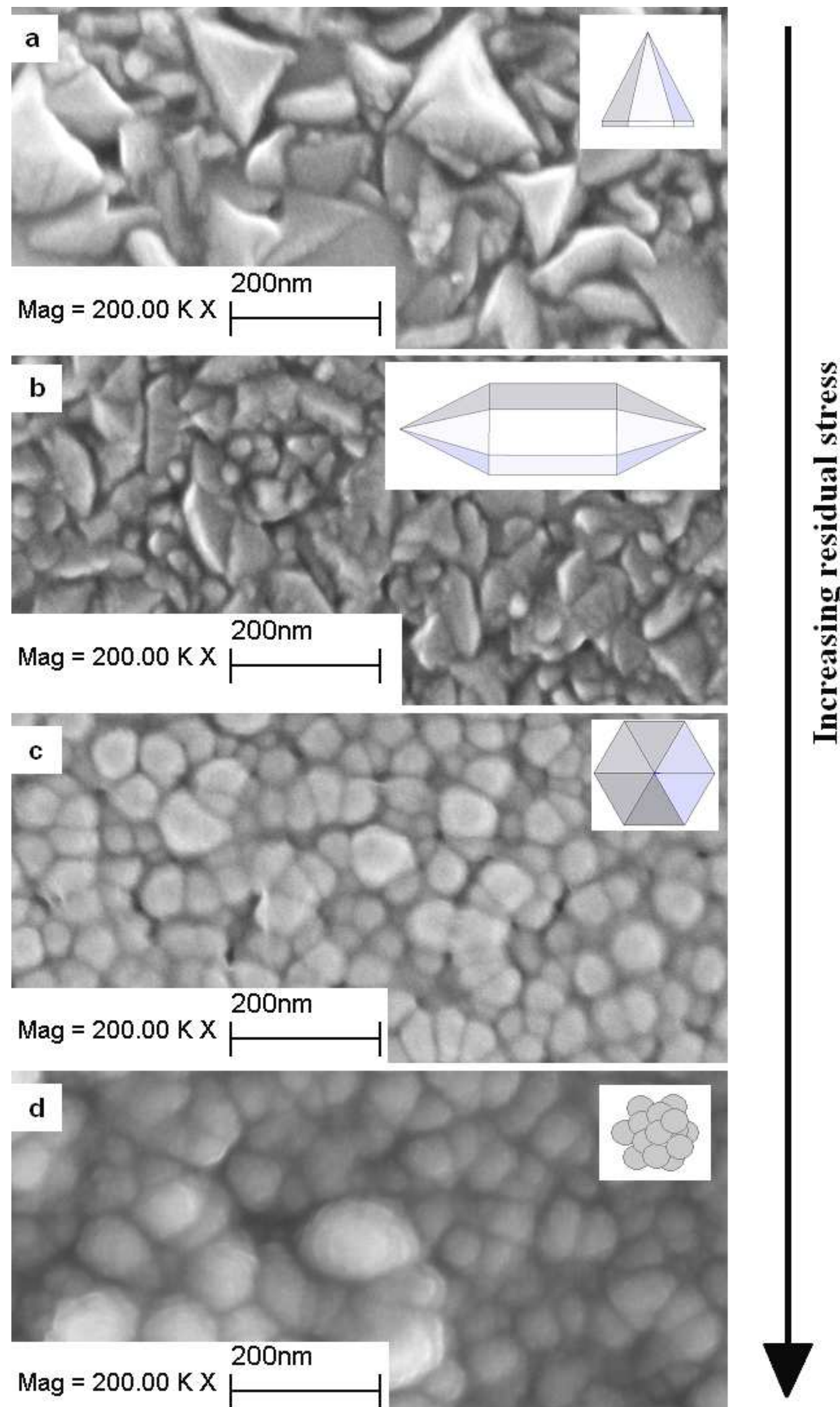

Figure 5.12. Microstructure of the as-deposited films, in order of increasing residual stress: (a) σ_c = -2.88 GPa (Set 6); (b) σ_c = -3.32 GPa (Set 8); (c) σ_c = -3.83 GPa (Set 7); (d) σ_c = -6.78 GPa (Set 3) (see Table 3.1 for sample labels).

In Fig. 5.12.c, the change in the grain shape compared to the (101)-textured films with tilted grains (Fig. 5.12.a and 5.12.b) could be seen upon decreased T_s at the same p and P_{RF}. At these conditions, the tilted grains vanished, and the grains with circular or hexagonal cross-section with better-defined continuous columns dominated (see also Fig. 4.14). These conditions produced an increase in residual compressive stress from -3.32 GPa to -3.83 GPa, compared to the films with the tilted grains (Table 4.4). Simultaneously, the (101)-reflection vanished in the XRD spectra (Fig. 4.18.e). Since the surface mobility decreased by decreasing T_s, although some initially (101)-oriented grains might have remained, they might not have been able to coalesce and grow further to gain a significant XRD intensity. The improvement in texture and the simultaneous increase in σ_c seem contradictory in respect to the previous discussion of decreasing stress with improved *c*-axis orientation.

When the pressure was increased further to 0.4 mbar, the residual compressive stress increased regardless of the other parameters (Table 4.4). All of the films that were deposited at the highest p value had a lower degree of crystallization, with much lower XRD peak intensities than the cases with lower pressure. An example could be seen in Fig. 4.8.a. These films also had *cauliflower-type* grains composed of smaller sub-grains (Fig. 4.13.d or Fig. 5.12.d). Moreover, among the high-pressure samples, the ones deposited at lower temperatures were more stressed. Due to the lack of mobility, the smaller grains could impinge on each other, competing for adsorbing atoms and forming hierarchical aggregates [51]. Extrapolating the previous structure zone models, this region of very low adatom mobility corresponds to Zone 1 with a high dislocation density and high residual stresses [51]. However, a relation between the increased dislocation density and increased residual stress in ZnO thin films cannot be found in the literature.

In order to sum up the observations it can be said that in the 0.2–0.4 mbar (150–300 mTorr) range, there was no inverse proportionality between the amount of residual compressive stress and the quality of (002)-orientation of the columns, in contradiction to the previous literature. In that range, it could be said that σ_c decreased with increasing T_s and decreasing p, regardless of P_{RF}. In other words, σ_c decreased with increased adatom mobility. However, σ_c did not decrease with increasing (002)-orientation. Instead, σ_c decreased with the introduction of the (101)-texture and the tilted grains at p = 150 mTorr and T_h = 0.21, compared to the previous lower T_h case at the same

conditions (see Fig. 5.12). Thus, the quality of the (002)-orientation of the columns was not the only factor playing a role in the evolution or reduction of growth-stresses. This fact is crucial for understanding the residual stress formation in Volmer–Weber films mentioned in the beginning of Sec. 5.2.3.

If the so-called CTC behavior [219] was valid for the films in our study, the increasing overall compressive stress could be interpreted as at least one of the following: increased compressive stress at the island formation regime or at the post-continuity film thickening regime, or decreased tensile stress at the island coalescence-film continuity regime.

i) If the (101)-oriented grains started to form at the interface (see the discussion in Sec. 5.1 and Fig. 5.2), the structure of the interface might have affected the amount of stress in the upper layers of the film. Since ZnO is crystallographically anisotropic, the surface stresses, hence the stresses inside the bulk of the grains, would differ depending on which surface was exposed and which surface formed the nucleus-substrate interface during island formation regime. If the islands were oriented such that their surface stresses were less, then the compressive stress inside the bulk of those islands would be less as well.

ii) Moreover, during the island combination and film continuity regime, the created tensile stresses would depend on the nature of the surfaces that were combining. Consider two islands that are orientated such that their surfaces facing each other interact more strongly with each other than two similar islands of a relatively different orientation. The first couple of islands would "feel" more stretched, hence they would have less tensile stress or more compressive stress during this stage.

iii) Finally, suppose continuous nucleation occurred during the film thickening stage (see Sec. 5.1.2). If these nuclei were randomly oriented with respect to each other, the interactions among these newly formed nuclei would be less than the case where they were oriented in the same direction. In that case the tensile stress they would exert on each other would be decreased.

The interactions between different crystallographic surfaces during different stages of film thickening could not be monitored in our study. Hence, there is not enough evidence to comment on the role of the so-called CTC behavior in the overall stress evolution in ZnO thin films. A more plausible explanation could be sought in the

model of atomic incorporation into grain boundaries, which was presented in Sec. 5.2.3 [219]. The driving force for this mechanism is the chemical potential different at the surface and the bulk of the film at the highly non-equilibrium conditions during film growth. Thus, the extent of the compressive stress that would be created by this route must depend on the following:

i) large chemical potential difference between the film surface and the bulk (requires high P_{RF}),

ii) high mobility of the adatoms to diffuse to the grain boundaries (requires high T_s and low p,

iii) large grain boundary area (depends on the resulting film microstructure).

Considering the results in our study, the first condition seems reasonable: the residual compressive stress increased with increasing P_{RF} when the other parameters were kept constant. However, the second item seems contradictory: the compressive stresses in our study decreased with increasing adatom mobility. Nevertheless, this conflict could be resolved by considering the changes in the microstructure of the film, hence the third item. If the deposition conditions were such that the overall grain boundary area was larger, then more atoms could be incorporated at the grain boundaries. The total grain boundary area in a material is inversely proportional to the grain size. Considering the comparison in Fig. 5.12, the decreasing trend in the compressive stress from (a) to (b) and from (c) to (d) could be related to the decreasing grain size and increasing grain boundary area. The difference in the grain boundary area between (b) and (c) could not be seen clearly. The only difference between these to samples was T_s, which was lower in the latter case. Thus, according to the mobility of the adatoms and related atomic incorporation to the grain boundaries, a lower compressive stress would be expected in the latter case. On the other hand, grain boundary area in the latter case could be higher as a result of the growth kinetics (which included the nucleation density relative orientation of the nuclei, competing growth rates of nucleation, nuclei growth, grain growth, column growth, and film thickening—see Sec. 5.1), allowing more atoms to be incorporated, creating a higher residual compressive stress. To definitely comment on this, accurate measurements of the grain boundary areas should be done.

Atomic diffusion in and out of grain boundaries was also considered to be a possible mechanism for stress relaxation [219]. In our case, in the presence of randomly

oriented grains in the initial film layer, there would be grain growth in many directions. This might have led to increased porosity within the film, as it grew thicker. If film atoms were incorporated at the grain boundaries during growth and created compressive stress due to the large chemical potential difference between the film surface and the bulk, the porosity at the grain boundaries might have eased atomic diffusion in the opposite direction (from the grain boundaries to the column surfaces, and from the column surfaces to the film surface) after the deposition was completed, enabling equilibrium between the chemical potentials of the bulk and the surface. Enabling such reverse motion of the incorporated atoms could be the reason of the reduced strain in those samples.

On the other hand, no such (101)-texture existed at lower pressures (0.02 mbar; Fig. 4.18.d), and an even lower residual compressive stress was measured (-2.68 GPa). These observations might be indicating that different mechanisms might be acting on the formation of growth-stresses depending on the deposition condition. In the lower pressure regime, the improvement of grain orientation by momentum-induced, increased adatom mobility, combined with a less dense nucleation (see Fig. 5.3) might decrease in the residual compressive stress [156]. Again, grain boundary area should be measured to comment on the possible role of atomic incorporation into the grain boundaries.

At least one of these factors (variation in the interaction strength of different crystal surfaces, orientation and the nucleation density at the early stages, porosity, atomic incorporation in the grain boundaries) could play a role in the decrease of compressive stress in the films with additional (101)-texture. However, deeper knowledge on the kinetics and thermodynamics of ZnO thin films should be known to implement any of these factors into stress evolution theory. For example, the atomic incorporation model was valid for a high-mobility Ag film with compressive strains on the order of 0.1% [219], where the compressive strains were on the order of 1% in our study. To comment on the validity of this model for low-mobility films such as ZnO deposited at low T_s and high p, and to conclude on the effect of formation of (101)-texture on the decrease of compressive stress, the following should be known: the relative mobility of Zn and O ions inside bulk ZnO and the grain boundaries, the relative surface energies of the ZnO crystal, and the kinetics of the formation of each surface at different deposition conditions. To close, the ideas of both atomic

incorporation at the grain boundaries causing compressive stress and the improved (002)-orientation decreasing the compressive stress should be handled with caution in explaining the stress evolution in low-mobility ZnO thin films.

5.2.3.2. Effects of the buffer layer on the "growth stresses"

As stated earlier, the initial stages of the film deposition is critical in terms of determining the properties, as the film grows further. To understand the role of the film-substrate interface better, a set of substrates was deposited with a very thin layer first (about 67 nm). Some of the buffer layer samples were later annealed in air and used as substrates for further film growth (Set 13; Table 3.2), and some of the buffer layers were used as substrates without being annealed. The microstructural evolution in ZnO films grown on these buffer layers and the improvement of the *c*-axis orientation was discussed in Sec. 5.1. Similar effects of the buffer layer on the microstructure and texture of the ZnO thin films have been observed in a few studies [141, 142]. However, the residual stress concept was not discussed in either of those studies. One study noted that the buffer layer in ceramic thin films reduced the lattice misfit, the stress at the interface, or dislocation migration [77].

The residual stress in the buffer layer before and after annealing could not be measured, since these layers were thin and did not generate sufficient diffracted intensity for reliable analysis. Among all the samples in our study, the films on a pre-annealed buffer layer had the minimum amount of residual stress (in the range from -1.09 to-1.73 GPa; Table 4.8). The films on a non-annealed buffer layer were more stressed than films on a pre-annealed buffer layer (in the range from -2.34 to-2.60 GPa), but still less stressed than the films deposited under the same conditions but without a buffer layer (Table 4.8). Grain growth and texture improvement upon annealing were also shown in Fig. 4.26 and Table 4.10, and discussed in Sec. 5.1. These findings suggested that the initial layer and its orientation distribution were very critical in determining the average stress in the film. As discussed in Sec.5.2.1 and 5.2.2, at the conditions of the buffer layer deposition, the films had a void structure and tilted grains, and the amount of residual stress was determined by the competition between random or textured orientation of the initial grains and the density of the columns which was determined by the competition between the nucleation and the growth rates. At those

conditions, although not all the grains were oriented perpendicular to the substrate, the void formation due to the tilted grains presumably decreased the stress. When the buffer layer was annealed, the role of the improved orientation was emphasized, and the stress decreased further. The decreasing stress in the latter case is consistent with the availability of more nucleation sites for the *c*-axis oriented grains after annealing of the buffer layer, resulting in a lower residual stress as discussed in Sec. 5.2.

In Fig. 4.21 and 4.22, it could be seen that at the same deposition conditions, using a buffer layer resulted in densification of the film as well as a decrease in the grain size, hence an increase in the grain boundary area. At the same time, the residual compressive stress decreased with the use of a buffer layer. This fact could not be explained with the incorporation of atoms to the grain boundaries during deposition, creating compressive stress. Because, according to that model, a larger grain boundary area would allow more atoms to be incorporated, and would cause a higher residual compressive stress.

5.2.4. Section Summary

In this section, the residual stresses in ZnO thin films were discussed in relation to the corresponding sections of the SZM constructed in Sec. 5.1. Various intrinsic and extrinsic effects were considered for residual stress formation. Mismatch of thermal expansion coefficient or crystal lattice between the film and the substrate, and incorporation of argon ions/atoms within the film during film growth were evaluated to be minor effects for stress evolution. The majority of the stresses were interpreted to arise from microstructural factors such as texturing at either the interfacial layer between the film and the substrate or within the bulk of the film. The effects of various deposition parameters in microstructural evolution and corresponding stress evolution were discussed. To summarize, as the mobility of adatoms was increased, whether by increasing T_s or decreasing p (or P_{RF}), the residual stresses decreased. This was presumed to be a result of,

i) the atoms finding the suitable lattice sites in a way to decrease the stress (not necessarily to form more (002)-planes),

ii) the grains orienting themselves in a way to decrease the stress (not necessarily in the *c*-direction being parallel to the substrate normal).

In the lower pressure ($p \leq 0.2$ mbar) the quality of the (002)-orientation of the columns might be the major mechanism that decreases the compressive stress. On the other hand, in the higher pressure regimes, incorporation of native atoms into the grain boundaries together with (101)-texture formation and increased porosity were considered to be factors that controlled the residual stresses.

In addition, a pre-deposited and pre-annealed thin buffer layer of ZnO resulted in the least amount of compressive stress, presumably due to the increased number of nucleation sites for the adatoms allowing them to be oriented in the direction to give the minimum stress in the upcoming layers. Decrease of compressive stress upon buffer layer use could not be explained by the model of atomic incorporation to the grain boundaries. Nevertheless, more accurate measurements on the grain boundary area and the thermodynamic parameters during film growth are necessary to conclude on this mechanism.

5.3. Stress Relaxation

Residual stresses in thin films affect the microstructure, and thus the functional (optical, electrical, magnetic) properties of those films as a consequence (see Sec. 1.3.3 and Appendix E). For example, void formation in the films influence the refractive index [151]. Films containing these stresses are unstable [49, 74, 76], and the microstructure may evolve in order to relieve the stresses [49]. If the amount of mechanical energy stored inside the film is considerable, such as several GPa, it may be released eventually by crack generation, crack propagation and delamination from the substrate [49]. Thus, such stresses are mostly unwanted. Post-deposition annealing has been widely used for stress minimization in thin films [95, 150-154]. The results concerning the release of stresses in our study are discussed below.

5.3.1. Stress Relaxation Mechanisms and Relevant Causes of Residual Stress

Our results showed that the residual compressive stresses in ZnO thin films could be reduced on any of the three types of substrates by annealing at 600 °C for 1 h. As seen in Fig. 4.24, upon annealing the (002)-peak of the film in the XRD spectra shifted closer to the (002)-peak of the powder, moving towards lower plane spacing (*d*). This indicated a lower axial strain a release of compressive stresses in the film plane. The planar compressive plane stresses decreased by ~90% for the film on the glass substrate, and ~95% for the film on the mica substrate (Table 4.9 and Fig. 4.25). The remaining stress amount was at the limits of the error range. For example, for the film on the Si(100) substrate, the residual stress changed sign upon annealing, and the residual stress was calculated as +0.48 GPa. This value corresponded to ~7% of the stress before annealing, when the absolute values were considered. In all films, the remaining amounts of residual stresses after annealing were very close to the previously calculated σ_{th} values (Table 4.3 and Fig. 4.8). This result is very important since it indicates that the so-called *growth stresses* were eliminated by thermal annealing. Post-annealing stresses were only due to the TEC-mismatch of the film and the substrates, which gave rise to differences in the amounts of shrinkage during cooling down to room temperature from 600 °C.

To understand the mechanism of stress release during annealing better, structural evolution was monitored in-situ by XRD measurement of some samples with increasing temperature. The intensity of the ZnO (002)-peak increased with temperature increase from 25 °C to 170 °C, but no change in the peak shift was observed (Fig. 4.27). The peak shift was minimized only after cooling down back to room temperature. The peak intensity was the highest for the cooled sample. This result was reasonable because the films were heated rapidly (in about 10 min), but cooled slowly (in about an hour). Stress relaxation is a kinetic process, and the time spent during heating might not be sufficiently long for stress relaxation at 170 °C (due to system limitations, isothermal annealing at 170 °C was not possible). However, since mobility is temperature dependent, the atomic movement in the film could have been initiated at that temperature, and continued with gradual slowing as the film cooled, eliminating defects along the way. In contrast, the peak intensity of the Si(100) substrate decreased during heating. This might be due to *i)* an increased fraction of the incident x-ray beam being

diffracted by the ZnO film, decreasing the fraction incident on atomic planes in Si(100), and/or *ii)* formation of an additional oxide layer at the Si-ZnO interface—the latter must be verified by TEM examination

Either isothermally or under increasing temperature, upon annealing, the (002)-peaks in the XRD spectra became more symmetric, being another indication of the decrease in the unit cell distortion [209] (other than the peak shift). These peaks also became narrower and more intense (Fig. 4.24 and 4.28). Thus, the stress release was accompanied by an improvement in the (002)-orientation and an increase in the grain size (see Sec. 5.1.4 for the discussion on the increase in grain size upon annealing). These observations were in accordance with the literature. In some studies, an optimum annealing temperature for annealing ZnO in air was found for stress relief, ranging from 480 °C [154] to 600 °C [95]. Annealing at that optimized temperature often led to the strongest texture, the largest grain size, and the maximum XRD peak intensity[190]. The increase in surface roughness upon annealing was attributed to the migration of atoms to lattice sites, driven by preferential grain growth along the [002]-direction to minimize the grain surface area [190]. In some studies, above that optimum temperature, the residual stress changed sign and became tensile, accompanied by a sudden increase in the grain size that was attributed to grain coarsening [151]. The annealing temperature in our study corresponded to T_h = 0.38, which was consistent with the grain growth and stress release arguments in the literature.

In Sec. 5.1 and 5.2, it was discussed that the texture evolution during film growth influenced the growth stresses. There was no direct relation between the orientation of the grains (*i.e.*, the (002) or the (101)-texture) and the total amount of residual stress in the films. The residual stress amount was determined by a combination of competing mechanisms, such as adatom flux, rates of nuclei formation and growth, growth rate of different crystallographic planes, shadowing effects, and growth rate of columns. However, during post-deposition annealing of the films, there was no nucleation or film growth. In that case, the leading mechanism would be the minimization of surface energy of the grains along with strain relaxation. The minimum surface energy of a ZnO crystallite is achieved with maximizing the length along the *c*-axis [137]. In Sec. 5.1, it was discussed that the columns were not necessarily single grains. It was shown earlier that at either high film deposition temperatures or high annealing temperatures, the atoms had enough energy to overcome the activation energy for diffusion and to occupy

the proper lattice sites and form large grains [220]. Thus, upon annealing, the grains within a column might have coalesced to form taller crystals with *c*-axis orientation all along that column.

Aging of the samples during storage in air for ~28 months caused a similar decrease in the residual stresses as by annealing, both for glass and the Si(100) substrate (Table 4.10, Fig. 4.29 and 4.30). The amounts of stress that remained after annealing and after aging were the same and negligible within reasonable error limits—the growth stresses were completely eliminated, either by the energy provided by the high annealing temperature, or by providing the time required for slow annealing at room temperature. For the aged ZnO film on the glass substrate, there still existed a residual compressive stress of -1.25 GPa. This indicated that the annealing process was slightly slower for these films than the films on the Si substrate. It had been mentioned before that the residual stresses in thin films change over time [49, 74, 76], with accompanying changes in the microstructure of the film [49]. However, to our knowledge, there is no other report in the literature on stress dynamics in ZnO thin films.

Another important point is that although thermal annealing and prolonged aging induced a similar decrease in the residual stress, the resulting microstructures were different from each other. This could be indicative of different mechanisms for stress relaxation depending on the energy flux provided to the film from the surroundings. This energy flux would obviously be higher during high-temperature annealing compared to room temperature aging (aging could be regarded as annealing at room temperature). There was considerable amount of surface porosity in the annealed films (Fig. 4.33 and 4.34.a). On the other hand, surface porosity was not of a size scale observable by SEM in either the as-deposited or the aged films (Fig. 4.35.a). However, significant porosity may still be revealed by cross-sectional transmission electron microscopy (TEM) imaging. As was discussed in Sec. 5.1, these films lie within Zone 1, Zone T, or Zone M, all of which have some amount of porosity and limited surface diffusion. Thus, it is still reasonable to claim that the films grew with some degree of porosity. The energy provided by thermal annealing could have overcome the activation energy for pore mobility, promoting pore coalescence and pore growth.

Along with grain growth or pore growth, the elimination of pre-existing defects can also contribute to stress relaxation [151, 156]. Wurtzite-type ZnO contain intrinsic defects such as oxygen vacancies $(V_O, V_O^{\bullet}, V_O^{\bullet\bullet})$ and zinc interstitials $(Zn_i, Zn_i^{\bullet}, Zn_i^{\bullet\bullet})$

[13, 33]. In our study, we investigated the role of possible oxygen vacancies in stress relaxation. Two identical samples were annealed in an air and in pure argon atmosphere at 600 °C for 6 hours to compare the effect of annealing at different oxygen partial pressures. If the films had oxygen vacancies, oxygen diffusion into the film from air would be expected during annealing at high temperature in air, with associated stress release. No such behavior would be expected for annealing in argon, the effectively neutral ambient. However, no significant difference in the XRD spectra could be observed between these two samples after annealing (Fig. 4.28). Thus, it could be claimed that the amount of oxygen vacancies were not high enough to cause a stress amount detectable by XRD, and the stress-relaxation was not a result of decreasing the amount of oxygen vacancies in the film. In a similar experiment by Isa *et al.* [214], no difference was observed between the effects of pure oxygen and pure nitrogen atmospheres during the annealing of ion-beam sputtered ZnO films on glass and Si substrates at 500 °C for 3 h. Both gases induced a similar decrease in the residual compressive stresses, *FWHM*, and increase in the intensity of the (002)-peak. Nonetheless, annealing experiments in complete vacuum followed by TEM analysis would provide more evidence on the oxygen vacancy status of these films in our study.

Based on the above discussion, possible oxygen vacancies in the films causing stress is not very likely. On the other hand, there might be oxygen or zinc interstitials in the films, causing stress. In addition, incorporation of excess atoms into the grain boundaries during film growth was considered to be a possible factor in the evolution of residual stresses (Sec. 5.2.3). Reverse motion of those incorporated atoms out of the grain boundaries towards the film surface was proposed to be a route for stress relaxation [219]. Gawlak and Aita discussed the possibility of oxygen or zinc interstitials as a cause of stress, and their diffusion as a cause of stress relaxation [155]. They calculated the activation energy for the stress relaxation process as 0.2 eV/diffusing species [155]. This value was one order of magnitude lower than the activation energy for diffusion of either zinc or oxygen in single crystal or powder ZnO [221]. The authors proposed that, although there might be rearrangement of interstitial atoms upon annealing, the diffusion of zinc or oxygen interstitials to the allowed lattice sites, or to any external surface, were not the rate-determining mechanism for strain relaxation. They also argued that the motion of interstitials inside the films could be initiated by local plastic deformation, and then retarded by the dislocations. Isa *et al.*

also proposed that the as-deposited ZnO films were non-stoichiometric, with excess Zn interstitials; in addition to stress relief, annealing these samples increased the stoichiometry in the films [214].

Aside from the elimination of point defects, the motion of dislocations and/or grain boundaries could be another possible mechanism for stress relaxation in thin films. The lattice mismatch strains in crystalline thin films on single crystal substrates with a non-matching crystalline structure are known to be accommodated by dislocation formation during film deposition [218]. The formation of dislocations diminishes during cooling to room temperature after deposition. In ZnO films deposited on sapphire substrates, the hardness was found to be 5.75–8.7 GPa (Table 1.5, Ref. [143, 146]). In these films, a sudden motion of dislocations, which were pinned by pre-existing defects, was observed upon loading along both the pyramidal (101) and the basal (001)-planes. Even on amorphous substrates, the residual stress amounts in our samples (see, for example, Table 4.10) were close to these hardness values. Thus, the residual stresses in the as-deposited films could be enough to enable dislocation mobility. Dislocation pile-up and/or elimination of grain boundaries can also explain the occurrence of pores within the films upon annealing. However, to investigate the role of dislocations in stress release (if any), TEM studies of the as-deposited and the annealed films are necessary.

5.3.2. Drawbacks of Stress Relaxation and Possible Solutions

There were simultaneous changes in the microstructure other than grain growth as the stresses were released. SEM examination of the films revealed the formation of porosity in the films upon annealing (Fig. 4.33). The pores formed within the film (Fig. 4.33.a), and/or at the film-substrate interface (Fig. 4.33.b). In some samples, the interface was damaged upon annealing by the formation of extended voids (Fig. 4.33.c). Some similar results in the literature were assigned to possible thermal stress creation [190] (the residual stresses were not measured in this study). Clearly, such changes in the microstructure upon annealing would change the functional (optical, electrical, piezoelectric) properties of the films significantly. Thus, annealing may not be a viable solution for stress-release in ZnO thin films.

In our study, SEM examination showed that the stressed films eventually faced buckling, cracking, and loss of adhesion to the substrate (Fig. 4.34–4.40), regardless of post-deposition thermal annealing treatment. Examining the planar surface of the annealed films revealed the presence of elongated crack-like defects upon pore coalescence on the surface (Fig. 4.34 or 5.13). No pore formation was observed on the surface of films that have been deposited at the same conditions, aged, but not annealed (Fig. 4.35). The cracks in those films followed the grain boundaries. These observations were consistent with reports in the literature where pore-grain size coupling and pore clustering altered the fracture strength and critical crack size in single crystal ZnO [47]. Gupta and Mansingh also observed micro-cracks and voids upon annealing, along with grain coalescence and increase of surface roughness [151], proving the formation of voids by refractive index measurements in addition to SEM analysis [151]. Thus, the accelerated pore formation and clustering induced by high-temperature annealing must have caused cracking in the annealed samples.

In fact, the micro-fracture dynamics were not confined to the film-substrate interface—perturbations in grain boundary structure in ZnO thin films have also been reported during annealing at lower annealing temperatures (*e.g.* 500 °C), along with decrease in residual compressive stress [222]. The upper limit of the annealing temperature was set by the phase equilibrium of the substrate materials, and lower annealing temperatures required much longer annealing times for stress release that caused micro-fracture and defective boundaries [222]. For this reason, methods other than high-temperature post-deposition annealing should be considered to produce stress-free films [214].

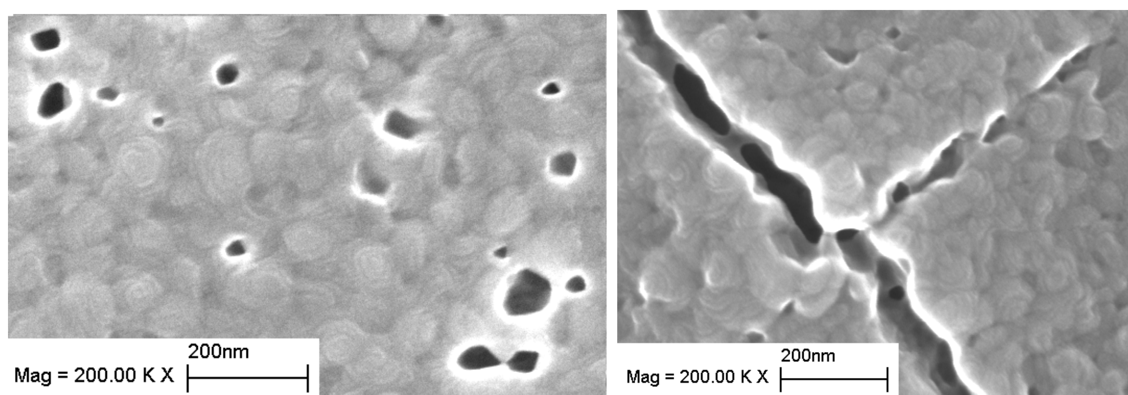

Figure 5.13. Void formation and consequent cracking in the annealed films.

Another consequence of annealing was the reversing of the film-substrate bending (Fig. 4.23). When the as-deposited film ($h \approx 400$ nm) on the thin glass microscope cover slide ($h \approx 160\ \mu$m) had residual compressive stress, the film-substrate laminate was bent towards the substrate (the other substrate systems were too thick for a naked-eye observation of bending of the laminate). Upon annealing, bending direction of this laminate reversed. An explanation for this phenomenon could be sought considering the SEM observations. The pores forming at the interface upon annealing (Fig. 4.33) of an initially high-compressive stress film could contribute to the formation of tensile stresses at the interface (Fig. 5.14). These pores could have accumulated at the film-substrate interface, since the diffusion of pores through the substrate was probably limited. In this case, pore coalescence would manifest itself as local film densification. Upon short-range interaction of the surfaces on either side of a pore, the film material would experience a stretch at these regions, hence would possess a tensile stress at the regions near that interface (like the tensile stress created during film continuity–see Sec. 5.2.3). This opposing stress would decrease the net compressive stress in the film. If it was large enough, the net average stress on the film could have turned to tensile; then the laminate would bend towards the film side (Fig. 1.14). The tensile stress at the interface of that film sample (where bending direction was reversed upon annealing) could have been high enough to create such an effect.

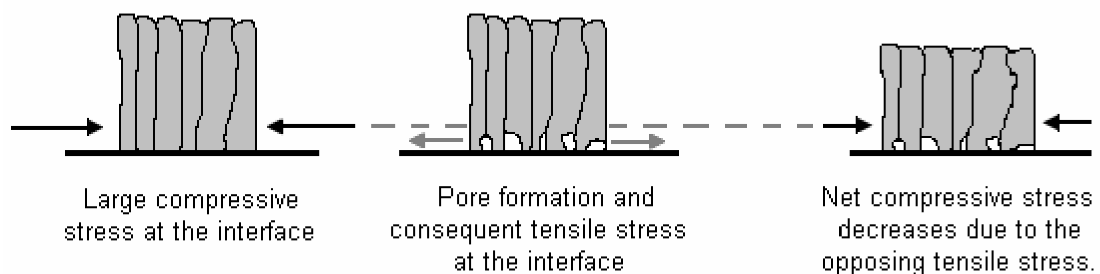

Figure 5.14. Pore formation at the interface decreasing the overall compressive stress.

The pore-coalescence at the film-substrate interface was also responsible for the film buckling and spalling on rigid and thicker substrates (the Si and the thick glass substrates). The magnitude of the residual strain and the quality of texture in the film has been interpreted as function of the film-substrate interface strength [155]. In our samples, film buckling induced cracking or local loss of adhesion upon either aging

(Fig. 4.36) or annealing (Fig. 4.37 and 4.38). Two different buckle types are shown in Fig. 4.37.a and Fig. 4.37.b: *i)* a *flat*-walled type and *ii)* a *curved*-walled type (δ = ~478 nm, b = ~666 nm), which are consistent with other reported observations in the literature (Fig. 1.18.c, 1.18.d, and 1.18.e.). Protrusions at the center of *axi-symmetric* buckles (Fig. 1.18.b.) in the annealed ZnO film were associated with cracking of the film on the Si(100) substrate (see Fig. 4.38). A similar behavior was also observed on the aged ZnO film on the glass substrate (Fig. 4.39). Further annealing of these aged films also led to crack propagation and delamination of the film from the substrate (Fig. 4.40). The residual stress level in our samples (see, for example, Table 4.10) which were close to the hardness values in the literature (Table 1.5, [143, 146]), they could have been high enough to overcome the fracture strength of the film leading to mechanical failure.

In order to comment on film failure due to residual stress, buckling mechanics of the films should be discussed. Buckling of a stressed film was shown to influence crack propagation: stress intensified at the buckle perimeter, providing a driving force for delamination and spalling [91]. Failure mechanics of thin films upon buckling was extensively covered in Sec. 1.2.3. Fig. 1.19 and 1.20 demonstrated at which conditions buckling occurs in the case of equibiaxial compressive stress [84]:

i) $\Pi \leq \Pi_c$: No buckling occurred for the whole range of Σ. Although local interface separation existed, the overall film adhesion was preserved—there was no buckling to cause the propagation of the interface separation.

ii) $\Pi > \Pi_c$ and $\Sigma \leq \Sigma_c$: Buckles were created but they did not propagate—they could be identified as *blisters* at the interface. The film adhesion was still stable.

iii) $\Pi > \Pi_c$ and $\Sigma > \Sigma_c$: Buckles were formed and they propagated. The occurrence of *spalling* depended on bending deformation due to buckling and the induced tensile stress development in the film.

Two examples of structural features upon stress release are shown in Fig. 5.15 and 5.16. Both films were aged for 28 months in air, and the residual stresses were eliminated by aging. The sample seen in Fig. 5.15 was later annealed in air at 600 °C for 6 hours.

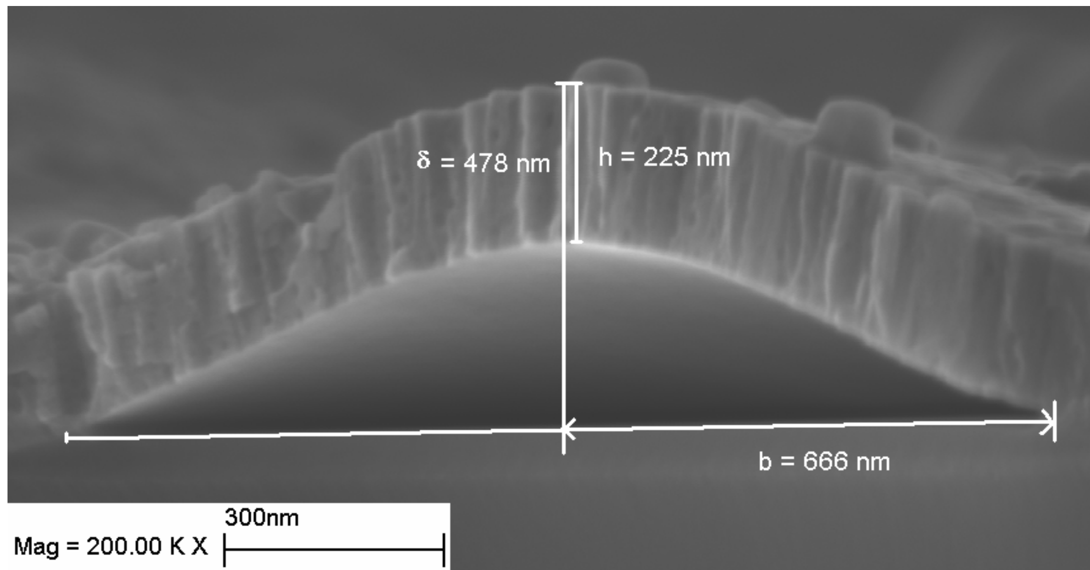

Figure 5.15. A curved-sided buckle on the ZnO film on Si(100) with T_s = 200 °C (Set 16 in Table 3.1). The residual compressive stress after deposition was -4.70 GPa. Film was aged 28 months in air, and later annealed in air at 600 °C for 6 hours. The residual stresses were eliminated by aging.

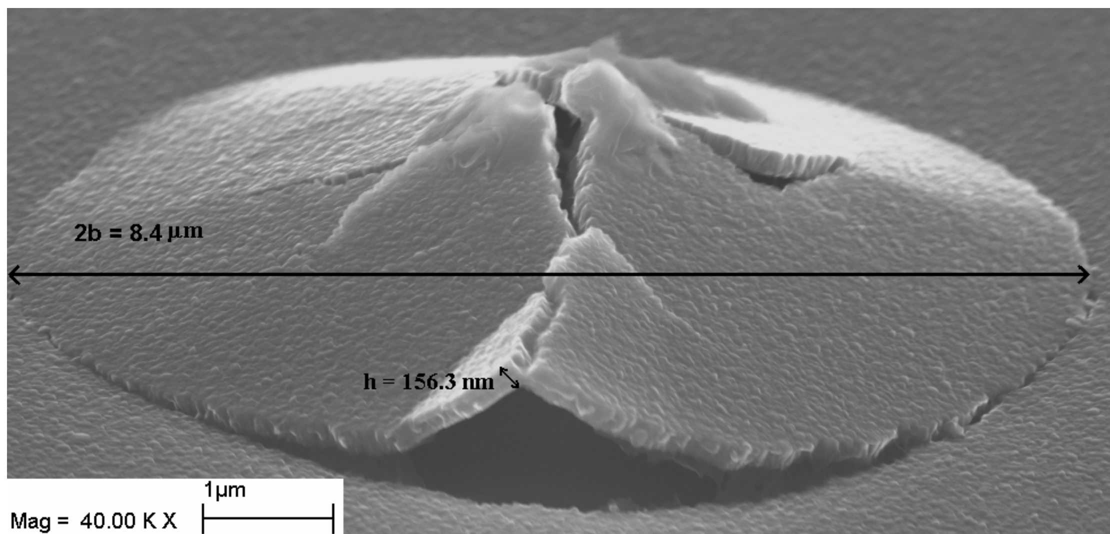

Figure 5.16. Bulging and cracking in the ZnO film on glass upon prolonged aging (Set 16 in Table 3.1; aged 28 months in air. The residual compressive stress after deposition was -3.94 GPa. The residual stresses were eliminated by aging.

Fig. 5.15 illustrates an example of film buckling due to stress build up in a ZnO film sample on a Si(100) substrate. The residual stress (σ_c) was -4.70 GPa in this sample

after deposition. The film thickness (h) was 225 nm. The lift-up (δ) and the buckling radius (b) were measured as 478 and 666 nm, respectively. If the elastic modulus (E) is assumed to be 111 GPa (Table 1.3), and the Poisson's ratio (v), to be 0.318 (Eq. 3.33), then application of Eq. 1.4 or 1.11 gives a critical stress (σ_{cr}) of -17.2 GPa for buckling formation. This value is much higher than the initial residual stress of -4.70 GPa. In other words, the initially compressive stress existing within the film was much lower than the calculated critical stress that would cause such buckling. In this case, either external pressure has been applied to the sample (for example, during handling or sample preparation for SEM), or the actual buckle radius was larger than we could measure. If $\sigma_{cr} = \sigma_c$ is assumed, then the theoretical buckle radius for buckle propagation is 1.2 μm (Eq. 1.12). In that case, Eq. 1.5 and 1.6 give an energy release of 8.4 GPa-m upon buckling.

As stated above, the buckling index (Π) and the adhesion index (Σ) determine the buckle formation and propagation. For the sample shown in Fig. 5.15, the difference between the buckling index and the critical buckling index (Π - Π_c) was calculated as 2.88 (Eq. 1.9). This result ($\Pi > \Pi_c$) was in agreement with the observed buckle formation. To check if the buckle would propagate or not, the adhesion index (Σ) should also be calculated (Eq. 1.10). For this calculation, the interfacial toughness, Γ_i, should be known. Since buckling propagates when $G = \Gamma_i$ (Eq. 1.7), we could assume $\Gamma_i = G$ = 8.4 GPa-m. Then, Eq. 1.10 gives $\Sigma = 1.9$. From Fig. 5.16, with $\Pi - \Pi_c = 2.88$ and Σ = 1.9, this calculation for the onset of buckle propagation is reasonable for a buckle size of that shown in Fig. 5.15. However, there is still a discrepancy between the calculated and measured values of the critical stress to cause buckling, and the corresponding critical buckle radii.

In Fig. 5.16, an example of bulging and cracking due to stress build up in a ZnO film sample on a glass substrate is seen. The residual stress in this sample after deposition was -3.94 GPa. The film was aged for 28 months in air, and the residual stresses were eliminated by aging. The film thickness (h) was 156.3 nm, and the measured buckling radius (b) 4.2 μm. This sample cracked without extensive buckling, and the lift-up, δ, was hard to measure. For these h and b values, application of Eq. 1.4 (or Eq. 1.11) gives a critical stress (σ_{cr}) of -0.21 GPa for buckling formation. This value is much lower than the initial residual stress of -3.94 GPa. Thus, the film must have cracked before the buckle could have propagated, due to the huge amount of residual

stress. Another possibility is that the film could be capable to handle more stress than the theoretically calculated amount for a buckle of this size. In other words, the actual σ_{cr} value could be much higher than the value calculated by Eq. 1.11. This kind of behavior was observed for ZrN [82] and TiN films [223] and has been attributed the pseudoelasticity caused by poor adhesion between the columnar grains, enabling columnar thin films to support external stresses better than uniformly dense films [82]. However, a more extensive study is required to make a reliable comment on the effects of columnar structure and residual stress on film failure.

As pointed out above, annealing might not be a viable solution for stress-relief in ZnO thin films. Aging also released the stress, which suggested that stresses in the thin films were dynamic. This might also influence the functional properties of the thin films over time. Therefore, in order to obtain a stable performance from devices based on ZnO thin films, the films should be produced with minimum amount of stress during film growth. For this reason, apart from the post-deposition treatments, the effect of heat treatment on the samples inside the deposition chamber was also investigated (Sec. 4.6). The residual stresses of these samples were 33–43% lower than those deposited at similar conditions without a heat treatment (Table 4.11 and Fig. 4. 31). At the same time, these heat treatments eliminated the (101)-peaks in the XRD spectra (Fig. 4.32). Thus the method of in-chamber heat treatment immediately after deposition (before letting the film cool down to room temperature) proved to be a better alternative for stress release, rather than using a separate post-deposition anneal at higher temperatures performed a while after the film deposition .

Another consequence of the post-deposition, high-temperature annealing was the growth of ZnO nano-crystals on the film surface (Fig. 4.41 and 4.42). The thickness of the crystallites varied between 82–149 nm, and their height was between ~36–174 nm. In addition, *hillock* formation on the surface (the pyramids extending upwards) can be observed (Fig. 5.17). In some samples, the nano-rods enlarged to 100 nm in width and 916 nm in height upon annealing (Fig. 5.18). This directional crystal growth on the surface of annealed films was indicative of mass transport through the film accompanying stress release. In the SEM images of ZnO films annealed at 400 °C or 600 °C by Gupta and Mansingh, similar growth on the film surface can be seen. However, the authors did not discuss this phenomenon in their paper [151]. As stated in Sec. 5.3, the activation energy for the stress relaxation process in ZnO thin films was

calculated as 0.2 eV/diffusing species [155]. This value was one order of magnitude lower than the activation energy for diffusion of either zinc or oxygen in single crystal or powder ZnO [221]. However, the high amount of residual stress in our sample could act as a driving force for stress release and mass transport at the same time. Thus, the observed directional growth of some crystals during annealing could be attributed to *stress-induced diffusion*, which was further facilitated by the energy provided by thermal annealing. The term stress-induced diffusion in ZnO thin films was not reported in literature. However, interstitial diffusion assisted by local plastic strain is a phenomenon known to relax the residual stresses in thin films [52].

These structures on a film surface can be detrimental for electronic devices (Fig. 5.19) [50].On the other hand, nano-structure growth of ZnO is desired for special purposes such as UV lasing. For example, chemical vapor deposition of ZnO has been achieved using Au as a catalyst, where ZnO was first reduced to Zn on silicon or sapphire substrates [224]. Then ZnO nano-rods grew by reacting with the oxygen provided by the ambient air at 800–1000 °C (Fig. 5.20.a). Similar nano-rod growth was achieved without a catalyst by metal-organic vapor-phase epitaxy (MOVPE) at 400–500 °C on sapphire substrates with a very thin buffer layer of ZnO [129, 130] (Fig. 5.20.b). Also, as discussed in Sec. 5.3.1, there might be Zn interstitials in the ZnO thin films [155, 214]. If the ZnO thin films in our study contained Zn interstitials that moved to the surface upon annealing, they might have acted as nucleation sites and reacted with the oxygen from air to form the nano-rods. By improving the nano-rod growth on our ZnO thin film samples, the drawback of annealing could be turned into an advantageous method for ZnO nano-rod growth.

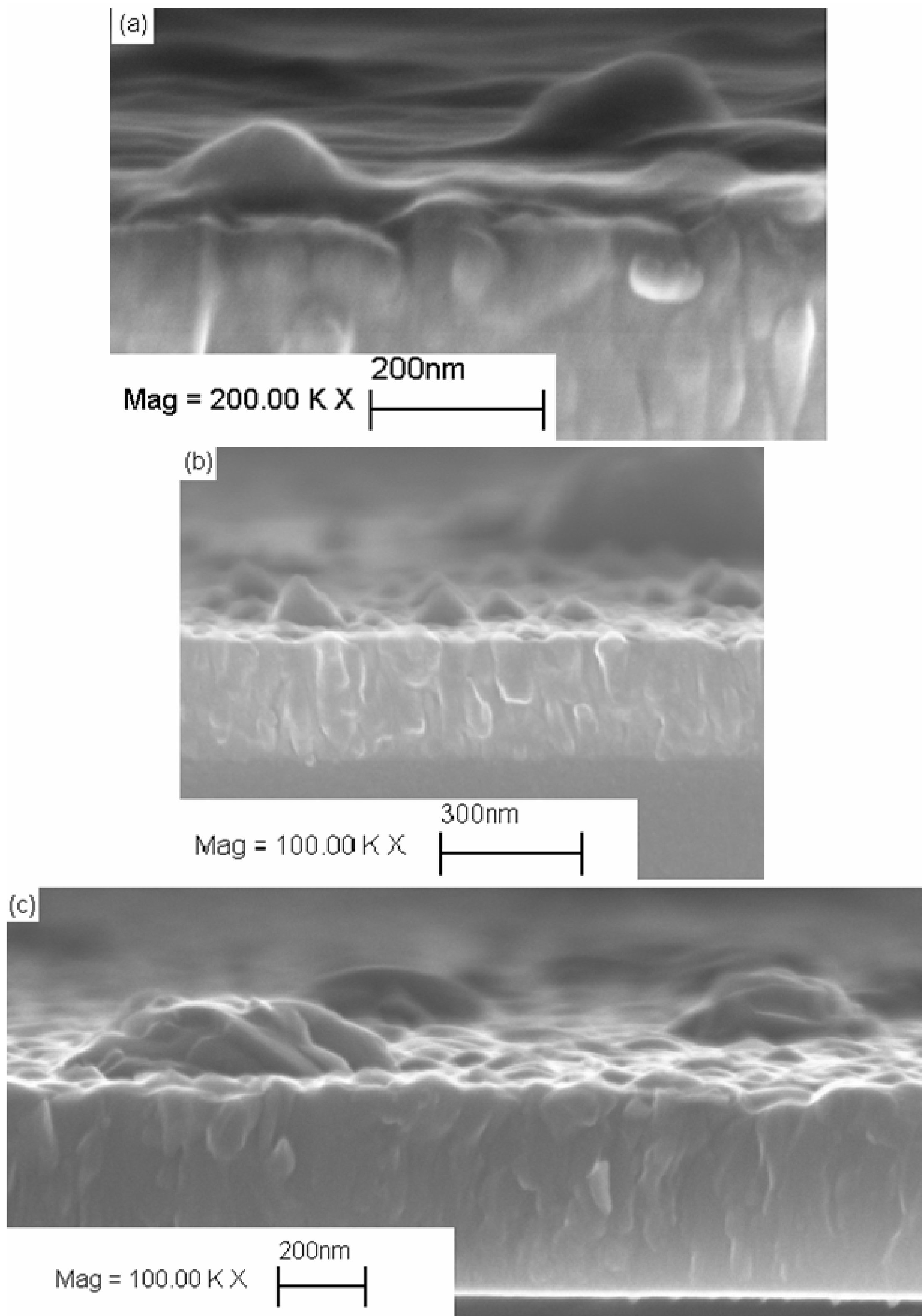

Figure 5.17. Demonstrations of mass transport on the surface of ZnO films, about one month after film deposition. (a) Set 8, (b) Set 3, (c) Set 6. (See Table 3.1 for sample labels.)

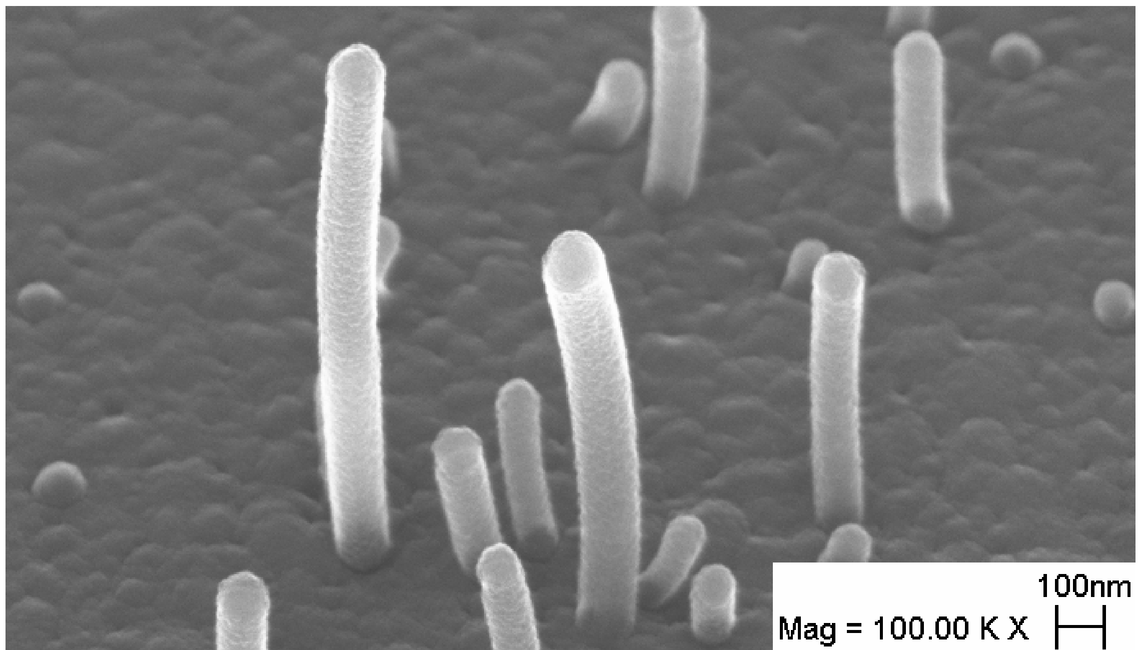

Figure 5.18. Growth of ZnO crystallites on the film surface upon annealing (Set 20 in Table 3.1). The nano-rod thickness was about 100 nm, and the rods elongated up to 916 nm.

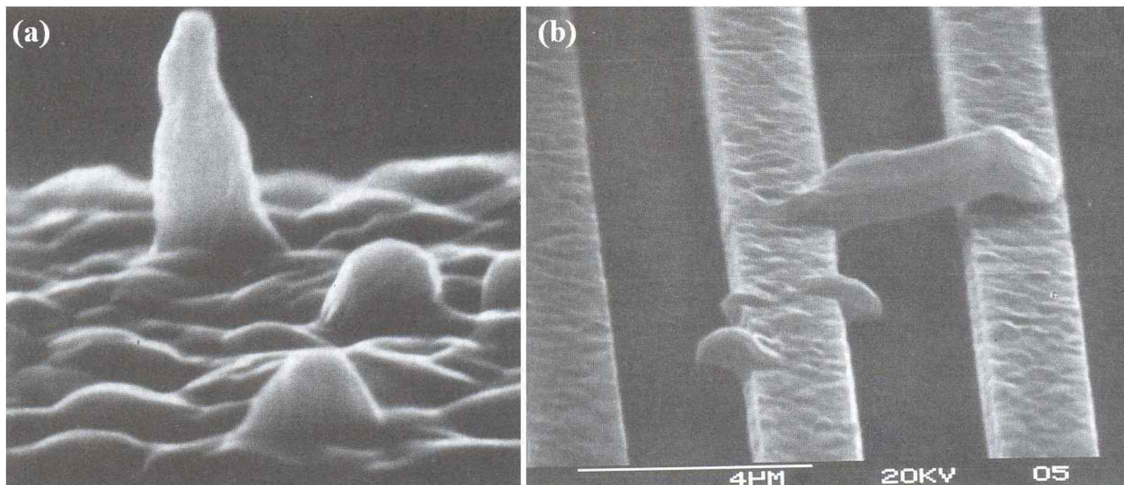

Figure 5.19. Demonstrations of elecromigration in Al films: (a) Hillock growth (original source: Ref. [225], courtesy of L. Berenbaum, reprinted from Ref. [50]); (b) Whisker bridging two conductors (courtesy of R. Knoell, AT & T Bell Laboratories, reprinted from Ref. [50]).

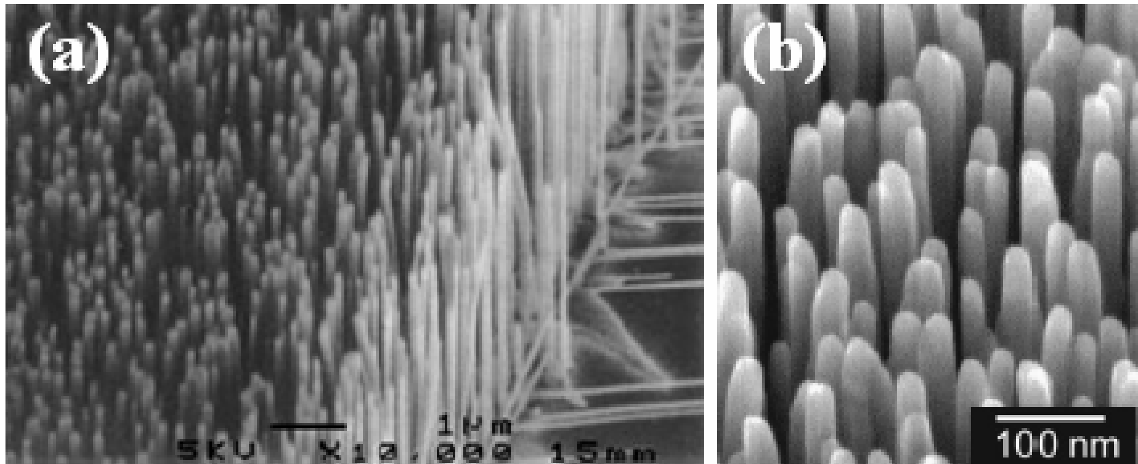

Figure 5.20. (a) Chemical vapor deposition of ZnO with Au catalyst [224]. (b) ZnO nano-rods grown by MOVPE on a very thin buffer layer of ZnO [129, 130].

5.3.3. Section Summary

In this section, the stress relaxation results, the possible mechanisms of stress relaxation, and the drawbacks of stress relaxation in terms of the film microstructure were discussed. The findings can be summarized as follows:

i) Thermal annealing relaxed the growth stresses, accompanied by grain growth. Any remaining compressive stress could be attributed to the TCE-mismatch of the film and the substrate at the annealing temperature.

ii) Although maintaining the minimum amount of residual compressive stress during film growth did not necessarily require the maximum amount of (002) orientation of the grains, the post-deposition stress relaxation was always accompanied by an improvement of the (002)-texture to minimize the surface energy of the grains.

iii) Time-dependent change of the compressive stresses in ZnO thin films were first reported. Aging at room temperature caused a similar decrease of the compressive stresses as by high-temperature annealing.

iv) Stress release by both thermal annealing and room-temperature aging caused buckling followed by cracking and film failure, but with different mechanisms. Thermal annealing could come over the energy barrier to cause pore growth and pore clustering, which led to extensive crack-like defects and loss of adhesion between the film and the substrate. Cracking in the aged samples were merely due to the loss of

adhesion between the grain boundaries. More detailed studies must be performed to determine the critical amount of stress causing buckle propagation and film failure.

v) Transformation of the excess atoms from the grain boundaries (where they have been incorporated during film growth) back to the film surface by stress-induced diffusion was considered to be a possible mechanism of stress release. Other possible factors in stress release related to defects and dislocations (such as the role of oxygen vacancies or zinc interstitials in stress evolution, or the dislocation glide induced by the high compressive stress) require TEM examination to comment on.

vi) Due to the microstructural changes it causes in the films, high-temperature annealing was not considered as a viable solution to minimize the residual stresses in ZnO thin films. Instead, in-chamber annealing immediately after the deposition before cooling down to room temperature or implementing a buffer layer prior to film deposition was proposed.

CHAPTER 6

CONCLUDING REMARKS AND FUTURE WORK

In this study, the evolution and relaxation of residual stresses in RF magnetron-sputtered ZnO thin films were investigated in combination with the evolution of the film microstructure. Variations from the previously developed structure zone models (SZM) were observed. In addition, the evolutions of microstructures in the pressure ranges beyond the previously developed SZMs (p > 30 mTorr) were investigated. Several mechanisms were proposed, based on the competition between the growth rate of different crystalline surfaces, the grains, the columns, and the film thickness. The relative domination of these factors determined the film's microstructure. It was emphasized that the structure zone models should be thought together with texturing and the changes in growth direction of surfaces with increasing adatom energy and flux.

The ZnO films showed a strongly preferred orientation along the *c*-axis of the crystallites, manifested by intense (002)-peak in XRD spectra. The surface mobility of the adatoms was a crucial parameter in determining the microstructure of the initial layers and the texture evolution in the fully-grown film. For example, increasing P_{RF} (thus high incident flux) resulted in high extent of nucleation, where decreasing p and increasing T_s enabled greater mobility of the adatoms on the surface, promoting coalescence of nuclei having the same orientation with each other. At specific conditions (T_s = 200 °C, p = 0.2 mbar = 150 mTorr, and P_{RF} = 125 W), the films contained grains of various shapes, and deviation from *c*-axis orientation as additional (101)-texture was observed. This was proposed to be due to the existence of a layer with randomly oriented grains at the initial stages of film growth, combined with increased growth rate on every direction (high energy and mobility of adatoms), limited amount of time between successive layer formations (high flux of adatoms), and continuous

nucleation during the course of film growth. When the surface mobility of the adatoms were lowered (either by decreasing T_s or increasing p), the film structure consisted mainly of columnar grains, with primarily the *c*-axis orientation. At the lowest surface mobility and lower adatom flux conditions, the films were close to being amorphous with very low XRD intensities and cauliflower like grains.

The films on crystalline substrates had a better-defined columnar structure. This was attributed to the increased number of nucleation sites for the *c*-axis orientation. A similar effect was observed upon buffer layer deposition prior to the full film growth. Annealing of the films caused grain growth due to increased bulk and surface diffusion.

Contributions have been made to the links between the microstructure of thin films and the residual stresses. It was shown that some of the stress-forming factors that have been proposed in literature were insignificant for the samples under study. These included the thermal expansion mismatch of the film and the substrate, lattice mismatch of the film and the substrate, and argon entrapment into the film during growth. Only about 5–11% of the total stresses were induced by the thermal expansion mismatch of the film and the substrate materials. The evolution of high compressive stresses was not limited to the crystalline substrates; stresses up to -8 GPa were measured on ZnO films on amorphous substrates as well. In addition, no trapped Ar could be measured inside the films. These results were indicative of the existence of other sources of residual stress, the majority being the so-called *growth stresses*.

The evolution of growth stresses and the related texture was studied under controlled deposition parameters (T_s, p, P_{RF}). The compressive stress results were in the -1 to -8 GPa range, depending on the substrate material and the deposition conditions. As the mobility of adatoms was increased, whether by increasing T_s or decreasing p (or P_{RF}), the residual stresses decreased. This was presumed to be a result of either the atoms finding the suitable lattice sites or to the grains orienting themselves both in a way to decrease the stress. In the lower pressure range ($p \leq 0.2$ mbar = 150 mTorr) the quality of the (002)-orientation of the columns might be the major mechanism that decreases the compressive stress. On the other hand, it was emphasized that, in the higher pressure regimes (0.2–0.4 mbar = 150–300 mTorr), the stress minimization of the residual compressive stress did not require the maximum *c*-orientation of the grains on the contrary to the previous works in the literature. The samples with the (101)-texture had the least amount of compressive stress in the 0.2–0.4 mbar range. In

addition, the shift of the (002)-peak of ZnO in the XRD spectra was affected by the presence of the (101)-peak, indicating the non-negligible effect of texture on residual stress. The film-substrate interface structure (the existence of a layer with randomly oriented grains at the initial stages of film growth) is believed to play a significant role on the residual stress, as it did on texture and microstructure. In addition, incorporation of film-forming atoms into the grain boundaries together with (101)-texture formation and increased porosity were considered to be factors that controlled the residual stresses. In order to elucidate the role of the initial layer of randomly oriented crystals in more detail, their exact texture throughout the whole film should be determined. This requires high-resolution through-thickness XRD studies and cross-sectional electron diffraction by TEM. To understand the regions of stress concentration in the film, combined SEM and Raman spectroscopy studies are underway [183]. Elucidating the role of atom incorporation in residual stress evolution require accurate measurement of the grain boundary areas and thermodynamic data at the film deposition conditions. In addition, molecular dynamic simulations might provide complementary information about the film growth kinetics and related stress evolution.

The stress relaxation results, the possible mechanisms of stress relaxation, and the drawbacks of stress relaxation in terms of the film microstructure were discussed. Time-dependent stress relaxation in ZnO thin films were first reported. Aging at room temperature caused a similar decrease of the compressive stresses as by high-temperature annealing. Any remaining compressive stress could be attributed to the TCE-mismatch of the film and the substrate at the annealing temperature. Although maintaining the minimum amount of residual compressive stress during film growth did not necessarily require the maximum amount of (002)-orientation of the grains, the post-deposition stress relaxation was always accompanied by grain growth and an improvement of the (002)-texture to minimize the surface energy of the grains. The roles of improving texture, grain growth, interstitial diffusion, and dislocation motions in stress relaxation mechanisms were discussed. Transformation of the excess atoms from the grain boundaries where they have been incorporated during growth back to the film surface by *stress-induced directional diffusion* was considered to be a possible mechanism of stress release. Other possible factors related to defects and dislocations (such as the role of oxygen vacancies or zinc interstitials in stress evolution, or the dislocation glide induced by the high compressive stress) require TEM examination to

comment on. In addition, further studies are required to elucidate the exact effects of the dynamic stresses on the functional (*e.g.* optical and electrical) properties of the ZnO thin films.

Stress release by both thermal annealing and room-temperature aging caused buckling followed by cracking and film failure, but with different mechanisms. Thermal annealing could come over the energy barrier to cause pore growth and pore clustering, which led to extensive crack-like defects and loss of adhesion between the film and the substrate. Cracking in the aged samples were merely due to the loss of adhesion between the grain boundaries. The buckling mechanics of the ZnO thin films was investigated briefly. Discrepancies were found between the theoretical and measured buckle radii. A more extensive study is required to make a reliable comment on the effects of residual stress on buckling and film failure.

Annealing also caused directional growth of ZnO crystals on the surface, presumably due to the diffusion of the pre-existing Zn interstitials to the surface and reaction with the oxygen from air. This kind of growth on the film surface could alter the functional properties of the films. For this reason, post-deposition thermal annealing did not seem to be a viable option for stress reduction in ZnO thin films. Instead, in-chamber annealing immediately after the deposition before cooling down to room temperature or implementing a buffer layer prior to film deposition was proposed. In addition, it was shown that the deposition of a buffer layer influenced the eventual microstructural and textural development of the films, presumably due to the increased number of nucleation sites for the adatoms allowing them to be oriented in the direction to give the minimum stress in the upcoming layers. Depositing a buffer layer and modifying it by annealing reduced further stress development as the film grew. Further studies are needed to optimize the conditions for in-chamber heat treatment and buffer layer treatment.

In addition, although it could be detrimental to the functional properties of the ZnO thin film devices, the directional growth method of nanostructures on the ZnO film surface could be improved to be used in advantage of ZnO nano-rod growth.

APPENDICES

A. Cleaning Procedure for Glass Substrates

Soda lime glass contains about 13% of sodium oxide [199]. The sodium hydroxide in a glass piece reacts with water in humid air, forming a layer of sodium hydroxide on the surface. In addition, this sodium hydroxide may react with the carbon dioxide in the air, forming sodium carbonate powder on the surface (*blooming*). These layers can alter the adhesive property of the substrate for further film deposition. Thus, the glass surface should be freed of impurities before film deposition.

Alkaline solutions slightly etch the glass surface; thus, acidic solutions should be preferred [199]. An example for a useful cleaning bath is a mixture of sulfuric acid and hydrogen peroxide with 2:1 volume ratio [199]. The acid–peroxide bath is useful in removing residual amounts of hydrocarbon contaminants (about one monolayer, *i.e.*, 1 nm or 1 g of contaminant per 1000 m^3 of surface) [199]. For this reason, it is necessary to remove most of the contaminants by surfactants (*e.g.* detergents) before using the acid baths. Cleaning fluids are often incompatible with each other. For this reason, it is important to rinse the samples carefully to clean them from one fluid before proceeding with the next one [2].

In standard ultrasonic baths, standing wave patterns are generated [199]. At this frequency, the imploding bubbles can produce instantaneous pressure values up to 1000 atm [2]. This high pressure is beneficial for preparing the surface for thin film depositions [2]. However, the standing waves cause vigorous cleaning of the sample surfaces at certain points, while leaving some points unaffected [199]. For this reason, during the rinsing, the samples were moved occasionally in the ultrasonic bath. Extended periods of ultrasonic cleaning may cause surface damage (micro–pits) on the

samples [198]. These micro–pits reduce transmittance and increase stray light [198]. They may also affect the adhesion of the film to the substrate [1, 81]. For this reason, the samples were held in the ultrasonic baths only for short periods. The proper temperature for acid cleaning of glass surfaces is 60–85 °C [2]. The temperature of all the baths used for this study was also in this range.

Finally, the success of the cleaning procedure should verified by wetting test [199]. After the final stage of distilled water rinse, the behavior of water on the surface is observed. If the water does not wet the substrate completely, *i.e.* if dry patches are observed, this means that there are unclean areas on the surface. If the surface is clean, water thins as it flows through the surface, and interference fringes are seen.

Water tends to adsorb contaminants from ambient air and re-deposit them on the substrate during drying [199]. In addition, clean surfaces tend to absorb contaminant form ambient air, due to their high surface energy [2, 199]. For these reasons, the wetting test and drying step were done immediately before the film deposition. A convenient drying agent is a jet of high-pressure pure nitrogen gas [199]. In this method, the substrates are held vertically and the high-pressure gas was blown from top to the bottom at an angle of about 45° to the substrate. To minimize the water streaks deposition surface, the reverse side is dried first. Tissues should not be used since they may leave pieces of cloth on the surface [198].

B. Powder Diffraction Standards

B.1. ZnO

Table B.1.1. JCPDS data of hexagonal wurtzite ZnO (No. 36-1451) [205].

Pattern: 36-1451		***Radiation:*** $CuK_{\alpha 1}$ (λ =1.540598 Å)		***Quality:*** High	
Formula: ZnO ***Name:*** Zincite, syn / Zinc oxide, Chinese white, zinc white					
Lattice: Hexagonal ***S.G.:*** P63mc (186)		***a*** = 3.24982 ***c*** = 5.20661	***Z*** = 2	***Mol. weight*** = 81.38 ***Volume [CD]*** = 47.62 D_x = 5.675	
2θ (°)	***d (Å)***	***I***	***h***	***k***	***l***
31.770	2.81430	57	1	0	0
34.422	2.60332	44	0	0	2
36.253	2.47592	100	1	0	1
47.539	1.91114	23	1	0	2
56.603	1.62472	32	1	1	0
62.864	1.47712	29	1	0	3
66.380	1.40715	4	2	0	0
67.963	1.37818	23	1	1	2
69.100	1.35825	11	2	0	1
72.562	1.30174	2	0	0	4
76.955	1.23801	4	2	0	2
81.370	1.18162	1	1	0	4
89.607	1.09312	7	2	0	3
92.784	1.06384	3	2	1	0
95.304	1.04226	6	2	1	1
98.613	1.01595	4	1	1	4
102.946	0.98464	2	2	1	2
104.134	0.97663	5	1	0	5
107.430	0.95561	1	2	0	4
110.392	0.93812	3	3	0	0
116.279	0.90694	8	2	1	3
121.572	0.88256	4	3	0	2
125.188	0.86768	1	0	0	6
133.932	0.83703	3	2	0	5
136.520	0.82928	1	1	0	6
138.513	0.82370	2	2	1	4
142.918	0.81247	3	2	2	0

Table B.1.1. *Continue.*

SAMPLE SOURCE OR LOCALITY: The sample was obtained from the New Jersey Zinc Co., Bethlehem, Pennsylvania, USA.
COLOR : Colorless
GENERAL COMMENTS: The structure was determined by Bragg (1) and refined by Abrahams, Bernstein (2).
POLYMORPHISM: A high pressure cubic NaCl-type of ZnO is reported by Bates et al. (3) and a cubic, sphalerite type is reported by Radczewski, Schicht (4).
TEMP. OF DATA COLLECTION: The approximate temperature of data collection was 26 C.
ADDITIONAL PATTERN: To replace 5-664 (5).
POWDER DATA: References to other early patterns may be found in reference (5).
OPTICAL DATA : B=2.013, Q=2.029, Sign=+
DATA COLLECTION FLAG: Ambient.

Powder Diffraction, volume 1, page 76, (1986)

Primary reference: McMurdie, H., Morris, M., Evans, E., Paretzkin, B., Wong-Ng, W., Ettlinger, L., Hubbard, C. *Dana's System of Mineralogy,* 7th Ed., volume 0, page 504.

Optical data: *Philos. Mag.*, volume 39, page 647, (1920).

1. Bragg, W. *Acta Crystallogr.*, Sec. B, volume 25, page 1233, (1969).
2. Abrahams, S., Bernstein, J. *Science*, volume 137, page 993, (1962).
3. Bates, C., White, W., Roy, R. *Naturwissenschaften*, volume 56

SS/FOM: F27=131(0.0071,29)	***Filter:*** Monochromator crystal	***d-sp:*** Diffractometer

B.2. Si

Table B.2.1. JCPDS data of face-centered cubic Si (No. 27-1402) [205].

<table>
<tr><td colspan="2">Pattern: 27-1402</td><td colspan="2">Radiation: CuK$_{\alpha 1}$ (λ =1.540598 Å)</td><td colspan="2">Quality : High</td></tr>
<tr><td colspan="6">Formula: Si
Name: Silicon, syn / Silicon</td></tr>
<tr><td colspan="2">Lattice: Face-centered cubic
S.G.: Fd-3m (227)</td><td>a = 5.43071</td><td>Z = 8</td><td colspan="2">Mol. weight = 28.09
Volume [CD] = 160.18
D_x = 2.329

I/Icor = 4.70</td></tr>
<tr><th>2θ (°)</th><th>d (Å)</th><th>I</th><th>h</th><th>k</th><th>l</th></tr>
<tr><td>28.443</td><td>3.13550</td><td>100</td><td>1</td><td>1</td><td>1</td></tr>
<tr><td>47.303</td><td>1.92010</td><td>55</td><td>2</td><td>2</td><td>0</td></tr>
<tr><td>56.122</td><td>1.63750</td><td>30</td><td>3</td><td>1</td><td>1</td></tr>
<tr><td>69.132</td><td>1.35770</td><td>6</td><td>4</td><td>0</td><td>0</td></tr>
<tr><td>76.379</td><td>1.24590</td><td>11</td><td>3</td><td>3</td><td>1</td></tr>
<tr><td>88.029</td><td>1.10860</td><td>12</td><td>4</td><td>2</td><td>2</td></tr>
<tr><td>94.951</td><td>1.04520</td><td>6</td><td>5</td><td>1</td><td>1</td></tr>
<tr><td>106.719</td><td>0.96000</td><td>3</td><td>4</td><td>4</td><td>0</td></tr>
<tr><td>114.092</td><td>0.91800</td><td>7</td><td>5</td><td>3</td><td>1</td></tr>
<tr><td>127.547</td><td>0.85870</td><td>8</td><td>6</td><td>2</td><td>0</td></tr>
<tr><td>136.897</td><td>0.82820</td><td>3</td><td>5</td><td>3</td><td>3</td></tr>
<tr><td colspan="6">TEMP. OF DATA COLLECTION: Pattern taken at 25(1) °C.
SAMPLE SOURCE OR LOCALITY: This sample is NBS Standard Reference Material No. 640.
GENERAL COMMENTS: Reflections calculated from precision measurement of a_0.
GENERAL COMMENTS: a_0 uncorrected for refraction.
ADDITIONAL PATTERN: To replace 5-565 and 26-1481.
COLOR : Gray
DATA COLLECTION FLAG: Ambient.</td></tr>
<tr><td colspan="6">CAS: 7440-21-3, Natl. Bur. Stand. (U.S.) Monogr. 25, volume 13, page 35, (1976)</td></tr>
<tr><td>SS/FOM:
F11=409(0.0021,13)</td><td colspan="2">Filter:
Monochromator crystal</td><td>d-sp: Diffractometer</td><td colspan="2">Internal standard: W</td></tr>
</table>

Table B.2.2. JCPDS data of face-centered cubic Si (No. 75-0589) [205].

Pattern : 75-0589 | ***Radiation:*** $CuK_{\alpha 1}$ (λ =1.540598 Å) | ***Quality :*** Calculated

Formula: Si
Name: Silicon

Lattice : Face-centered cubic
S.G. : Fd-3m (227)

a = 5.43071 | ***Z*** = 8

Mol. weight = 28.09
Volume [CD] = 160.17
$\boldsymbol{D_x}$ = 2.329

I/Icor = 4.55

2θ (°)	***d (Å)***	***I***	***h***	***k***	***l***
26.848	3.31800	22	2	0	0
33.038	2.70914	100	2	1	1
38.334	2.34618	1	2	2	0
47.420	1.91565	<1	2	2	2
51.485	1.77355	61	3	2	1
55.332	1.65900	14	4	0	0
59.008	1.56412	5	4	1	1
62.547	1.48385	3	4	2	0
65.975	1.41480	4	3	3	2
69.315	1.35457	<1	4	2	2
72.582	1.30143	7	4	3	1
78.957	1.21156	7	5	2	1
82.088	1.17309	4	4	4	0
85.196	1.13806	1	4	3	3
88.289	1.10600	3	6	0	0

ICSD COLLECTION CODE : 029287
TEST FROM ICSD: No R value given.
TEST FROM ICSD: At least one TF missing.
DATA COLLECTION FLAG: Ambient.

Calculated from ICSD using POWD-12++, (1997)
Primary reference : Bond, W.L., Kaiser, W., J. Phys. Chem. Solids, volume 16, page 44, (1960).

Filter: Not specified | ***d-sp:*** Calculated spacings

Table B.2.3. JCPDS data of body-centered cubic Si (No. 72-1088) [205].

Pattern: 72-1088	***Radiation:*** $CuK_{\alpha 1}$ (λ =1.540598 Å)	***Quality:*** Calculated

Formula: Si
Name: Silicon

Lattice: Body-centered cubic ***S.G.:*** Ia-3 (206)	***a*** =6.63600	***Z = 16***	***Mol. weight*** = 28.09 ***Volume [CD]*** = 292.23 D_x = 2.553 D_m = 2.550 ***I/Icor = 3.96***

2θ (°)	***d (Å)***	***I***	***h***	***k***	***l***
28.444	3.13542	100	1	1	1
47.305	1.92005	55	2	2	0
56.125	1.63742	30	3	1	1
58.859	1.56771	<1	2	2	2
69.133	1.35768	7	4	0	0
76.380	1.24589	10	3	3	1
88.035	1.10854	12	4	2	2

ICSD COLLECTION CODE : 016569
TEST FROM ICSD : No R value given.
TEMPERATURE FACTOR : ITF
ADDITIONAL PATTERN : See PDF 17-901.
DATA COLLECTION FLAG: Ambient.

Calculated from ICSD using POWD-12++
Primary reference: Kasper, J.S., Richards, S.M., *Acta Crystallogr.*, volume 17, page 752, (1964).

Filter: Not specified	***d-sp:*** Calculated spacings

B.3. Mica

Table B.3.1. JCPDS data of monoclinic mica (No. 83-1808) [205].

Pattern : 83-1808		***Radiation:*** CuK$_{\alpha1}$ (λ =1.540598 Å)		***Quality :*** Calculated	
Formula: K (Mg2.665 Li0.225 Na0.110) (Si3.312 Fe0.688 O10) F2 ***Name:*** Mica / Potassium Magnesium Lithium Sodium Iron Silicate Fluoride					
Lattice : Monoclinic ***S.G. :*** C2/m (12)		***a*** = 5.32900 ***b*** = 9.23000 ***c*** = 10.21910 ***a/b*** = 0.57736 ***c/b*** = 1.10716	***Beta*** = 99.98 ***Z*** = 2	***Mol. weight*** = 437.39 ***Volume [CD]*** = 495.04 ***D_x*** = 2.934 ***I/Icor*** = 0.57	

2θ (°)	***d (Å)***	***I***	***h***	***k***	***l***
8.779	10.06450	87	0	0	1
17.610	5.03223	16	0	0	2
19.217	4.61500	20	0	2	0
19.441	4.56236	28	1	1	0
20.106	4.41286	8	-1	1	1
21.162	4.19500	1	0	2	1
22.559	3.93823	21	1	1	1
24.259	3.66600	57	-1	1	2
26.179	3.40125	84	0	2	2
26.548	3.35482	55	0	0	3
28.291	3.15198	78	1	1	2
30.581	2.92094	52	-1	1	3
32.982	2.71360	24	0	2	3
33.742	2.65423	50	1	3	0
*33.742	*2.65423	50	-2	0	1
34.145	2.62381	100	2	0	0
*34.145	*2.62381	100	-1	3	1
35.493	2.52717	7	1	1	3
35.704	2.51275	15	1	3	1
*35.704	*2.51275	15	-2	0	2
36.845	2.43749	69	2	0	1
*36.845	*2.43749	69	-1	3	2
38.123	2.35865	1	-1	1	4
39.002	2.30750	3	0	4	0
39.122	2.30073	7	-2	2	1
39.471	2.28118	6	2	2	0
39.726	2.26712	10	1	3	2
*39.726	*2.26712	10	-2	0	3
40.057	2.24914	6	0	4	1
40.866	2.20643	6	0	2	4
*40.866	*2.20643	6	-2	2	2
41.455	2.17643	33	2	0	2
*41.455	*2.17643	33	-1	3	3
41.870	2.15584	6	2	2	1

Table B.3.1. *Continue.*

2θ (°)	*d (Å)*	*I*	*h*	*k*	*l*
43.092	2.09750	5	0	4	2
43.582	2.07504	<1	1	1	4
44.502	2.03427	2	-2	2	3
45.000	2.01289	18	0	0	5
45.352	1.99807	16	1	3	3
*45.352	*1.99807	16	-2	0	4
46.057	1.96911	1	2	2	2
46.447	1.95351	<1	-1	1	5
47.527	1.91160	3	2	0	3
*47.527	*1.91160	3	-1	3	4
47.803	1.90120	<1	0	4	3
49.354	1.84503	<1	0	2	5
49.699	1.83300	1	-2	2	4
51.699	1.76669	2	2	2	3
52.197	1.75102	6	1	3	4
*52.197	*1.75102	6	-2	0	5
52.326	1.74699	4	1	1	5
52.508	1.74138	3	1	5	0
*52.508	*1.74138	3	-2	4	1
52.789	1.73275	1	2	4	0
*52.789	*1.73275	1	-1	5	1
53.260	1.71855	<1	3	1	0
*53.260	*1.71855	<1	-3	1	2
53.902	1.69959	4	1	5	1
*53.902	*1.69959	4	-2	4	2
54.719	1.67613	49	2	0	4
*54.719	*1.67613	49	-1	3	5
55.393	1.65732	1	-1	1	6
55.739	1.64785	10	3	1	1
*55.739	*1.64785	10	-3	1	3
56.156	1.63658	1	-2	2	5
56.891	1.61718	12	1	5	2
*56.891	*1.61718	12	-2	4	3
58.212	1.58359	9	2	4	2
*58.212	*1.58359	9	-1	5	3
59.686	1.54796	5	3	1	2
*59.686	*1.54796	5	-3	1	4
60.097	1.53835	54	-3	3	1
*60.097	*1.53835	54	0	6	0
60.869	1.52067	9	0	6	1
*60.869	*1.52067	9	-3	3	2
61.038	1.51686	5	0	4	5
61.338	1.51016	1	1	5	3
*61.338	*1.51016	1	-2	4	4
61.673	1.50276	1	1	1	6
62.838	1.47767	3	2	0	5
*62.838	*1.47767	3	-1	3	6
63.664	1.46047	1	-2	2	6
64.790	1.43778	2	0	0	7

Table B.3.1. *Continue.*

2θ (°)	***d* (Å)**	***I***	***h***	***k***	***l***
64.949	1.43466	3	-1	1	7
*64.949	*1.43466	3	-3	1	5
66.348	1.40776	2	2	2	5
66.840	1.39858	2	3	3	2
*66.840	*1.39858	2	-3	3	4
67.041	1.39488	2	1	5	4
*67.041	*1.39488	2	-2	4	5
68.271	1.37271	2	0	2	7
68.712	1.36498	19	1	3	6
*68.712	*1.36498	19	-2	0	7
69.184	1.35680	3	0	4	6
*69.184	*1.35680	3	2	4	4
70.728	1.33093	8	-4	0	1
*70.728	*1.33093	8	-2	6	1
70.962	1.32711	15	2	6	0
*70.962	*1.32711	15	-4	0	2
71.674	1.31566	2	1	1	7
71.876	1.31247	11	0	6	4
*71.876	*1.31247	11	-3	3	5
72.127	1.30851	7	-2	2	7
72.608	1.30103	8	2	6	1
*72.608	*1.30103	8	-4	0	3
74.076	1.27883	1	-4	2	1
*74.076	*1.27883	1	1	7	0
74.312	1.27535	1	-1	7	1
*74.312	*1.27535	1	-4	2	2
74.486	1.27281	5	4	0	1
*74.486	*1.27281	5	-2	6	3
74.700	1.26969	3	3	5	0
*74.700	*1.26969	3	-3	5	2
75.123	1.26359	3	2	2	6
75.511	1.25806	2	0	0	8
75.932	1.25212	2	-1	7	2
*75.932	*1.25212	2	-4	2	3
76.489	1.24439	<1	2	4	5
*76.489	*1.24439	<1	-1	5	6
76.782	1.24037	3	3	5	1
*76.782	*1.24037	3	-3	5	3
77.755	1.22726	4	4	2	1
*77.755	*1.22726	4	1	7	2
78.133	1.22226	5	0	6	5
*78.133	*1.22226	5	-3	3	6
78.284	1.22028	4	0	4	7
*78.284	*1.22028	4	-2	0	8
78.915	1.21211	3	-1	7	3
*78.915	*1.21211	3	-4	2	4
79.176	1.20876	2	3	1	5
*79.176	*1.20876	2	-3	1	7
79.978	1.19865	1	2	6	3
*79.978	*1.19865	1	-4	0	5

Table B.3.1. *Continue.*

2θ (°)	*d (Å)*	*I*	*h*	*k*	*l*
80.188	1.19604	2	3	5	2
*80.188	*1.19604	2	-3	5	4
81.562	1.17933	1	-2	2	8
*81.562	*1.17933	1	1	7	3
81.942	1.17482	1	1	5	6
*81.942	*1.17482	1	-2	4	7
82.479	1.16852	<1	1	1	8
83.234	1.15983	<1	-1	7	4
*83.234	*1.15983	<1	-4	2	5
83.617	1.15549	1	4	0	3
*83.617	*1.15549	1	-2	6	5
83.844	1.15294	<1	-4	4	1
84.075	1.15036	<1	-4	4	2
84.447	1.14624	<1	0	8	1
84.860	1.14171	1	2	4	6
*84.860	*1.14171	1	-1	5	7
85.615	1.13356	9	2	6	4
*85.615	*1.13356	9	-4	0	6
86.324	1.12606	<1	-1	1	9
86.467	1.12457	1	0	8	2
86.785	1.12126	<1	4	2	3
*86.785	*1.12126	<1	1	7	4
87.075	1.11827	<1	0	0	9
87.425	1.11470	<1	4	4	1
87.971	1.10918	1	3	1	6
*87.971	*1.10918	1	-3	1	8
88.434	1.10456	<1	0	4	8
88.571	1.10321	<1	-4	4	4
88.831	1.10065	1	-1	7	5
*88.831	*1.10065	1	-2	0	9
89.826	1.09103	<1	0	8	3

ICSD COLLECTION CODE: 100726
TEMPERATURE FACTOR: ATF
SAMPLE SOURCE OR LOCALITY: Specimen from Cupaello, Italy.
DATA COLLECTION FLAG: Ambient.

*Calculated from ICSD using POWD-12++, (1997)
Primary reference : Hazen, R.M., Finger, L.W., Velde, D., *Am. Mineral.*, volume 66, page 586, (1981)

Filter : Not specified | ***d-sp :*** Calculated spacings

C. Representative XRD Spectra of the Crystalline Substrates

C.1. Si

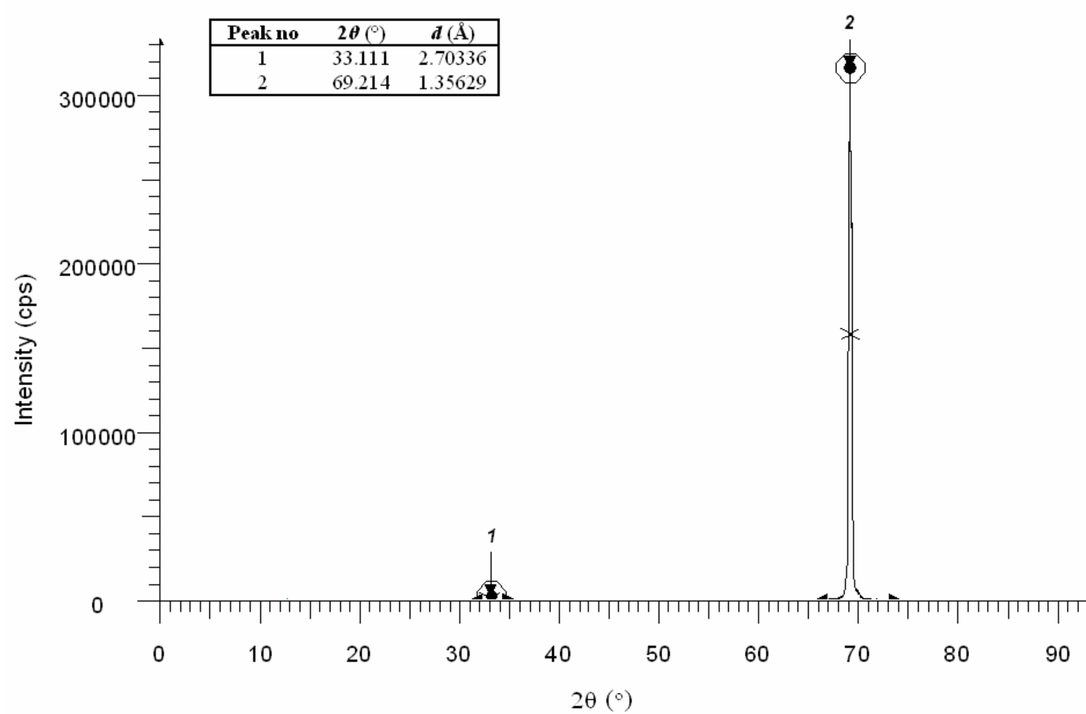

Figure C.1.1. A representative XRD spectrum of Si(100) wafer.

C.2. Mica

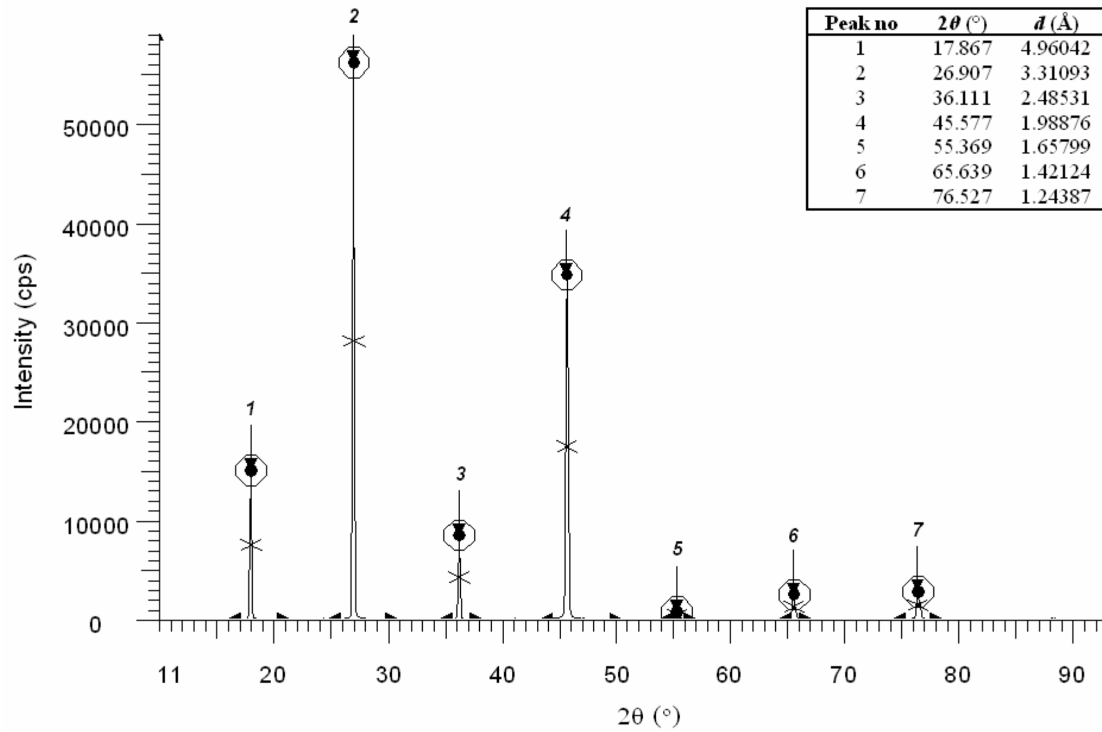

Peak no	2θ (°)	d (Å)
1	17.867	4.96042
2	26.907	3.31093
3	36.111	2.48531
4	45.577	1.98876
5	55.369	1.65799
6	65.639	1.42124
7	76.527	1.24387

Figure C.2.1. A representative XRD spectrum of mica (muscovite) sheet.

D. Temperature Calibrations for the RFMS System

D.1. Equilibrium temperature around the substrate holder during film deposition

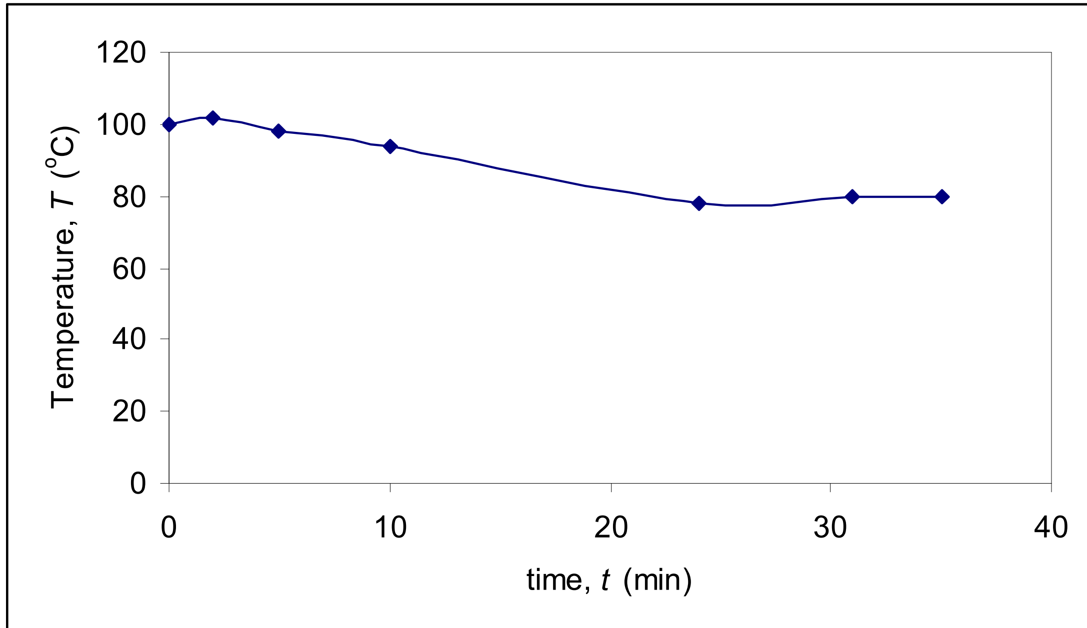

Figure D.1.1. Temperature near the substrate holder (~1 cm), as measured by a thermocouple (see Fig. 3.3). The plasma conditions were: P_{RF} = 150 W, P_{DC} = 30 W, V_{Ar} = 35 cm^3/min, p_{Ar} = 0.1 mbar. The chamber was initially heated up to 300 °C for 5 min, then the heater was turned off. The temperature had decreased down to 100 °C when the deposition started. It reached equilibrium at ~80 °C during the course of deposition.

D.2. Heading and cooling curves of the main chamber and the substrate holder before and after deposition.

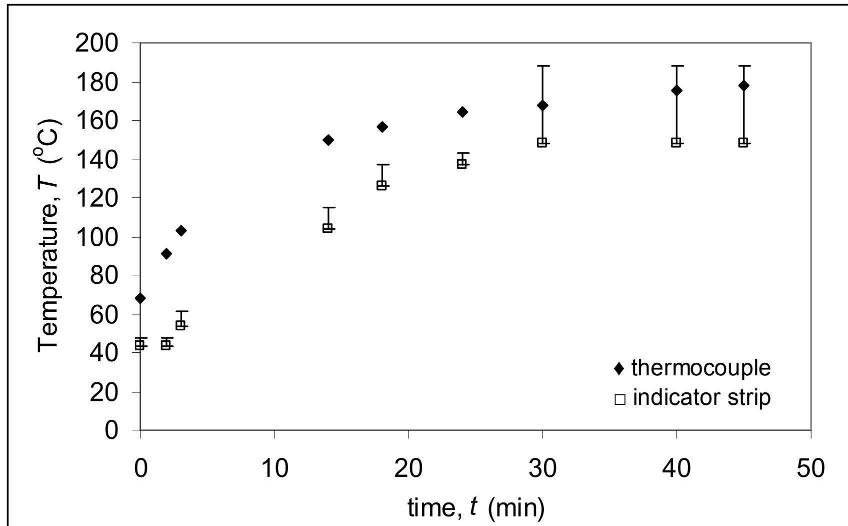

Figure D.2.1. Temperature during heating before deposition, as measured by a thermocouple near the substrate holder (~1 cm; see Fig. 3.3) and temperature indicator strips on the substrate holder (see Fig. 3.4). The measurements were done under vacuum.

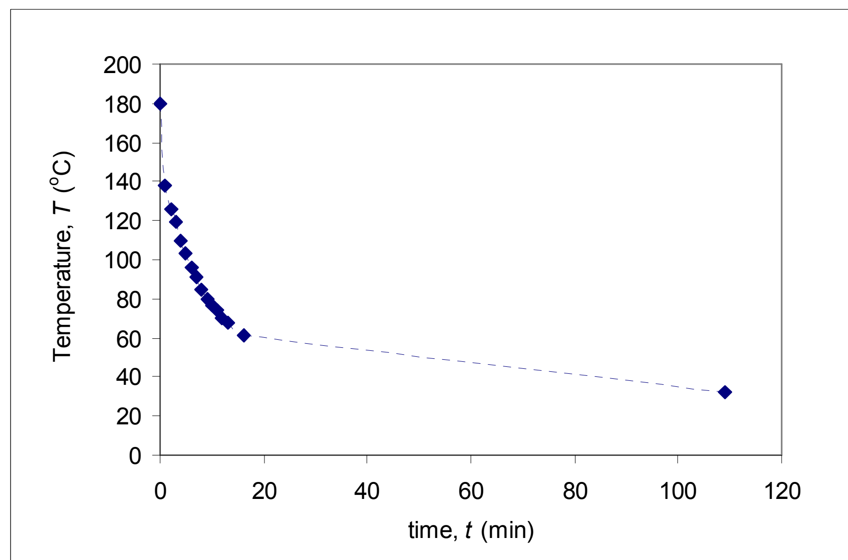

Figure D.2.2. Temperature during cooling after deposition, as measured by a thermocouple near the substrate holder (~1 cm; see Fig. 3.3). The conditions were: V_{Ar} = 20 cm^3/min, p_{Ar} = 0.02 mbar, turbo pump at full speed.

E. Optical Transmittance Measurements

E.1. Experimental Procedure

As discussed in Chapter 1, ZnO is an important transparent conductive oxide material. For this reason, the optical transmission of the stressed films was measured, both before and after thermal annealing. The measurements were performed with a ultraviolet–visible–near infrared (UV–VIS–NIR) spectrophotometer (Schimadzu 3150) in the 1000–200 nm range (Fig. E.1.1). The light from the lamp was chopped of with a 2 mm-wide slit, and the corresponding beam was 2 mm wide and 16 mm high. Two different light sources were used: the tungsten halogen lamp provided the light with 1000–300 nm wavelength (NIR–VIS), and the deuterium (D_2) lamp in the 300–200 nm wavelength range (UV). Two different types of detectors were the PbS cell for near-infrared and the photomultiplier tube for ultra violet radiation ranges. The switching between these two detectors was done at 850 nm. A baseline correction was performed prior to each measurement. The sample scan was normalized with respect to the empty reference (Fig. E.1.2). The sampling interval was 0.5 nm.

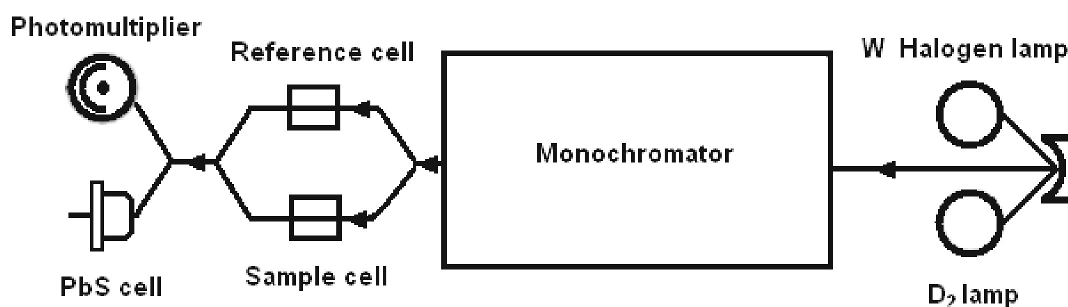

Figure E.1.1. The measurement set-up of the UV–VIS–NIR spectrophotometer.

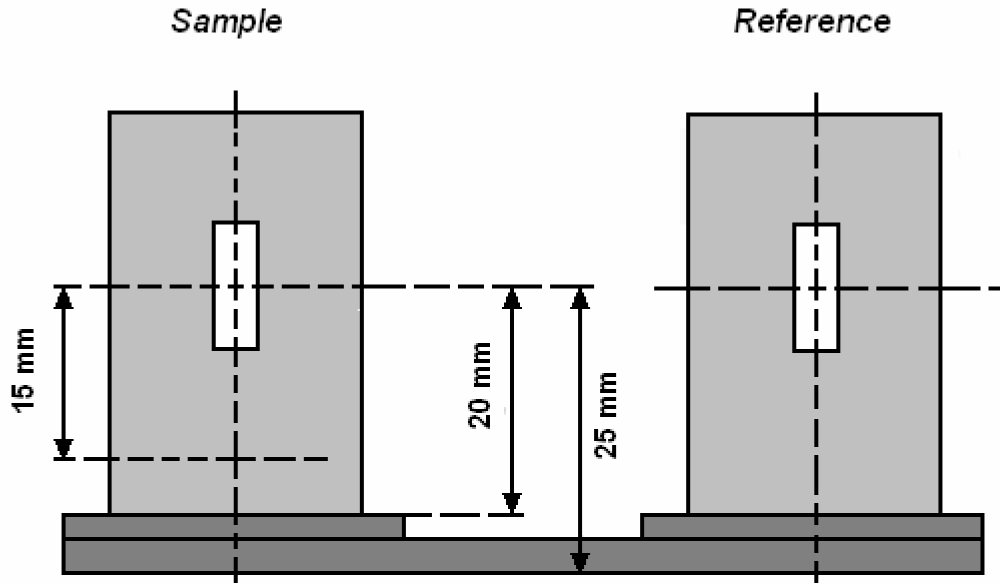

Figure E.1.2. The sample holder for the spectrophotometer. The sample was stuck vertically to the frame on the left, and the frame on the right was left empty for reference measurement. The beam passed through the hole inside each frame.

E.2. Results

The ZnO films were highly transparent (Fig. E.2.1) with the percent transmittance (%T) ranging from %74.809 to %89.203, depending on the deposition conditions and post-deposition treatments (Table E.2.1). The optical spectra results were compared as a function of T_s, p, and P_{RF}, in Fig. E.2.2–E.2.7. The %T amount at 600 nm, the maximum %T value (%T_{max}), and the wavelength at %T_{max} (λ_{max}) are presented in Table E.2.1. The λ_{max} values shifted to higher wavelengths as T_s was decreased or either p or P_{RF} was increased.

It should be noted that %T_{max} of the uncoated glass substrate was %91.389, and it was reached at 544 nm. Among the film samples, the closest %T to that of the bare substrate was reached when the film was annealed immediately after the deposition in the deposition chamber at 200 °C under vacuum for 30 min (Set 11; %90.857 at 545 nm). No linear relationship could be

Figure E.2.1. Transparent ZnO film on glass substrate.

Table E.2.1. Variation of residual stress in the (002) plane depending on the deposition conditions for ZnO films on glass substrate. See Table 3.1 for sample labels. For ease of comparison, the compressive stresses were listed in decreasing order. $\sigma_{c,ave}$ was calculated from Eq. 3.16a with the data from the (002) XRD peak for each sample. The error range is ±0.55 GPa.

Sample	T_s (°C)	P_{RF} (W)	p (mbar)	%T at 600 nm	%T_{max}	λ_{max} at %T_{max} (nm)
Glass substrate				91.051	91.389	544
Set9	200	125	0.02	80.513	90.462	518.5
Set8	200	125	0.2	83.432	89.737	530
Set5	200	125	0.4	86.157	89.709	648
Set2	200	100	0.4	84.554	89.317	705
Set7	RT	125	0.2	87.585	90.479	563
Set4	RT	125	0.4	84.499	89.789	657
Set3	RT	100	0.4	77.499	89.038	848.5
Set10*	200	100	0.2	74.809	84.425	411.5
Set11**	200	125	0.2	89.203	90.857	545
Set8-Ann. §	200	125	0.2	80.614	88.696	848
Set10-Ann.*,§	200	100	0.2	83.360	84.984	996
Set11-Ann.**,§	200	125	0.2	85.190	87.941	465

* 30 min annealing at 200 °C under vacuum in the chamber.
** 30 min annealing at 200 °C in O_2:Ar (2:5 v/v) in the chamber.
§ 6 h annealing at 600 °C in air after deposition.

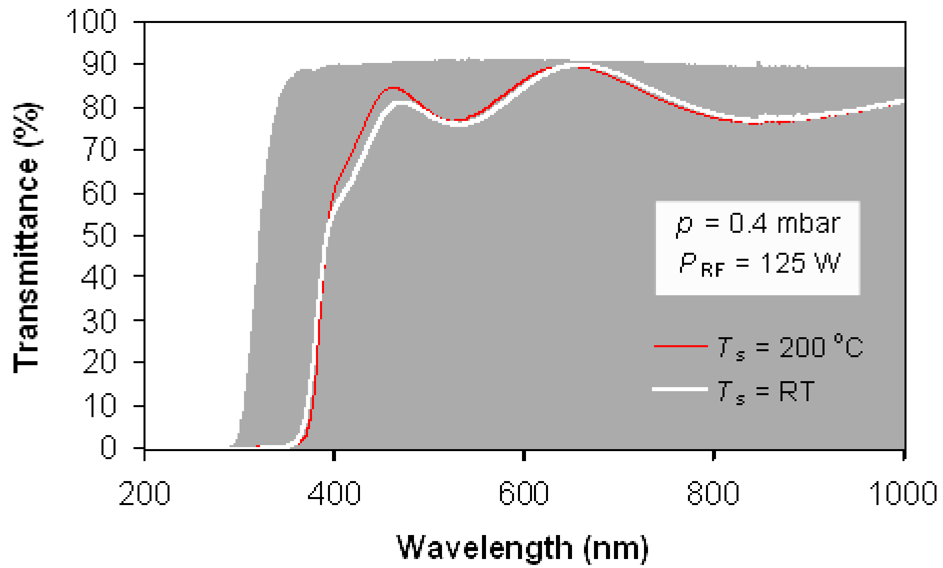

Figure E.2.2. Optical transmittance as a function of substrate temperature during deposition, at p = 0.4 mbar and P_{RF} = 125 W. The T_s values were 200 °C (Set 5) and RT (Set 4). (The shaded area represents the transmittance of the glass substrate.)

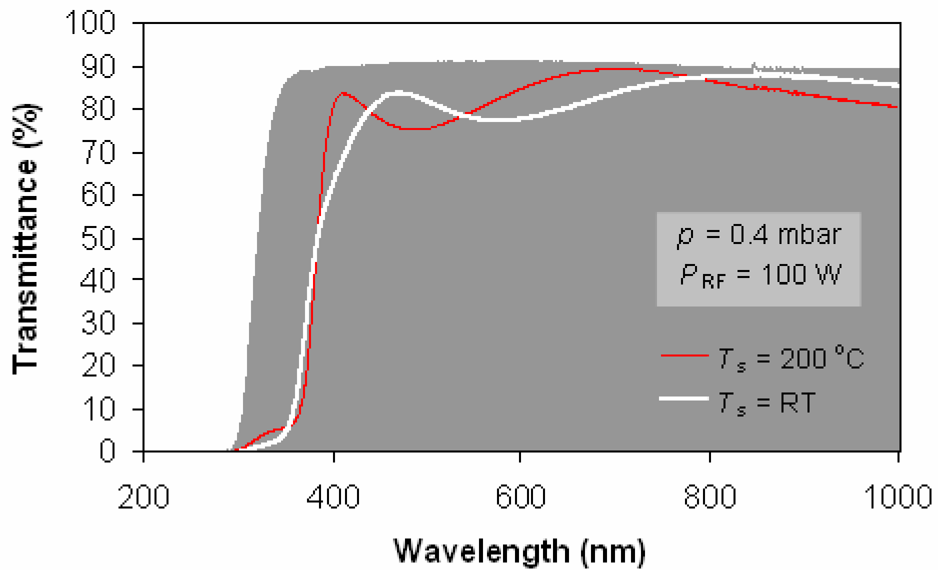

Figure E.2.3. Optical transmittance as a function of substrate temperature during deposition, at p = 0.4 mbar and P_{RF} = 100 W. The T_s values were 200 °C (Set 2) and RT (Set 3). (The shaded area represents the transmittance of the glass substrate.)

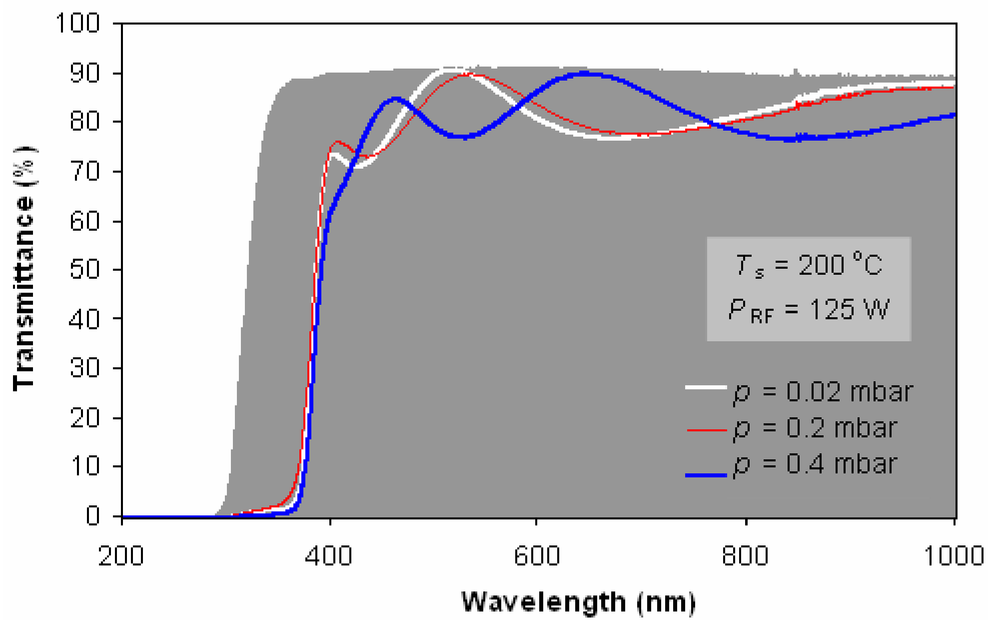

Figure E.2.4. Optical transmittance as a function of chamber (argon) pressure during deposition, at T_s = 200 °C and P_{RF} = 125 W. The pressure values were 0.02 mbar (Set 9), 0.2 mbar (Set 8), and 0.4 mbar (Set 5). (The shaded area represents the transmittance of the glass substrate.)

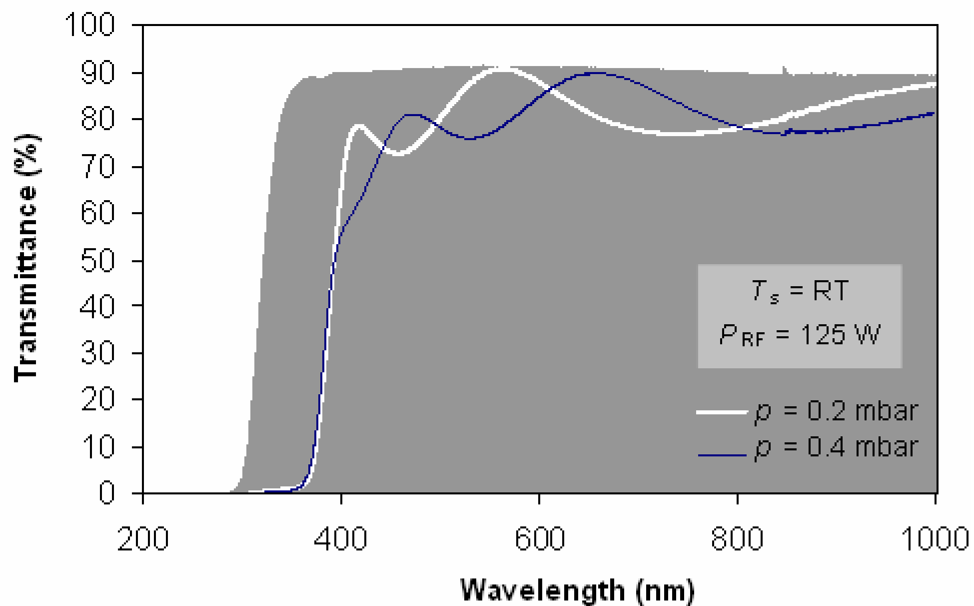

Figure E.2.5. Optical transmittance as a function of chamber (argon) pressure during deposition, at T_s = RT and P_{RF} = 125 W. The pressure values were 0.2 mbar (Set 7) and 0.4 mbar (Set 4). (The shaded area represents the transmittance of the glass substrate.)

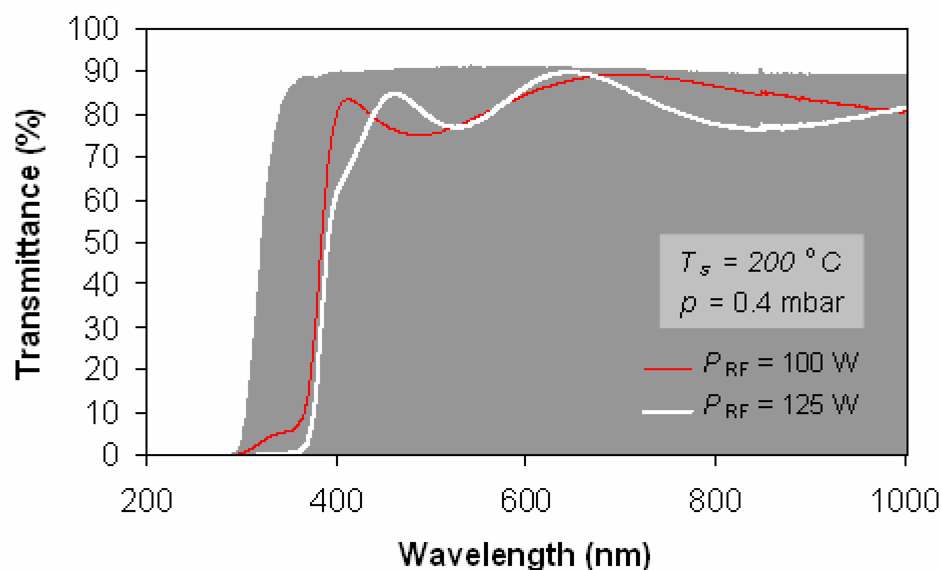

Figure E.2.6. Optical transmittance as a function of RF power during deposition, at T_s = 200 °C and p =0.4 mbar. The P_{RF} values were 100 W (Set 2) and 125 W (Set 5). (The shaded area represents the transmittance of the glass substrate.)

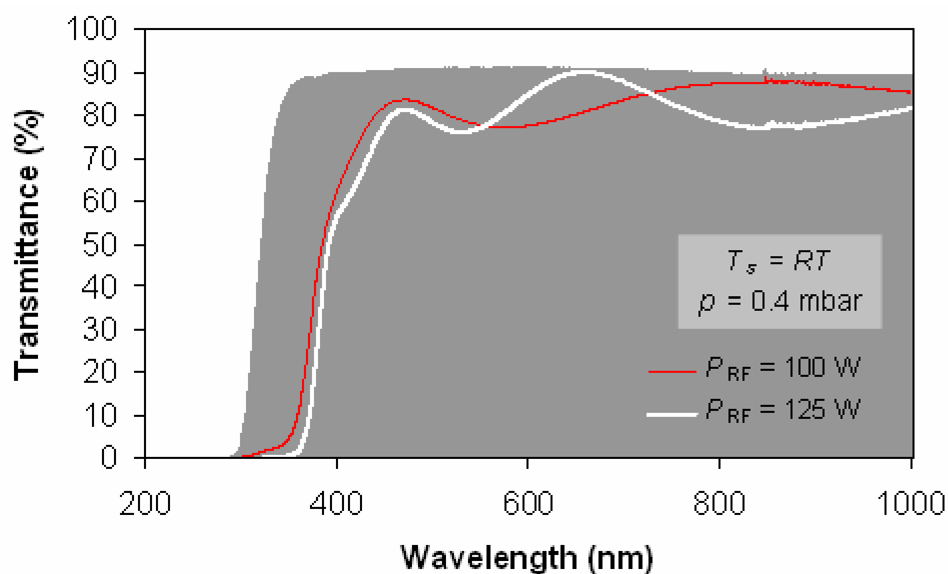

Figure E.2.7. Optical transmittance as a function of RF power during deposition, at T_s = RT and p =0.4 mbar. The P_{RF} values were 100 W (Set 3) and 125 W (Set 4). (The shaded area represents the transmittance of the glass substrate.)

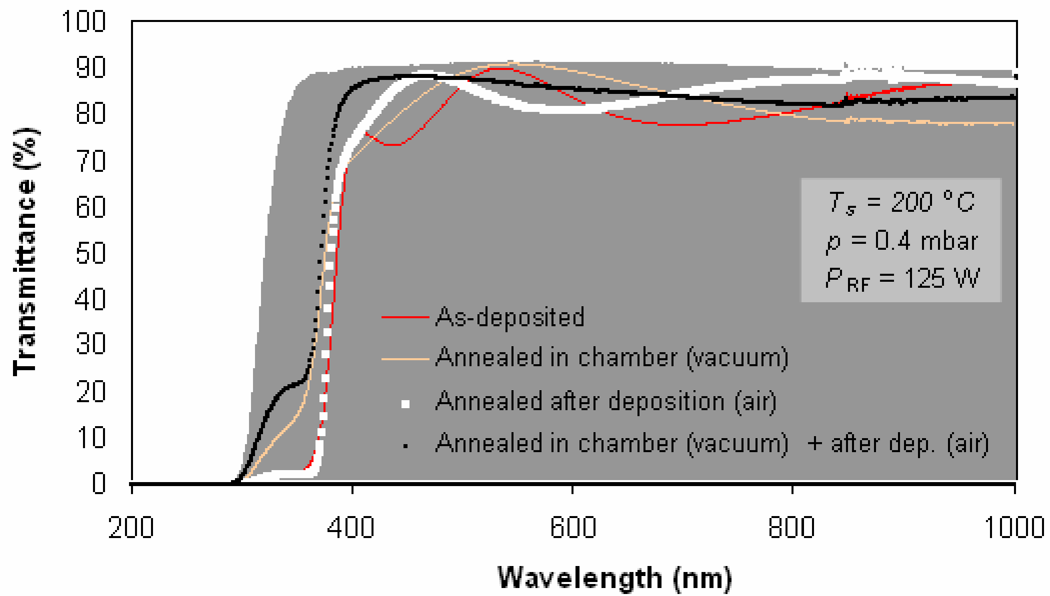

Figure E.2.8. Optical transmittance as influenced by annealing. The deposition conditions were: T_s = 200 °C, p = 0.2 mbar, and P_{RF} = 125 W (Set 8). The film sample was treated in the chamber at 200 °C for 30 min in O_2:Ar (2:3 v/v) atmosphere (Set 11). Post-deposition annealing was applied in air at 600 °C for 6 h to both the as-deposited and the in-chamber annealed samples. (The shaded area represents the transmittance of the glass substrate.)

BIBLIOGRAPHY

1. Chapman, B., *Glow Discharge Processes*, 1980, Wiley-Interscience, USA.

2. Pulker, H. K., *Coatings on Glass*, 2nd Ed., 1999, Elsevier Science, Amsterdam.

3. Granqvist, C. G., *Solar Energy Materials,* Advanced Materials, **15**(21), 1789 (2003).

4. Arbab, M., Shelestak, L. J., and Harris, C. S., *Value-Added Flat-Glass Products for the Building, Transportation Markets, Part 2,* American Ceramic Society Bulletin, **84**(4), 33 (2005).

5. Ginley, D. S. and Bright, C., *Transparent Conducting Oxides,* MRS Bulletin, 15 (2000).

6. Clarke, D. R. and Levi, C. G., *Materials Design for the Next Generation Thermal Barrier Coatings,* Annual Review of Materials Research, **33**, 383 (2003).

7. Livingston, J. D., *Electronic Properties of Engineering Materials*, 1999, Wiley New York.

8. CERAC, *The Need for Alternate Transparent Conduction Oxides,* CERAC Coating Materials News, **11**(2) (2001).

9. CERAC, *Transparent Conductive Oxides: ITO Replacements,* CERAC Coating Materials News, **15**(1) (2005).

10. Köhler, M., *Etching in Microsystem Technology*, 1999, Wiley-VCH Verlag GmbH, Weinheim, Germany.

11. Tian, Z. R., Voigt, J. A., Liu, J., McKenzie, B., McDermott, M. J., Rodriguez, M. A., Konishi, H., and Xu, H., *Complex and Oriented ZnO Nanostructures,* Nature Materials, **2**, 821 (2003).

12. Look, D. C., *Recent Advances in ZnO Materials and Devices,* Materials Science and Engineering B: Solid State Materials for Advanced Technology, **80**, 383 (2001).

13. Özgür, Ü., Alivov, Y. I., Liu, C., Teke, A., Reshchikov, M. A., Doğan, S., Avrutin, V., Cho, S.-J., and Morkoç, H., *A Comprehensive Review of ZnO Materials and Devices,* Journal of Applied Physics, **98**, 041301 (2005).

14. Van de Walle, C. G., *Defect Analysis and Engineering in ZnO,* Physica B, **308-310**, 899 (2001).

15. Niinistö, L., Päiväsaari, J., Niinistö, J., Putkonen, M., and Nieminen, M., *Advanced Electronic and Optoelectronic Materials by Atomic Layer Deposition: An Overview with Special Emphasis on Recent Progress in Processing of High-k Dielectrics and other Oxide Materials,* Physica Status Solidi A-Applied Research, **201**(7), 1443–1452 (2004).

16. Niesen, T. P. and De Guire, M. R., *Review: Deposition of Ceramic Thin Films at Low Temperatures from Aqueous Solutions,* Journal of Electroceramics, **6**, 169–207 (2001).

17. Ohta, H. and Hosono, H., *Transparent Oxide Optoelectronics,* Materials Today, **7**(6), 42 (2004).

18. Chiang, Y.-M., Brinie III, D., and Kingery, W. D., *Physical Ceramics*, The MIT Series in Materials Science and Engineering, 1997, John Wiley & Sons, Inc., USA.

19. Lee, G. H., Kawazoe, T., and Ohtsu, M., *Difference in Optical Bandgap between Zinc-blende and Wurtzite ZnO Structure Formed on Sapphire (0001) Substrate,* Solid State Communications, **124**, 163 (2002).

20. http://www.webmineral.com.

21. http://www.mindat.org.

22. Çuhadar, O. O., Özen, İ., and Gülgün, M. A., *Microwave Synthesis of ZnO Nanostrucutres,* Unpublished study, Sabancı University, (2004).

23. Baler, C. H., White, W. B., and Rustum, R., Science, **137**, 993 (1962).

24. Levin, E. M., Robbins, C. R., and McMurdie, H. F., *B. Metal Oxide Systems I. One Oxide*, in *ACERS-NIST Phase Equilibria Diagrams Compiled at the National Bureau of Standars*, Vol. II, 1969, American Ceramic Society, Inc. p. 76.

25. Ellmer, K., *Magnetron Sputtering of Transparent Conductive Zinc Oxide: Relation between the Sputtering Parameters and the Electronic Properties,* Journal of Physics D: Applied Physics, **33**, R17 (2000).

26. Hao, X.-T., Ma, J., Zhang, D.-H., Yang, T., Ma, H.-L., Yang, Y.-G., Cheng, C.-F., and Huang, J., *Thickness Dependence of Structural, Optical and Electrical Properties of ZnO:Al Films Prepared on Flexible Substrates,* Applied Surface Science, **183**(1-2), 137 (2001).

27. Ley, L., Pollak, R. A., McFeely, F. R., Kowalczyk, S. P., and Shirley, D. A., *Total Valence-band Densities of States of III-V and II-VI Compounds from X-ray Photoemission Spectroscopy,* Physical Review B, **9**(2), 600 (1974).

28. Xiong, G., Wilkinson, J., Tüzemen, S., Ucer, K. B., and Williams, R. T., *Toward a New Ultraviolet Diode Laser: Luminescence and p-n Junctions in ZnO Films*, in *Proceedings - SPIE The International Society for Optical Engineering*, 2003, SPIE, USA. p. 256.

29. Hao, X.-T., Ma, J., Zhang, D.-H., Yang, Y.-G., Ma, H.-L., Cheng, C.-F., and Liu, X.-D., *Comparison of the Properties for ZnO:Al Films Deposited on Polyimide and Glass Substrates,* Materials Science and Engineering B: Solid State Materials for Advanced Technology, **90**(1-2), 50 (2002).

30. Li, B. S., Liu, Y. C., Zhi, Z. Z., Shen, D. Z., Lu, Y. M., Zhang, J. Y., Kong, X. G., and Fan, X. W., *Effect of the Growth Temperature on ZnO Thin Films Grown by Plasma Enhanced Chemical Vapor Deposition,* Thin Solid Films, **414**(2), 170 (2002).

31. Tjhen, W., Tamagawa, T., Ye, C.-P., Hsueh, C.-C., Schiller, P., and Polla, D. L. *Properties of Piezoelectric Thin Films for Micromechanical Devices and Systems*. in *IEEE Micro Electro Mechanical Systems Workshop*. 1991. Nara, Japan, IEEE.

32. Look, D. C., Reynolds, D. C., Sizelove, J. R., Jones, R. L., Litton, C. W., Cantwell, G., and Harsch, W. C., *Electrical Properties of Bulk ZnO,* Solid State Communications, **105**(6), 399 (1997).

33. Kohan, A. F., Ceder, G., Morgan, D., and Van de Walle, C. G., *First-Principles Study of Native Point Defects in ZnO,* Physical Review B, **61**(22), 15019 (2000).

34. Minami, T., Sato, H., Nanto, H., and Takata, S., Jpn. J. Appl. Phys., **Part 2 24**, L781 (1985).

35. Park, C. H., Zhang, S. B., and Wei, S.-H., *Origin of p-Type Doping Difficulty in ZnO: The Impurity Perspective,* Physical Review B, **66**, 073202 (2002).

36. Tüzemen, S., Xiong, G., Wilkinson, J., Mischuck, B., Ucer, K. B., and Williams, R. T., *Production and Properties of p–n Junctions in Reactively Sputtered ZnO,* Physica B: Condensed Matter, **308-310**, 1197 (2001).

37. Kadota, M., Miura, T., and Minakata, M., *Piezoelectric and Optical Properties of ZnO Films Deposited by an Electron–Cyclotron-Resonance Sputtering System,* Journal of Crystal Growth, **237-239**(Part 1), 523 (2002).

38. Walukiewicz, W., *Defect Formation and Diffusion in Heavily Doped Semiconductors,* Physical Review B, **50**, 5221 (1994).

39. Walle, G. V. d., Laks, D. B., Neumark, G. F., and Pantelides, S. T., Phys. Rev. B, **47**, 9425 (1993).

40. Kucheyev, S. O., Bradby, J. E., Williams, J. S., Jagadish, C., and Swain, M. V., *Mechanical Deformation of Single-Crystal ZnO,* Applied Physics Letters, **80**(6), 956 (2006).

41. Trolier-McKinstry, S. and Muralt, P., *Thin Film Piezoelectrics for MEMS,* Journal of Electroceramics, **12**, 7 (2004).

42. Gualtieri, J., Kosinski, J., and Ballato, A., *Piezoelectric Materials for Acoustic Wave Applications,* IEEE Transactions on Ultrasonics, Ferroelectrics, and Frequency Control, **41**(1), 54 (1994).

43. Carlotti, G., Socino, G., Petri, A., and Verona, E. *Elastic Constants of Sputtered ZnO Films*. in *Ultrasonics Symposium, IEEE 1987*. 1987.

44. Dubois, M.-A. and Muralt, P., *Properties of Aluminum Nitride Thin Films for Piezoelectric Transducers and Microwave Filter Applications,* Applied Physics Letters, **74**(20), 3032 (1999).

45. Tsubouchi, K., Sugai, K., and Mikoshiba, N. *AlN Material Constants Evaluation and SAW Properties on AlN/Al2O3 and AlN/Si*. in *IEEE Ultrasonics Symposium, 1981*. 1981.

46. Ledermann, N., Muralt, P., Baborowski, J., Gentil, S., Mukati, K., Cantoni, M., Seifert, A., and Setter, N., *{1 0 0}-Textured, piezoelectric Pb(Zrx, Ti1-x)O3 Thin Films for MEMS: Integration, Deposition and Properties,* Sensors and Actuators A: Physical, **105**(2), 162 (2003).

47. Lu, C., Danzer, R., and Fischer, F. D., *Scaling of Fracture Strength in ZnO: Effects of Pore/Grain-Size Interaction and Porosity,* Journal of the European Ceramic Society, **24**, 3643 (2004).

48. Detavernier, C., Ozcan, A. S., Jordan-Sweet, J., Stach, E. A., Tersoff, J., Ross, F. M., and Lavoie, C., *An off-Normal Fibre-Like Texture in Thin Films on Single-Crystal Substrates,* Nature, **426**(6967), 641 (2003).

49. Birkholz, M., *Thin Film Analysis by X-ray Scattering*, 1rst Ed., 2006, Wiley-VCH, Weinheim.

50. Ohring, M., *The Material Science of Thin Films*, 1rst Ed., 1991, Academic Press, New Jersey.

51. Lakhtakia, A. and Messier, R., *Sculptured Thin Films - Nanoengineered Morphology and Optics*, 2004, SPIE, Washington.

52. Bunshah, R. F., *Handbook of Deposition Technologies for Films and Coatings: Science, Technology and Applications*, 1994, Noyes Publications.

53. Stokes, R. J. and Evans, D. F., *Thin Films - Solid-Solid Interfaces Processed from the Vapor Phase*, in *Fundamentals of Interfacial Engineering*, 1996, Wiley-VCH, Inc., New York.

54. Thornton, J. A., *The Microstructure of Sputter-Deposited Coatings,* Journal of Vacuum Science & Technology A: Vacuum, Surfaces, and Films, **4**, 3059 (1986).

55. Movchan, B. A. and Demchishin, A. V., *Investigation of the Structure and Properties of Thick Vacuum-Deposited Films of Nickel, Titanium, Tungsten, Alumina and Zirconium Dioxide,* Physics of Metals and Metallography, **28**(83), 653 (1969).

56. Thornton, J. A., *Influence of Apparatus Geometry and Deposition Conditions on the Structure and Topography of Thick Sputtered Coatings,* Journal of Vacuum Science and Technology, **11**, 666 (1974).

57. Thornton, J. A., *High Rate Thick Film Growth,* Annual Review of Materials Science, **7**(1), 239 (1977).

58. Grovenor, C. R. M., Hentzell, H. T. G., and Smith, D., *The Development of Grain Structure During Growth of Metallic Films,* Acta Metallurgica, **32**(5), 773 (1984).

59. Messier, R., Giri, A. P., and Roy, R. A., *Revised Structure Zone Model for Thin Film Physical Structure,* Journal of Vacuum Science and Technology A: Vacuum, Surfaces, and Films, **2**, 500 (1984).

60. Messier, R., *Toward Quantification of Thin Film Morphology,* Journal of Vacuum Science and Technology A: Vacuum, Surfaces, and Films, **4**, 490 (1986).

61. Messier, R., Krishnaswamy, S. V., Gilbert, L. R., and Swab, P., *Black a-Si Solar Selective Absorber Surfaces,* Journal of Applied Physics, **51**(3), 1611 (1980).

62. Messier, R. and Ross, R. C., *Evolution of Microstructure in Amorphous Hydrogenated Silicon,* Journal of Applied Physics, **53**(9), 6220 (1982).

63. Messier, R. and Trolier-McKinstry, S., *Processing of Ceramic Thin Films*, in *Encyclopedia of Materials: Science and Technology*, Ed: Mahajan, S., 2001, Elsevier, Amsterdam.

64. Meakin, P., *Fractal Scaling in Thin Film Condensation and Materials Surfaces,* Critical Reviews in Solid State and Materials Sciences, **13**(2), 143 (1987).

65. Müller, K. H., *Stress and Microstructure of Sputter-Deposited Thin Films: Molecular Dynamics Investigations,* Journal of Applied Physics, **62**(5), 1796 (2006).

66. Vaudin, M. D. *Accurate Texture Measurements on Thin Films Using a Powder X-Ray Diffractometer*. in *Twelfth International Conference on Texture of Materials*. 1999. Ottawa, National Research Council of Canada Research Press.

67. Detavernier, C., Lavoie, C., Jordan-Sweet, J., and Özcan, A., *Texture of Tetragonal a-FeSi2 films on Si(001),* Physical Review B, **69**(17), 174106 (2004).

68. Kennedy, K. *The Effect of Substrate Temperature on the Crystalline Properties of Metals and Alloys*. in *AVS Vacuum Metallurgical Conference*. 1968, American Vacuum Society.

69. Turk, C. F. and Marcus, H. L., *The Mechanical Properties of Physical Vapor Deposited Titanium,* Transactions of The Metallurgical Society of AIME, **242**(11), 2251 (1968).

70. Kocks, U. F., Tomé, N., and Wenk, H.-R., *Texture and Anisotropy: Preferred Orientations in Polycrystals and Their Effect on Material Properties*, 2000, Cambridge University Press, Cambridge.

71. Randle, V. and Engler, O., *Introduction to Texture Analysis: Macrotexture, Microtexture and Orientation Mapping*, 2000, Gordon & Breach.

72. Bunge, H. J., *Texture Analysis in Materials Science: Mathematical Methods*, 1982, Butterworths, London.

73. Novikov, V., *Grain Growth and Control of Microstructure and Texture in Polycrystalline Materials*, 1997, CRC Press Boca Raton.

74. Buckel, W., *Internal Stresses,* Journal of Vacuum Science and Technology, **6**(4), 606 (1969).

75. Withers, P. J. and Bhadeshia, H. K. D. H., *Residual Stress Part 2 – Nature and Origins,* Materials Science and Technology, **17**, 366 (2001).

76. Noyan, I. C., Huang, T. C., and York, B. R., *Residual Stress/Strain Analysis in Thin Films by X-Ray Diffraction,* Critical Reviews in Solid State and Materials Sciences, **20**(2), 125 (1995).

77. Wunderlich, W., *Ceramics Processing on Atomic Scale by Control of Interface Parameter,* InterCeram: International Ceramic Review, **51**(3), 190 (2002).

78. Yeom, H. Y., Lanier, C., Chason, E., and Paine, D. C., *Stress and Microstructure Evolution During the Deposition and Crystallization of Dc-Magnetron Sputter Deposited Amorphous ITO,* Proceedings of the Materials Research Society Symposium, **666**, F2.5.1 (2001).

79. Windischmann, H., *Intrinsic Stress in Sputter-Deposited Thin Films,* Critical Reviews in Solid State and Materials Sciences, **17**(6), 547 (1992).

80. Thornton, J. A. and Hoffman, D. W., *Stress-Related Effects in Thin Films,* Thin Solid Films, **171**(1), 5 (1989).

81. Chapman, B. N., *Thin-Film Adhesion,* Journal of Vacuum Science and Technology, **11**(1), 106 (1973).

82. Chen, C.-S., Liu, C.-P., Yang, H.-G., and Tsao, C.-Y. A., *Influence of Substrate Bias on Practical Adhesion, Toughness, and Roughness of Reactive DC-Sputtered Zirconium Nitride Films,* Journal of Vacuum Science and Technology A: Vacuum, Surfaces, and Films, **22**(5), 2041 (2004).

83. http://www.iof.fraunhofer.de/departments/optical-coatings/properties/index_e.html.

84. Wang, J.-S. and Evans, A. G., *Measurement and Analysis Of Buckling and Buckle Propagation in Compressed Oxide Layers on Superalloy Substrates,* Acta mater., **46**(14), 4993 (1998).

85. Leterrier, Y., Me´dico, L., Demarco, F., Manson, J.-A. E., Betz, U., Escola, M. F., Olsson, M. K., and Atamny, F., *Mechanical Integrity of Transparent Conductive Oxide Films,* Thin Solid Films, **460**, 156 (2004).

86. Hutchinson, J. W. and Suo, Z., *Mixed Mode Cracking in Layered Materials,* Advances in Applied Mechanics, **29**, 63–191 (1992).

87. He, M. Y., Evans, A. G., and Hutchinson, J. W., *Effects of Morphology on the Decohesion of Compressed Thin Films,* Physica Status Solid A: Applied Research, **166**, 19 (1998).

88. Faulhaber, S., Mercer, C., Moon, M.-W., Hutchinson, J. W., and Evans, A. G., *Buckling Delamination in Compressed Multilayers on Curved Substrates with Accompanying Ridge Cracks,* Journal of the Mechanics and Physics of Solids, **54**, 1004–1028 (2006).

89. Hutchinson, J. W., *Delamination of Compressed Films on Curved Substrates,* Journal of the Mechanics and Physics of Solids, **49**, 1847 – 1864 (2001).

90. Moon, M.-W., Chung, J.-W., Lee, K.-R., Oh, K. H., Wang, R., and Evans, A. G., *An Experimental Study of the Influence of Imperfections on the Buckling of Compressed Thin Films,* Acta Materialia, **50**, 1219 (2002).

91. Evans, A. G. and Hutchinson, J. W., *Mechanics of Delamination and Spalling in Compressed Films,* International Journal of Solids and Structures, **20**(5), 455 (1984).

92. Cook, R. F. and Suo, Z., *Mechanisms Active during Fracture under Constraint,* MRS Bulletin - Materials Research Society, **27**(Part 1), 45 (2002).

93. Chen, J. and Bull, S. J. *Assessment of the Adhesion of Ceramic Coatings*. in *CIMTEC 2006: 11th International Ceramics Congress and 4th Forum on New Materials*. 2006. Acireale, Sicily, Italy.

94. Chen, J. and Bull, S. J., *Assessment of the Toughness of Thin Coatings Using Nanoindentation under Displacement Control,* Thin Solid Films, **494**, 1 (2006).

95. Water, W. and Chu, S.-Y., *Physical and Structural Properties of ZnO Sputtered Films,* Materials Letters, **55**, 67 (2002).

96. Bachari, E. M., Baud, G., Ben Amor, S., and Jacquet, M., *Structural and Optical Properties of Sputtered ZnO Films,* Thin Solid Films, **348**, 165 (1999).

97. Kim, K. S., Kim, H. W., and Kim, N. H., *Growth of ZnO Thin Film on SiO_2 Substrates by the Rf Magnetron Sputtering Method,* Journal of Materials Science Letters, **22**, 1155 (2003).

98. Jou, J.-H., Han, M.-Y., and Cheng, D.-J., *Substrate Dependent Internal Stress in Sputtered Zinc Oxide Thin Films,* Journal of Applied Physics, **71**(9), 4333 (1992).

99. Bachari, E. M., Ben Amor, S., Baud, G., and Jacquet, M., *Photoprotective Zinc Oxide Coatings on Polyethylene Terephthalate Films,* Materials Science and Engineering B, **79**, 165 (2001).

100. Chang, Y.-S. and Ting, J.-M., *Growth of ZnO Thin Films and Whiskers,* Thin Solid Films, **398-399**, 29 (2001).

101. Exarhos, G. J. and Sharma, S. K., *Influence of Processing Variables on the Structure and Properties of ZnO Films,* Thin Solid Films, **270**, 27 (1995).

102. Giancaterina, S., Ben Amor, S., Bachari, E. M., Baud, G., Jacquet, M., and Perrin, C., *Elaboration and Adhesion of Zinc Oxide Coatings on Poly-Ether-Ether-Ketone Films,* Surface and Coatings Technology, **138**, 84 (2001).

103. Giancaterina, S., Ben Amor, S., Baud, G., Gardette, J. L., Jacquet, M., Perrin, C., and Rivaton, A., *Photoprotective Ceramic Coatings on Poly(Ether Ether Ketone),* Polymer, **43**, 6397 (2002).

104. Han, B. M., Chang, S., and Kim, S. Y., *Chopping Effect on the Crystallinity of ZnO Films Prepared by an R. F. Planar Magnetron Sputtering Method,* Thin Solid Films, **338**, 265 (1999).

105. Heideman, R. G., Lambeck, P. V., and Gardeniers, J. G. E., *High Quality ZnO Layers with Adjustable Refractive Indices for Integrated Optics Applications,* Optical Materials, **4**(6), 741 (1995).

106. Tvaro, V., Novotny, I., Cerven, I., Kovac, J., and Lacko, T., *R.f. Reactive Sputtering of Zinc Oxide Films on Silicon and Si-SiO2-TiN Substrates,* Sensors and Actuators A: Physical, **30**(1-2), 123 (1992).

107. Croitoru, N., Seidman, A., and Yassin, K., *Some Physical Properties of ZnO Sputtered Films,* Thin Solid Films, **150**(2-3), 291 (1987).

108. Xue, Z. Y., Zhang, D. H., Wang, Q. P., and Wang, J. H., *The Blue Photoluminescence Emitted from ZnO Films Deposited on Glass Substrate by R. F. Magnetron Sputtering,* Applied Surface Science, **195**, 126 (2002).

109. Dumont, E., Dugnoille, B., and Bienfait, S., *Simultaneous Determination of the Optical Properties and of the Structure of R. F.-Sputtered ZnO Thin Films,* Thin Solid Films, **353**, 93 (1999).

110. Krupanidhi, S. B. and Sayer, M., *Position and Pressure Effects in R. F. Magnetron Reactive Sputter Deposition of Piezoelectric Zinc Oxide,* Journal of Applied Physics, **56**(11), 3308 (1984).

111. Gong, H., Wang, Y., Yan, Z., and Yang, Y., *The Effect of Deposition Conditions on Structure Properties of Radio Frequency Reactive Sputtered Polycrystalline ZnO Films,* Materials Science in Semiconductor Processing, **5**(1), 31 (2002).

112. Zhang, Y., Du, G., Liu, D., Wang, X., Ma, Y., Wang, J., Yin, J., Yang, X., Hou, X., and Yang, S., *Crystal Growth of Undoped ZnO Films on Si Substrates under*

Different Sputtering Conditions, Journal of Crystal Growth, **243**(3-4), 439 (2002).

113. Subramanyam, T. K., Naidu, S. B., and Uthanna, S., *Effect of Substrate Temperature on The Physical Properties of DC Reactive Magnetron Sputtered ZnO Films,* Optical Materials, **13**, 239 (1999).

114. Ataev, B. M., Kamilov, I. K., Bagamadova, A. M., Mamedov, V. V., Omaev, A. K., and Rabadanov, M. K., *Epitaxial ZnO Films on Non-Crystalline Substrates,* Materials Science and Engineering B, **68**, 56 (1999).

115. Meng, L. and dos Santos, M. P., *Direct Current Reactive Magnetron Sputtered Zinc Oxide Thin Films- The Effect of The Sputtering Pressure,* Thin Solid Films, **250**(1-2), 26 (2002).

116. Kamalasanan, M. N. and Chandra, S., *Sol-Gel Synthesis of ZnO Thin Films,* Thin Solid Films, **288**, 112 (1996).

117. Dinescu, M. and Verardi, P., *ZnO Thin Film Deposition By Laser Ablation of Zn Target in Oxygen Reactive Atmosphere,* Applied Surface Science, **106**, 149 (1996).

118. Liu, Z. G., Hu, W. S., Guo, X.-L., Zhu, S. N., Feng, D., and Lin, C., *Preparation of c-Axis Oriented ZnO Optical Waveguiding Films on Fused Silica by Pulsed Laser Reactive Ablation,* Materials Letters, **25**(1-2), 5 (1995).

119. Makino, T., Isoya, G., Segawa, Y., Chia, C. H., Yasuda, T., Kawasaki, M., Ohtomo, A., Tamura, K., and Koinuma, H., *Optical Spectra in ZnO Thin Films on Lattice-Matched Substrates Grown with Laser-MBE Method,* Journal of Crystal Growth, **214-215**, 289 (2000).

120. Ohtomo, A., Kawasaki, M., Sakurai, Y., Yoshida, Y., Koinuma, H., Yu, P., Tang, Z. K., Wong, G. K. L., and Segawa, Y., *Room Temperature Ultraviolet Laser Emission From ZnO Nanocrystal Thin Films Grown by Laser MBE,* Materials Science and Engineering B, **54**, 24 (1998).

121. Zu, P., Tang, Z. K., Wong, G. K. L., Kawasaki, M., Ohtomo, A., Koinuma, H., and Segawa, Y., *Ultraviolet Spontaneous Emissions from ZnO Microcrystalline Thin Films at Room Temperature,* Solid State Communications, **103**(8), 459 (1997).

122. Mitra, A., Thareja, R. K., Ganesan, V., Gupta, A., Sahoo, P. K., and Kulkarni, V. N., *Synthesis and Characterization of ZnO Thin Films for UV Laser,* Applied Surface Science, **174**, 232 (2001).

123. Wang, X., Yang, S., Yang, X., Liu, D., Zhang, Y., Wang, J., Yin, J., Liu, D., Ong, H. C., and Du, G., *Zno Thin Film Grown on Silicon by Metal-Organic Chemical Vapor Deposition,* Journal of Crystal Growth, **243**(1), 13 (2002).

124. Ng, H. T., Li, J., Smith, M. K., Nguyen, P., Cassell, A., Han, J., and Meyyappan, M., *Growth of Epitaxial Nanowires at the Junctions of Nanowalls,* Science, **300**(5623), 1249 (2003).

125. Huang, M. H., Mao, S., Feick, H., Yan, H., Wu, Y., Kind, H., Weber, E., Russo, R., and Yang, P., *Room-Temperature Ultraviolet Nanowire Nanolasers,* Science, **292**(5523), 1897 (2001).

126. Dong, L., Jiao, J., Tuggle, D. W., Petty, J. M., Elliff, S. A., and Coulter, M., *ZnO Nanowires Formed on Tungsten Substrates and Their Electron Field Emission Properties,* Applied Physics Letters, **82**(7), 1096 (2003).

127. Keis, K., *Nanostructured Zinc Oxide Electrodes for Solar Cell Applications, PhD Thesis*. 2001, Uppsala Universitet (Sweden).

128. Ladenburger, A., Haupt, M., Sauer, R., Thonke, K., Xu, H., and Goedel, W. A., *Characterization of Regular ZnO and ZnxCd1-xO Nano-'Donuts' Cast in Particle Templated Porous Membranes,* Physica E, **17**, 489 (2003).

129. Park, W. I., Kim, D. H., Jung, S. W., and Yi, G.-C., *Metalorganic Vapor-Phase Epitaxial Growth of Vertically Well-Aligned ZnONanorods,* Applied Physics Letters, **80**(22), 4232 (2002).

130. Park, W. I., Jun, Y. H., Jung, S. W., and Yi, G.-C., *Excitonic Emissions Observed in ZnO Single Crystal Nanorods,* Applied Physics Letters, **82**(6), 964 (2003).

131. Xiong, G., Wilkinson, J., Lyles, J., Ucer, K. B., and Williams, R. T., *Luminescence and Stimulated Emission in Zinc Oxide Nanoparticles, Films, and Crystals,* Radiation Effects and Defects in Solids, **158**, 83 (2003).

132. Guo, L., Cheng, J. X., Li, X.-Y., Yan, Y. J., and Yang, S. H., *Synthesis and Optical Properties of Crystalline Polymer-Capped ZnO Nanorods,* Materials Science and Engineering C, **16**(1-2), 123 (2001).

133. Sayago, I., Aleixandre, M., Martinez, A., Fernandez, M. J., Santos, J. P., Gutierrez, J., Gracia, I., and Horrillo, M. C., *Structural Studies of Zinc Oxide Films Grown by RF Magnetron Sputtering,* Synthetic Metals, **148**(1), 37 (2004).

134. Polley, T. A., Cartera, W. B., and Poker, D. B., *Deposition of Zinc Oxide Thin Films by Combustion CVD,* Thin Solid Films, **357**, 132 (1999).

135. Polley, T. and Carter, W., *Zone Model for Zinc Oxide Deposited by Combustion Chemical Vapor Deposition,* Thin Solid Films, **384**(2), 177 (2001).

136. Mirica, E., Kowach, G., and Du, H., *Modified Structure Zone Model to Describe the Morphological Evolution of ZnO Thin Films Deposited by Reactive Sputtering,* Crystal Growth and Design, **4**(1), 157 (2004).

137. Mirica, E., Kowach, G., Evans, P., and Du, H., *Morphological Evolution of ZnO Thin Films Deposited by Reactive Sputtering,* Crystal Growth and Design, **4**(1), 147 (2004).

138. Cebulla, R., Wendt, R., and Ellmer, K., *Aluminium-Doped Zinc Oxide Films Deposited by Simultaneous RF-and DC-Excitation of a Magnetron Plasma: Relationships Between Plasma Parameters and Structural and Electrical Properties of the Films,* Journal of Applied Physics, **83**, 1087–95 (1998).

139. Minami, T., Sato, H., Takata, S., Ogawa, N., and Mouri, T., *Large-Area Milky Transparent Conducting Al-Doped ZnO Films Prepared by Magnetron Sputtering,* Japanese Journal of Applied Physics, **31**, L1106 (1992).

140. Lim, W. T. and Lee, C. H., *Highly Oriented ZnO Thin Films Deposited on Ru/Si Substrates*. Thin Solid Films. Vol. 353. 1999.

141. Bang, K.-H., Hwang, D.-K., and Myoung, J.-M., *Effects of ZnO Buffer Layer Thickness on Properties of Zno Thin Films Deposited by Radio-Frequency Magnetron Sputtering,* Applied Surface Science, **207**(1-4), 359 (2003).

142. Muthukumar, S., Gorla, C. R., Emanetoglu, N. W., Liang, S., and Lu, Y., *Control of Morphology and Orientation of ZnO Thin Films Grown on SiO2/Si Substrates,* Journal of Crystal Growth, **225**(2-4), 197 (2001).

143. Coleman, V. A., Bradby, J. E., Jagadish, C., Munroe, P., Heo, Y. W., Pearton, S. J., Norton, D. P., Inoue, M., and Yano, M., *Mechanical Properties of ZnO Epitaxial Layers Grown on a- and c- Axis Sapphire,* Applied Physics Letters, **86**, 203105 (2005).

144. Page, T. F., Riester, L., and Hainsworth, S. V., *Fundamentals of Nanoindentation and Nanotribology*, in *Proceedings of Materials Research Society Symposium*, Vol. 522, Ed: Baker, S. P., 1998, MRS, Warrendale, PA. p. 113.

145. Bradby, J., Williams, J., and Swain, M., *Pop-in Events Induced by Spherical Indentation In Compound Semiconductors,* Journal of Materials Research, **19**(1), 380 (2004).

146. Navamathavan, R., Kim, K.-K., Hwang, D.-K., Park, S.-J., Hahn, J.-H., Lee, T. G., and Kim, G.-S., *A Nanoindentation Study of The Mechanical Properties of*

ZnO Thin Films on (0 0 0 1) Sapphire, Applied Surface Science, **253**(2), 464 (2006).

147. Rossington, C., Evans, A. G., Marshall, D. B., and Khuri-Yakub, B. T., *Measurements of Adherence of Residually Stressed Thin Films by Indentation. II. Experiments with ZnO/Si,* Journal of Applied Physics, **56**(10), 2639 (1984).

148. Huang, B., Zhao, M.-H., and Zhang, T.-Y., *Indentation Fracture and Indentation Delamination in ZnO film/Si Substrate Systems,* Philosophical Magazine, **84**(12), 1233 (2004).

149. Maniv, S., Westwood, W. D., and Colombini, E., *Pressure and Angle of Incidence Effects in Reactive Planar Magnetron Sputtered ZnO Layers,* Journal of Vacuum Science and Technology, **20**(2), 162 (1982).

150. Hong, R., Huang, J., He, H., Fan, Z., and Shao, J., *Influence of Different Post-Treatments on the Structure and Optical Properties of Zinc Oxide Thin Films,* Applied Surface Science, (2004).

151. Gupta, V. and Mansigh, A., *Influence of Postdeposition Annealing on the Structural and Optical Properties of Sputtered Zinc Oxide Film,* Journal of Applied Physics, **80**(2), 1063 (1996).

152. Takada, S., *Relation between Optical Property and Crystallinity of ZnO Thin Films,* Journal of Applied Physics, **73**(10), 4739 (1993).

153. Aghamalyan, N. R., Gambaryan, A., Goulanian, E. K., Hovsepyan, R. K., Kostanyan, R. B., Petrosyan, S. I., Vardanyan, E. S., and Zerrouk, A. F., *Influence of Thermal Annealing on Optical and Electrical Properties of ZnO Films Prepared by Electron Beam Evaporation,* Semiconductor Science and Technology, **18**, 525 (2003).

154. Fang, Z. B., Yan, Z. J., Tan, Y. S., Liu, X. Q., and Wang, Y. Y., *Influence of Post-Annealing Treatment on the Structure Properties of ZnO Films,* Applied Surface Science, **241**(3-4), 303 (2004).

155. Gawlak, C. J. and Aita, C. R., *Stress Relief of Basal Orientation Zinc Oxide Thin Films by Isothermal Annealing,* Journal of Vacuum Science and Technology A, **1**(2), 415 (1983).

156. Cimpoiasu, A., van der Pers, N. M., de Keyser, T. H., and Venema, A., *Stress Control of Piezoelectric ZnO Films on Silicon Substrates,* Smart Materials and Structures, **5**(6), 744 (1996).

157. Tominaga, K., Umezu, N., Mori, I., Ushiro, T., Moriga, T., and Nakabayashi, I., *Effects of UV Light Irradiation and Excess Zn Addition on ZnO: Al Film Properties in Sputtering Process,* Thin Solid Films, **316**(1-2), 85 (1998).

158. Minami, T., Sato, H., Nanto, H., and Takata, S., *Group III Impurity Doped Zinc Oxide Thin Films Prepared by RF Magnetron Sputtering,* Japanese Journal of Applied Physics, **24**, L781 (1985).

159. Igasaki, Y. and Saito, H., *The Effects of Deposition Rate on the Structural and Electrical Properties of Zno: Al Films Deposited on (112¯0) Oriented Sapphire Substrates,* Journal of Applied Physics, **70**(7), 3613 (2006).

160. Bellingham, J. R., Phillips, W. A., and Adkins, C. J., *Intrinsic Performance Limits in Transparent Conducting Oxides,* Journal of Materials Science Letters, **11**(5), 263 (1992).

161. Ellmer, K., Kudella, F., Mientus, R., Schiek, R., and Fiechter, S., *Influence of Discharge Parameters on the Layer Properties of Reactive Magnetron Sputtered ZnO:Al Films,* Thin Solid Films, **247**(1), 15 (1994).

162. Wager, J. F., *Transparent Electronics,* Science, **300**, 1245 (2003).

163. Waits, R. K., *Planar Magnetron Sputtering*, in *Thin Film Processes*, Ed: Kern, W., 1978, Academic Press, London.

164. Davidse, P. D. and Maissel, L. I., *Dielectric Thin Films Through Rf Sputtering (RF Sputtering of Insulators, Noting Effects of Auxiliary Magnetic Field, Electrode Size, Oxygen Concentration, Substrate Temperature and Target Material on Thin Dielectric Film Formation),* Journal of Applied Physics, **37**, 574 (1966).

165. Davidse, P. D., *Theory and Practice of R.F. Sputtering (RF Sputtering of Insulators Noting Deposition Rate, Film Properties, etc),* Semiconductor Products and Solid State Technology, **9**, 30 (1966).

166. Wehner, G. K. and Anderson, G. S., *The Nature of Physical Sputtering*, in *Handbook of Thin Film Technology*, Ed: Glang, R., 1970, McGraw-Hill, New York, NY, USA. p. 3.9.

167. http://www.angstromsciences.com.

168. Thornton, J. A., *Influence of Substrate Temperature and Deposition Rate on Structure of Thick Sputtered Cu Coatings,* Journal of Vacuum Science and Technology, **12**, 830 (1975).

169. Penning, F. M., *Introduction of an Axial Magnetic Field in The Discharge Between Two Coaxial Cylinders,* Physica, **3**, 873–894 (1936).

170. Hoffman, R. W., *Physics of Nonmetallic Thin Films, NATO Advanced Study Institutes Series: Series B, Physics*, Ed: Cachard, A., 1976, Plenum Press, New York.

171. Oel, H. J. and Fréchette, V. D., *Stress Distribution in Multiphase Systems: I, Composites with Planar Interfaces,* Journal of American Ceramic Society, **50**(10), 542–49 (1967).

172. Han, M.-Y. and Jou, J.-H., *Determination of the Mechanical Properties of R.F.-Magnetron-Sputtered Zinc Oxide Thin Films on Substrates,* Thin Solid Films, **260**(1), 58 (1995).

173. Simmons, G. and Wang, H., *Single Crystal Elastic Constants and Calculated Aggragate Properties*, 1971, M.I.T., Cambridge, Massachusetts.

174. Krishnan, R. S., Srinivasan, R., and Devanarayanan, S., *Thermal Expansion of Crystals*, 1979, Pergamon Press, Oxford.

175. Perry, A. J., Sue, J. A., and Martin, P. J., *Practical Measurement of the Residual Stress in Coatings,* Surface and Coatings Technology, **81**(1), 17 (1996).

176. Atar, E., Sarioglu, C., Demirler, U., Kayali, E. S., and Cimenoglu, H., *Residual Stresses in (Zr,Hf)N Films (up to 11.9 at.% Hf) Measured by X-Ray Diffraction Using Experimentally Calculated XECs,* Surface and Coatings Technology, **191**, 188 (2005).

177. Badawi, F. and Villain, P., *Stress and Elastic-Constant Analysis by X-Ray Diffraction in Thin Films,* Journal of Applied Crystallography, **36**(3), 869 (2003).

178. Atar, E., Sarioglu, C., Demirler, U., Kayali, E. S., and Cimenoglu, H., *Residual Stress Estimation of Ceramic Thin Films by X-Ray Diffraction and Indentation Techniques,* Scripta Materialia, **48**(9), 1331 (2003).

179. Bhushan, B. and Li, X., *Nanomechanical Characterisation of Solid Surfaces and Thin Films,* International Materials Reviews, **48,**(40), 125 (2003).

180. Gelfi, M., Bontempi, E., Roberti, R., Armelao, L., and Deperoa, L. E., *Residual Stress Analysis of Thin Films and Coatings Through XRD2 Experiments,* Thin Solid Films, **450**, 143 (2004).

181. Gheeraert, E., Deneuville, A., Bonnot, L., and Abello, A. M., *Defects and Stress Analysis of the Raman Spectrum of Diamond Films,* Diamond and Related Materials, **1**(5-6), 504 (1992).

182. Merlani, E., Schmid, C., and Sergo, V., *Residual Stresses in Alumina/Zirconia Composites: Effect of Cooling Rate and Grain Size,* Journal of American Ceramic Society, **84**(12), 2962 (2001).

183. Pezzotti, G., *The Scanning Electron Microscope as a Tool for Experimental Nanomechanics,* JEOL News, **38**(1), 13 (2003).

184. Welzel, U., Ligot, J., Lamparter, P., Vermeulen, A., and Mittemeijer, E., *Stress Analysis of Polycrystalline Thin Films and Surface Regions by X-Ray Diffraction,* Journal of Applied Crystallography, **38**, 1 (2005).

185. Dally, J. and Riley, W., *Experimental Stress Analysis*, 1978, McGraw-Hill Book Company, New York.

186. Griffel, W., *Handbook of Formulas for Stress and Strain*, 1966, F. Ungar Pub. Co.

187. Eigenmann, B. and Macherauch, E., *Röntgenographische Untesuchung von Spannuungszuständen in Werkstoffen. II: Fortsetzung von Matwiss. und Werktofftechn. Heft 3/1995, S. 148-160,* Materialwissenschaft und Werkstofftechnik, **26**(4), 199 (1995).

188. Hauk, V., *Zum Stand der Bestimmung von Spannugen mit Beugungsverfahren,* HTM. Härterei-technische Mitteilungen, **50**(3), 138 (1995).

189. Dölle, H., Journal of Applied Crystallography, **12**, 489–501 (1979).

190. Kim, H. W. and Kim, N. H., *Annealing Effect for Structural Morphology of ZnO Film on SiO2 Substrates,* Materials Science in Semiconductor Processing, **7**, 1 (2004).

191. Kelly, P. J., Zhou, Y., and Postill, A., *A novel Technique for the Deposition of Aluminium-Doped Zinc Oxide Films,* Thin Solid Films, **426**(1-2), 111 (2003).

192. Campbell, S. A., *The Science and Engineering of Microelectronic Fabrication*, 2001, Oxford University Press, New York. p. 356.

193. Ramchal, R., *In Situ Magnetic Domain Imaging at The Spin-Reorientation Transition of Ultrathin Ni- and Fe/Ni-Films*. Fachbereich Physik. 2004, Universität Duisburg-Essen: Duisburg.

194. Grachev, S. Y., *Manipulation and Control of the Growth of Magnetic Iron Nitride Films, PhD Thesis*. 2003, Rijks Universiteit Groningen.

195. Chang, Y. A., Jan, C.-H., and Chen, C.-P., *Process for Preparing Schottky Diode Contacts with Predetermined Barrier Heights*. United States Patent 5516725. 1996, Wisconsin Alumni Research Foundation (Madison, WI).

196. Parsons, R., *Sputter Deposition Processes*, in *Thin Film Processes II*, Ed: Kern, W., 1991, Academic Press Limited, London.

197. Chakrabarti, S., Ganguli, D., and Chaudhuri, S., *Preparation of Hydroxide-Free Magnesium Oxide Films by an Alkoxide-Free Sol–Gel Technique,* Materials Letters, **57**(29), 4483 (2003).

198. Rancourt, J. D., *Optical Thin Films: User Handbook*, 1996, SPIE - The International Society for Optical Engineering, Washington.

199. Birch, W. R., *Coatings : An Introduction to the Cleaning Procedures*. 2000, The Sol-Gel Gateway (http://www.solgel.com/Tutorials/tutframe.htm).

200. Talim, S. P., *The Preparation of Optical Surfaces for Thin Film Deposition,* Optica Acta, **28**(10), 1405 (1981).

201. http://www.galleries.com/minerals/silicate/muscovit/muscovit.htm.

202. Groshart, E. C., *Pickling and Acid Dipping*, in *Metal Finishing: 67th Guidebook and Directory Issue*, Vol. 97, no 1, Ed: Murphy, M., 1999, Elsevier Science Inc., New York.

203. Lad, R. J., Funkenbusch, P. D., and Aita, C. R., *Postdeposition Annealing Behavior of Rf Sputtered ZnO Films,* Journal of Vacuum Science and Technology, **17**(4), 808 (1980).

204. STRESS, *Residual Stress Determination Software Manual, Bruker-AXS GmbH.*

205. JCPDS-Files, *XRD Database Maintenance Manual, Bruker-AXS GmbH.*

206. Hellwege, K. H. and Hellwege, A. M., *Numerical Data and Functional Relationships in Science and Technology, Landolt-Bornstein Series*, in *Landolt-Bornstein Series*, Vol. Group III, Vol. 2, 1969, Springer, Berlin. p. 58.

207. Wagers, R. S., *PhD Thesis, Stanford University*. 1972.

208. Zenxing, Q., Xiaozhong, Z., Mingzhou, Z., Xizhang, W., and Yujin, L., *A Modified ZnO Film Model for Calculating Elastic and Piezoelectric Properties,* Sonics and Ultrasonics, IEEE Transactions on, **32**(5), 630 (1985).

209. Cullity, B. D., *Elements of X-Ray Diffraction*, 2nd Ed., 1978, Addison-Wesley Publishing Company, USA.

210. Kajikawa, Y., *Texture Development of Non-Epitaxial Polycrystalline ZnO Films,* Journal of Crystal Growth, **289**(1), 387 (2006).

211. Yoshino, Y., Inoue, K., Takeuchi, M., and Ohwada, K., *Effects of Interface Micro Structure in Crystallization of ZnO Thin Films Prepared by Radio Frequency Sputtering,* Vacuum, **51**(4), 601 (1998).

212. Ow-Yang, C., Spinner, D., Shigesato, Y., and Paine, D., *A time-resolved reflectivity study of the amorphous-to-crystalline transformation kinetics in dc-magnetron sputtered indium tin oxide,* Journal of Applied Physics, **83**(1), 145 (2006).

213. Bandyopadhyay, S., Paul, G. K., Roy, R., Sen, S. K., and Sen, S., *Study of Structural and Electrical Properties of Grain-Boundary Modified ZnO Films Prepared by Sol-Gel Technique,* Materials Chemistry and Physics, **74**, 83 (2002).

214. Isa, S. A. and Ghosh, P. K., *Stress Relief in Ion-Beam Deposited ZnO Thin Films due to Post-Deposition Treatment,* Nuclear Instruments and Methods in Physics Research B: Beam Interactions with Materials and Atoms, **61**(4), 580 (1991).

215. Goldstein, J. I., Newbury, D. E., Echlin, P., Joy, D. C., Romig, J. A. D., Lyman, C. E., Fiori, C., and Lifshin, E., *Scanning Electron Microscopy and X-Ray Microanalysis: A text for Biologists, Materials Scientists, and Geologists*, 1992, Plenum Press, New York.

216. Hoffman, D. W. and Thornton, J. A., *Effects of Substrate Orientation and Rotation on Internal Stresses in Sputtered Metal Films,* Journal of Vacuum Science and Technology, **16**, 134 (1979).

217. Hoffman, D. W. and Thornton, J. A., *Internal Stresses in Sputtered Chromium,* Thin Solid Films, **40**, 355 (1977).

218. Srikant, V. and Clarke, D. R., *Optical Absorption Edge of ZnO Thin Films: The Effect of Substrate,* Journal of Applied Physics, **81**(9), 6357 (1997).

219. Floro, J. A., Chason, E., Cammarata, R. C., and Srolovitz, D. J., *Physical Origins of Intrinsic Stresses in Volmer–Weber Thin Films,* MRS Bulletin, **27**(1), 19 (2002).

220. Ye, J., Gu, S., Zhu, S., Chen, T., Hu, L., Qin, F., Zhang, R., Shi, Y., and Zheng, Y., *The Growth and Annealing of Single Crystalline ZnO Films by Low-Pressure MOCVD,* Journal of Crystal Growth, **243**(1), 151 (2002).

221. Neumann, G., in *Current Topics in Materials Science*, Vol. 7, Ed: Kaldis, E., 1981, North-Holland, Amsterdam. p. 280.

222. Hamilton, D. J. and Howard, W. G., *Basic Integrated Circuit Engineering*, 1975, McGraw-Hill.

223. Ma, K. J., Bloyce, A., and Bell, T., *Examination of Mechanical Properties and Failure Mechanisms of TiN and Ti-TiN Multilayer Coatings,* Surface and Coatings Technology, **76**, 297 (1995).

224. Yang, P., Yan, H., Mao, S., Russo, R., Johnson, J., Saykally, R., Morris, N., Pham, J., He, R., and Choi, H.-J., *Controlled Growth of ZnO Nanowires and Their Optical Properties,* Advanced Functional Materials, **12**(5), 323 (2002).

225. Rosenberg, R. and Ohring, M., *Void Formation and Growth During Electromigration in Thin Films,* Journal of Applied Physics, **42**(13), 5671 (1971).

VITA

İstem Özen was born on the 12th of September in Ankara, Turkey. She was raised in Ankara and she graduated from Gazi Anatolian High School in 1994. She received her Bachelor of Science degree in 1998 and her Master of Science degree in January 2001, both from the Chemical Engineering Department of Middle East Technical University, Ankara. Her Master of Science thesis title was "Thermal and Photocatalytic Oxidation of Carbon Monoxide over Titanium Dioxide—Effects of Platinum Deposition", and her thesis supervisor was Prof. Dr. Deniz Üner. During her M.S. period, she served as a teaching assistant in various chemical engineering core courses, including Heat Transfer in Radiating and Combusting Systems, Physical Chemistry, Fluid Mechanics, Chemical Process Calculations, and Chemical Engineering Laboratories for juniors and seniors.

She continued her graduate studies in Sabancı University, Istanbul under full scholarship, starting from February 2001. Her main research interest covered thin film processing and characterization for the analysis of residual stresses. She obtained her Doctor of Philosophy degree with top honors from the Material Science and Engineering program of Sabancı University in August 2006 under the supervision of Assoc. Prof. Dr. Mehmet Ali Gülgün. Her dissertation title is "RF Magnetron-Sputtered ZnO Thin Films: On the Evolution of Microstructure and Residual Stresses".

Between October 2000 and February 2007, she served as a teaching assistant for the junior and senior courses of the Materials Science and Engineering program including Introduction to Ceramics, Phase Equilibria, Composite Materials, Materials Science II, as well as the freshman and sophomore courses including Materials Science I, Thermodynamics, What is there in the Universe?, Science of Nature I, and Science of Nature II. She also supervised two freshman projects on slip casting of alumina and microwave-synthesis of ZnO nanostructures. She took responsibility the laboratory

orientation programs within the Faculty of Engineering and Natural Sciences on general laboratory safety and on the use of several laboratory equipments including the x-ray diffractometer, simultaneous thermal analyzer, Fourier transform infrared spectrophotometer, ultraviolet spectrophotometer, and dilatometer.

She published and presented her research work in several journals and conferences, which are listed below. With two of her works, she received the Graduate Student Silver Award in 14th International Conference on Surface Modification of Materials by Ion Beams (SMMIB 2005; 4–9th September 2005, Kuşadası, İzmir, Turkey) and the 3rd Best Oral Presentation Award in the 17th National Electron Microscopy Congress with International Participation (22–24th June 2005, Gebze, İzmit, Turkey).

REFEREED JOURNAL ARTICLES AND CONFERENCE PROCEEDINGS

1. Ozen, I. and Gulgun, M. A., *Residual Stress Relaxation and Microstructure in ZnO Thin Films*, Advances in Science and Technology, **45** (2006) 1316–1321
2. Ozen, I. and Gulgun, M. A., *ZnO İnce Film Kaplamaların Mikroyapısı ve Gerilme Analizi*, Proceedings of the 17th National Electron Microscopy Congress with International Participation (2005)
3. Ozen, I., Gulgun, M. A., and Ozcan, M., *Self-induced Crystallinity in RF Magnetron Sputtered ZnO Thin Films*, Key Engineering Materials, **264-268** (2004) 1225–1228
4. Uner, D., Tapan, N. A., Ozen, I. and Uner, M., *Oxygen Adsorption and Spillover on Pt/TiO_2 Catalysts,* Applied Catalysis A: General, **251** (2003) 225–234
5. Ozen, I. and Uner, D., *Heterogeneous Photo and Thermal Catalytic Oxidation of CO: Effects of Metal Deposition*, Studies in Surface Science and Catalysis, **133** (2001) 445–452
6. Uner, D. and Ozen, I., *Benzenin Pt/TiO_2 Üzerinde Termal ve Fotokatalitik Olarak Parçalanması Tepkimesi: Metalin Rolü Nedir?*, Proceedings of the 4th National Chemical Engineering Congress (2000)

REFEREED PRESENTATIONS

1. Ozen, I. and Gulgun, M. A., *Residual Stress Relaxation and Microstructure in ZnO Thin Films*, 11th International Ceramics Congress and 4th Forum of New Materials (CIMTEC 2006), 4–9th June 2006, Acireale (Catania), Sicily, Italy.
2. Ozen, I. and Gulgun, M. A., *ZnO İnce Film Kaplamaların Mikroyapısı ve Gerilme Analizi*, 17th National Electron Microscopy Congress with International Participation, 22–24th June 2005, Gebze, İzmit, Turkey.
4. Ozen, I., Chhay, B., Ichou, R., Gulgun, M. A., Ila, D., *Stress Relaxation in ZnO Thin Films by Ion Bombardment*, 14th International Conference on Surface Modification of Materials by

Ion Beams (SMMIB 2005), 4–9th September 2005, Kuşadası, İzmir, Turkey.

7. Ozen, I., Gulgun, M. A., Ow-Yang, C., and Ozcan, M., *Substrate-dependent Property Changes in RF Magnetron-sputtered ZnO Thin Films*, Micro and Nano Technology Workshop and Turkish-Greek-German Symposium on ''Polymers in Materials Science and Biology'', 4–5th October 2004, Koç University, Istanbul, Turkey.
8. Ozen, I., Gulgun, M. A., Ow-Yang, C., and Ozcan, M., *Optical Properties and Microstructure in r. f. Magnetron Sputtered ZnO Thin Films*, Material Research Society (MRS) 2004 Spring Meeting, 12–16th April 2004, San Francisco, CA, USA..
9. Ozen, I. and Gulgun, M. A., *Effects of Residual Stresses on the Microstructure and Optical Properties of RF Magnetron-Sputtered ZnO Thin Films*, 106th Annual Meeting and Exposition of the American Ceramic Society (ACerS), 18–21rst April 2004, Indianapolis, IN, USA.
10. Ozen, I., Gulgun, M. A., and Ozcan, M., *Self-induced Crystallinity in RF Magnetron Sputtered ZnO Thin Films*, 8th International Conference and Exhibition of the European Ceramic Society (ECERS), 29th June–3rd July 2003, Istanbul, Turkey.
11. Uner, D. and Ozen, I., *Elucidating the Mechanism of Pt/TiO_2 Interactions in the Gas Phase Photo-catalytic Oxidation of Organic Materials*, 18th North American Catalysis Society Meeting, 1–6th June 2003, Cancun, Mexico.
12. Ozen, I. and Uner, D., *Heterogeneous Photo and Thermal Catalytic Oxidation of CO: Effects of Metal Deposition*, 3rd International Symposium on Reaction Kinetics and the Development and Operation of Catalytic Processes, 22–25th April 2001, Oostende, Belgium.
13. Uner, D. and Ozen, I., *Benzenin Pt/TiO_2 Üzerinde Termal ve Fotokatalitik Olarak Parçalanması Tepkimesi: Metalin Rolü Nedir?*, 4th National Chemical Engineering Congress (UKMK), 4–7th September 2000, Istanbul.

Contact: istem@sabanciuniv.edu